The University Of Sheffield.

Investigation of material removal mechanism and thermal response of compressor abradable materials

Andreas Hadjisoteriou

A thesis submitted in partial fulfilment of the requirements for the degree of

Doctor of Philosophy

The University of Sheffield

Faculty of Engineering

Department of Mechanical Engineering

Submission Date

April 2022

Acknowledgements

First and foremost, I would like to express my gratitude to my supervisor Prof. Matthew Marshall for all the support and guidance throughout the duration of my PhD. His understanding and support during difficult and stressful times was extremely appreciated and it was very important toward achieving this feat.

In addition, I want to express my thanks and gratitude to everyone I have met from my industrial sponsor Rolls Royce Plc for providing the materials required to perform this research. Especially, I would like to thank Glen Pattinson, Lloyd Pallet and Mike Keanan who were my most frequent contacts with the sponsor. The numerous discussions we had during our meetings helped me to contexualise the importance of the research and refocus my research.

I would also like to thank all of my fellow PhD students who have worked with me throughout these year for all the support they provided, improving both my work and personal experience. I would like to give special thanks to Julian Garcia Panizo, Eldar Rahimov and Alvaro Parody Martin for all the fun times we had this time. I feel blessed to have met and worked with these people and I look forward to spending more time with them (outside the labs!).

Next, I would like to thank the very good friends I made in Sheffield all these years and especially Nicolas Poyiatzis and George Chrysostomou. Their emotional support provided a much needed relief during the stressful life as a PhD student.

Lastly, but most importantly, I would like to express my unconditional gratitude to my parents, Kyriakos and Sidonia Hadjisoteriou and my sister Anna Hadjisoteriou. Their love and support has been most reassuring during all the difficult times I faced these years and I hope they can celebrate and enjoy with me this accomplishment.

Abstract

Abradable linings are used in jet engines to minimise the clearances between rotary and stationary parts of the engine. The aim of this investigation was to assess the performance of two abradables used in the compressor stages of jet engines and to gain a better understanding on the underlying reasons that drive their wear behaviour. The abradables of interest in this study were Aluminium Silicon/polyester (AlSi/polyester) and Aluminium Silicon/hexagonal Boron Nitride (AlSi/hBN). These abradables were rubbed against a Titanium alloy blade (Ti-6A-4) using an experimental test rig developed at The University of Sheffield that accurately represents the actual contact in the engine. This thesis developed novel testing methodologies that provide a fundamental understanding of the material removal mechanism and heat response of the material during the contacts. Key findings in this investigation include the fact that AlSi/polymer abradable exhibits localised thermal response, which is more significant in the lowest incursion rates and leads to high adhesion and blade wear mechanisms. In contrast, AlSi/polyester has a more distributed heat dissipation resulting in more mild wear performance. However, at high incursion rates the response of the materials is governed by the ability of the hBN/polymer phases to provide a release mechanism. In the case of AlSi/hBN this is achieved to a high extent resulting in good cutting. In contrast, in AlSi/polymer less release is achieved, so the response of this material only improves partially with increasing incursion rates. The findings of this thesis can help the engine manufacturer understand what drives the performance of the considered materials and at what conditions their performance is more optimal. This might help the manufacturer to decide under what conditions to use these materials as well as how to improve them.

Contents

Chapter 1

Introduction

1.1 The problem

Aero-engine manufacturers are constantly seeking to increase engine efficiency and lower fuel consumption. A way to achieve this is to minimise the clearance between rotor blade tips and the stationary casing. Figure 1.1 shows a schematic of a typical jet engine highlighting the different stages found in it.

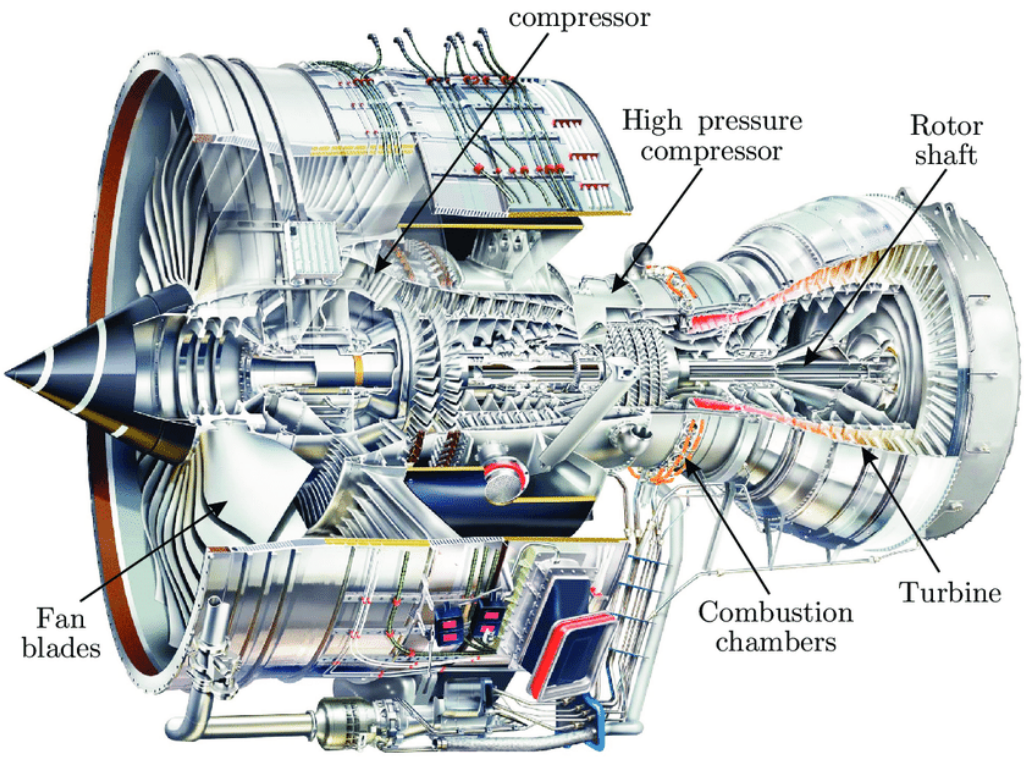

Figure 1.1: Schematic of jet engine showing different stages present in it [1].

At the presence of a high clearance, a pressure difference is generated between the suction and pressure sides of the blade. This results in leakage of the primary flow and aerodynamic losses [2, 3, 4]. On the other hand if the clearance is too small, contact between the blade and the casing may arise due to thermal expansion and centrifugal forces. At the occurrence of contact between the blade tip and the casing, the blade tip wears resulting in a permanently increased clearance and an undesired drop in efficiency (Figure 1.2, Case A). Moreover, excessive blade wear may lead to a catastrophic failure of the blade.

Since the late 1960's thermally sprayed abradable linings have been used on the inside of the casing to fill this clearance for this reason. These linings are composites that have high abradability and act as a sacrificial layer, which gets abraded when hit by a blade without damaging it, resulting in only a localised increase of the clearance (Figure 1.2, Case B). This effectively minimises the aerodynamic losses caused by secondary airflows by sealing the clearance and preserving the integrity of the blade, resulting in improved engine performance [5, 6]. An ideal abradable should wear in preference to the blade when contact occurs, whilst having high erosion resistance to withstand the high speed flows present in an engine. These flows are high speed air flows, which can contain particles such as sand or hail that can cause the abradable linings to erode. In addition, it is important that the surface of the of lining remains as smooth as possible after the contact with the blade to further minimise aerodynamic loses [7].

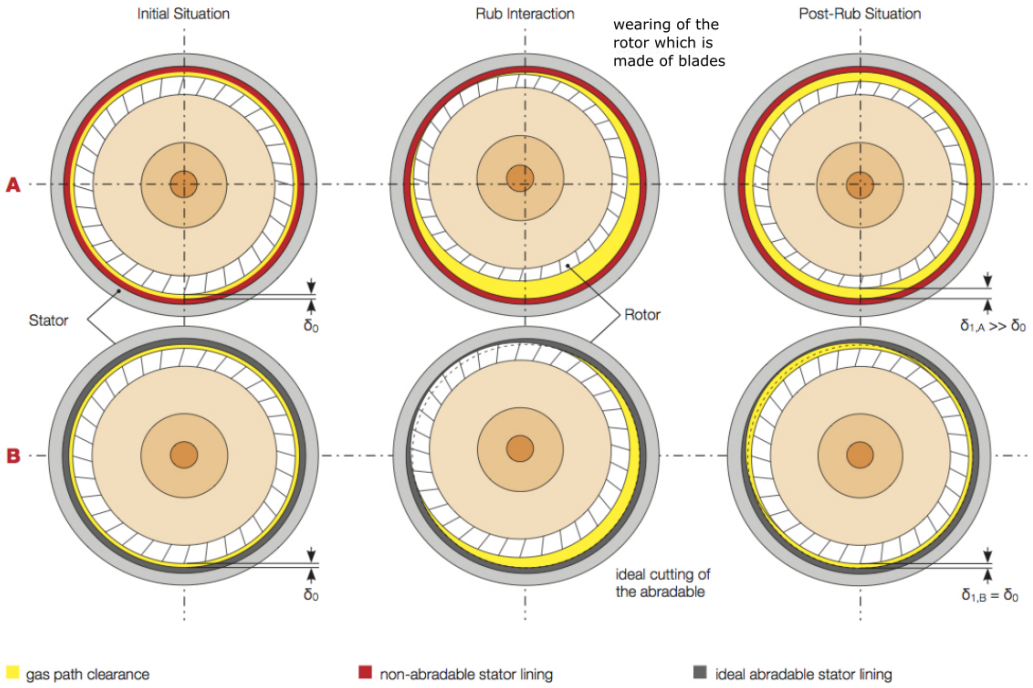

Figure 1.2: Difference in resulting clearances from contact of the blade tip with: A) no abradable lining and B) abradable lining [8].

Minimising blade tip clearances has clear economic benefits. It is estimated that by reducing the tip clearance by 25 μm in a high pressure turbine, an 0.1 percent reduction in the specific fuel consumption is achieved. This reflects to 0.02 billion gallons of fuel savings annually. This suggests that the optimisation of the abradable seal linings is an important step for the improvement of current engines and hence it is vital to establish a sound understanding on the mechanisms involved during their operation [9].

1.2 Material composition

The typical composition of an abradable material includes three structural components. The first one is a metal matrix, which provides the abradable's strength, while at the same time it protects it from oxidation and hot-corrosion [10, 11]. The second component is a dislocator phase and it is normally a solid lubricant. This second phase is designed to shear easily by providing a way for cracks to initialise and propagate. This provides the material with the required abradability and also helps to reduce the transfer of abradable material on the blade, as well as reducing the size of

the debris. This is essential since large debris particles can block cooling holes and also cause erosion further down in the engine [10, 12, 13].

Figure 1.3 shows characteristic images of the material composition of the abradables and it highlights the differences between a hard (R15Y 82) Metco 601 NS sample (1.3(a)) and a soft (R15Y 55) sample(1.3(c)). These materials are shown as examples because they are further considered later in this thesis. The light colour in the pictures represents the AlSi phase, while the darker spots represent the filler phase. It is apparent that in the case of the harder sample the amount of filler is less compared to the softer sample. Moreover, figure 1.3(e) illustrates the difference between the two abradables of interest at the same hardness.

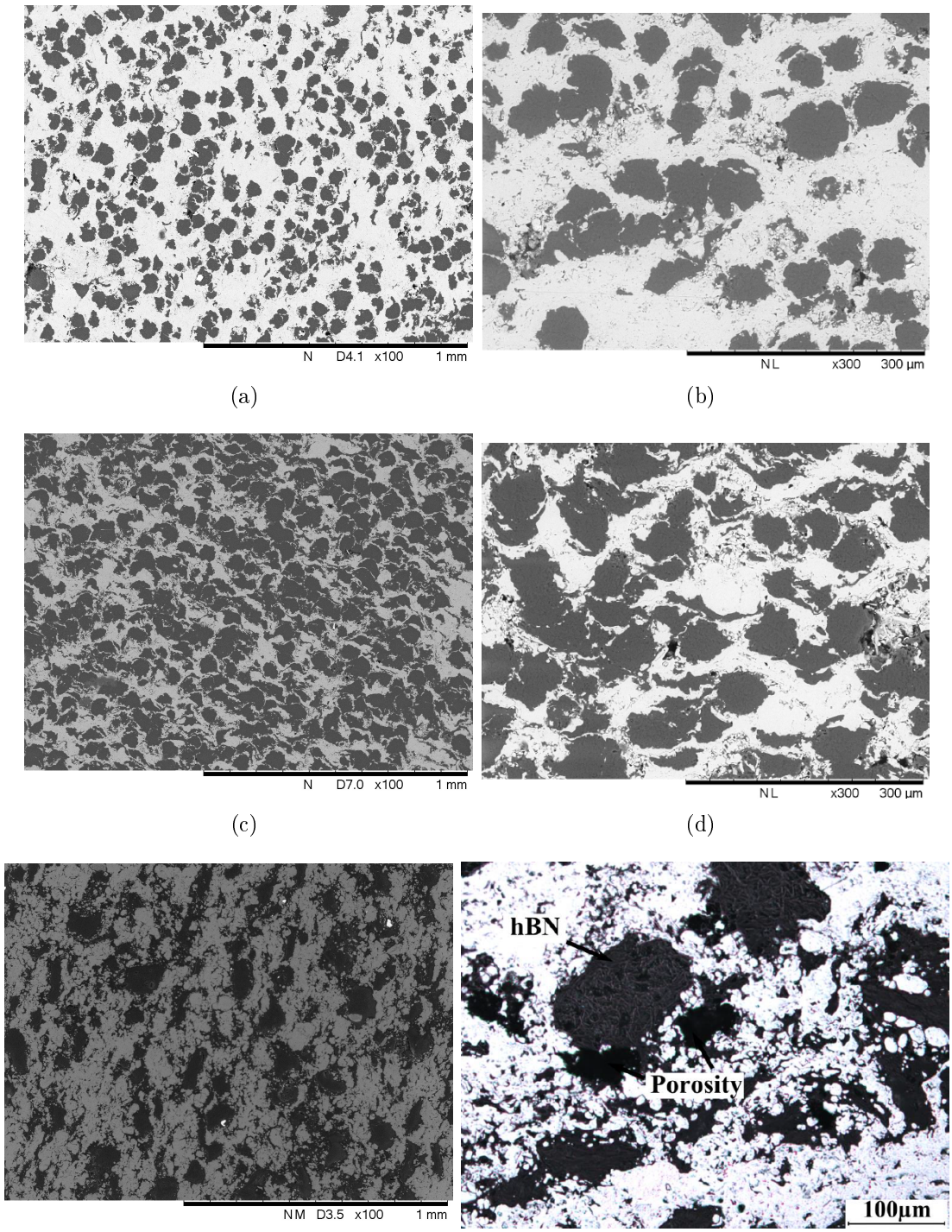

Figure 1.3: (a) SEM image of Metco 601 with hardness of R15Y 82, (b) SEM image of Metco 601 with hardness of R15Y 82 at higher magnification [14], (c) SEM image of Metco 601 with hardness of R15Y 55, (d) SEM image of Metco 601 with hardness of R15Y 55 at higher magnification [14], (e) SEM image of Metco 320 with hardness of R15Y 55, (f) SEM image of Metco 320 with hardness of R15Y 55 at higher magnification [15].

Furthermore, the hardness of the abradables is very important. This is because abradable materials should have high erosion resistance since they are subjected to high speed flows present in the compressor stages. These high speed air flows can contain particles such as sand and hail that can erode the abradable coating. Therefore, it can be concluded that an ideal abradable needs to be 'hard' enough to have adequate erosion resistance and withstand the high speed flows, while being 'soft' enough to wear instead of the blade (harder materials provide better erosion resistance [16]).

1.3 Wear mechanisms

Studies have shown [7] that there are a number of different wear mechanisms associated with abradable linings and blade tips, both in the compressor and the turbine stages. These wear mechanisms are divided into two categories: 1) contact and 2) non-contact mechanisms. Non-contact mechanisms include erosion, oxidation and corrosion and they are undesired mechanisms since they cause wear damage on the blade resulting to increased blade tip clearance. Moving specifically to the compressor, cutting is the desired contact mechanism since the blade effectively acts as a cutting tool and cleanly removes the abradable lining without wearing, resulting in only a localised increase in the blade tip clearance. Moreover, the rub on the lining is smooth ensuring minimal aerodynamic losses. Contact mechanisms include deformation, melting and tribo-oxidation and they are all undesired mechanisms because they cause wear damage to the blade. The final observed contact mechanism is temperature driven adhesive transfer, where temperatures generated are high enough to cause the abradable to stick on the blade. This results in grooving in the lining and is unwanted since it leads to aerodynamic losses. Moreover, when adhered material breaks off it can be carried down the engine causing cooling holes to block [7]. Figure 1.4 shows a summary of the blade wear mechanisms, which are commonly observed from in service blade samples.

A wide range of parameters affect which wear mechanisms occur in each case. Some of these parameters are mechanical properties of the contact, such as the blade tip vertical velocity and the incursion rate. Other parameters are properties that depend on the abradable such as its hardness, its thermal conductivity and what dislocator phase is present in the abradable. Studies aim to observe and characterise the wear mechanism by trying to replicate the contact either by full-scale, or scaled test rigs, or even simulation models. However, due to the complexity of monitoring the wear

mechanism during the contact most studies have been focused to post test observations.

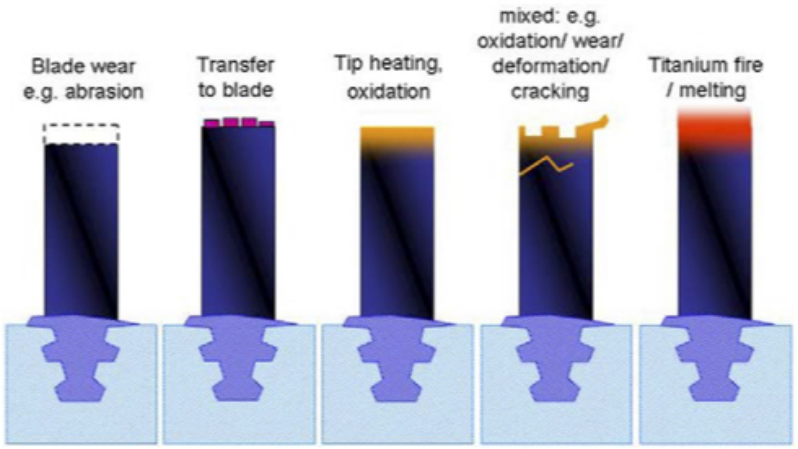

Figure 1.4: Summary of commonly observed blade wear mechanisms [9]

Even though this helps to identify the wear mechanisms present, it does not give insight to what drives the wear mechanisms and what is happening during a contact. Fois et al. used a test rig developed at The University of Sheffield, which has an innovative stroboscopic imaging technique, to characterise the wear mechanisms during the contact of Metco 320 [17] with a titanium blade. This is an Aluminium-Silicon hexagonal Boron Nitride (AlSi-hBN) abradable, that is currently used in the compressor stages of Rolls-Royce engines [15]. This study aims to use similar methods, as well as to develop new tools and techniques to fully characterise the wear mechanism of another abradable material which is currently used in the compressor stages of Rolls-Royce engines, namely Metco 601. This is important because it has been identified by the engine manufacturer that even though the two materials (Metco 320 and Metco 601) are very similar in terms of constituents they have very different performance. Whilst Fois et al. [15] managed to characterise the wear mechanics of Metco 320 and link it to its performance, the reason the two materials have such dissimilar performance is not understood. This provides a fundamental gap in knowledge that this thesis aims to fill.

1.4 Project aims and objectives

The aim of this project was to investigate the wear mechanisms that occur in the compressor stages of an aero-engine between the abradable lining and the compressor

blades. For the purposes of this research two abradable materials were considered. The first one was Aluminium Silicon Polymer (Metco 601) and the second was Aluminium Silicon hexagonal Boron Nitride (Metco 320). Both of these materials were developed by Oerlikon Metco and are currently used in the compressor stages of Rolls-Royce aero-engines. A titanium alloy (Ti-6Al-4V) was also used for the blades. A previous study focused on characterising the wear mechanisms observed during the contact of Metco 320 with a titanium blade [15]. This study performed an extensive characterisation of the wear mechanisms that occur when Metco 601 was rubbed against titanium blades. The aim of this study was to identify and explain the differences between the behaviour and performance of Metco 601 and Metco 320.

To achieve these aims the following objectives were set:

- Develop a new, novel approach for testing using the experimental test rig to include the capturing of images at the point of contact. These images will show debris ejection patterns and material removal mechanisms and will enhance the fundamental understanding of the wear mechanism that happens during the contact. Both Metco 601 and Metco 320 will be tested with this method.
- Develop a novel analysis technique that provides insight on the compressive and tensile strain field generation in the sub-surface of the abradable during the contact (both Metco 601 and Metco 320 were considered). This was achieved by observing a cross section of the abradable for the whole duration of the contact and employing a Digital Image Correlation (DIC) algorithm to calculate the resulting strain fields.
- Create a new testing procedure to observe the material adhesion or the blade wear that occurs during the contact along the length of the blade, instead of observing along its width. This provides invaluable insight on what drives the mechanism, as well as, where and why material build up and/or blade wear initiate.
- Use a novel testing methodology to link temperature variations in the surface of the considered abradables during the contact and the resulting wear mechanism. A thermal camera was used to provide the temperature variation of the abradables surface and this information is used in conjunction with the along the blade length's observations to correlate the wear mechanisms to thermal phenomena.

1.5 Thesis structure

In this section a plan of the work required to achieve the stated aims and objectives is provided. The next chapter includes a basic literature review on the manufacturing and testing of abradable materials. Chapter 3 contains details on the methodology used throughout this project, including details on the experimental test platform set-up and the techniques used to collect, process and analyse data. Chapter 4 consists of a detailed characterisation of the performance of Metco 601 as well as an extensive comparison of the performance of the two abradables considered. The next chapter 5 examines the debris ejection mechanism for the two abradables considered and provides more insight on the wear mechanisms that occur. Chapter 6 uses a different imaging approach to capture images of the side of the abradable during the contact that allows the investigation of the cracks and chips that were formed in the abradable's surface and sub-surface. This also allowed DIC analysis performed to identify the compressive and tensile strain fields that are generated in the abradables during the contact. Chapter 7 captures stroboscopic images from the front on direction and with the aid of thermal imaging it provides a link between temperature variation in the abradable and the wear mechanism. The scientific insights found in this research are discussed in chapter 8, while chapter 9 provides a summary of the main points discussed and the key findings of this research. Finally, future work and improvements on this research are considered in chapter 10.

Chapter 2

Literature Review

This chapter provides a detailed discussion for abradable materials used in the compressor stages as this is the focus of this study. The abradable materials manufacturing methods, operational range and performance are detailed. Furthermore, their wear behaviour and its influence on the overall performance of the engine is explained. In addition, this chapter provides an extensive overview of how these materials have been tested in the past. Experimental testing is the most widely used method for assessing the performance of abradables used in gas turbine engines and a number of different approaches to testing exist. Firstly, commonly used testing equipment is used to analyse the material response of the abradable. In addition, full-scale test rigs and scaled experimental test rigs have been developed for this purpose. Finally modelling and simulations methods are used, but are mostly followed by experimental validation.

2.1 Abradable Materials

This section provides a summary of typical abradable materials used in the compressor stages of jet engines and the method used for manufacturing these materials.

2.1.1 Types of abradables

There is a wide range of abradable materials that are employed in gas turbine aero engines and the main way to classify them is by their operational temperature range.

Figure 2.1 shows the operational temperature range of a typical aero-engine at different stages [9], while figure 2.2 shows the equivalent abradable and blade technology employed in that stage [17].

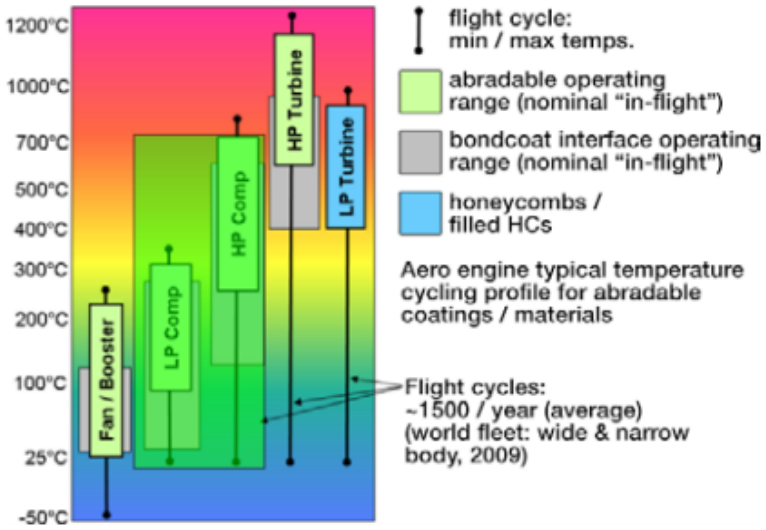

Figure 2.1: Temperature range of different stages in an aero-engine [9].

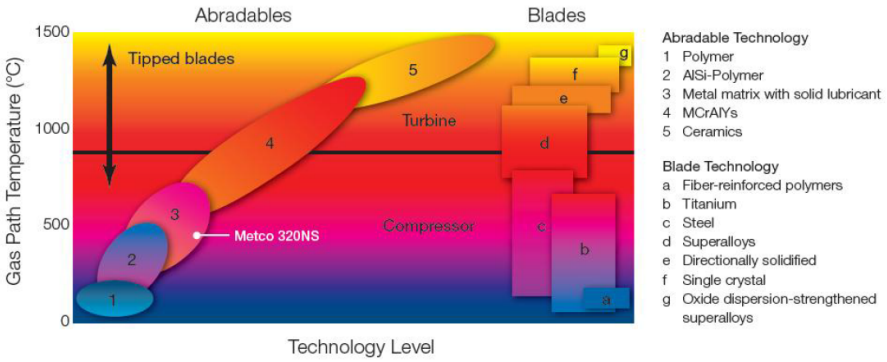

Figure 2.2: Temperature range at which different abradable and blade technologies are employed [17].

As mentioned previously, this study focuses on the compressor stages (shown by the green box in figure 2.1) and therefore only some of the abradables used in these stages are discussed in this section. The abradables selected for further discussion in this section are Metco 601, Metco 320 and Metco 314. This was done because these abradables are typical materials used in the compressor stages, which are of interest in this investigation.

Aluminium Silicon - Polyester

AlSi-polyester is an abradable which is commercially available as a powder from Oerlikon Metco (Oerlikon Metco, Churerstrasse, Switzerland) and has the commercial name of Metco 601. The commercial powder is made by blending a 40% polyester, 7% Silicon mixture and has a nominal particle size distribution of -125 + 11 μm. To manufacture the abradable from the powder, an atmospheric plasma spraying procedure is used (atmospheric plasma spraying process is described in more detail in the next section) as recommended by the manufacturer. The resulting abradable has a maximum service temperature of 325 ^oC and can be used against un-tipped titanium, nickel alloy and steel blades and consequently it is widely used in the LP stages of the compressor. In this composite material the AlSi provides the required strength and erosion resistance, while the polyester acts as a the solid lubricant and allows the abradable to have the required wear characteristics [9, 18].

Aluminium Silicon - hBN

This material is very similar to Metco 601, but has some significant differences. It is also commercially available as a powder from the same manufacturer and has the commercial name of Metco 320. The composition of the commercial powder is 8% Silicon, 20% hBN and 8% organic binder, while the particle size range distribution is -212 + 22 μm. A microscope image of the powder is shown in figure 2.3. The first main difference, compared to Metco 601, is the fact that the powder is made by mechanical cladding, which creates a greater variability in the particle size and composition. Mechanical cladding is a process where particles of one material are bonded onto a core of a different material by applying high pressure (for example by passing them through a pair of rollers). Heat is sometimes also used [19]. Atmospheric plasma spraying is also used for the manufacture of the abradable from the powder. Metco 320 has a higher maximum service temperature limit of 450 ^oC, and as a result this abradable can be used even further up the compressor stages. As in the case of Metco 601, this abradable provides a good abradability and erosion resistance combination, but the two abradable's performance has quite a few differences that are discussed in more detail in later chapters [9]. The main differences in terms of performance is caused by the difference between the solid lubricant phases (hBN and polyester) since they cause different wear mechanisms. In the case of Metco 320 the

hBN acts as a solid lubricant, while AlSi provides the required erosion resistance and strength to the abradable [20].

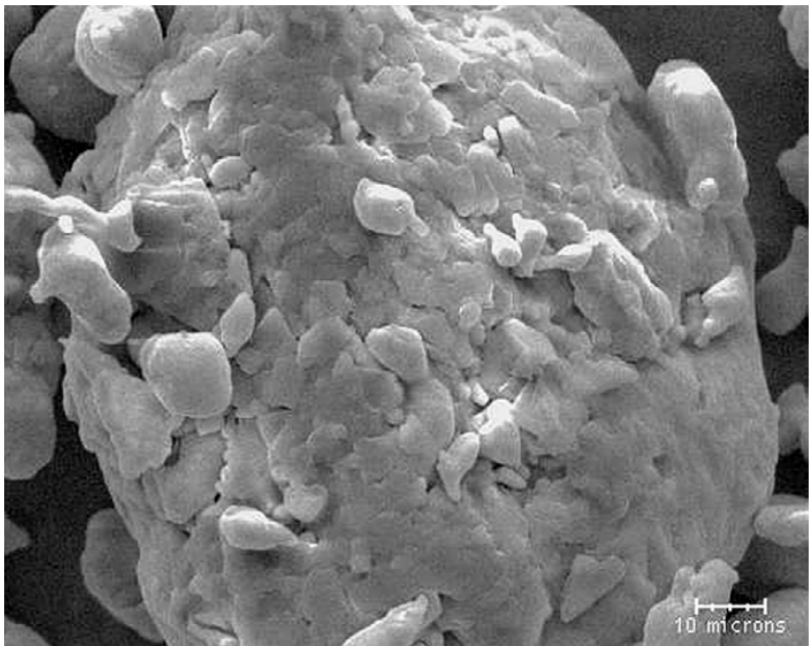

Figure 2.3: SEM image of Metco 320 commercial powder [20]

Nickel Chromium Aluminium - Bentonite

NiCrAl based abradables have a much higher temperature capability, compared to AlSi based ones, and are therefore employed in the last stages of a compressor. At these later stages, due to the increased temperatures, nickel blades are used and as a result NiCrAl based abradables are designed to have good abradability against such blades. An example of such materials is Metco 314, which is commercially available by the same manufacturer in powder form. The powder is a fully encapsulated combination of a NiCrAl alloy with bentonite and this is achieved by chemical cladding. The powder has a particle size distribution of -177 + 74 μm and a chemical composition of 4% Chromium, 4% Aluminium and 21% Bentonite and the abradable is formed from the powder by employing a combustion powder thermospary process. Figure 2.4 shows an SEM image of the commercial power. The resultant abradable has a maximum service temperature of 650 ^oC for long term use and it can therefore be used in the further back stages of the HP compressor. In the case of Metco 314 the solid lubricant that provides the abradability of the material is Bentonite [9, 21].

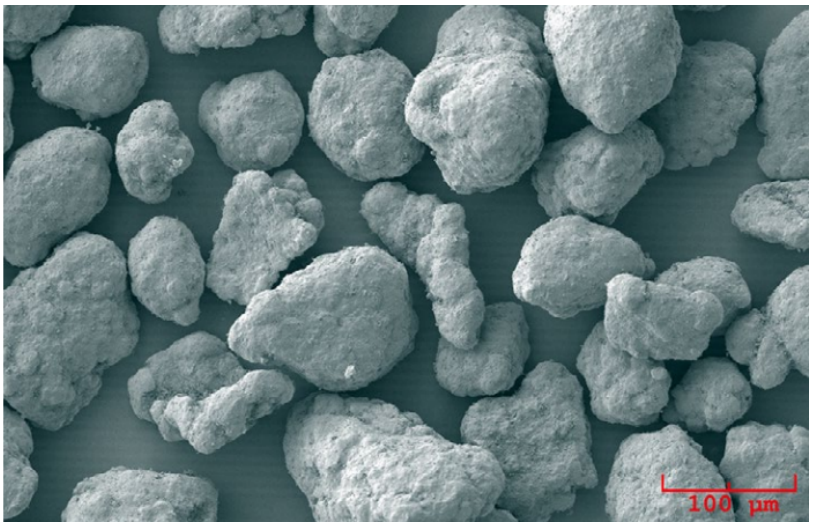

Figure 2.4: SEM image of Metco 314 commercial powder [21]

2.1.2 Thermal spraying process

As discussed in the previous sections, there are various options for abradable materials used in the compressor stages and they are mostly commercially available in powder form. To create the abradable lining from the powder a technique called thermal spraying is used. In this process a strong electric arc ionises the carrier gases and forces them into a plasma state with high thermal and kinetic energies. The abradable powders are then fed into this plasma stream, where the extremely high temperatures (approximately 16000 ^oC) result in the melting of the metal components. Then the stream is ejected from a nozzle towards a surface that will form the substrate of the lining and it rapidly cools down forming the abradable. Figure 2.5 shows a schematic of a cross section of an example atmospheric spray gun. This process is very difficult to control and usually causes inconsistencies in the abradable microstructures. Previous studies have shown that some of the spraying parameters can be controlled to provide some of the desirable properties. Some of these parameters are the voltage of the arc, the deposition rate and the temperature and speed of ejected particles [22, 23, 24]. By varying these parameters the manufacturer of the abradable can achieve a result with the required properties. For example, the hardness of the resultant abradable is inversely correlated with the deposition rate, since higher deposition rates result in a lower hardness abradable [25]. The greatest advantage of using the thermal spraying manufacturing method is the fact that there is degree of control to the resulting abradable's micro-structure. Also, another advantage is that abradables can be sprayed on components to any required thickness [24]. Alternative techniques

for manufacturing abradable materials exist, such as making oxidation resistant metal honeycomb structures and filling them with thermal carrier coating ceramic powders. These are usually vacuum brazed onto engine components. The problem with this method is that the performance of the abradable greatly depends on the honeycomb structure to maintain its integrity as it is abraded [26]. Another method is pressing together oxidation resistant metal strips or wires in a material called feltmetal. These are also vacuum brazed onto the engine components. Feltmetals have good abradability, but because of their highly porous structure they do not provide ideal sealing [27].

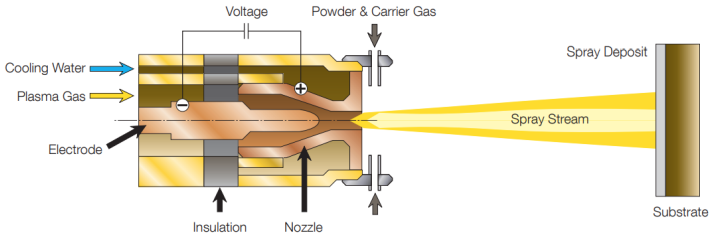

Figure 2.5: Schematic of an atmospheric plasma spray gun [25]

2.2 Performance Requirements

This section provides a summary of the required properties of a good abradable material. Also the wear mechanisms resulting from the contact between the abradable and the blades, as well as their impact on the overall performance of the engine are discussed in this section.

2.2.1 Design criteria

As previously discussed, an ideal abradable should be have a wide combination of optimal material properties. Its primary function is to act as a sacrificial material and abrade instead of the blade in the case of a contact, resulting to minimal thermal and wear damage on the blade. In addition to this primary aim, it is very important that a clean, smooth surface is produced when the abradable is rubbed against the blade A typical abradable surface in service has a surface roughness of 600 μin [7]. This is because rough, worn surfaces cause uneven sealing and localised increases in the clearance between the lining and the blade, resulting in aerodynamic losses. Therefore, it can be concluded that the surface roughness of an abradable after contact with a

blade has occurred is a very important performance criterion. Furthermore, another vital design criterion of abradable materials is that they need to have high enough erosion resistance to withstand the high temperature, high speed gas flows (often injected with particles such as debris from runways, dust and humidity) present in the compressor of an aero-engine [28, 29]. Moreover, since these materials are used in harsh engine environments they must have adequate resistances to oxidation, corrosion, thermal shock and thermal cycling and chemical resistances [30, 31]. The degree to which these are required varies depending on where in the engine the abradables will be employed. A final, but important parameter that needs to be considered is the compatibility of the contact generated debris, in terms of size and composition, with later stages in an engine. It must be ensured that debris generated in an early stage of an engine will not cause problems such as blockages as it is carried in the gas flow [32].

2.2.2 Material removal and wear mechanisms

The main function of an abradable is to provide the required sealing between the blades and the casing, while ensuring any contact preserves the condition of the blade. These materials are designed for contact scenarios, so in this section the observed wear and material removal mechanisms that result from such a contact are considered. There are two main material removal mechanisms suggested in literature, by which material is removed from the abradable during the contact with a blade.

The first one is a clean efficient cutting mechanism (blade effectively acts as a cutting tool) that removes the abradable, does no form of damage on the blade and leaves the abradable surface as smooth as possible. In this material removal mechanism the blade has enough energy to cause chip formation and removal from the front of the blade as it passes in a similar way to a traditional machining process [7, 33, 34].

The second material removal mechanism found in the literature is an abradability model suggested by Schmid [35]. This model suggested that the kinetic energy from the rotational speed and the vertical incursion of the blade into the abradable is transferred to push the abradable's surface particles into the abradable. This causes a build-up of elastic energy within the abradable and the particles below the blade (that has now passed) are pushed towards the surface. If the elastic energy is large enough to break the bonds that hold the abradable particles together material is removed and ejected after the blade has passed. Effectively this model suggested

that when a blade passes over an abradable incurring into it, it will compress it until the particles have enough elastic energy to spring back and be removed from the abradable's surface taking with it most of the energy that has been transferred from the blade. It was therefore suggested that the presence of weakness points (such as, release agents and porosity) in the abradable are necessary to ensure material release will take place. Schmid also identified that abradability depends on blade tip speed, incursion rate as well as geometry factors, such as blade thickness and blade tip angle [35]. Figure 2.6 shows a schematic that describes this material removal mechanism.

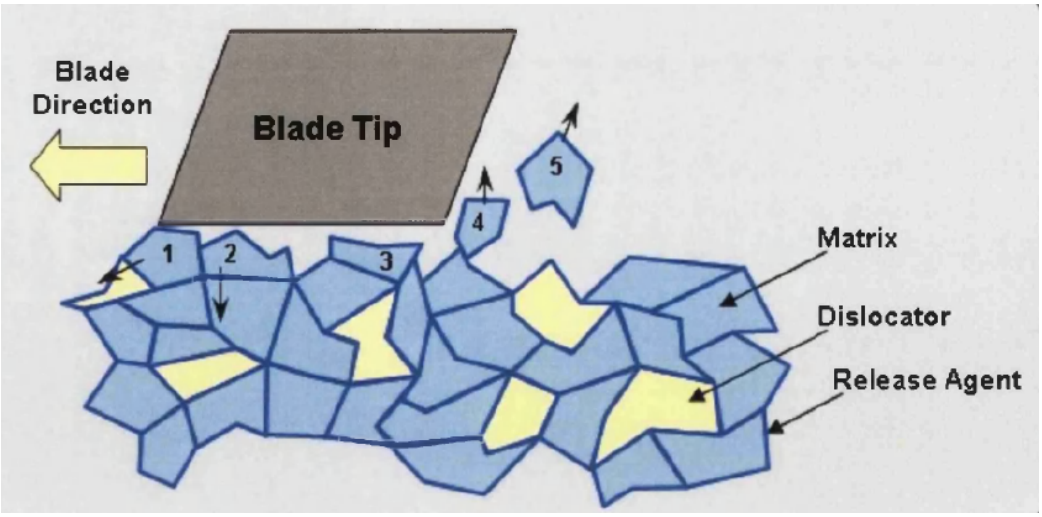

Figure 2.6: Schematic of elastic compress and release mechanism suggested by the Schmid model [35]. The image was taken from [36].

As shown in figure 2.6 the blade pushes particles 1 and 2 into the abradable as it is passing. Particle 3 stopped moving into the abradable storing elastic energy. Particle 4 has accumulated enough elastic energy to break some of the bonds that hold it in the abradable and starts to move away from the surface of the abradable. Finally, particle 5 has enough elastic energy stored so that it can break all bonds that hold it in the abradable and be ejected upwards at the wake of the blade's pass.

However, these material removal mechanisms assume that the abradable is removed efficiently, which is not always the case. The most undesirable effect in these contacts is permanent damage on the blade and there is a number of observed wear mechanisms that cause such damage. These include mechanisms such as abrasive wear, thermal damage and melting on the blade, blade deformation (such as bending or even cracking). These types of wear mechanism are detrimental to the function of

the abradable lining as they permanently damage the blade, thus permanently increasing the overall clearance, while they also put the actual blade at risk of failure. Another significant wear mechanism that has been observed is adhesive transfer of abradable material on the blade tip [7, 9, 37]. Studies have shown that this is a heat transfer related wear mechanism and it is an undesirable performance for the abradable since this mechanism causes two major problems [7]. The first problem is that adhered material that builds up on the blade tip causes deeper rubs in the case of a contact and this results in grooved abradable surfaces, consequently leading to aerodynamic losses. The second problem is that if a large piece of adhered material breaks of at some point it can cause serious problems in later stages in the engine, such as blocking cooling holes [38]. There are a number of parameters that can affect the type of the resulting wear and material removal mechanism during a contact, including the abradable-blade pair materials, the hardness of the abradable, the incursion rate at which the contact is happening, the speed of the blade tip at the time of the contact and material properties such as thermal conductivity of both the blade and the abradable [15]. Several studies have made an attempt to investigate the effect of these parameters to the resulting wear mechanism in an attempt to try and identify an operating region where optimal performance is observed. The observations from these studies have been obtained from, either in service experience, or by experimental (full-scale, scaled test rigs) techniques [7, 37, 39]. However, these are mostly dependent on post-service/post-test observations and they fail to provide an insight on how the wear mechanism has developed during the contact and therefore the fundamental understanding of what drives this mechanisms is lacking. A few studies have attempted to remedy this by developing an experimental platform that is capable of monitoring the behaviour of the blade and abradable during the contact and can consequently monitor the development of the conditions (such as temperature and forces) that drive the resulting wear mechanics[15, 40, 41, 42, 43, 44]. The aim of this investigation was to use and expand on these methodologies to provide more insight to the underlying physics behind what drives the wear mechanisms that result during a blade-abradable contact. With this fundamental knowledge, the design and operation of abradable materials can be optimised to ensure an ideal wear mechanism occurs during the in service contacts.

2.3 Performance testing

This section provides a review of the testing performed in the literature on abradable materials to assess their material properties and the resulting performance. Different techniques have been used to achieve this aim and these include material properties testing, development of experimental test rigs that simulate the contact, full-scale test rigs that replicate the engine contact conditions and computational modelling of the material properties or the contact mechanism. The aim of this review is to understand how the performance of abradables has been tested and assessed in the literature. This will allow the identification of what has not been previously done by other studies in order to develop new methodologies for testing and assessing the performance in this research.

2.3.1 Material based testing

In this section some of the research done on abradables based in material testing using common techniques and testing equipment is described.

Firstly, simple scratch testing was performed by Ma and Matthews [45, 46] to assess the performance of three abradable materials (Ni/graphite, AlSi/graphite and AlSi/polyester) as an alternative to complicated replication test platforms. The aim of the study was to provide a quick and easy way to test abradables and provide a universal metric by which they can be compared. In their studies they introduced Progressive Abradability Hardness (PAH) as an indicator of abradability. PAH shows how much energy is required to create a grove on an abradable by using a stylus to scratch its surface. It is the ratio of the energy used in the scratching and the volume of the grove that is created. The results from their testing were similar to those obtained from more advanced methods and it was suggested that this is a valid method for gaining a reasonable degree of insight prior to full-scale engine tests. Furthermore, an attempt was made to link mechanical properties such as the Young's Modulus, Ultimate Tensile Strength (UTS) and hardness with PAH, but even though a relationship was identified, it was recommended that mechanical properties should not be used alone to determine the abradability of a material. Their studies conclude that Metco 601 had the best abradability of all the three samples tested, whereas Metco 308 had the worst. PAH can be a useful tool to quickly assess the abradability of a material, however, due to the simplicity of the test, which did not replicate the

contact conditions, this method cannot be used without further and more advanced testing. Moreover, these simple tests did not provide any information of how the wear mechanisms had developed during the contact or what had caused the observed behaviour.

Sutter et al. [47] developed an experimental device based on a pneumatic gun capable of producing high speed orthogonal cutting. The abradable material used in this research was Metco 601 (AlSi-polyester) with hardness of R15Y 51 and it was tested against a titanium alloy blade. The pneumatic gun is able to eject the abradable sample on the blade sample at speeds up to 120 m/s. The cutting velocity and interaction depth are the two variables that could be controlled during the tests. It was found that interaction forces were proportional with incursion depth and interaction speed. Moreover, the influence of the blade tip geometry was identified. The nature of the contact during the test (impact) between the abradable occured as a single strike and in a straight line and this is quite different from the actual case. Consequently, mechanisms present in continuous, circular rubs, such as heat generation and material build-up cannot be observed using this kind of testing.

Yi et al. [48] made an attempt to characterise the friction and wear characteristics of abradable materials using a block-ring sliding wear testing method. The block part was the abradable sample and the ring was a AISI152100 steel with HRC63 (36 mm diameter and 10 mm width). The abradable materials considered in this study were M307, M310, M313, and M601. The results obtained by this method suggested that abradability decreased with increasing hardness of a given abradable. However, hardness cannot be alone used as an indicator, as different abradables with similar hardness' exhibit significantly different abradability. Furthermore, abrasive wear, adhesion and wear due to oxidation were observed. A significant difference in this study was the fact that the abradable materials were rubbed against steel, contrary to other studies that used titanium alloys. In a subsequent study, Yi et al. [49] performed another investigation on the erosion wear performance of the abradable materials tested previously, along with four additional abradables. These additional materials were similar to the abradables produced by Metco, but with slightly different compositions. The erosion wear testing was performed by using a self-made erosion machine. The input parameters, besides the different abradable materials, were the particle injection speed and injection angle. The study concluded that a linear relationship existed between mass loss and erosion time, while the erosion rate increased exponentially with impact speed. Furthermore, the maximum erosion

was observed at an angle of 60^o for all the tests. This study provided valuable insight about the erosion resistance of the tested abradables, which is a very important performance criterion for abradables.

2.3.2 Full scale test rigs

In this section, testing performed on abradable materials using full scale test rigs, such as the Sultzer Metco testing facility are reviewed.

Sultzer Metco developed an abradable testing facility with a full scale test rig that can reach blade tip speeds up to 430 m/s at incursion speeds of up to 2000 $\mu m/s$. The test rig is able to heat up the abradable to temperatures of up to 1200 ^{o}C [50]. A schematic of the test rig is provided in figure 2.7.

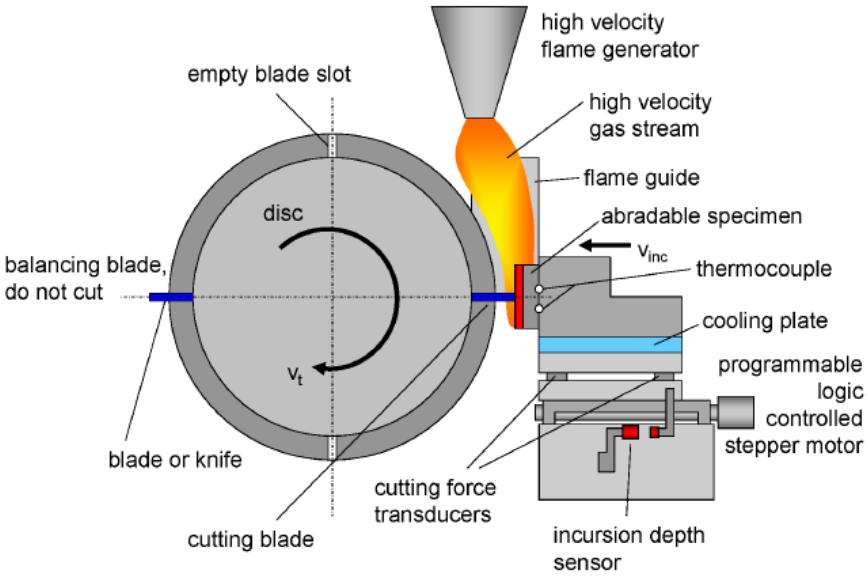

Figure 2.7: Schematic of the Sulzer Metco full scale experimental test rig [50]

Borel et al. investigated abradable samples, which have been worn in service, to identify the different types of wear mechanisms. The abradables investigated were AlSi-plastic and Nickel-graphite. The investigation concluded that there are two categories of wear mechanisms. The first category consisted of wear mechanisms where contact between the blade and the coating occurs, including mechanisms such as cutting, smearing, adhesive transfer, crushing, melting and tribo-oxidation. The second category includes non contact mechanisms such as erosion, corrosion and high-temperature oxidation. Moreover, in this study the Sultzer Metco full-scale test rig was used in an attempt to replicate the mechanisms that occur in service and link them

with operating conditions and material properties. The results obtained from this testing suggested that there was a correlation between coating surface roughness and blade weight variation after the test with the resulting wear mechanism. Furthermore, this study suggested that there was a correlation between the wear mechanism and the coating temperature, as it was observed that an adhesive mechanism raised the coating temperature only by a small amount, whereas a cutting mechanism resulted in higher heating of the coating. Finally, this study generated wear maps that showed the resulting wear mechanisms at different operating conditions, however, they were generated with only a small number of data points. Even though a correlation was established between operating conditions and the resulting wear mechanisms, this study did not consider the effect of material properties such as the hardness on the resulting mechanism. Moreover, the examination of worn abradable samples post service gave very little insight on the development of the resulting wear mechanisms [7].

Sporer and Wilson [9, 50] analysed different technologies of abradable materials used in the compressor and turbine stages of a gas turbine engine. They also used the same test rig to assess the abradability of the reviewed technologies by testing them at a range of speed and incursion conditions. The mechanisms that were observed from the testing for each material are summarised in figure 2.8. The results from this study were obtained by visual inspection of the post test surface of the abradable samples. The importance of hardness and erosion resistance was identified, however, their effect in the resulting mechanisms was not investigated in these studies.

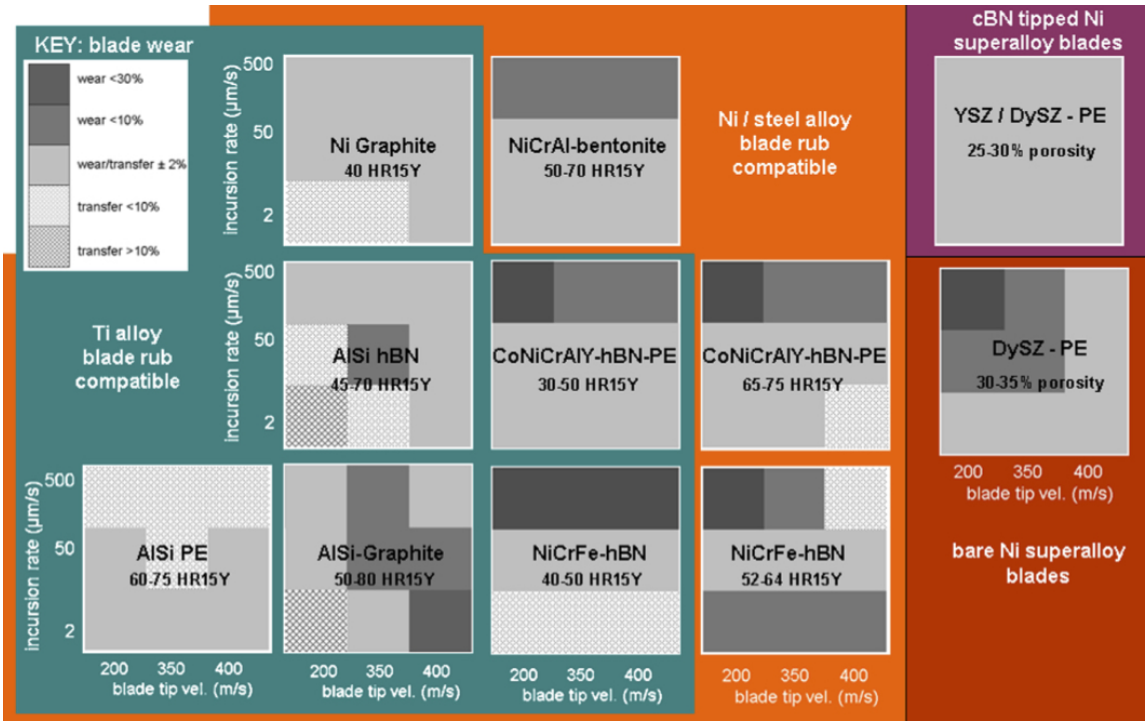

Figure 2.8: Wear mechanisms observed at different incursion rate and speed conditions for each material. [9]

Using the Sultzer Metco testing rig, Bounazef et al. [37] investigated the performance of an AlSi/hBN abradable with HR15Y hardness of 60.74, when rubbed against a titanium blade under a range of different conditions. After a series of tests that simulated conditions of engine operation, the study concluded that material transfer from the abradable to the blade decreases with increasing speed and incursion rate. Two wear maps were generated, one showing the thickness of the material transfer and the other showing the observed wear mechanisms under the different testing conditions as shown in figure 2.9.

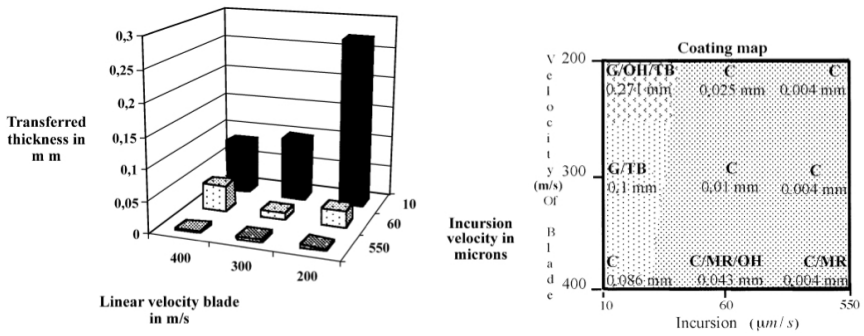

(a) (b)

Figure 2.9: (a) Thickness of material transfer at different blade speed and incursion rate conditions, (b) Observed wear mechanisms, C=cutting, G=grooving, TB=transfer on blade, OH=over heating, MR=micro rupture [37]

Even though this study gave valuable insight on whether transfer occurred or not, it was based only on post test observation of the samples. This leads to little understanding of how the material transfer build-up was happening since only information about the material transfer thickness at the end of the test was available, which might not be representative. The effect that the hardness of the abradable had on the resulting material transfer and wear mechanism was not investigated as this was not the aim of this study.

Ghasripoor et al. [39] also used the Sultzer Metco test rig to assess the performance of three abradable technologies based on AlSi, but with different filler phases. The three abradables were AlSi/polyester, AlSi/graphite and AlSi/hBN and they are low temperature coatings used in the compressor stages of gas turbines. All the abradables were rubbed against titanium alloy blades similar to those found in the compressors of gas turbines. The abradables were tested on a range of conditions similar to the operating conditions of actual gas turbines in an attempt to identify the wear mechanisms that took place. To achieve this, visual observation was carried out during the testing using a camera to identify sparking and hot spot generation and link them to the resulting wear mechanisms. Samples were also observed under an optical stereo microscope post testing, while some samples were sectioned and examined through a scanning electron microscope with X-Ray elemental analysis capabilities. This allowed the investigation of the abradables micro-structure after the test, whilst also allowing elemental analysis to be performed on wear tracks to identify material transfer from and to the blade. This research concluded that for the AlSi/polyester abradable the primary wear mechanism was the removal of a superficial layer of

molten material, while material transfer from the abradable to the blade and micro rupture also occurred. In the case of the two other abradables (AlSi/graphite and AlSi/hBN), the prevailing wear mechanism observed was micro rupturing and it was suggested that this was because of the brittle nature of the filler phases, which broke readily initiating cracks and promoting micro rupturing. Using the results from this investigation, wear maps were generated summarising the wear mechanisms observed for the three abradables under a range of different conditions and they are shown in figure 2.10. The wear maps were used to illustrate the wear track in terms of its roughness and the wear mechanisms that took place. The wear track roughness was calculated using Rc, which is know as the Weighted Coating Roughness and it is calculated by the following equation:

$$R_c = 9.2R_a + 1.3R_z + R_{max} \tag{2.1}$$

where R_a, R_z and R_{max} are values of the wear tack profile and are measured perpendicular to the rub direction. The roughness of the track was then categorised depending on the value of R_c as very smooth, smooth, rough or very rough. This study gave a good summary of the performance of AlSi based abradables under different conditions similar to those of actual gas turbine engine operations. It also suggested useful tools that could be used to analyse the wear mechanisms of other abradables. However, the wear mechanism identification was mainly based on post test examination of the abradables and it did not explain how these mechanisms develop during the test or if two or more mechanisms occurred at the same time. Furthermore, the comparison was made between three different abradables, but the hardness of the samples was not considered even though it was significant as to the resulting wear mechanism. Finally, there was no link made with the forces and temperatures that were produced during the contact with the resulting wear mechanisms as this was not part of this investigation.

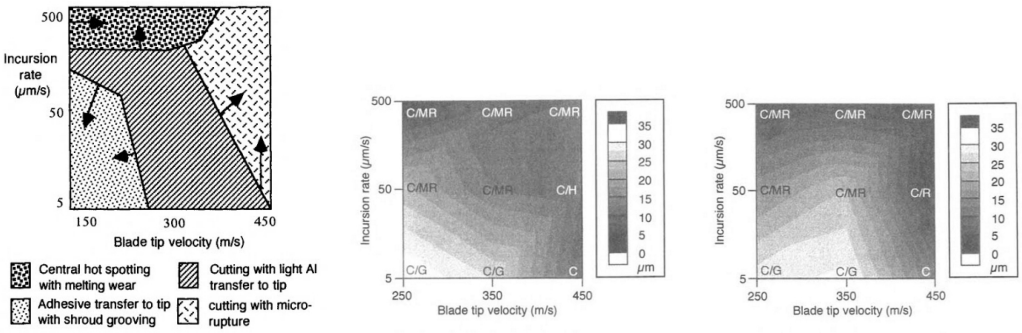

(a) (b) (c)

Figure 2.10: 2.10(a) Wear map of Aluminium Silicon/polyester tested at room temperature, 2.10(b) Wear map of Aluminium Silicon/graphite tested at 450^{o}C, C=cutting, G=grooving, R=rupture, MR=micro rupture, H=hot spot, 2.10(c) Wear map of Aluminium Silicon/hBN tested at 450^{o}C, C=cutting, G=grooving, R=rupture, MR=micro rupture [39].

2.3.3 Scaled experimental test rigs

Scaled experimental test rigs were developed to offer a simplified alternative to the full scale testing equipment, while at the same time replicating the actual contact conditions in a satisfactory manner.

Stringer and Marshall [51] developed an experimental test rig capable of replicating the contact between an abradable lining and a blade. The test rig was described in detail in previous studies [51, 42, 41, 40]. This test rig is based on a machine tool spindle that has attached a disc to it. The spindle is capable of spinning the disc to a rotational speed of up to a maximum of 21000 rpm. The disc has a holder that allows the attachment of a blade sample. Below the spindle and disc couple there is a microscope stage, on which abradable samples are mounted. The stage is used to raise the abradable towards the spinning disc, replicating in this way the incursion contact between a blade and an abradable. An innovative stroboscopic imaging technique was used to monitor the blade length change over the duration of a test allowing great insight on the development of material transfer and other wear mechanisms during the test. More details about the set-up of the rig and the sensors are provided in section 3.1. Figure 2.14 shows a schematic of the experimental set-up of the test rig.

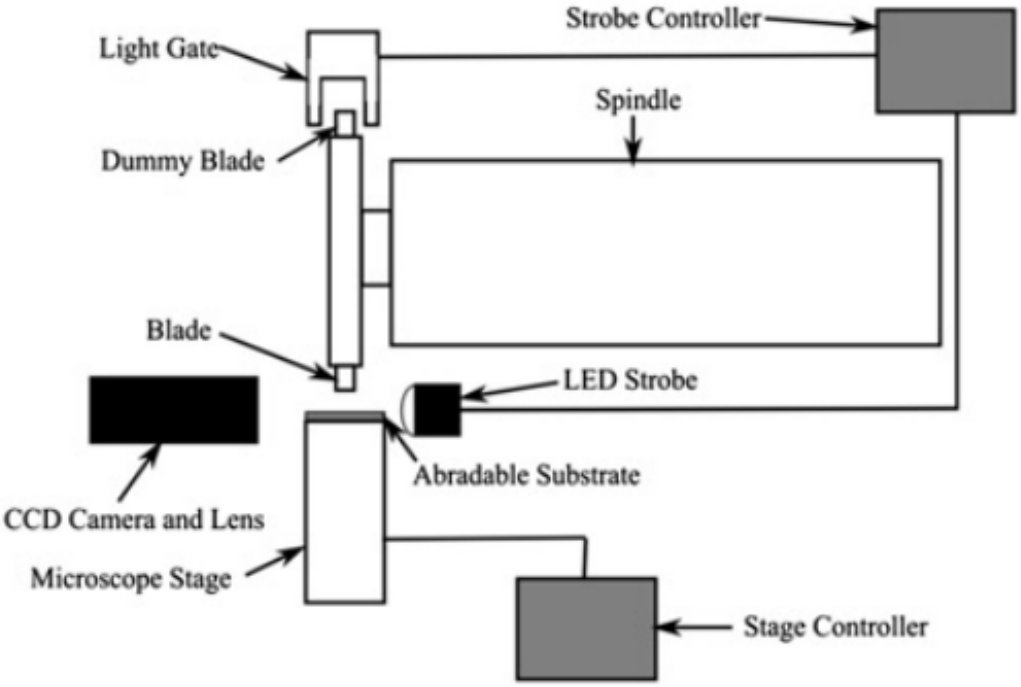

Figure 2.11: Schematic of the test rig set-up [51].

The tests performed by Stringer and Marshall [51] were done using an AlSi/hBN abradable and a Ti/6Al/4V blade. The study concluded that a low incursion rate led to adhesive transfer and blade wear, whereas high incursion rates led to a cutting mechanism. Moreover, it was found that the blade tip speed had a lesser effect on the resulting mechanism, since increasing blade tip speed resulted in a less severe wear mechanism. Another very important finding of this study was that it was possible that blade wear and adhesive material transfer on the blade tip both happened in one test. It was, therefore, concluded that it was inadequate to assess the wear mechanism only based on maximum blade length and weight changes. Figure 2.12(a) shows the post-test samples from this research, while figure 2.12(b) shows the variation of blade length increase with incursion depth.

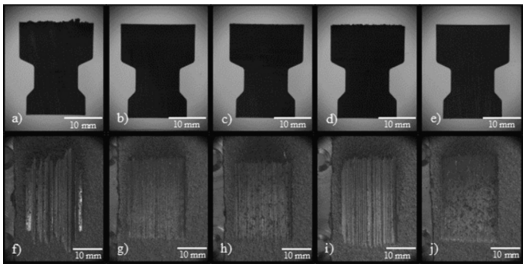

(a)

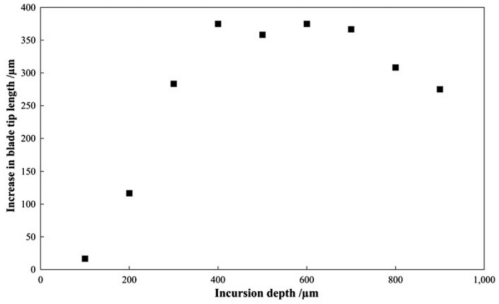

(b)

Figure 2.12: (a) Post-test samples tested in this study, (b) Plot that shows the increase in blade length variation with incursion depth [51].

Fois et al. [40] performed another study with the same test rig and materials to further investigate the adhesive material transfer on the blade tip. The rate of material transfer was found to not be uniform during the test and it was in fact divided into an initiation phase and a steady state phase. Analysis performed in this study concluded that the adhesion rate was initially high at low incursion rates, until a critical incursion rate at which it reached a steady state. Furthermore, in some tests it was observed that the adhered material fractured during the test with a re-initiation of adhesion following. This suggested that observation of the blade length and weight after a test was not adequate to fully characterise the extent of adhesion. Figure 2.13(a) shows an example of a post-test sample showing both adhesion and wear, while figure 2.13(b) shows how the rate of blade length change varies with blade speed and incursion rate.

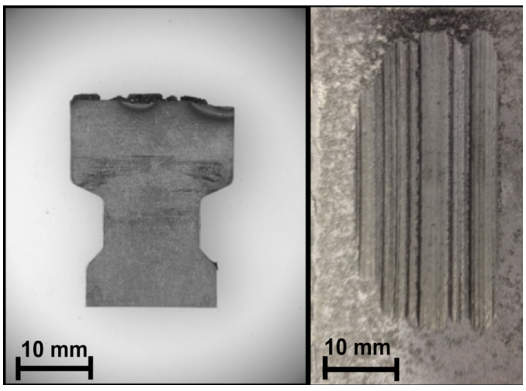

(a)

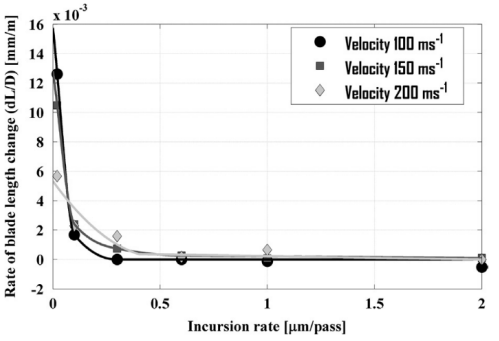

(b)

Figure 2.13: (a) Tested sample showing both adhesion and wear, (b) Rate of blade length plots that show variation with speed and incursion rate [40].

The experimental test rig used in the previous studies was then further instrumented with the addition of a dynamometer to measure the contact forces in both normal and tangential directions. A pyrometer was also used to measure the temperature of a point on the abradable. A schematic of the updated test rig is shown in figure 2.14. Using the data from all the instrumentation it was identified that at low incursion rates consolidation and solidification of the abradable occurs (figure 2.15(a)), thus resulting in a low tangential to normal force ratio. Moreover, a low friction melt layer was identified at the surface, suggesting a consolidation mechanism took place. In contrast, at high incursion rates a higher force ratio was recorded as well as no consolidation was observed (figure 2.15(b)), suggesting a cutting mechanism. These results were also supported by optical microscopy examinations. Finally, a transition from adhesion to cutting occured at incursion rates higher than 0.06 μm per pass [41].

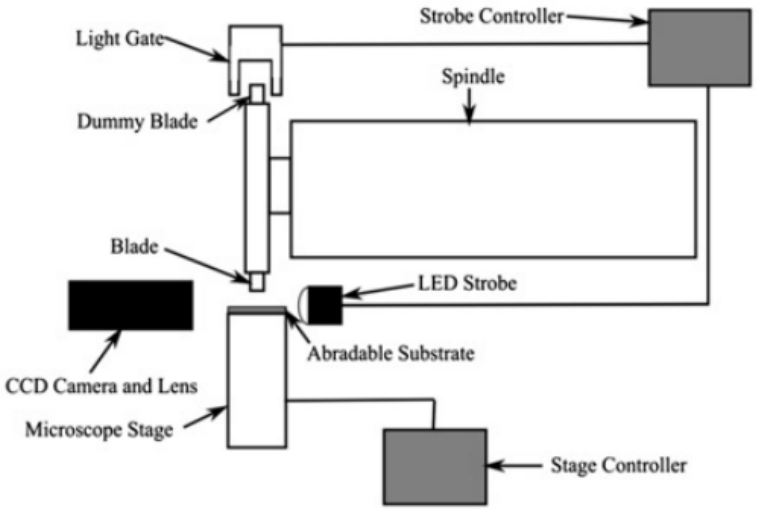

Figure 2.14: Updated schematic of the test rig set-up to include the added sensors [41].

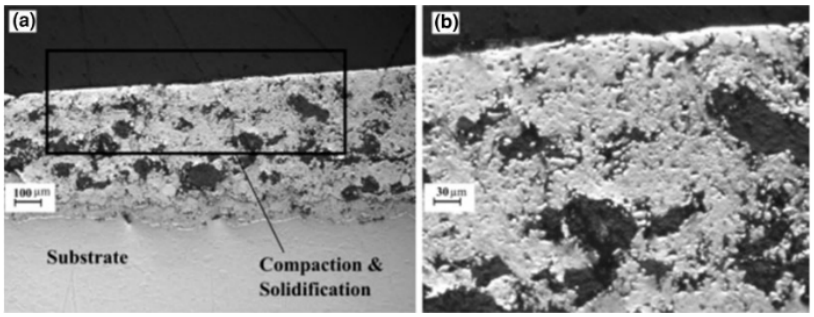

(a)

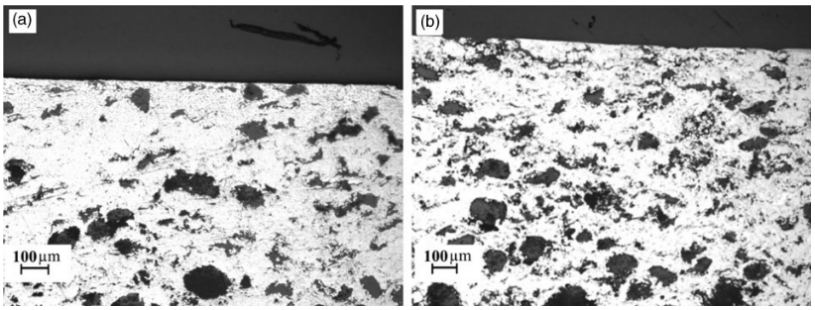

(b)

Figure 2.15: (a) Optical microscopy image showing consolidation, (b) Optical microscopy image showing no consolidation and consequently a good efficient cut [41].

Fois used this test rig to carry out an in depth investigation and analysis of the performance of Metco 320 NS. Adhesion/wear rate was used as a descriptor of the abradability performance of the material and a wear map (figure 2.16) was constructed which summarises the wear mechanisms that occur at different conditions. A modified peclet number was used for the x axis of this wear map because it was found in literature that this dimensionless number was a good combination of the thermal and mechanical components of the contact. The normal peclet number represents the concentration of heat in a sliding contact. At a high peclet number (typically $Pc > 10$) the blade rotates faster than the heat can build-up and therefore the heat is carried in the debris that is generated. At low peclet numbers ($Pc < 10$) some of the heat is propagated into the abradable coating. Effectively this dimensionless number is a measure of whether the heat generated in the contact because of mechanical energy inputs of the contact, such as the incursion rate, the blade tip speed and the contact geometry, is transferred to the chips and debris that are generated or propagated in the abradable. The normal peclet number assumes that the cutting tool (blade) does not pass the same point twice, which is not accurate. Therefore the modified peclet number takes into account the feed velocity (product of incursion rate and rotational

speed) to compensate this. As a result the modified peclet number represents the heat propagation in the abradable or in the chip formed after each pass taking into account the previous passes. The modified peclet number can be calculated by the following equation:

$$Pc_{modified} = \frac{V_{blade} * I_{rate}^2}{\alpha * \pi * D} \tag{2.2}$$

where V_{blade} is the blade tip speed, I_{rate}^2 is the incursion rate, α is the thermal diffusivity and D is the diameter of the rotating disc [15, 52, 53, 54].

Furthermore, a heat partition coefficient was used as a y axis. This heat partition is a dimensionless number independent of the contact, that estimates the amount of energy in the form of heat that is dissipated in the components of the contact. It only varies with the material properties therefore different hardnesses have different heat partitions. This heat partition can be calculated by the following equation:

$$Hp = \frac{Cp_{blade} * \rho_{blade} * \lambda_{blade}}{Cp_{abradable} * \rho_{abradable} * \lambda_{abradable}} \tag{2.3}$$

where Cp is the specific heat, ρ is the density and λ is the thermal conductivity [15, 55].

This wear map and the adhesion/wear rate descriptor was successful in identifying a progression from unwanted to good behaviour, as well as identifying regions of optimal performance for Metco 320. Furthermore, it was found that a cutting wear mechanism was dominant at high incursion rates, whereas adhesion and wear occurred at low incursion rates. Also it was shown that the effect of speed was limited to affecting the severity of the mechanism [15].

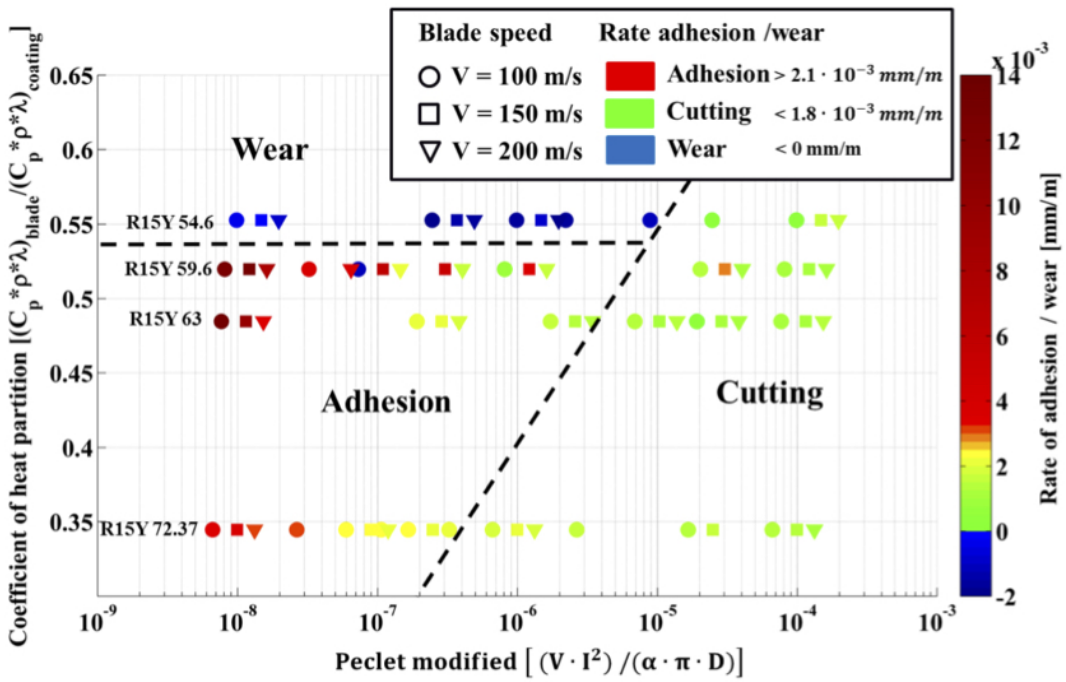

Figure 2.16: Wear map of Metco 320 NS constructed with the heat partition and modified Peclet number [15].

In addition, this study showed a progressive decrease of maximum temperature with increasing incursion rate (figure 2.17(a)). Also an increase of force ratio was observed with increasing incursion rate further enhancing the suggestion that a cutting chip formation mechanism was more prevalent as incursion rate increases (figure 2.17(b)).

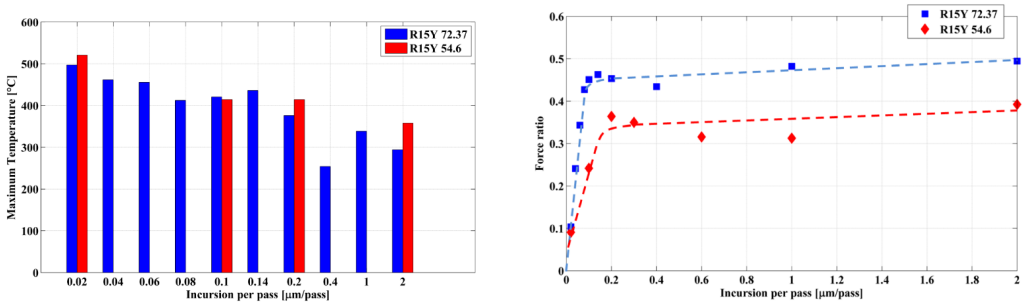

(a) (b)

Figure 2.17: (a) Maximum temperature variation with incursion rate for two abradable hardnesses, (b) Force ratio variation with incursion rate for two abradable hardnesses [15].

Finally, figure 2.18 shows the post-test blade and abradable samples from two different

hardnesses of the abradable considered in this study (Metco 320), tested at the two extreme considered incursion rates to highlight the differences in their performance under these conditions.

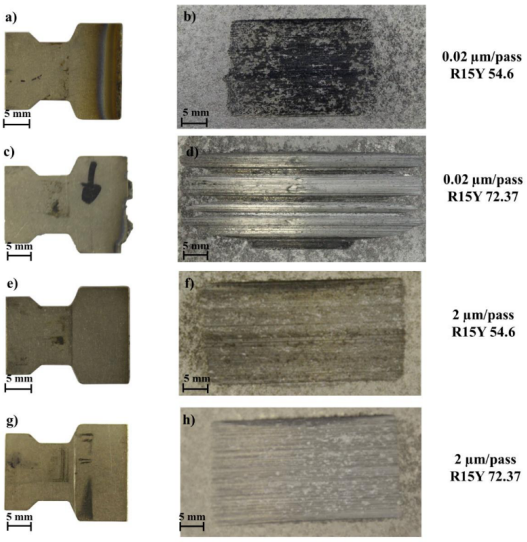

Figure 2.18: Post-test abradable and blade samples of two different hardnesses of Metco 320, tested at 0.02 and 2 microns/pass [15].

Watson et al. [43] used the test rig described in the previous studies to assess the effect of blade surface treatment on the abradable performance. For this study a NiCrAl-Bentonite abradables were used against an Inconel 718 blade. Some of the blade samples were prepared with surface treatment and were compared to those without surface treatment. Surface treatments included coating with Cr(Al)N and coating with cBN grits. Also, flat tip and 30^o chamfered tips were tested, as well as coatings with a range of hBN grit sizes. This study concluded that adding grits on the tip of the blades resulted in an initial period of good cutting. However, the failure mechanism observed once they were loaded was more severe than the un-tipped blade. At low incursion rate the tip with the larger grit size cut the abradable efficiently throughout the whole test. At high incursion rate adhesion on the tip took place loading the grits and resulting in a tip failure. The time to failure was mostly dependent on grit size. It was found that the introduction of chamfer increased the time to failure and in the case of low incursion rates, no failure took place at all. It was also noticed that at lower tip speeds, the compaction and macro rupture of the abradable was more severe and it was, therefore, suggested that a future investigation was carried out at higher blade tip speeds.

In a further investigation, Watson et al. [56], extensively studied the wear mechanisms resulting from the contact between abradables and blades. In this investigation, NiCrAl-bentonite was rubbed against Inconel blades, while AlSi-polymer was rubbed against titanium alloy blades. The aim of this study was to provide statistical correlations of testing conditions such as the forces and temperatures generated during the contact to the wear mechanisms that resulted. The forces that resulted from the contacts have been shown to have strong statistical correlation to the proposed linear models of the wear mechanism, while the observed temperatures and blade length changes were found to be less correlated. An important limitation of this approach was that it used mean values of the parameters, such as force, temperature and blade length changes to perform the statistical analysis, but these vary significantly throughout the duration of the contact. Moreover, the models failed to address the non-linear behaviour of a contact, such as the discontinuous adhesion of material during the test. Overall this statistical approach had a few limitations, but still provided a useful tool to compare new abradables to typical performance of existing systems, as long as there was enough data.

Moreover, Watson et al. [44] developed a novel image segmentation technique that used SEM images of abradables to automatically identify and separate cracks in the microstructure of an abradable. This gave the possibility to attempt and model more accurately the abradable's material properties. This study showed that using this technique had lower systematic bias to the brightness and contrast of the original images compared to alternative techniques. Figure 2.19 shows an example of an original SEM image and an images produced by this technique. In this investigation, Watson et al., also created a finite element model that estimated the density and specific heat capacity of AlSi based abradables (both Metco 320 and Metco 601 were investigated) using the images from this segmented imaging technique. The results obtained for these material properties were within experimental error even though the material properties were lower than expected mostly due to the two dimensional approach of the model.

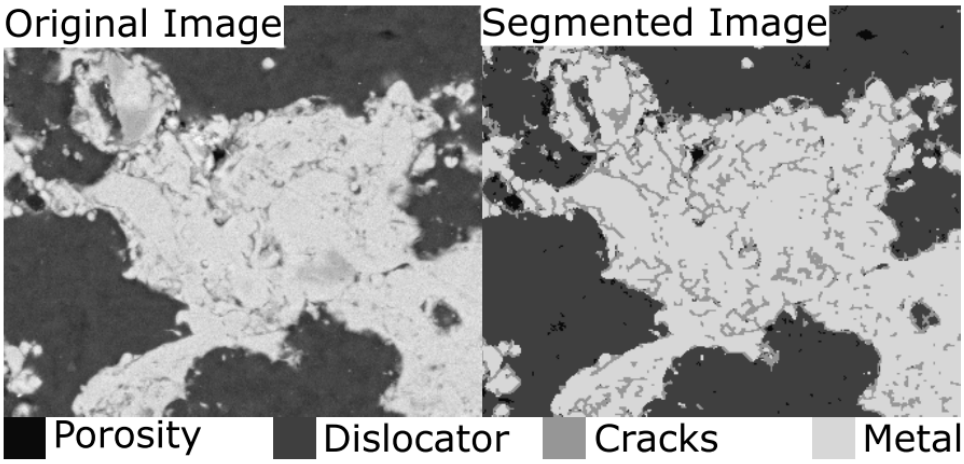

Figure 2.19: Original SEM image of an abradable microstructure and an image obtained after processing with the novel image segmentation technique describe in this study [44].

Another scaled experimental test rig (figure 2.20) was developed by Baiz et al. [57] in an attempt to investigate the contact between an AlSi/hBN abradable with a Titanium alloy blade, taking into account blade kinetics.

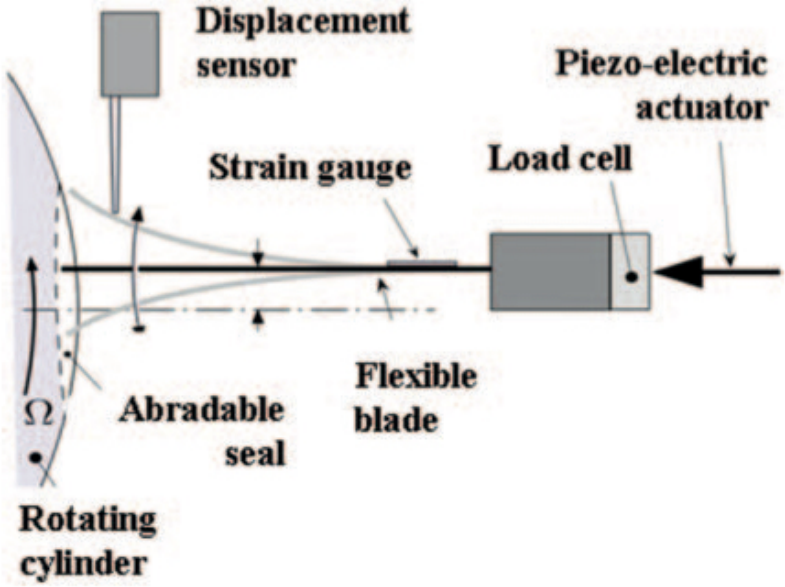

Figure 2.20: Schematic of the experimental test rig [57].

The study focused on short duration and single strike testing. It was found that higher incursion rate and depth increased drastically the amount of blade deflection. Moreover, it was shown that already worn surfaces result in further excitation, thus increasing the blade deflection amplitude and bouncing frequencies even more. Fi-

nally, it was shown that blade deflection amplitude and frequency were affected by dynamic coupling [57].

In a subsequent study by Mandard et al. an attempt was made to explain how blades were excited by using time-frequency analysis techniques such as Fast Fourier Transform (FFT) and Continuous Wavelet Transform (CWT). The same test rig, dataset and testing conditions with the previous study [57] were used. This study concluded that there were two types of rubbing: blade coating bounced and isolated contacts. The first type of rubbing was observed at high incursions and their characteristics were blade vibrations about a non zero position and significant abradable material loss. The second type of rubbing was observed at low incursions and had blade vibrations about zero and very low material loss. Also, there was strong correlation identified between blade dynamics and abradable wear [58]. However, these two studies were limited by the very low tangential speed at which testing was performed (19 m/s).

To address this limitation, Mandard et al. used the same test rig with an additional induction heating mechanism, which allowed heating of the abradable surface at temperatures of up to 300 ^{o}C, to investigate the contact between a flexible blade and the abradable seal further, at higher tangential speeds of up to 92 m/s. In an initial study, a correlation was shown between the force measurements and the abradable wear profile [59]. In a subsequent study, with the same testing conditions, Mandard et al. tried to propose different experimental techniques by which the wear mechanisms could be evaluated from the single pass testing. These techniques included SEM analysis of the rubbed surfaces, X-Ray microtomography for examination of porosity loss and wear debris analysis using the high speed camera. Four wear mechanisms were observed including debris release, surface shearing, compaction by porosity closure and reversible deformation. It was identified that these mechanisms had a strong correlation with incursion depth and interaction force [60]. These studies provided important insight regarding the contact between an abradable seal and a flexible blade, but the single strike scenario and the convex shape of the contact were significant limitations. Moreover, even the higher speeds tested (92 m/s) were not equivalent to the actual engine conditions.

2.3.4 Modelling

The final section of the literature on abradable testing was focused on modelling. Researchers used modelling techniques to simulate the material properties of the abradable coatings and also the actual contact between the coating and the blade.

One of the first attempts to create a model of abradable material properties was made by Hougang and Wang [61]. In this study, a thermal model was developed aiming to simulate the temperatures of the contact. The investigation was focused on the contact of NiCrAl-silicate and AlSi abradables rubbed against titanium alloy blades. Experimental tests were also carried out to validate the results obtained using the model. The model was successful in predicting the performance of the tested materials, while it also showed that elastic modulus and stress criteria could be used to predict performance under the specified testing conditions.

A numerical model was developed by Bolot et al. [62], which attempted to estimate the thermal conductivity of the AlSi/polyester abradable using two different finite element approaches (Cell-Centered and Nodal Discretization). Both techniques managed to yield values similar to those obtained from experimental procedures and it was thus difficult to distinguish between them. Even though the results of the numerical model were close to experimental ones, further improvements should be made to refine the model.

Another study performed by Peyraut et al. [63] used a finite element analysis model to simulate the hardness measurement of an abradable to identify its plastic parameters. This investigation concluded that hardness decreases with decreasing thickness and the results were validated from experimental procedures.

Instead of trying to model the material properties of the abradable, Legrand et al. [64] created a numerical model aimed to simulate the contact between a blade and the abradable coating. Results from this model included an abradable wear level and blade vibration responses in an attempt to establish a link between them. The study concluded that a low level of wear induced the highest vibration response in the blade, whereas pure unilateral conditions limited blade displacements and thus reduced vibrations. However, it was acknowledged that these results were highly dependent on the selected interaction scenario. Finally, the results obtained from this model were not validated using experimental procedures.

2.4 Summary

This chapter provided a detailed description on the function of abradable materials (with a focus on AlSi based abradables), the design criteria which these materials should meet and the required performance they must have in an aero-engine. Furthermore, in this section an extensive review of how abradable materials have been tested was provided. This includes testing done to measure the material properties of abradables, scaled and full-scale experimental test rigs developed to assess their performance and modelling techniques employed to predict abradable behaviour. One of the main gaps identified in the literature was that most inferences on the performance of these materials was based on post-test/post-service observations. A lot of information could be acquired in this way about the wear mechanisms that result from a contact, however, this method provided little insight on the development of the wear mechanisms during the contact and what caused these mechanism to occur in the first place. Fois [15] and Watson [43, 56, 44] identified this gap and used an experimental test rig developed by the Abradables Research group in The University of Sheffield to extensively monitor and explain underlying mechanisms of abradable-blade contacts. Fois focused on the investigation of Metco 320 (AlSi-hBN), while Watson focused on the research of Metco 314 (NiCrAl-Bentonite). These studies have provided invaluable information about the development of wear mechanisms and their causes during a contact. The research performed in this thesis, aimed to use the same experimental test rig to perform an exhaustive investigation on Metco 601 (AlSi-polyester) since this has not been performed in the literature. The aim was to develop novel techniques that will provide scientific insight on how the wear mechanisms evolve during a contact and what drives these mechanism to occur. Another very important gap that was identified in the literature has to do with the two AlSi based abradables, Metco 601 and Metco 320. These materials are very similar in terms of constituents, but their performance varies significantly and there is little understanding as to why this is the case. Also, since most studies on these materials were based on post-test/post-service observations it has been impossible to identify the differences in the development of the wear mechanisms. This research aimed to extensively test both of these materials and examine their behaviour with a range of novel techniques developed in this study. This aimed to provide invaluable understanding on what causes the significant differences in their performance of these two abradables.

Chapter 3

Methods

3.1 Experimental test platform

The testing required for this research was performed on an experimental test platform developed in The University of Sheffield abradables research group. This test rig has been successful in replicating the wear mechanisms observed in an aero-engine and it has been described in detail in previous studies [51, 42, 41, 43, 40]. Figure 3.1 shows a schematic of the test rig with the the sensors that were used in the standard set-up and in this section each component was described in more detail. This was the standard set-up and the only changes from the set-up described in previous studies were the addition of a webcam and containment. The webcam was added because it allowed monitoring of the test as well as observation of sparks, while the containment was added for safety. Further changes were done on this set-up according to the testing needs in later chapters, but these are discussed in more detail in the relevant chapters.

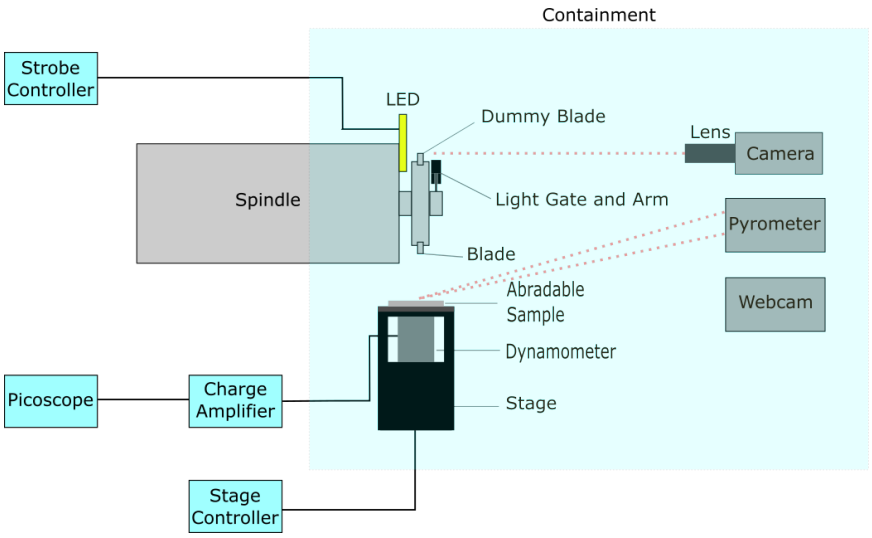

Figure 3.1: Schematic of the standard test rig set-up from the side (not to scale).

3.1.1 Spindle and disc

The rig is based on a machine tool spindle (GMN HSP 120g, GMN PAUL MÜLLER INDUSTRIE GMBH and CO. KG), which has a maximum rotational speed of 21000 rpm and has mounted on it a metal disc. The disc is attached to the spindle via an HSK-C40 coupling tool (Coventry Engineering Group Ltd, Coventry UK), which can be seen in figure 3.2(a). The disc is made out of grade 5 titanium alloy and is of 92.5 mm radius, has two removable blade holders 180^o apart, which are used to mount the blade sample and also a dummy blade on the disc. The blade is 3.5 mm long titanium alloy sample, while the dummy blade is made from the same material and has the same shape as the actual blade but it is 2 mm shorter and it is used to balance the disc and minimise the rotational vibrations. Figure 3.2 shows the disc, blade holder and blades assembly form the front and side-on views.

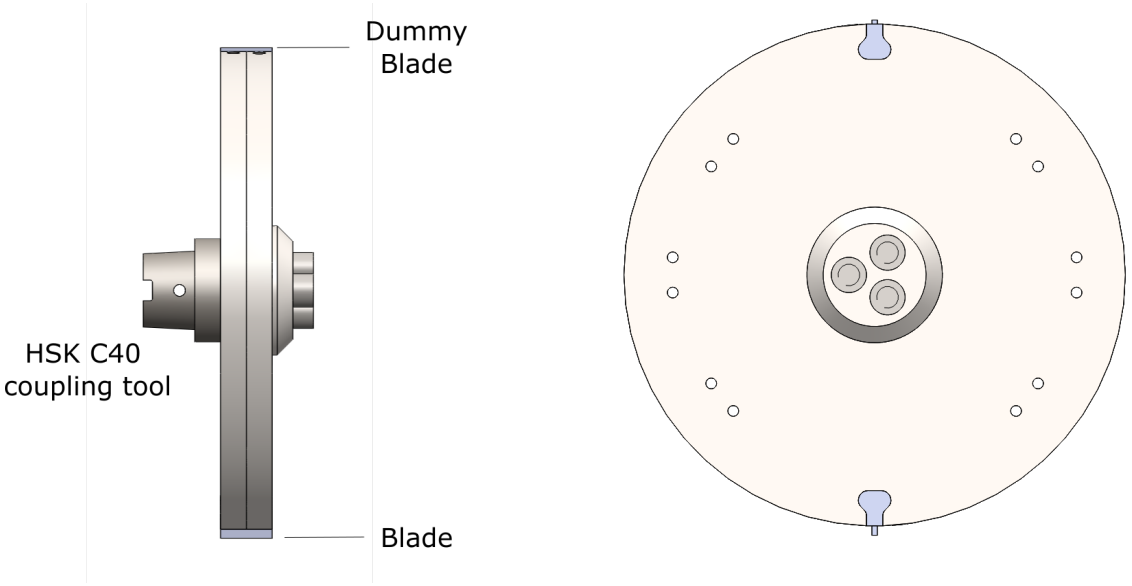

(a) (b)

Figure 3.2: (a) CAD showing the disc and blade assembly from the side, (b) CAD showing the disc and blade assembly from the front

3.1.2 Microscope stage

Abradable samples are mounted on a Z-axis microscope stage (OptoSigma SGSP80-20ZF, Laser 2000 (UK) Ltd., Northants, UK), which is situated below the disc. This is used to raise the abradable sample towards the disc in a pre-set and controlled way, replicating the incursion condition of an actual contact. The Z-axis microscope stage is able to create incursion rates in the range of 0.1 - 2000 $\mu m/s$ at intervals of 0.1 $\mu m/s$. A stage controller (OptoSigma, Laser 2000 (UK) Ltd., Northants, UK) is then used to set the incursion rate at the start of each test.

3.1.3 Stroboscopic imaging technique

A stroboscopic imaging technique is used in this test rig to capture images of the blade tip over the duration of the test, allowing the real time recording of blade length changes. A stroboscopic imaging is a technique where white light is flashed on a rotating object. The flashing matches the speed of rotations and this has as an effect the object ot appear stationary [65].

This is achieved by using a camera (Basler Ace acA1300-60gm Monochrome) with

a macro zoom lens (Computar MLH- 10x, Scorpion Vision Ltd, Hants, UK) and an LED (Cree CXB3070-0000-000N0HAD30G, RS Components Ltd., Northants., UK) with a strobe controller (Gardasoft RT200F-20, Stemmer Imaging Ltd.,Surrey, UK) and a light gate (Optek OPB916B, RS Components Ltd., Northants., UK). Figure 3.3 shows the LED and its dimensions, while table 3.1 summarises its specifications. This specific LED was chosen because of its high luminus flux (9967 lm), which translates to high brightness lighting.

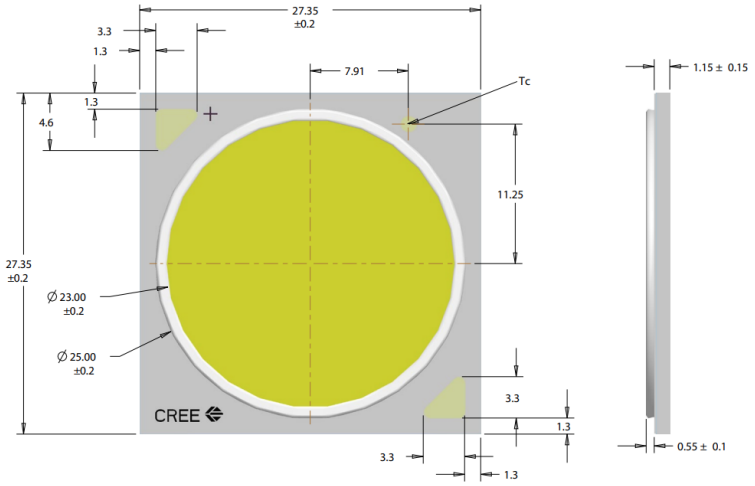

Figure 3.3: Engineering drawing of the LED that shows its dimensions (in mm)

Table 3.1: Summary of LED specifications

Attribute	Value
Typical Luminous Flux (lm)	9967
Optical Source Diameter (mm)	23
Colour Temperature (K)	3000
Radiant Flux (W)	107
Series	CXA2
Viewing Angle (°)	115
Colour Rendering	80
LED Colours	White
Forward Voltage (V)	36
Forward Current (mA)	2800
Dimensions (mm)	27.35 x 27.35 x 1.7

A metallic arm, which is attached on the disc (see figure 3.1), interrupts the light gate sending a signal to the strobe controller, which in turn sends a high energy, short duration pulse to the LED (1 microsecond, 48 V, 20 A). The LED is positioned directly in front of the camera and it is timed in such a way that it flashes when the blade is between the LED and the camera as shown in figure 3.4.

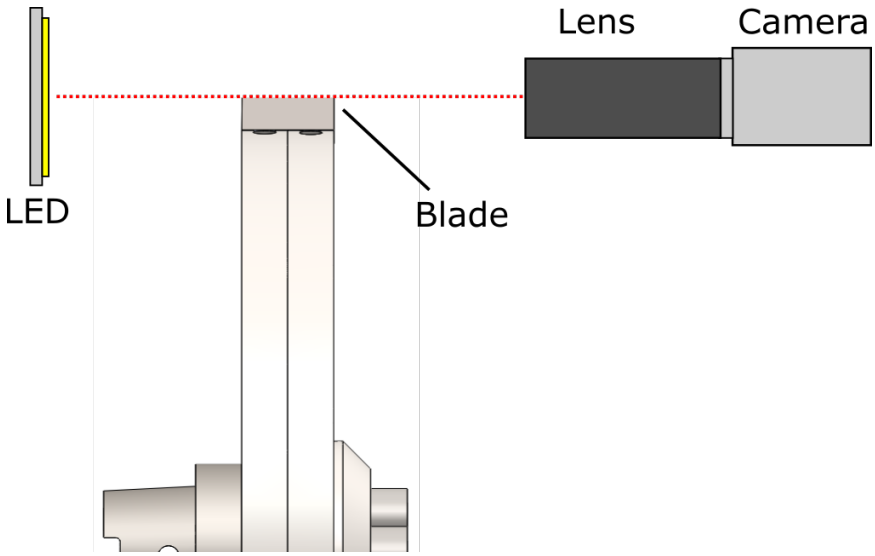

Figure 3.4: Schematic that shows the position of the blade and LED at the point when an image is acquired.

This camera set-up produces high quality images with a resolution of 1280 x 1024 pixels (px) at a frame rate of 27 frames per second. Due to the camera's shutter speed several rotations are captured at a single image depending on the rotation speed.

A web camera is also added to the test platform, which captures pictures of the system at regular intervals. The web camera serves two purposes. The first one is to allow the capture of spark images during the test and the second is to allow the user to see what is happening during the test. The camera and web cam are mounted on an adjustable support, which is only connected to the ground and does not have any physical contact with the test platform to ensure minimal vibrations of the cameras. The user has the option to choose which of the cameras to enable for each test using the LabVIEW program and this is described in more detail in section 3.1.6.

3.1.4 Force measurement

Contact forces are measured during the test using a piezo-electric dynamometer (Kistler Instruments Ltd, Hook, (UK), Type 9347 C), which is situated below the abradable sample. Figure 3.5 shows the dynamometer as well as its dimensons.

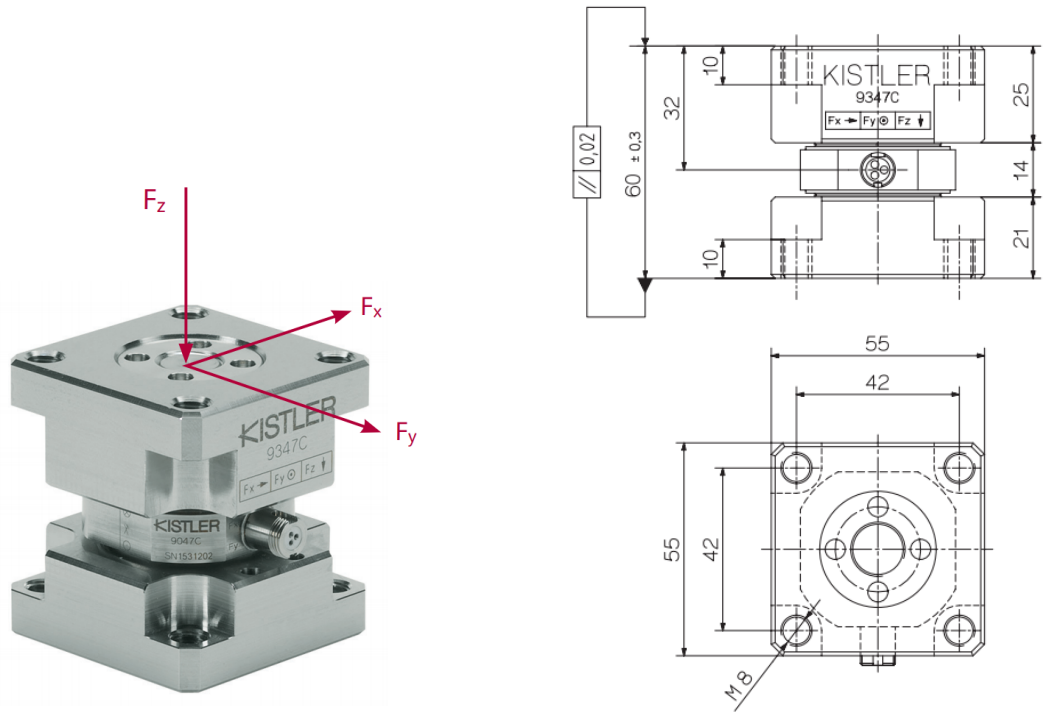

(a) (b)

Figure 3.5: (a) Picture of the dynamometer used for measuring forces generated in the contact, (b) Engineering drawings of the dynamometer showing its dimensions

The signal obtained from the dynamometer is amplified by a charge amplifier (Kistler

Table 3.2: Summary of key dynamometer specifications

Attribute	Value
Normal Range (N)	-30 to 30
Tangential Range (N)	-5 to 5
Sensitivity (pC/N)	-3.739 (Normal) -7.923 (Tangential)
Natural Frequency (kHz)	10 (Normal) 3.6 (Tangential)

Instruments Ltd, Hook, (UK), Type 5070A) and recorded using a digital oscilloscope (PicoTechnology, Cambridge, (UK), 3000 series, PicoScope 3404 B). The dynamometer can measure tangential forces in the range of -5 kN to 5kN and normal forces in the range of -30 kN to 30 kN. An electrical signal proportional to the applied forces is produced by the dynamometer, amplified by a charge amplifier and then recorded and displayed by a digital oscilloscope. The system has been calibrated and previous studies [15, 41] have shown that the forces measured are representative and there is no need for compensation of the dynamic response of the system. A summary of the force measurement system specifications is provided in table 3.2.

3.1.5 Temperature measurement

To record the temperature of the abradable samples, an infra-red pyrometer (CTLM-3H1CF3-C3, Micro-Epsilon, Koenigbacher, Germany) was used. The pyrometer has a spectral range of 2.3 μm and a temperature reading range of 150 ^{o}C to 1000 ^{o}C and it is used to measure the temperature of the abradable at the point of contact. To make accurate measurements, the emissivity setting of the pyrometer is calibrated for the abradables. To do this, the abraables are places in an oven until they reach a stable temperature. Then readings on the temperature of the abradable are made with the pyrometer and a K type thermocouple and the emissivity is adjusted until they match. This is repeated for several temperatures to ensure the highest possible accuracy [66, 67].

3.1.6 Data acquisition and synchronisation

As described in previous studies [51, 42, 41, 43, 40], a LabVIEW program was developed to control the test and collect all the data from the sensors. This was found to be significantly more convenient for synchronising the data rather than using the

software of each device or sensor. The LabVIEW program from previous studies is adjusted to include the additional cameras. An option is available to the user as to which cameras to use in each test (figure 3.6 red box). The output of the enabled cameras is then displayed on the front panel of the program (figure 3.6 blue box). The user can input the test conditions, such as the incursion rate, the blade tip vertical speed and the incursion depth, in the program and then start the test (figure 3.6 red box). When the test starts, the stage controller moves the stage towards the rotating disc at a predefined incursion rate. During the test and for each revolution of the disc, when the metal arm interrupts the light gate, a signal is sent to the stage controller, which in turn sends a pulse to either, one or both LEDs to flash. The LEDs flash allowing a picture of the blade to be captured. Appropriate delays have been introduced between the light gate interception and the LED flashes to ensure the position of the blade at the time of image capturing is correct.

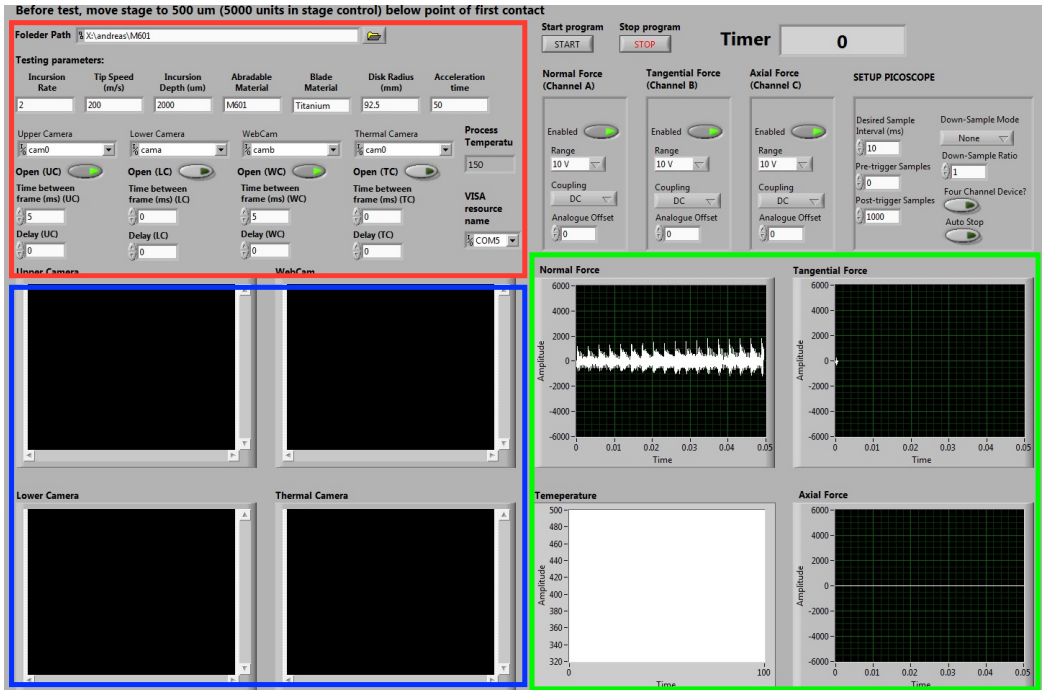

Figure 3.6: Front Panel of LabView program

At the same time, dynamometer readings for each strike and pyrometer measurements are recorded and displayed on live monitors (figure 3.6 green box). All the collected data are saved using a time label name convention allowing easy synchronisation of the data. When the test is completed the user manually stops it using the LabVIEW program and this stops the data collection.

3.1.7 Containment

Another modification made on the test platform is the addition of a containment unit built around the rig for enhanced health and safety purposes and this is shown in figure 3.7. It is made of a sandwich structure consisting of an aluminium sheet in the inside and a steel sheet on the outside both bolted on a piece of wood holding the structure together. The test platform can be easily accessed for test preparation since the containment is mounted on a rail and can be moved to the back when not testing. It is not in direct contact with the test platform and therefore it does not affect its operation.

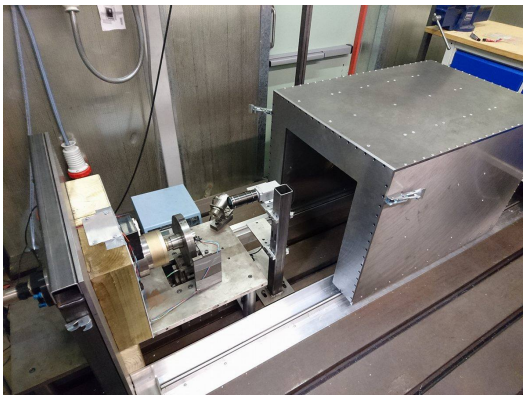

(a)

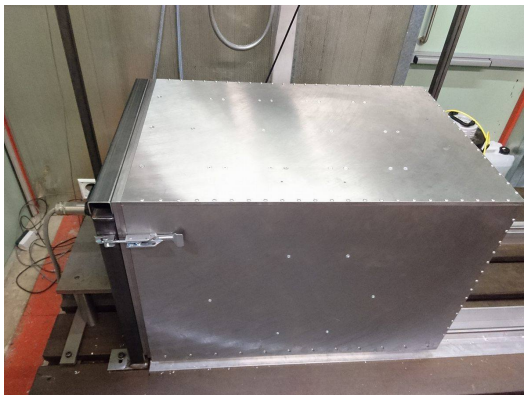

(b)

Figure 3.7: (a) Open containment, (b) Closed containment,

3.2 Test samples

3.2.1 Abradable samples

This section consists of a description of how the abradable samples are manufactured and their composition. As previously mentioned this research is focused on two different abradables, which are both rubbed against titanium (Ti-6Al-4V) blades. The first one is an AlSi-Polymer and the second one is AlSi/hBN, both of which are used in the compressor stages of current aero-engines and are commercially available from Oerlikon Metco as Metco 601 NS and Metco 320 NS as powders. Metco 601 NS powder is manufactured by blending and has the particle size is in range of 114 - 136 μm, while Metco 320 NS is manufactured by mechanical cladding and the resulting particle sizes are in the range of 190 - 234 μm.

Rolls-Royce provided samples of both materials, which were created by thermally spraying approximately 60 mm square patches on 80 mm square stainless steel plates with a thickness of 3 mm. The resulting surface roughness of the abradable samples received is typically around 15.24 μm [68]. A characteristic abradable sample is shown in figure 3.8.

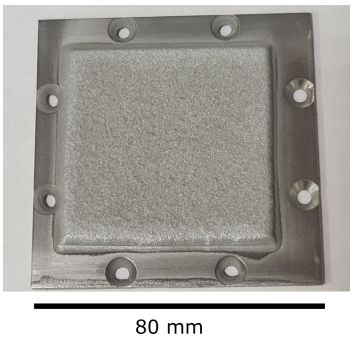

Figure 3.8: Abradable sample as manufactured.

The properties of the samples could be varied by changing the deposition rate of the spraying process to achieve the required hardness. The deposition rate is a function of the powder flow rate, the current input, the spray distance and the primary gas flow [69]. It was shown that hardness decreases with increasing the primary gas flow. This was because an increase in the primary flow decreases the temperature of the particles and colder particles were less densely distributed resulting in lower hardness abradables to form. Furthermore, input current was found to be directly proportional to the particle temperature. That meant that by increasing the input current particle temperature increased resulting in more dense and high hardness abradables. Finally it was shown that lower particle speeds resulted in more dense distribution and higher hardness abradables [69]. The two materials were sprayed into batches of different hardnesses equivalent to the ones used in the actual engines. To establish an understanding of the effect of hardness on the resulting wear mechanisms, low, intermediate and high hardness samples were sprayed for both materials in the range of which each material is used in the actual engines, as per Roll-Royce specifications [17, 70]. Table 3.3 summarises the typical engine operation range for the hardness of the two materials, as well as the hardness of sprayed samples used for testing. The hardness of the samples was measured with a superficial Rockwell hardness scale R15Y, which is commonly used for soft and thin materials [71].

Table 3.3: Summary of hardness values tested

Material	Operational Hardness Range (R15Y)	Mean Hardnesses		
Metco 320	45 -70	45.4	59.7	70.3
Metco 601	55-85	55.3	69.9	81.6
Titanium alloy (blade)	78.3		78.3	

The thermal properties of the abradables were experimentally determined by using a flash method machine (FLASHLINE 3000, anter corporation [72]). Five repeats of the measurements taken at 50 ^{o}C and the average value, as well as the standard deviation recorded are presented in table 3.4. The blade material was not tested in this way and instead typical material properties were found from literature and added to table 3.4 [73]. This was done as titanium alloy material properties do not vary that much compared to abradables.

The results shown in table 3.4 were used in the calculation of the heat partition and Peclet number, which were needed for the generation of the wear maps. Moreover, the thermal properties were essential later in the thesis where the thermal response of the abradable is considered [74].

Table 3.4: Thermal properties

	Mean	Standard Deviation
M601 R15Y 82		
Heat Capacity (J/gK)	1.225	0.079
Thermal Diffusivity (cm^2/s)	0.0754	0.0029
Thermal Conductivity (W/mK)	16.18	1.32
M601 R15Y 70		
Heat Capacity (J/gK)	1.087	0.048
Thermal Diffusivity (cm^2/s)	0.0430	0.0007
Thermal Conductivity (W/mK)	7.09	0.26
M601 R15Y 55		
Heat Capacity (J/gK)	1.185	0.086
Thermal Diffusivity (cm^2/s)	0.0267	0.0012
Thermal Conductivity (W/mK)	4.38	0.25
M320 R15Y 70		
Heat Capacity (J/gK)	1.174	0.129
Thermal Diffusivity (cm^2/s)	0.104	0.0124
Thermal Conductivity (W/mK)	19.85	3.23
M320 R15Y 64		
Heat Capacity (J/gK)	1.115	0.086
Thermal Diffusivity (cm^2/s)	0.091	0.0084
Thermal Conductivity (W/mK)	17.47	1.26
M320 R15Y 58		
Heat Capacity (J/gK)	1.074	0.135
Thermal Diffusivity (cm^2/s)	0.075	0.0061
Thermal Conductivity (W/mK)	13.52	1.78
Titanium alloy (Ti-6Al-4V)		
Heat Capacity (J/gK)	0.5263	-
Thermal Diffusivity (cm^2/s)	0.142	-
Thermal Conductivity (W/mK)	6.7	-

3.2.2 Blade samples

This research focus is the contact between the abradable and the blade of the compressor stages of an engine. For this reason the blade samples used in this investigation were made of a grade 5 titanium alloy (Ti-6Al-4V), which is typically used in these stages [7, 75, 76]. The blades used previously in The Sheffield University abradable research group, which are described in more detail in previous studies [51, 15], were causing some problems with bending at higher force contacts because they were clamped at the short neck in the middle of the blade. For this reason the design of the blades was changed in this investigation to a more short and compact design. The

old and new designs are displayed in figure 3.9, while the exact dimensions of the new design are shown in figure 3.10. The flat shape of the blade might not be an exact simulation of the actual engine blades, but it was shown in previous studies that this approximation produces the same wear mechanisms as the actual engine conditions [7, 37].

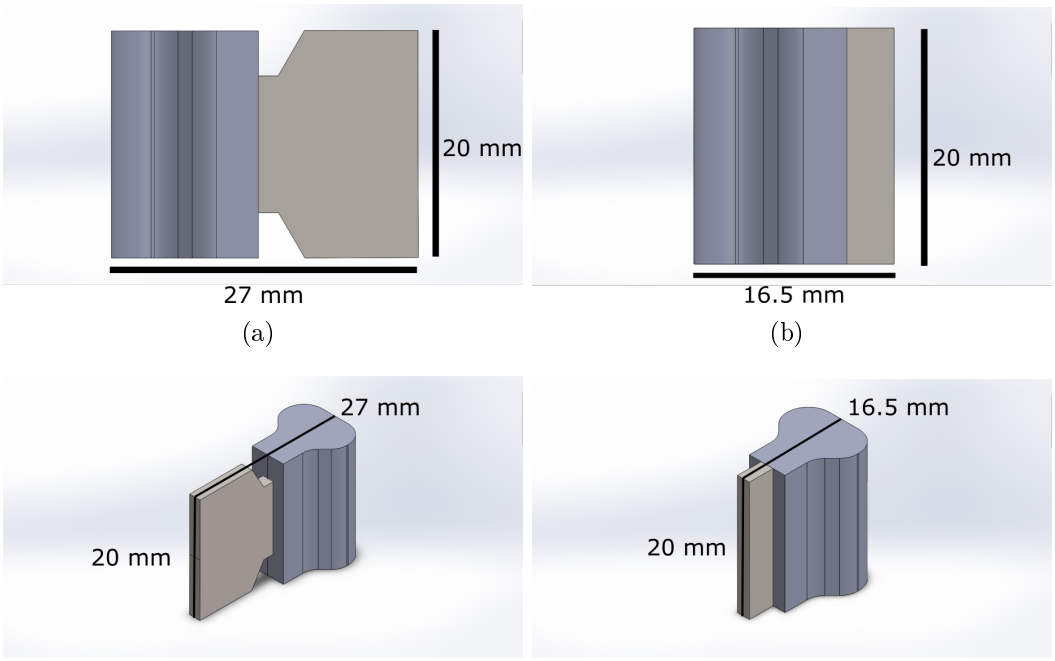

Figure 3.9: (a) CAD showing the old blade-clamp assembly from the side view, (b) CAD showing the new blade-clamp assembly from the side view, (c) CAD showing the old blade-clamp assembly from the isometric view, (d) CAD showing the new blade-clamp assembly from the isometric view.

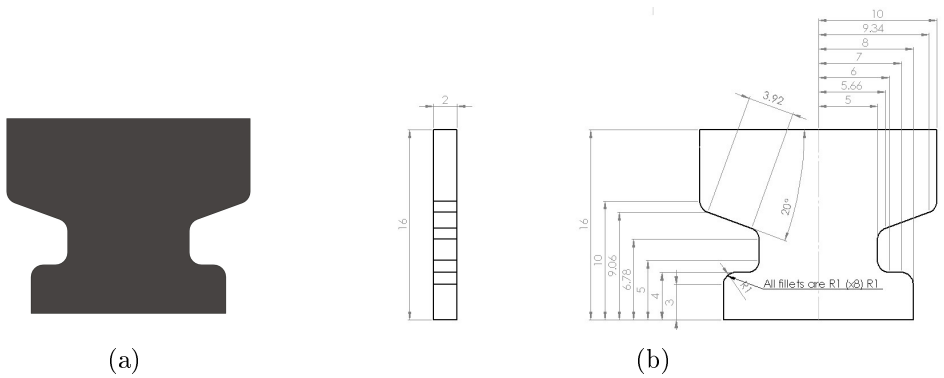

Figure 3.10: (a) CAD showing the new blade design, (b) Engineering drawing that show the exact dimensions of the new blade design (dimensions are in mm).

As shown in figure 3.10 the height of the blade is 16 mm and its length 20 mm, while it is 2 mm wide. The blade is then clamped at 12.5 mm from the bottom (along the longer 20 mm section) and this results in an overhang of 3.5 mm.

3.3 Test conditions

Generally for the purposes of this research the standard parameters to consider were the incursion speed, the blade tip speed, the abradable material and its hardness as these are shown to influence the rub response of abradables [77]. The first parameter considered in this investigation was the incursion rate. Previous studies highlighted the importance of the incursion rate in the resulting wear mechanism and therefore it is an important parameter to consider. A range between 0.02 and 2 microns/pass was used throughout this investigation (unless specified otherwise), since these values represent the two extreme scenarios that occur in real engine operation. The high incursion rate represents contact that occurs during the service life of an engine, such as thermal and centrifugal expansions and not perfectly balanced and aligned parts. The low incursion rate represents the running and handling procedure performed on engines [78, 79]. The targeted rub depth is another parameter that influences the contact time of a rub and it needs to be specified. The range of rub depths usually observed in engines is between 1 and 2.4 mm and consequently for this study a value of 2 mm was chosen [7, 37, 75, 80] . The blade tip speed is another parameter that needs to be assessed in terms of its importance towards the performance of the abradable. During a real engine operation the blade tip speed is around 400 m/s, however the rig used in this investigation is only capable of reaching tip speeds of up to 200 m/s. Studies performed previously on this test rig have shown that the effect of speed on the resulting wear mechanism was not so significant ([15, 42, 41, 44]), therefore for most of the investigation in this study only the highest (most representable) speed is considered (200 m/s). In addition to these parameters, the material tested can be varied and in this investigation two abradable materials were considered (Metco 601 and Metco 320) because the main aim of this study was to identify and explain the differences in the performance of these two materias. Finally three different hardness values were examined to assess the effect of hardness on the resulting wear mechanism. The range of hardness values was different for each material and it was chosen to be representative of the actual specification range the engine manufacturer uses in the engines. These values are summarised in table 3.3. Depending on the methodology

of each testing procedure described in the following chapters some alterations were made to these general testing conditions and parameters and these are described in more detail in the relevant chapters.

Table 3.5: Test parameters considered

Test Number	Abradable Material	Hardness (RY15)	Speed (m/s)	Incursion Rate (microns/pass)	Target Depth (mm)
1	M601	55	200	2	2
2	M601	55	200	0.2	2
3	M601	55	200	0.02	2
4	M601	70	200	2	2
5	M601	70	200	0.2	2
6	M601	70	200	0.02	2
7	M601	79	200	2	2
8	M601	79	200	0.2	2
9	M601	79	200	0.02	2
10	M320	58	200	2	2
11	M320	58	200	0.2	2
12	M320	58	200	0.02	2
13	M320	64	200	2	2
14	M320	64	200	0.2	2
15	M320	64	200	0.02	2
16	M320	70	200	2	2
17	M320	70	200	0.2	2
18	M320	70	200	0.02	2

3.4 Testing procedure

This is a general testing procedure that is true for all the experimental procedures that follow unless otherwise stated. Some alterations to this standard procedure were required for some of the tests and these are explained further in the later chapters. In order to perform a test the abradable sample was mounted on the stage and then the titanium blade and dummy blade were mounted on the disc, using the removable blade holders and the disc was then mounted on the spindle. Then, the stage was manually adjusted so as to ensure that the blade was just touching the abradable. Next it was moved down, away from the blade for 5 mm to ensure no contact occured before the start of the test. The next step was to input the test conditions, such as the incursion speed, the vertical blade tip speed and the incursion depth in the LabVIEW program. After this, the spindle's rotational speed was set and the spindle was spun. When it reached the required rotational speed the test was initialised from the LabVIEW program and the incursion began at the same time at which all the sensors started to record data. After the defined incursion depth was reached the stage returned to the original position, ie. 5mm below the blade. After this all the

data was collected and could be used for post-processing and analysing.

3.5 Data processing and analysis

This section includes a detailed description of how the data obtained during a test was processed and analysed to obtain useful information and insight about the contact.

3.5.1 Visual inspection

The first analysis performed after a test was the visual inspection of the samples. In this process the blade sample was observed for indications of any visible changes, such as any adhesion, wear or thermal damage. Furthermore, the height and weight of blades could be measured and compared to the pre-test recorded values to estimate length changes and material transfer. This step also helped to validate that the blade length change calculations of the algorithm described in section 3.5.3 were accurate. At the same time, the abradable sample's surface was inspected after testing. The aim of this was to assess the roughness of the surface and observe any visible wear phenomena, such as delamination or material transfer. For example figure 3.11 shows how the surface of an abradable looked like before a test (3.11(a)) and how the surface looked like after testing (3.11(b)), illustrating how visual inspection can provide insight about the wear mechanism (grooves and material transfer).

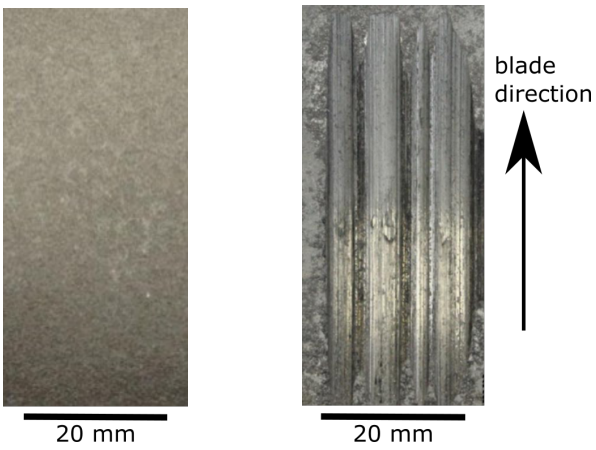

Figure 3.11: (a) Example of an untested abradable sample's surface, (b) Example of a tested sample that shows severe grooving and material transfer (data taken from an M320, hardness RY15 70, 200 m/s, 0.02 microns/pass test)

3.5.2 Rub length

The data obtained through the LabView data acquisition system was timestamped and synchronised to allow the observations from different sensors to be overlaid and provide a complete insight about the contact. However, it was shown in previous studies that the abradability of a material is dependent on the length of the rub that is generated [48, 52, 81]. For this reason time readings were converted into rub length measurements for the analysis performed on the acquired data. Rub length is the accumulated length of the arc that the blade rubs the abradable on each pass. As a result the total rub length is dependent on several key parameters that control the wear mechanisms, such as the blade tip speed, the incursion rate, the disc radius and the time of the contact. Therefore, it provides more useful information that just the time a reading was taken and this is why it was used in this study. The total rub length for a test can be calculated by equation 3.1, where L_P is the total rub length after P passes, R_p is the calculated radius of the disc (taking into account any pick up adhesions or blade wear) at pass p, I is the incursion rate per pass and p is the current pass value.

$$L_P = \sum_{p=1}^{P} 2R_p cos^{-1}\left(\frac{R_p - Ip}{R_p}\right) \tag{3.1}$$

3.5.3 Blade length

The blade length change calculations were performed by processing the raw images obtained from the stroboscopic imaging system described in 3.1.3 using a MATLAB analysis code previously developed by The University of Sheffield abradable research group. Using this code the raw images are imported into MATLAB and then converted to binary. An edge detection algorithm is then used to identify the blade profile, which allows the tracking of blade's length changes for each image. These steps are summarised in figure 3.12. Figure 3.13 shows an overlay of an image in the middle of a test, with the first image that is taken before the contact initiates and the resulting edges that are detected from the algorithm. To calculate the blade length the algorithm assigns coordinates to the images and subtracts the first image's coordinates from the current image's coordinates. The final step is to convert the coordinates to mm which is done using the pixels/mm rating of the lens used at the test.

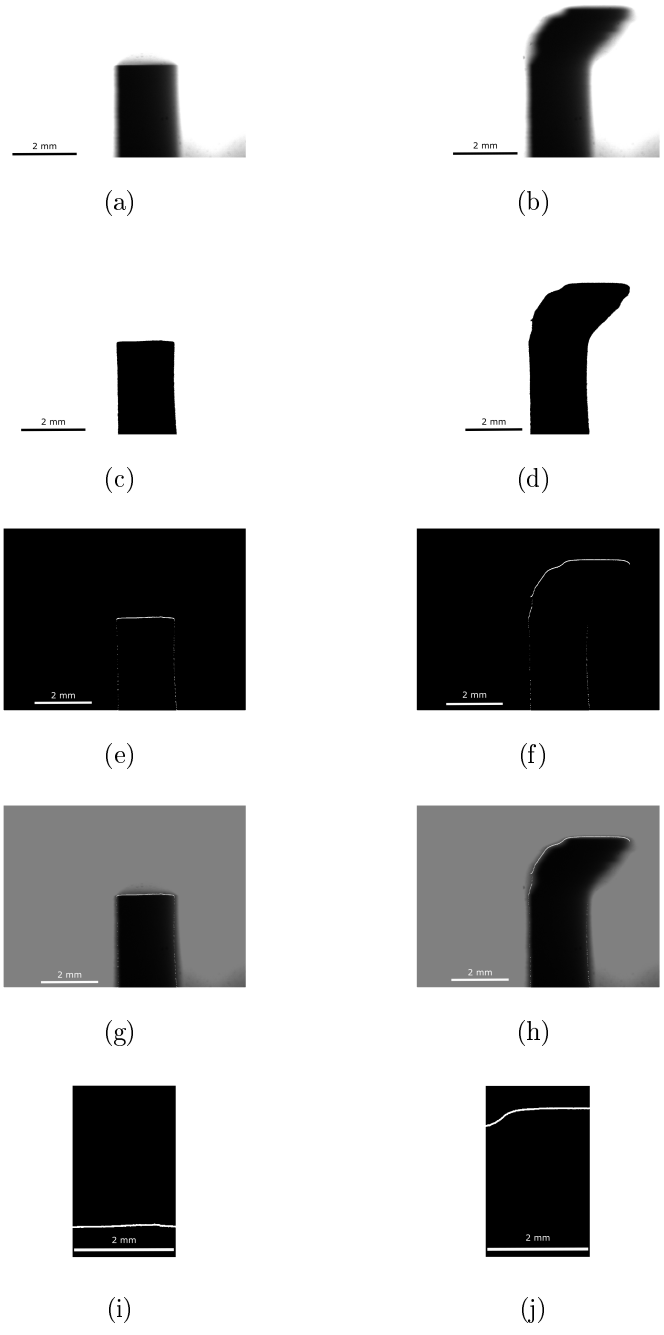

Figure 3.12: (a) Raw blade image before any contact, (c) Binarised image of (a) , (e) Edge detection, (g) An overlay of the edge detection and the original raw image to assess the accuracy, (i) Edge identified from the edge detection algorithm cropped out for measurement, (b) Raw blade image at the middle of a test, (d) Binarised image of (b) , (f) Edge detection, (h) An overlay of the edge detection and the original raw image to assess the accuracy, (j) Edge identified from the edge detection algorithm cropped out for measurement (data taken from an M320, hardness RY15 55, 200 m/s, 0.02 microns/pass test)

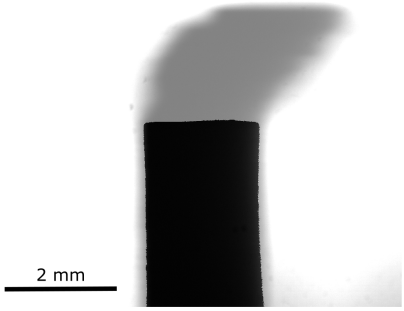

(a)

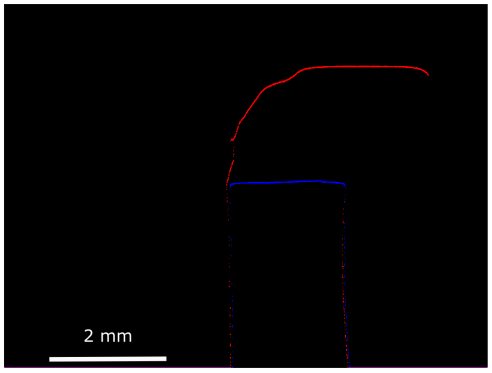

(b)

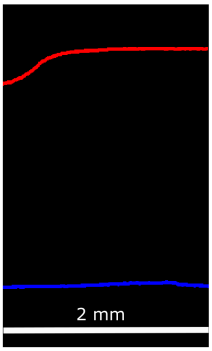

(c)

Figure 3.13: (a) Overlay of the first image obtained before contact is initiated and an image obtained in the middle of the test, (b) Overlay of the edges detected from the 2 images, (c) The cropped overlay of the edges detected that are used for calculating the blade length changes (data taken from an M320, hardness RY15 70, 200 m/s, 0.02 microns/pass test)

3.5.4 Forces

The forces are measured using the piezoelectric dynamometer described in 3.1.4. The signal generated from each strike is amplified from the charge amplifier and recorded and displayed at the digital oscilloscope. The digital oscilloscope is then connected to the LabView data acquisition system, which timestamps the measurements and stores them for processing. Figure 3.14 shows an example of 5 consecutive strikes obtained from an example test.

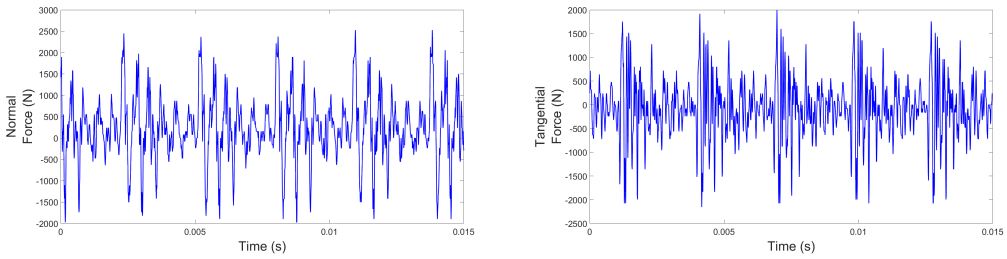

(a) (b)

Figure 3.14: (a) Example of normal force recorded data for 5 consecutive strikes, (b) Example of tangential force recorded data for 5 consecutive strikes (data taken from an M601, hardness RY15 82, 200 m/s, 2 microns/pass test)

As observed, each strike was followed by a free vibration period in the measuring system, however, it was shown by Fois ([15]) that these vibrations do not affect the accuracy of the measurement and no dynamic compensation is required. Consequently, in the post processing of this data the magnitude of the peaks was extracted and used to generate force over time/rub length plot for the duration of the contact.

3.5.5 Temperature

The temperature of the abradable was measured using the pyrometer described in 3.1.5. The pyrometer is connected to the LabView data acquisition system, which in turn timestamps and stores the recorded values. These values are then directly imported in MATLAB and are used to generate temperature over time/rub length plots for the duration of the contact.

3.6 Sample preparation

Optical and scanning electron microscopy was used in this investigation to meet two aims. The first aim was taking images of the blade and abradable microstructure after testing, while the second aim was the examination of the debris that was ejected during the contact. This section provides a summary of the methodology followed in the preparation of samples to be used for optical and scanning electron microscopy for these two cases.

3.6.1 Abradable sample preparation

The first step required making microscopy samples from the tested abradables, was to section the specimens into thin strips. The abradable was sectioned across the longitudinal direction of the rub into thin strips of 5-10 mm width, using a ferrous abrasive cutting blade (MetAbrase 11-4207-010) at a rotational speed of 2500 RPM and a feed rate of 2 mm/s, attached to a high precision cutting tool (Secotom-50 Struers Ltd., Denmark). Previous studies provided a guideline on the recommended preparation procedures for porous coatings similar to abradables and these guidelines were followed in this study. The abradable strips were vacuum impregnated with epoxy resin (EpoThin2, Buehler Ltd., USA), which is the recommended procedure as epoxy fills porous materials and allows an easier distinction between different phases and porosity. After this the samples (up to 6 at a time) were mounted on a grinding and polishing machine (Automet 250, Buehler Ltd., USA). Firstly, the samples were ground to remove any damage introduced in the sectioning phase and to produce a flat surface. As recommended, a sequence of grinding steps was performed starting from a coarse grinding paper and progressively moving to finer ones (P240, P360, P600, P1200 SiC grinding papers used). The mounted samples were ground for two minutes at each coarseness level with a force of 30 N per sample and at a rotational speed of 300 RPM. Water lubricant was used during this process to avoid thermal damage on the samples. Finally, 6.3 and 1 micrometer diamond suspension were used to polish the samples for 5 minutes each and at a rotational speed of 150 RPM and a force of 30 N per sample. This step was done to remove any scratches left from the grinding and create a highly reflective surface for better optical microscopy images. [82, 83, 84, 85, 86, 87]

3.6.2 Blade sample preparation

The tested blade samples could be examined by hot mounting them using a conductive mounting compound (KonductoMet, Buehler Ltd., USA), which is ideal for SEM inspection. The whole blade was mounted and therefore there was no need for grinding and polishing the samples. An optical microscope (Nikon Eclipse LV150) and an SEM (TM3030 Hitachi, Tokyo, Japan) was then used to examine the micro-structures of the samples.

Figure 3.15 displays images of mounted blade and abradable strips samples ready for microscopy.

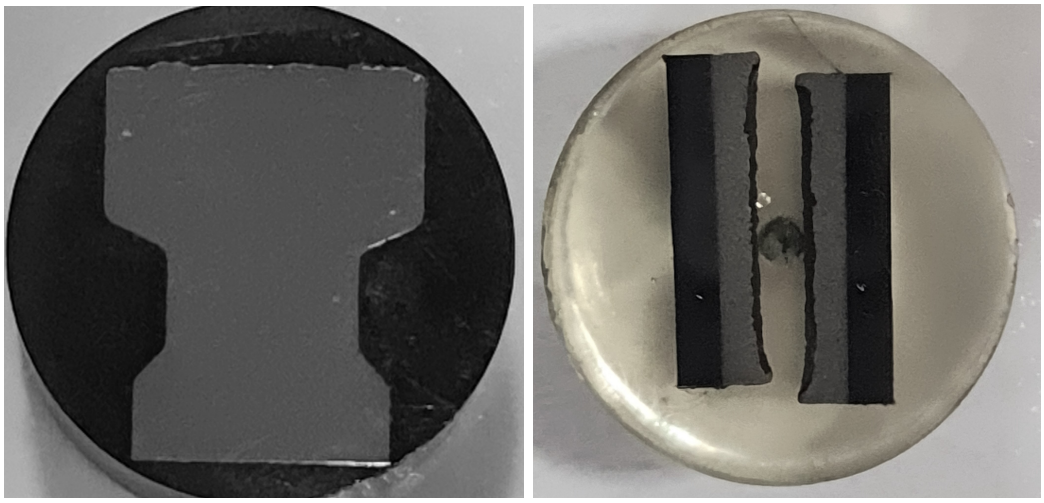

(a) (b)

Figure 3.15: (a) Image of a blade sample prepared for microscopy, (b) Image of a abradable strip pair prepared for microscopy

3.6.3 Debris preparation

Debris generated during the contact was collected while testing in order to examine the size and distribution of particles removed from the material during the event. This was achieved by mounting a holder next to the abradable sample and in the direction of the blade strike, which holds a conductive carbon adhesive disc (Carbon adhesive discs AGG3347N, Agar Scientific Ltd., Essex, UK) attached on an SEM stub (SEM Specimen Stubs, 12.5mm dia, 3.2 x 8mm pin, Agar Scientific Ltd., Essex, UK). The debris from the contact was ejected towards the carbon adhesive discs and collected. Post-test the SEM stubs were carefully removed and stored to avoid contamination

and were later examined with the SEM. Figure 3.16 shows a schematic of how the holder was attached next to the abradable sample to allow the collection of the debris [88].

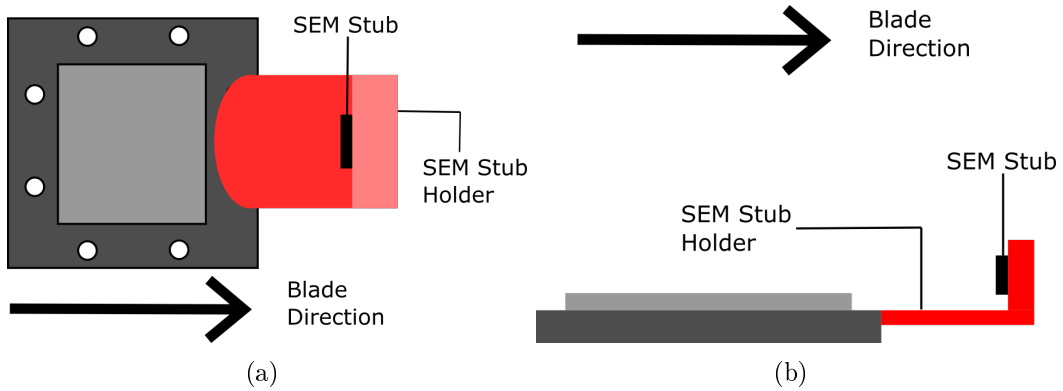

Figure 3.16: (a) Schematic showing how the holder is attached next to the abradable sample to allow the collection of the debris from the top view, (b) Schematic showing how the holder is attached next to the abradable sample to allow the collection of the debris from the side view.

3.7 Summary

This chapter provides an overview of the standard experimental techniques and set-up used throughout this investigation. Firstly, the choice of blade and abradable samples was explained and justified. Next, a detailed description of the standard set-up of test rig and all the sensors was provided. Furthermore, the selection of the testing parameters, the testing procedure and the way data is processed and analysed was discussed. The last section of this chapter provided a summary of how samples were prepared for microscopy. Some changes are made in this standard setup, depending on the specific methodology of each technique developed in the following chapters, and these changes are described in the relevant chapters. Finally, any additional techniques and analysis tools used in following chapters are also described in the relevant chapter.

Chapter 4

Performance Characterisation

4.1 Introduction

This chapter includes the characterisation of the wear performance of Metco 601. Moreover, an extensive comparison of its performance with the performance of Metco 320 was performed. This allowed the identification of the main and key differences in the two abradable's performance which was the main aim of this chapter. Finally, the current performance metrics were re-considered and different metrics were suggested where it was relevant.

A previous study [15] had performed an in depth characterisation of the performance of Metco 320. More specifically, this study provided links between the wear mechanism resulting from the contact with testing condition, such as incursion rate and blade tip speed. This was done to identify whether there are "safer" regions where the abradables can be operated. Trends between the testing conditions and the resulting forces and temperature were also examined in this previous study. The first step of the research performed in this thesis was to follow a similar methodology and perform an extensive characterisation of the performance of Metco 601.

4.2 Methodology

4.2.1 Materials

For this set of tests the abradable material Metco 601 was examined. Three different hadnesses that cover the operational range provided by the engine manufacturer were

considered (R15Y 55, R15Y 70, R15Y 82).

4.2.2 Test conditions and test matrix

As the main aim of this chapter was to examine in depth the performance of the Metco 601 abradable a wide range of testing conditions that covers all the operating range of an engine was required. For this reason 5 incursion rates, 2 blade tip speeds and 3 material hardnesses were considered. A range of 5 incursion rates between 0.02 and 2 μm/pass was selected as this represents the operating range of the actual engines [78, 79]. Also, two blade tip speeds were considered to assess the effect of speed as usually this is an important parameter in machining like contacts [89]. Finally, 3 different hardnesses allow the assessment of the effect of material hardness for a given abradable.

The testing parameters are summarised in table 4.1:

Table 4.1: Testing matrix and test parameters for the set of tests performed in this chapter

Test Number	Abradable Material	Hardness (RY15)	Blade Material	Tip Speed (m/s)	Incursion Rate(μm/pass)	Target Depth (mm)
1	Metco 601	55	Ti-6Al-4V	100	0.02	2
2	Metco 601	55	Ti-6Al-4V	100	0.2	2
3	Metco 601	55	Ti-6Al-4V	100	0.6	2
4	Metco 601	55	Ti-6Al-4V	100	2	2
5	Metco 601	55	Ti-6Al-4V	100	3	2
6	Metco 601	55	Ti-6Al-4V	200	0.02	2
7	Metco 601	55	Ti-6Al-4V	200	0.2	2
8	Metco 601	55	Ti-6Al-4V	200	0.6	2
9	Metco 601	55	Ti-6Al-4V	200	2	2
10	Metco 601	55	Ti-6Al-4V	200	3	2
11	Metco 601	70	Ti-6Al-4V	100	0.02	2
12	Metco 601	70	Ti-6Al-4V	100	0.2	2
13	Metco 601	70	Ti-6Al-4V	100	0.6	2
14	Metco 601	70	Ti-6Al-4V	100	2	2
15	Metco 601	70	Ti-6Al-4V	100	3	2
16	Metco 601	70	Ti-6Al-4V	200	0.02	2
17	Metco 601	70	Ti-6Al-4V	200	0.2	2
18	Metco 601	70	Ti-6Al-4V	200	0.6	2
19	Metco 601	70	Ti-6Al-4V	200	2	2
20	Metco 601	70	Ti-6Al-4V	200	3	2
21	Metco 601	82	Ti-6Al-4V	100	0.02	2
22	Metco 601	82	Ti-6Al-4V	100	0.2	2
23	Metco 601	82	Ti-6Al-4V	100	0.6	2
24	Metco 601	82	Ti-6Al-4V	100	2	2
25	Metco 601	82	Ti-6Al-4V	100	3	2
26	Metco 601	82	Ti-6Al-4V	200	0.02	2
27	Metco 601	82	Ti-6Al-4V	200	0.2	2
28	Metco 601	82	Ti-6Al-4V	200	0.6	2
29	Metco 601	82	Ti-6Al-4V	200	2	2
30	Metco 601	82	Ti-6Al-4V	200	3	2

4.2.3 Experimental set-up and procedure

This set of tests was performed on the experimental test rig described in chapter 3, with the standard equipment and set-up. Also the standard analysis procedure described previously was also followed. Any additional analysis techniques used were described in more detail in their respective sections.

4.3 Results

The various results obtained from the experimental testing of Metco 601 are summarised in this section. These results include visual examination of post-tested samples, blade length changes during testing (obtained using the stroboscopic imaging technique), force and temperature data.

4.3.1 Visual examination

In this section, some of the images of the abradable coatings and the blades taken after the test are displayed. Due to the large number of tests, only some of the images were presented. The images chosen were examples of cases where the resulting wear mechanisms were observed. The remaining images from all the tested samples performed in this study were shown in appendix A.

Figure 4.1 illustrates the main wear mechanisms observed from visually inspecting the abradable and blade samples after testing. These wear mechanisms were previously described in section 2.2.2. The images at the top are the abradable coating samples and the images at the bottom are the equivalent blade samples used in the same test. Figure 4.1(a) showed a smooth surface with minimal grooving and this suggested an efficient cutting mechanism. However, by closely observing figure 4.1(d), small amounts of adhered material could be seen on the tip of the blade. This was a quite common phenomenon throughout the tests. A more grooved rub surface was observed by looking at figure 4.1(b). In this case, slightly longer adhesions of material were observed at the tip of the blade justifying the deeper grooving by inspecting the equivalent blade (figure 4.1(e)). The final wear mechanism that could be identified from visual inspection was blade wear and it was clearly shown by figures 4.1(c) and 4.1(f). The blade shown in figure 4.1(f) was clearly shorter than the other blades

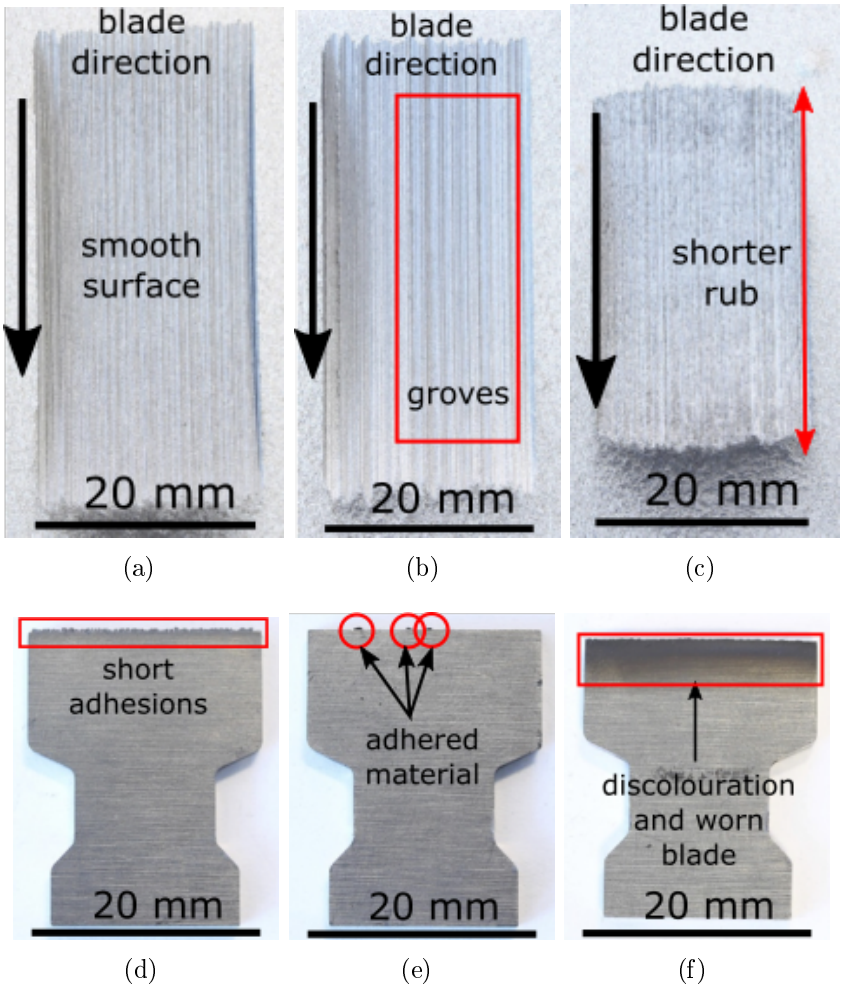

Figure 4.1: Images of characteristic abradable and blade samples taken after the following tests: for (a) and (d) R15Y 55, 200 m/s, 2 μm/pass, for (b) and (e) R15Y 70, 200 m/s, 0.2 μm/pass and for (c) and (f) R15Y 82, 200 m/s, 0.02 μm/pass.

indicating wear. Moreover, the length of the rub was significantly smaller for this test, as shown in figure 4.1(c), enhancing the blade wear inference.

Table 4.2 provides a summary of the observed wear mechanism for all the tests carried out.

Table 4.2: Summary of the wear mechanisms identified by visual inspection

Test No.	Hardness (RY15)	Tip Speed (m/s)	Incursion Rate (um/pass)	Wear Mechanism (Visual Inspection)
1	55	100	0.02	Adhesion, Grooving
2	55	100	0.2	Some Adhesion, Some Grooving
3	55	100	0.6	Cutting
4	55	100	2	Cutting, Some Grooving
5	55	100	3	Adhesion, Grooving
6	55	200	0.02	Adhesion, Grooving, Blade Wear
7	55	200	0.2	Adhesion, Grooving
8	55	200	0.6	Cutting
9	55	200	2	Cutting
10	55	200	3	Cutting
11	70	100	0.02	Adhesion, Grooving
12	70	100	0.2	Adhesion, Grooving
13	70	100	0.6	Cutting
14	70	100	2	Cutting, Some Grooving
15	70	100	3	Cutting
16	70	200	0.02	Cutting, Some Grooving
17	70	200	0.2	Adhesion, Grooving
18	70	200	0.6	Adhesion, Grooving
19	70	200	2	Cutting
20	70	200	3	Cutting
21	82	100	0.02	Severe Blade Wear
22	82	100	0.2	Blade Wear
23	82	100	0.6	Blade Wear
24	82	100	2	Blade Wear
25	82	100	3	Blade Wear
26	82	200	0.02	Blade Wear
27	82	200	0.2	Blade Wear
28	82	200	0.6	Blade Wear
29	82	200	2	Slight Blade Wear, Slight Adhesion/Grooving
30	82	200	3	Blade Wear

Concluding, the three main wear mechanisms observed from visual inspection were cutting, adhesion and blade wear and characteristic examples were displayed above.

4.3.2 Stroboscopic imaging technique

The stroboscopic imaging technique described in chapter 3 was used to monitor the blade length changes over the duration of the tests. The results obtained were plotted against the individual test rub lengths. Positive blade length change corresponded to an increase in blade length, while a negative blade length change represented a decrease in the blade length. As previously, due to the large number of tests only a characteristic sample of plots were presented in this section. The samples chosen were the ones that showed the most significant results and were used to explain the general trend of all the samples and were displayed in figure 4.2. The first plot, presented in figure 4.2(a), represented the typical response of all the abradable samples with hardness value of R15Y 82. A continuous negative blade length change was observed suggesting continuous blade wear. Maximum blade wear and wear rate varied between different testing conditions, but the same trend was observed for all the tests performed on this hardness. However, in the testing conditions described by figure 4.2(b), even though wear still occurred, the rate was so small that an almost perfect cut resulted (there was also an initial adhesion at the start of the test). The plot in figure 4.2(c) shows another significant characteristic observed from a large number of tests performed on Metco 601, which was the 'saw-tooth' like adhesion. This was indicated by an increase in the blade length, which suggested adhesion, that continued up to a certain point and then it sharply reduced to a near zero value. This behaviour suggested that all of the adhered material breaks off as a whole chip each time this happened. It is interesting to note that apart from the first peak, the adhered material broke off after a similar adhesion length was reached. This effect was further discussed along with other observations in section 8. Figure 4.2(d) shows a more conventional adhesion pattern where the adhesion was continuous and at an approximately constant rate. It is worth noting that the adhesion rate was similar and high for both cases. The vast majority of the performed tests (except for R15Y 82) exhibited the behaviour of either figure 4.2(c) or figure 4.2(d). Figure 4.2(e) shows a special case, which was observed in a few test conditions. This included both wear and adhesion mechanisms taking place over a significant rub length during the test. These tests were more difficult to classify and were discussed in more detail later on. Finally, an efficient cutting mechanism was observed for a minority of the tests, as shown in figure 4.2(f). A slight adhesion was observed in these cases as well, but the rate and maximum adhesion were so small that could be considered as negligible.

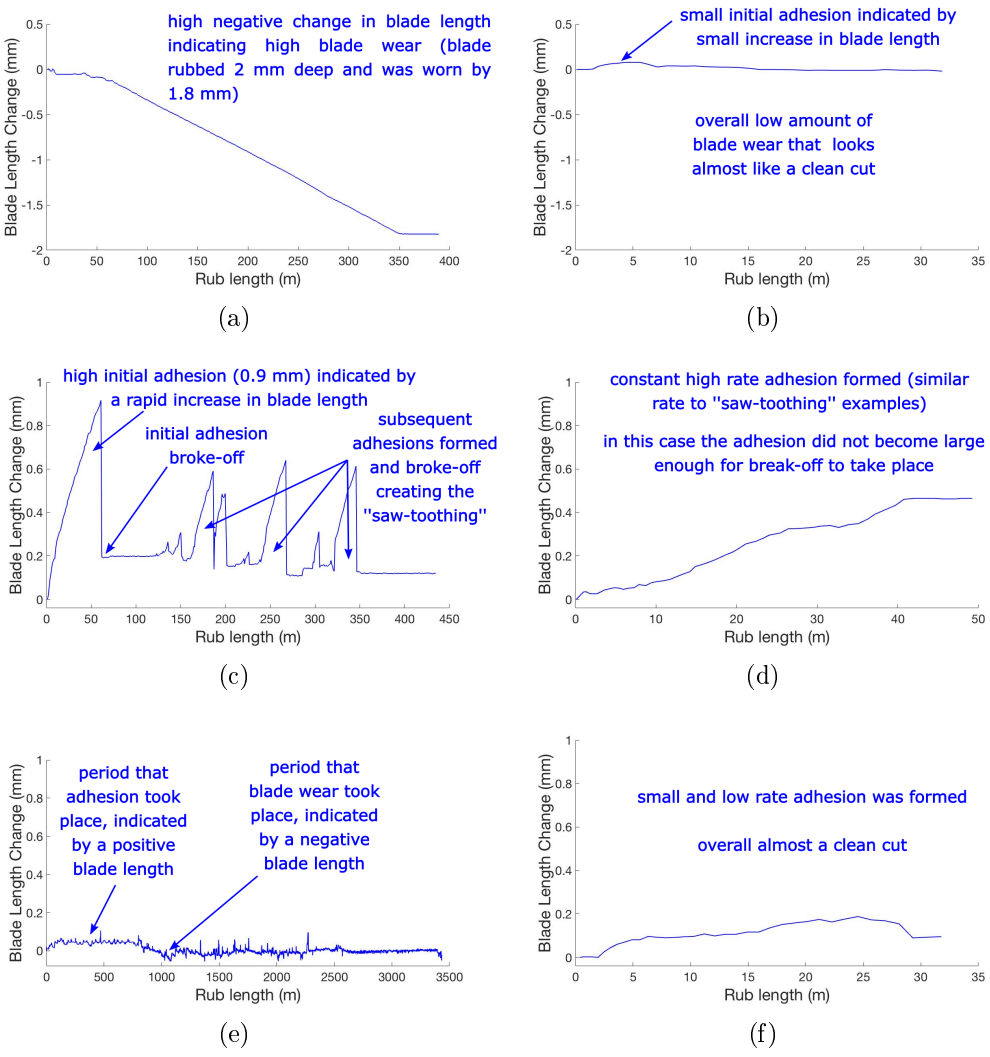

Figure 4.2: Characteristic testing data of blade length change plotted against rub length. The test conditions for each are as follows (a) R15Y 82, 200 m/s, 0.2 μm/pass, (b) R15Y 82, 200 m/s, 3 μm/pass, (c) R15Y 70, 200 m/s, 0.2 μm/pass, (d) R15Y 55, 200 m/s, 2 μm/pass, (e) R15Y 55, 200 m/s, 0.02 μm/pass, (f) R15Y 70, 200 m/s, 3 μm/pass.

4.3.3 Force measurements

The normal and tangential force data collected was plotted against rub length and displayed in this section. Figure 4.3 shows the variation of normal force with rub length, while figure 4.4 shows tangential variation with rub length (equation 3.1).

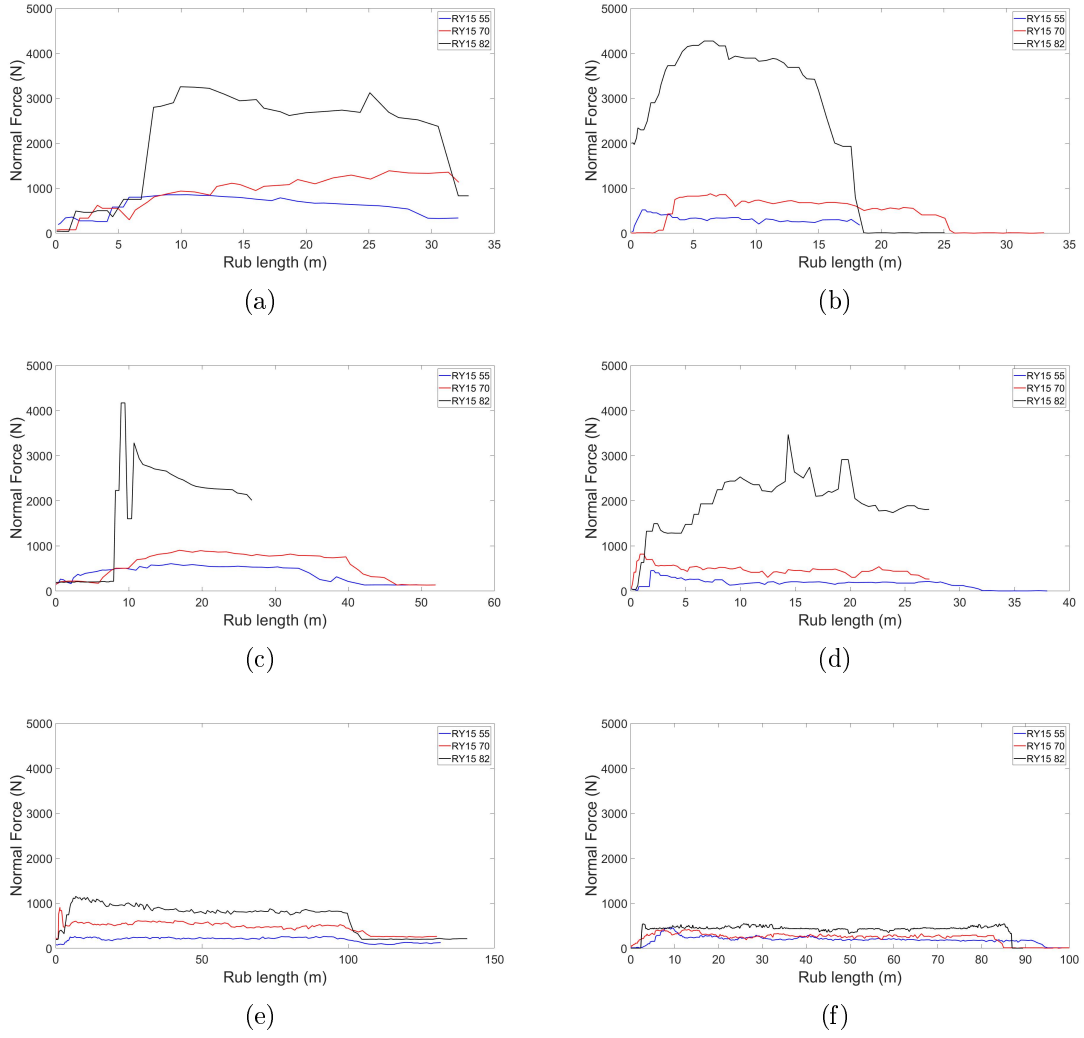

Figure 4.3: Test results of normal forces plotted against rub length. The black lines show tests with hardness R15Y 55, the red lines show tests with hardness R15Y 70 and the blue lines show tests with hardness R15Y 82. The test conditions for each are as follows:(a) 200 m/s, 3 μm/pass, (b) 100 m/s, 3 μm/pass, (c) 200 m/s, 2μm/pass, (d) 100 m/s, 2 μm/pass, (e) 200 m/s, 0.6 μm/pass, (f) 100 m/s, 0.6 μm/pass.

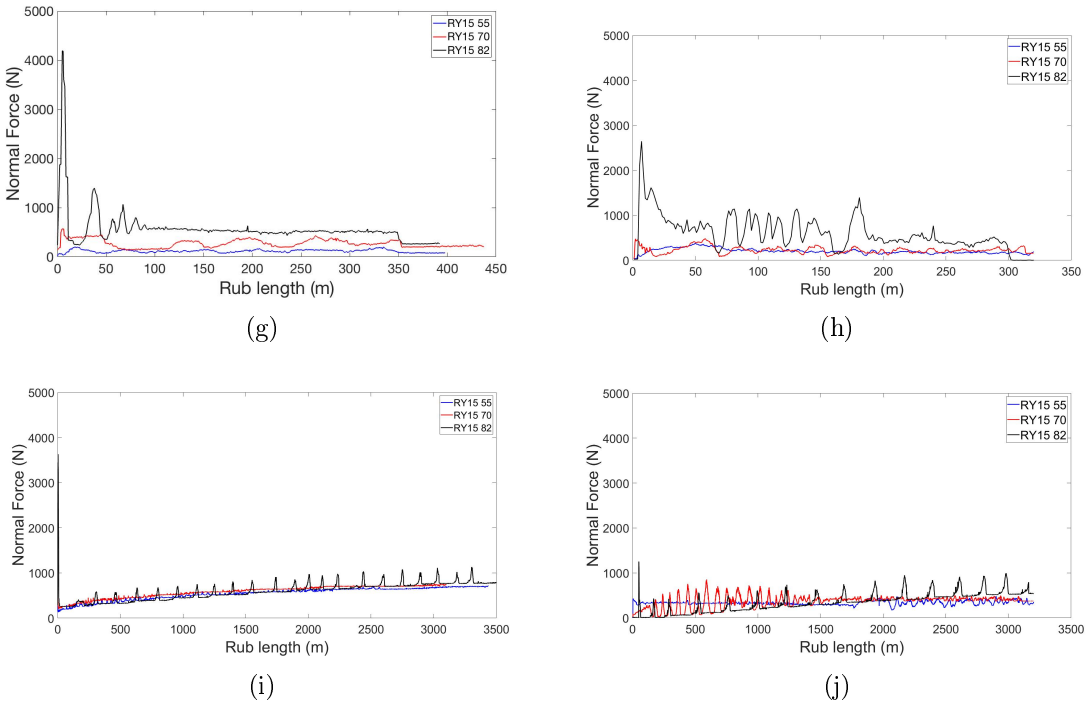

Figure 4.3: Test results of normal forces plotted against rub length. The black lines show tests with hardness R15Y 55, the red lines show tests with hardness R15Y 70 and the blue lines show tests with hardness R15Y 82. The test conditions for each are as follows:(g) 200 m/s, 0.2 μm/pass, (h) 100 m/s, 0.2 μm/pass, (i) 200 m/s, 0.02 μm/pass, (j) 100 m/s, 0.02 μm/pass.

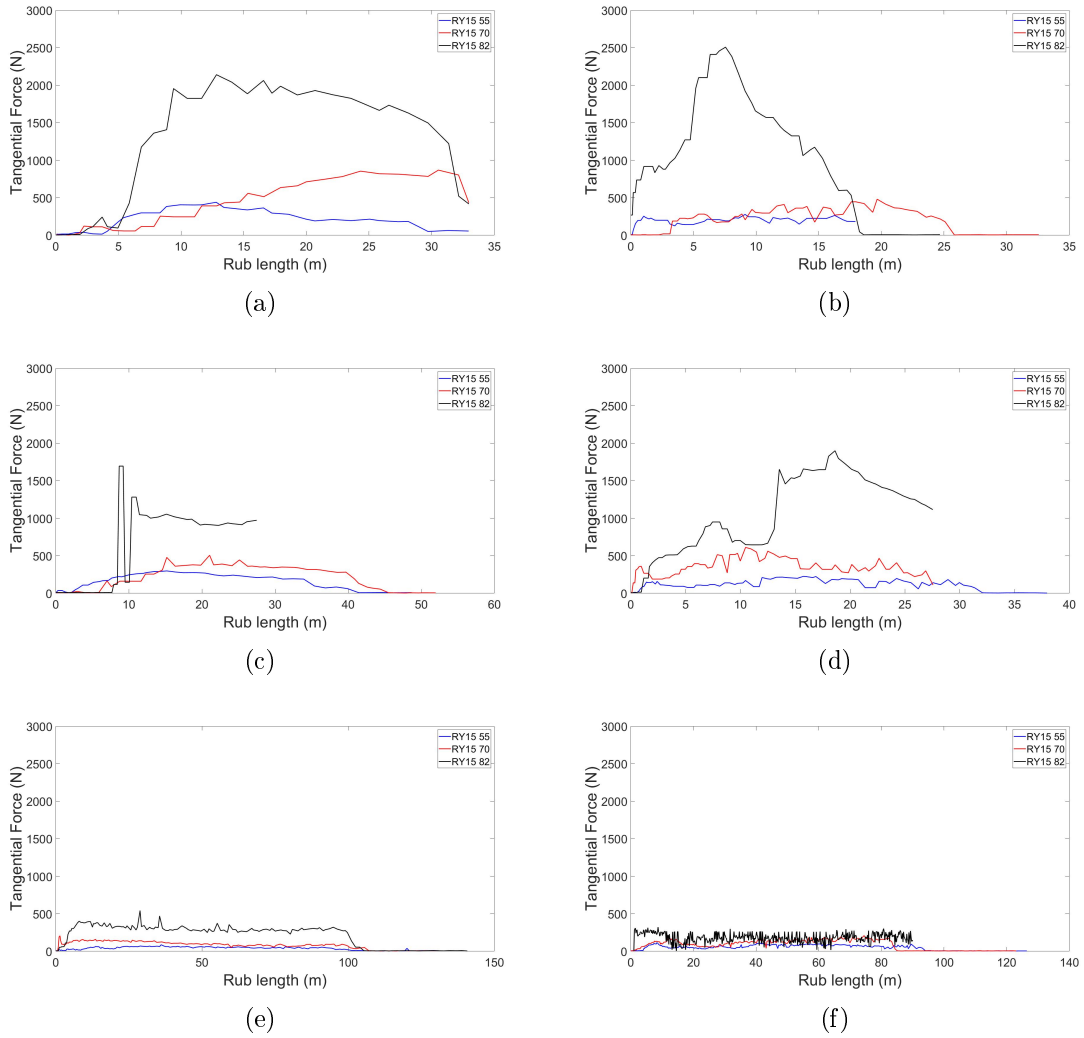

Figure 4.4: Test results of tangential forces plotted against rub length. The black lines show tests with hardness R15Y 55, the red lines show tests with hardness R15Y 70 and the blue lines show tests with hardness R15Y 82. The test conditions for each are as follows: (a) 200 m/s, 3 μm/pass, (b) 100 m/s, 3 μm/pass, (c) 200 m/s, 2μm/pass, (d) 100 m/s, 2 μm/pass, (e) 200 m/s, 0.6 μm/pass, (f) 100 m/s, 0.6 μm/pass.

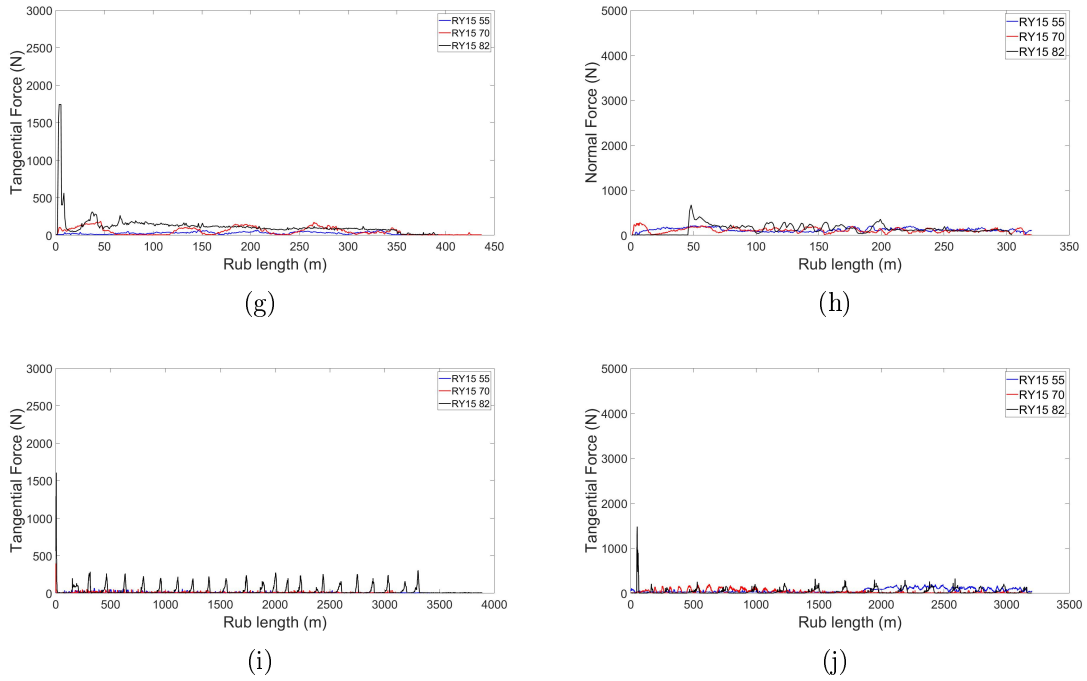

Figure 4.4: Test results of tangential forces plotted against rub length. The black lines show tests with hardness R15Y 55, the red lines show tests with hardness R15Y 70 and the blue lines show tests with hardness R15Y 82. The test conditions for each are as follows: (g) 200 m/s, 0.2 μm/pass, (h) 100 m/s, 0.2 μm/pass, (i) 200 m/s, 0.02 μm/pass, (j) 100 m/s, 0.02 μm/pass.

The first observation that could be made is that both normal and tangential forces increased with increasing hardness (see figures 4.3 and 4.4). Moreover, it is worth noting that for all tested hardness values normal and tangential forces followed similar patterns for a given test condition; however, the magnitude was different since normal forces were always higher. A more careful examination of the force test results showed that for most test conditions there were two characteristics in the resulting forces. The first characteristic was a spike in the force measurement and the second was a more steady state behaviour. By examining the maximum force there was no apparent correlation with incursion rate or speed (see figures 4.5(a) and 4.5(b)). However, by comparing the steady state value it could by seen that there was a positive correlation with the incursion rate for normal and tangential forces (see figures 4.5(c) and 4.5(d)). In contrast, the resulting normal and tangential forces did not seem to vary significantly with the blade tip speed. Another interesting observation was the periodic spiking observed for both normal and tangential forces at the lowest incursion rate (4.4(i), 4.5(i)). Finally, the maximum forces were recorded from tests with the

highest hardness abradables and they were in the range of 3000-4000 N.

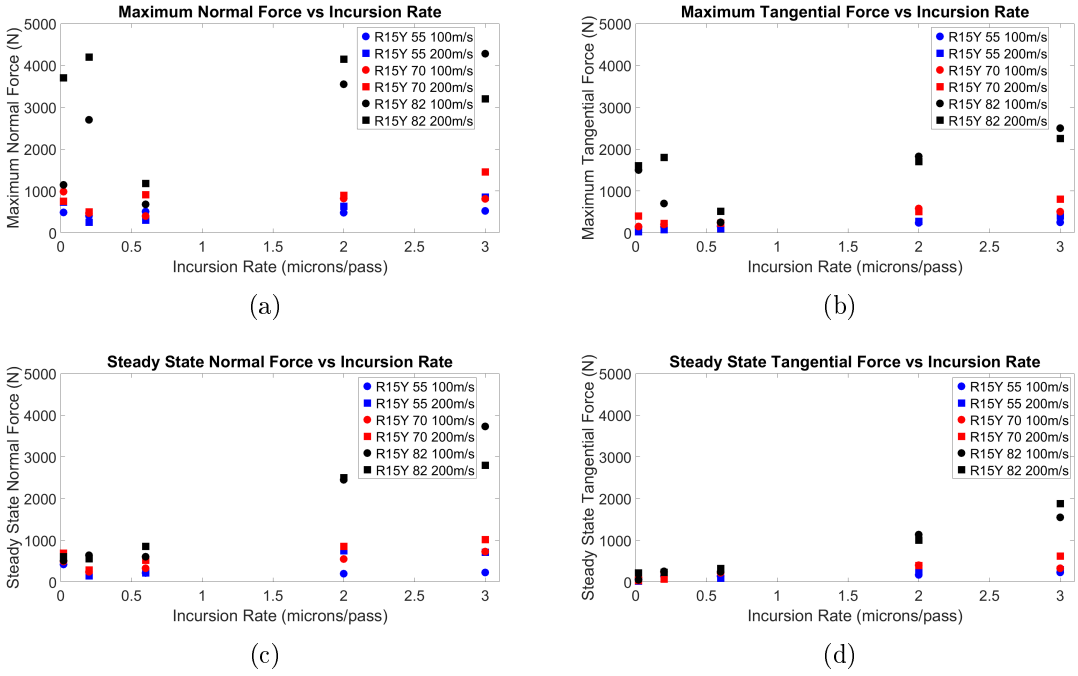

Figure 4.5: (a) Maximum normal force vs incursion rate, (b) Maximum tangential force vs incursion rate, (c) Steady state normal force vs incursion rate, (d) Steady state tangential force vs incursion rate

The resulting forces are expected to be strongly linked with the resulting wear mechanisms and thus they were analysed and discussed in more detail in section 4.4. Moreover, a link was made with temperature and blade length change measurements to gain a better understanding of the wear mechanisms.

4.3.4 Temperature

In this section some example results related with the temperature response of the abradables were presented. Not all of the results were shown, since the main aim was to identify the general trends and to later use the temperature as a tool to examine the behaviour of the abradable.

Figure 4.6 shows that like the forces, temperature increased with increasing hardness at a given test condition. However, in the case of temperature measurements this was less apparent for lower incursion rates. Furthermore, figure 4.6 shows that temperature increased with increasing speed. The effect of incursion rate was not so obvious, but higher temperatures were generally observed at the higher incursion rates and

speeds. Periodicity was observed for low incursion rate condition (4.6(h)). Another significant observation made by looking at figure 4.6 was that in some tests the maximum temperature of the abradable was very close or even exceeded the melting point of AlSi (577 ^{o}C) [70]. This occurred mostly at some of the tests performed on the high hardness samples of Metco 601. This result suggests that damage to the abradable material is possible, or even a change in its micro-structure due to these high temperatures. This should be investigated further by examining the micro-structure of the sample sections under optical and scanning electron microscopy.

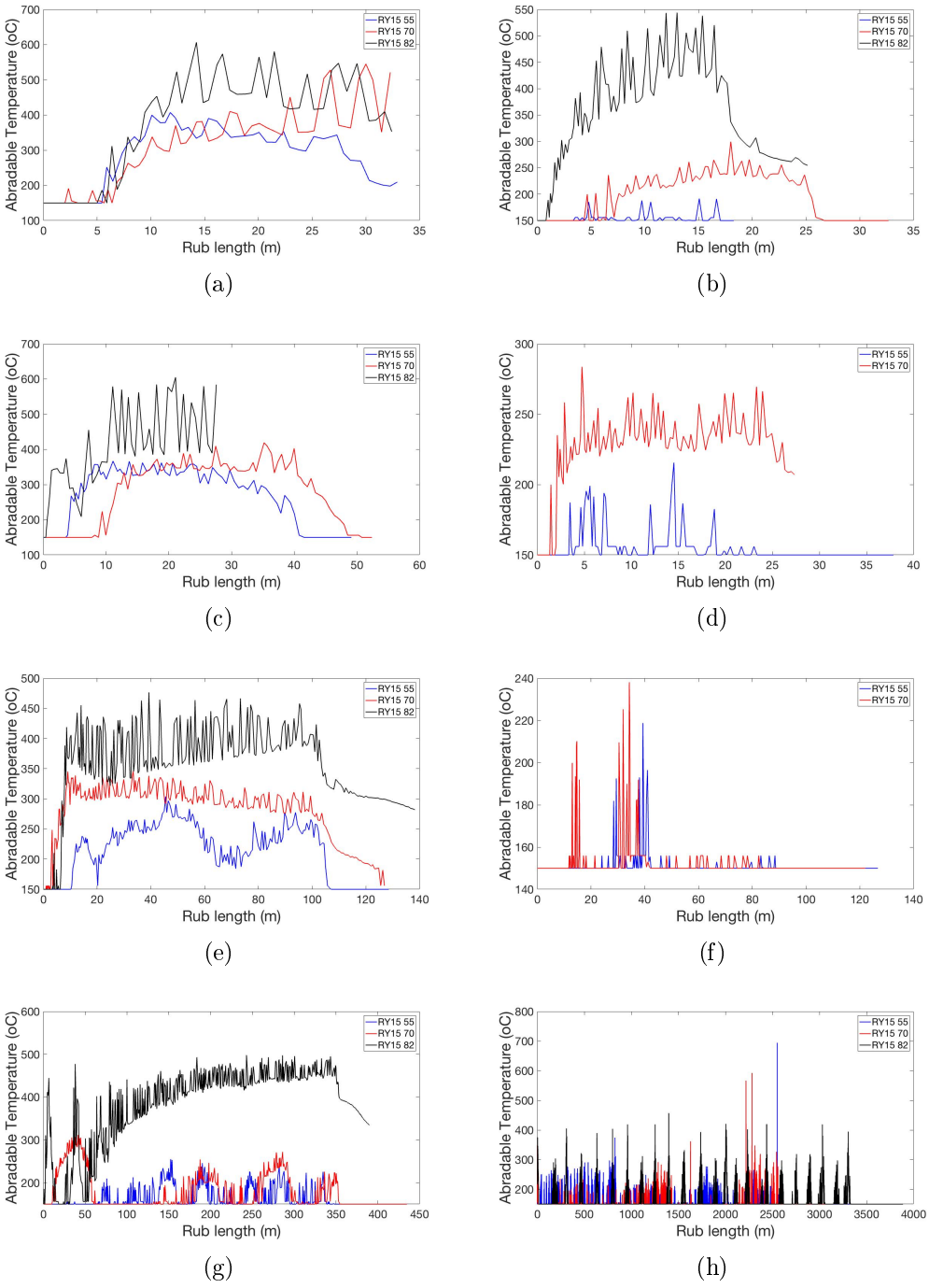

Figure 4.6: Test results of the coating temperature plotted against rub length. The black lines show tests with hardness R15Y 55, the red lines show tests with hardness R15Y 70 and the blue lines show tests with hardness R15Y 82. The test conditions for each are as follows: (a) 200 m/s, 3 μm/pass, (b) 100 m/s, 3 μm/pass, (c) 200 m/s, 2μm/pass, (d) 100 m/s, 2 μm/pass, (e) 200 m/s, 0.6 μm/pass, (f) 100 m/s, 0.6 μm/pass, (g) 200 m/s, 0.2 μm/pass, (h) 200 m/s, 0.02 μm/pass.

4.4 Discussion

This section consists of a more detailed discussion on the results presented in section 4.3. Firstly, the performance of Metco 601 was examined using the results obtained up to this point. The second half of this section provides a comparison between the observed performance of Metco 320 and Metco 601 in an attempt to identify any differences in the performance of these two materials. The Metco 320 data used for the comparison was a combination of data taken from the study performed by Fois [15] and data created for the purposes of subsequent chapters of the study in this thesis. Finally, wear maps were used as descriptors to classify the performance of the abradables and their effectiveness was assessed.

4.4.1 M601 performance

To fully analyse the abradable's performance a wide range of techniques discussed previously were used. This section was divided into two parts: Performance of the R15Y 82 sample and performance of R15Y 55, 70 samples. This was done because the R15Y 55, 70 samples had similar behaviour and wear mechanisms, whereas the R15Y 82 sample were completely different. In this analysis the force ratio (normal/tangential force) was calculated because this metric is used in machining processes to assess if an efficient cutting and material removal mechanism takes place (the studied contact can be considered similar to machining). A high force ratio suggests an efficient cutting mechanism [90], while a low force ratio suggest an inability of the cutting tool to remove the material effectively resulting in compression and deformation of the material [91]. It must be highlighted that Chae et al. have shown that this low force ratio, compression and deformation wear mechanism occurs when the incursion rate is lower than the smaller chip that the cutting tool (in this case the blade) can create [92].

Performance of Metco 601 with R15Y 82 hardness

Results from the different techniques presented in section 4.3 highlight the fact that for the abradable with hardness of R15Y 82 the main wear mechanism was blade tip wear.

Firstly, figures 4.7(a), 4.7(c), 4.7(e) show the blade length change overlaid with normal force and temperature measurements of characteristic samples, while Figures 4.7(b), 4.7(d), 4.7(f) show the blade length change overlaid with force ratio (tangential divided by normal) and temperature. These were plotted against rub length and were used to investigate what happened when blade wear occurred. By examining figure 4.7 it was shown that during periods of blade wear an increase in the temperature of the abradable occurred. Another important observation was that even though blade wear was observed to some extent under all conditions, the amount of wear and the way it occurred changed with the incursion rate. Figures 4.7(a), 4.7(b) show that at the lowest incursion rate tested, the blade wear had a step like characteristic, where periods of blade wear succeeded periods of no blade wear. A close inspection of these figures shows that just before blade wear began, a drastic increase in the force and temperature measurements occurred, which effectively caused the blade wear. A possible reason is that since the abradable was very hard it was very difficult for the blade to remove the material. Instead, the blade compacted the abradable for a few incursions. Eventually, this caused the blade to hit a block of compacted abradable causing the drastic peaks in force and temperature measurements, as well as damage on the blade. This was previously observed in tipped abradable testing [43].

Another significant observation was that force ratio during the low incursion rate test shown in figure 4.7(b) was low (around 0.25). The low force ratio suggested that cutting the material was difficult and instead deformation of the material occurred. This meant that at low incursion rates the impact was not strong enough to fracture the material. Figure 4.7(f) further highlights the significance of the force ratio in respect to the resulting wear characteristics. For the test shown in figure 4.7(f), despite the very high forces and temperatures (figure 4.7(e)), the amount of wear was much less compared to the other two tests and this could be attributed to the higher force ratio (around 0.5). The higher force ratio suggested that the tangential forces caused chips from the material to shear, fracture and be removed more easily. As shown in figure 4.7(f), most of the wear at these conditions occurred at the early stages of the test (after a small initial adhesion), where the force ratio was low (0.05). After the point at which the force ratio increased there was very little change in the blade length.

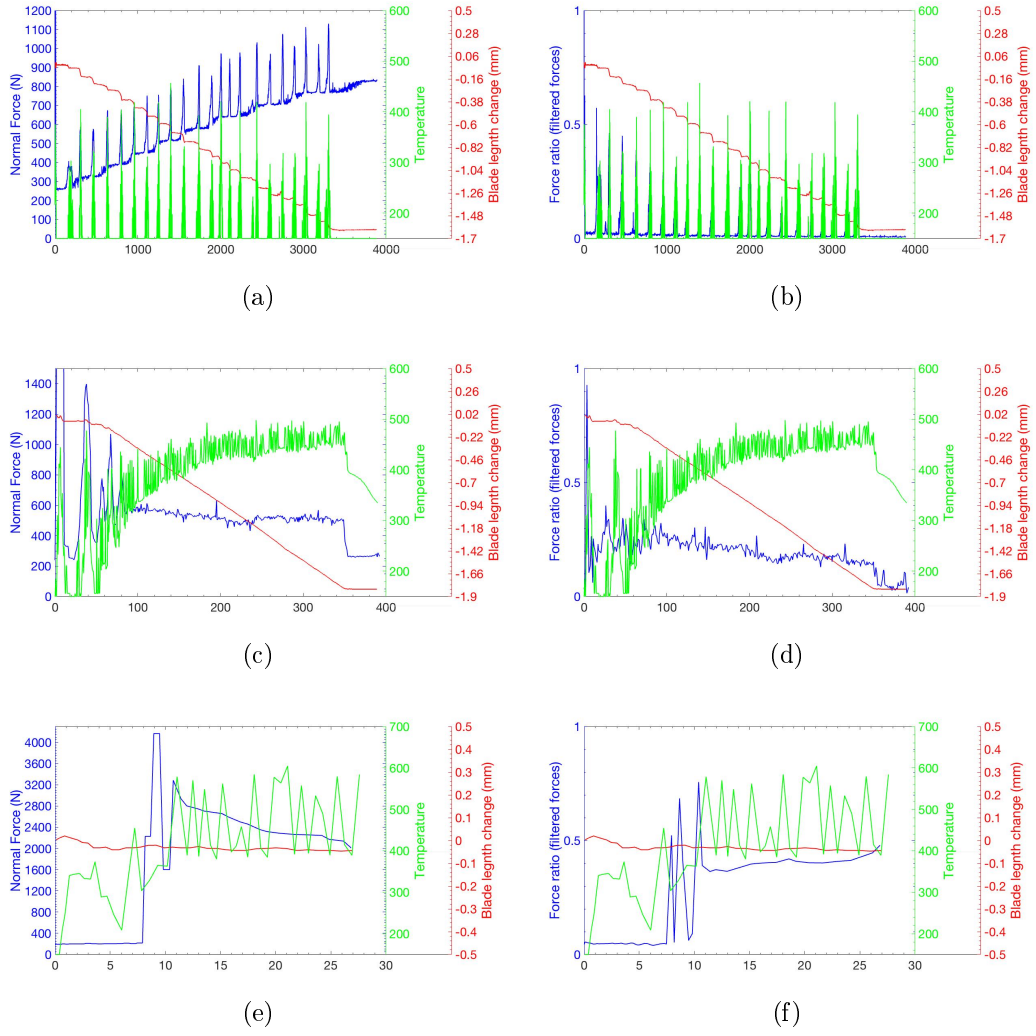

Figure 4.7: Overlay of normal force, force ratio, temperature and blade length change against rub length used for analysis. The test conditions for each are as follows: (a) and (b) 200 m/s, 0.02 μm/pass, (c) and (d) 200 m/s, 0.2 μm/pass, (e) and (f) 200 m/s, 2 μm/pass.

Performance of Metco 601 with R15Y 55 and 70 hardness

The abradables with a hardness value of R15Y 55 and 70 showed similar adhesion/wear rate characteristics. Almost all of the samples showed a high adhesion rate and no significant correlation with incursion rate or speed was observed (figure 4.12).

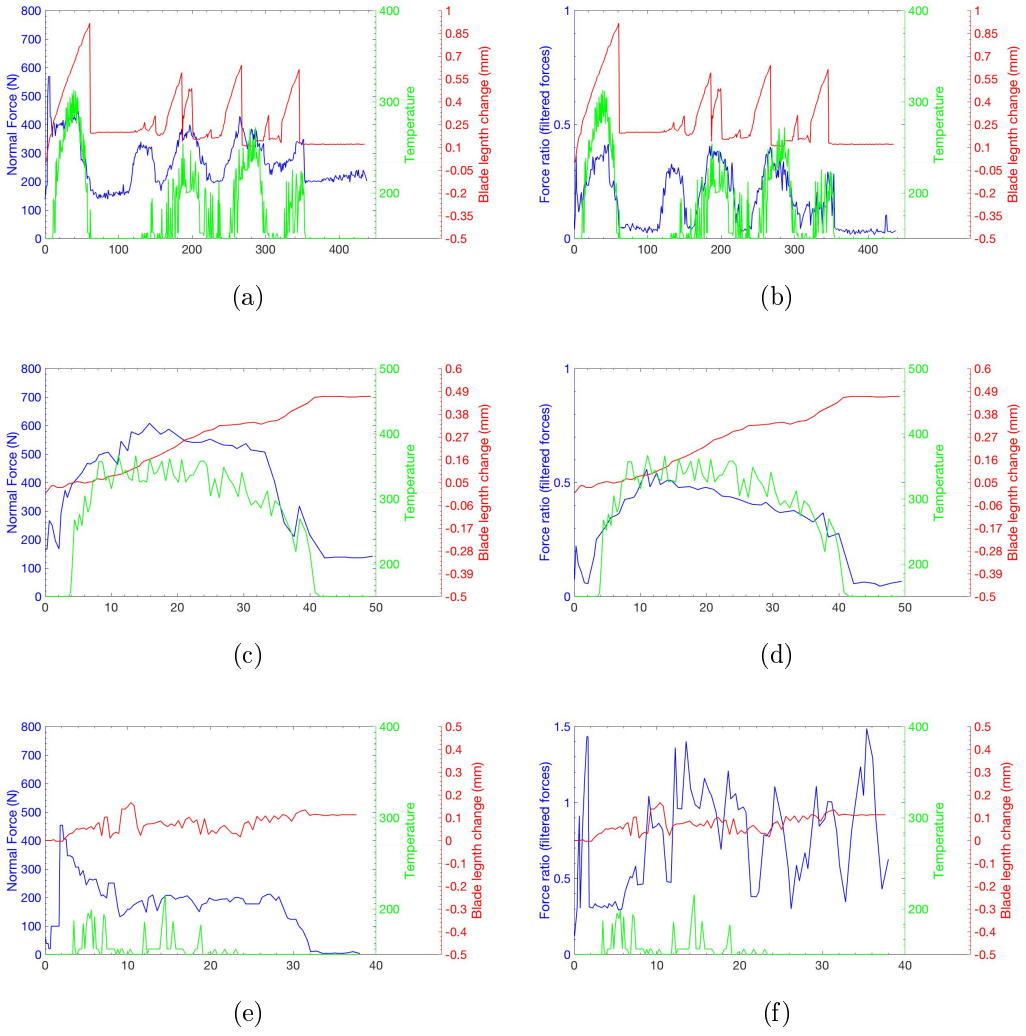

Figure 4.8: Overlay of normal force, force ratio, temperature and blade length change against rub length used for analysis. The test conditions for each are as follows: (a) and (b) R15Y 70, 200 m/s, 0.2 μm/pass, (c) and (d) R15Y 55, 200 m/s, 2 μm/pass, (e) and (f) R15Y 55, 100 m/s, 2 μm/pass.

Figures 4.8(a), 4.8(c), 4.8(e) show characteristic normal contact force data overlaid with the temperature and the blade length change measurements, while figures 4.8(b), 4.8(d), 4.8(f) show the force ratio overlaid with the temperature and blade length change measurements. Only these three samples were shown since they represent the behaviour of all the abradable samples tested with hardness values of R15Y 55 and 70.

A significant number of samples have shown a wear characteristic similar to the one illustrated in figures 4.8(a) and 4.8(b). An initial adhesion occurred and then a sudden

drop to a value close to zero followed. This effect was repeated multiple times during a test creating a 'saw-tooth' response. This effectively meant that material was adhered at the end of the blade and then all the adhered material broke off from the tip at one go. Also, the peak and trough force and temperature response suggested that there was a period of no contact due to a clearance that was created when the chip broke- ff. This could be inferred since force and temperature readings fell to very low values during this time while there was also no blade length change. All these results led to the conclusion that for these samples an initial adhesion occurred, resulting in a change in the contact, since at such conditions abradable was rubbed against abradable leading to heat generation and a rise in temperature and forces. This pick-up mechanism was also observed in the previous study [40], which was focused on Metco 320, but this 'saw-tooth' response was not observed. Instead, in the case of Metco 320, the adhered material continued to grow up to a point at which some of it broke off and then continued to grow at the same rate as before. This difference in the response of the two materials might be one reason why the adhesion/wear rate was not as accurate descriptor of the overall abradability performance of Metco 601 as it was for Metco 320. Figure 4.8(a) shows that the rate at which adhesion occurred was very high, but since it broke down to a near zero value each time, severe adhesion was prevented. Metco 320 with a similar wear rate would have continued to increase in length resulting in much worse adhesion and consequently much deeper grooving on the abradable's surface. Further investigations were performed on samples that showed this type of response in an attempt to understand what drove it and the findings were discussed later in this section.

A smaller set of samples showed a response similar to the one shown in figures 4.8(c) and 4.8(d) continuous growth of the blade length occurred, resembling continuous adhesion with approximately constant rate, accompanied by moderate temperature, forces and force ratio. The rise in forces and temperature occurred when pick-up began suggesting that this was due to rubbing of the adhered abradable on the abradable sample surface. It should be noted that whilst the 'saw tooth' behaviour was not observed for these samples, the maximum adhesion that was recorded was less than the values at which break-off occurred. This suggested that it was possible that there was a critical height at which break-off happened.

Finally, a few samples had a close to ideal response in the sense that almost no blade length change was observed, accompanied with smooth rub surfaces. As it could be seen from figures 4.8(e) and 4.8(f) only an insignificant amount of pick-up occurred

for these tests, resulting in the generation of only very low force and temperature increases. Moreover, for these samples high force ratio was recorded indicating an effective material removal process and an efficient cut wear mechanism as previously explained, which justified the slower pick-up rate.

Further investigation was carried out to understand what drove the 'saw tooth' response that was observed for many of the samples tested with these hardnesses. A visual inspection of the images captured from the camera was performed in addition to the usual analysis performed by the MATLAB program. It was found that adhesion of material mostly occurred at the leading edge of the blade. A characteristic image was shown in figure 4.9(a).

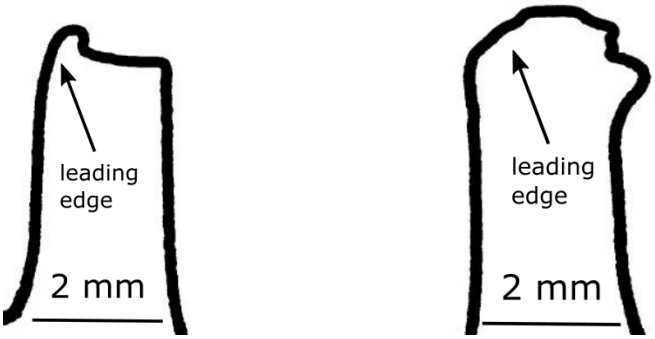

(a) (b)

Figure 4.9: (a) Processed blade profile from test done on Metco 601 sample with hardness H15Y 70 at 200 m/s and 0.2μm/pass, (b) Processed blade profile from test done on Metco 320 sample with hardness H15Y 59 tested at 200 m/s and 0.02 μm/pass.

Similar inspections were made to all the tests performed with these hardnesses and a similar observation was made. As shown from figure 4.9(a), material adhered only near the leading edge of the blade and took up only a small percentage of the blade width. As a result, the consequent adhesions were thin, which could explain why the adhered material broke off all in one go. Moreover, it was previously suggested that a critical height could be the limit at which this break-off occurred, however, using this observation it could be suggested that a critical height to adhesion width ratio was what drove the break-off. The critical height to width ratio was suggested since the adhesions that form on the blade were thin and were building-up at a fast rate becoming long. Long and thin adhesion on the blade did not have a stable base and when they rubbed against the abradable surface all the force (tangential force in the direction of the blade rotation) was focused on the thin base from a relatively long

distance causing high bending forces at the intersection of the adhesion to the blade. This caused the adhesion to break-off in one go. Figure 4.9(b) highlights the adhesion mechanism of Metco 320. Adhesion initiated at a random spot on the blade tip width and it kept growing until it became too large and some of it broke off. Then adhesion re-initiated at the same rate as before.

4.4.2 Comparison between M320 and M601

One of the main aims of this work was to identify the differences in the response of Metco 601 and Metco 320 and to understand why these occurred so a comparison between the two abradables of interest was made.

The first significant difference between the two was the different adhesion mechanism as discussed in the previous section and illustrated in figure 4.9. Due to this difference in the adhesion mechanism, adhesion in Metco 601 could not become too long (maximum recorded adhesion was approximately 1 mm) despite the really high adhesion rates. In comparison, adhered material for Metco 320 built up at a lower adhesion rate, but due to the fact that this was continuous, longer adhesions could form (maximum recorded adhesion was approximately 2.5 mm) [15]. As a result, much deeper grooving of the abradable surface was observed from the Metco 320 testing. Figure 4.10 highlighted the difference between two of the most deeply grooved samples obtained from testing the two abradables. The images were taken from middle hardness, 200 m/s, and 0.02 μm/pass tests from both abradables. It is apparent that grooving was much deeper and more severe in the case of Metco 320.

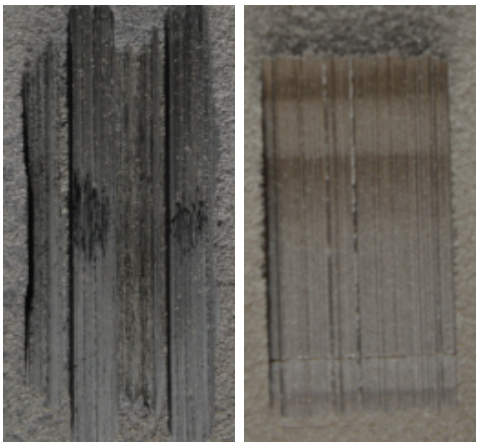

(a) (b)

Figure 4.10: Difference between maximum grooving observed from the two abradables. (a) Metco 320 with medium hardness of R15Y 64 and tested at 200 m/s and 0.02 μm/pass, (b) Metco 601 with medium hardness of R15Y 70 and tested at 200 m/s and 0.02 μm/pass.

The connection between the rate of the wear mechanism and the surface roughness response of the two abradables was another significant difference between them. In the case of Metco 320 the adhesion/wear rate was closely correlated to the resulting rub surface. High adhesion rates (adhesion wear mechanism) were causing deep grooving, low adhesion rates (efficient cutting mechanism) resulted in a smooth surface and finally, shorter rub tracks were observed from negative adhesion rates (blade wear mechanism). In the case of Metco 601 the performance of the abradable had to be differentiated, since the rub surface and the wear mechanism were not directly correlated. Therefore, the performance of this abrdable was differentiated firstly in terms of what mechanism was taking place and its severity, and secondly to the resulting rub surface roughness. Consequently, because these were not correlated, new metrics and descriptors of the abradable's behaviour had to be introduced, since both are important to assess its performance.

4.4.3 Wear maps

Wear maps are a tool used in an attempt to identify operational condition regions, where required behaviour occurs. As a result wear maps are able to reflect the functional performance of abradable. The previous study that extensively investigated the performance of Metco 320 used a wear map based on wear rate. The research

performed in this thesis used a similar wear mapping method to attempt and identify the differences between Metco 320 and Metco 601. Additionally, this study aimed to identify a good performance descriptor for Metco 601 so additional wear mapping methods were discussed and compared in the following section. For the plotting of the wear maps a modified Peclet number was used as the x axis because it was found in literature that this dimensionless number is a good combination of the thermal and mechanical components of the contact. This number provides an indication of how heat is diffused at a given contact [52, 53, 54]. The Peclet number is discussed in detail in section 2.3.3 and it is calculated by equation 2.2 using the data shown in table 3.4. Furthermore, a heat partition coefficient was used as a y axis. This heat partition is a dimensionless number independent of the contact, that estimates the amount of energy in the form of heat that is dissipated in the components of the contact [55]. The heat partition is also discussed in detail in section 2.3.3 and it is calculated by equation 2.3 using the data shown in table 3.4.

Wear Rate

In this section the results from the adhesion/wear rate analysis were shown. The adhesion/wear rate was estimated by calculating the gradient of the blade length change against rub length plot. Since the gradient of the data varied significantly over the testing period a best fit line was applied to estimate it. The best fit line was chosen using a univariate linear regression model, which minimised the squared error between the line and the data points. Moreover, to increase the accuracy of this method, the rate was calculated over a manually selected rub length, avoiding the inclusion of test initiation and contact inaccuracies. Figure 4.11 shows an example of how this calculation was carried out. The red area was discarded and the wear rate was evaluated for the rub length in the blue area. The red line was the best fit line as estimated from the univariate linear regression model with these limits. Figure 4.11(a) shows an example of a sample that had negative blade length change. This corresponded to blade wear. Figure 4.11(b) shows an example of a sample with the typical saw-toothing behaviour. This was rapidly increasing positive blade length change, which was equivalent to adhesion build-up. In this case long adhesions were formed and broke-off. After the break-offs a period of no adhesion build-up followed because there was no contact during that period (long adhesions rubbed deeper that targeted rub depth). In order to avoid taking into account periods of no contact only

the rate of the peaks was measured as shown in figure 4.11(b). In this example the first peak was measured.

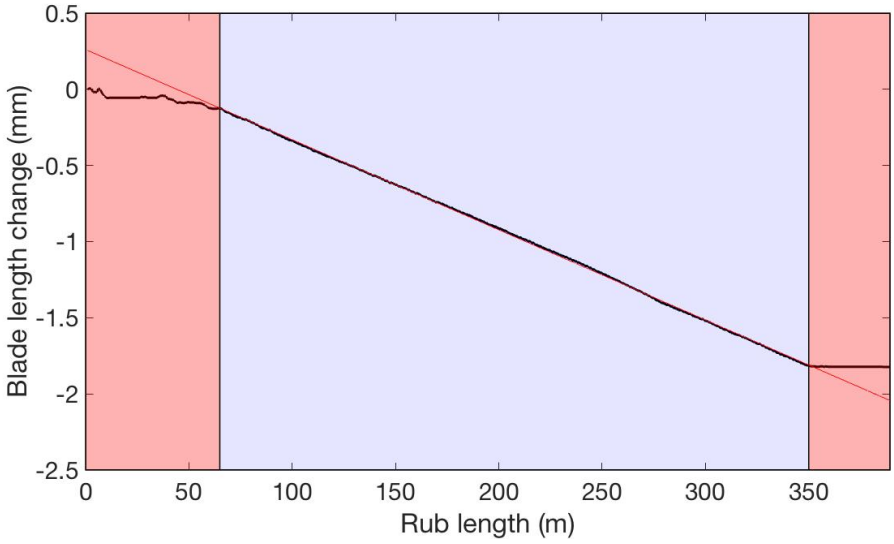

(a)

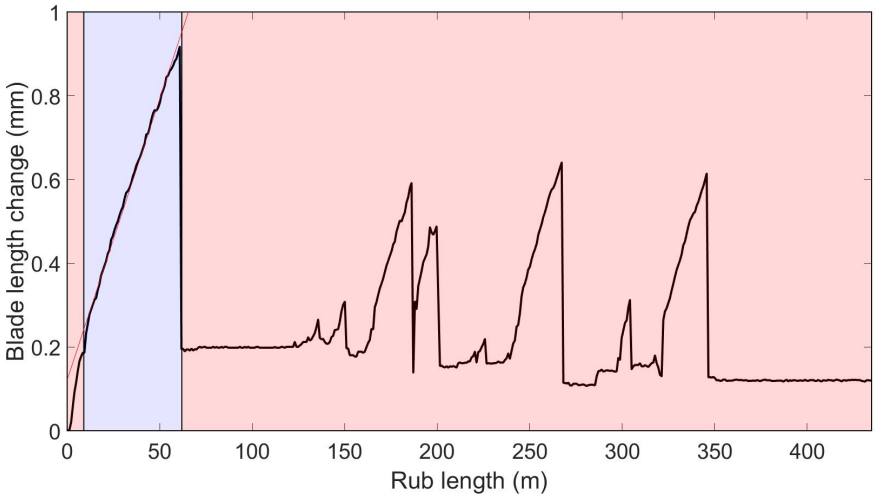

(b)

Figure 4.11: (a) Calculation of wear rate for a sample that shows wear (testing conditions: hardness of R15Y 82 tested at 200 m/s and 0.2μm/pass),(b) Calculation of wear rate for a sample that showed adhesion (testing conditions: hardness of R15Y 70 tested at 200 m/s and 0.2μm/pass).

Table 4.3 summarises the adhesion/wear rate results for all the tests performed. Figure 4.12 plotted the tests using a heat partition and a modified peclet number and a colour map was used to categorise them in terms of their adhesion/wear rate perfor-

mance. This was done since adhesion/wear rate was previously found to be a good descriptor of the performance of Metco 320 [15].

Table 4.3: Adhesion/Wear rate results.

Test Number	Hardness (R15Y)	Tip Speed (m/s)	Incursion Rate (um/pass)	Wear/Adhesion Rate (mm/m)
1	55	100	0.02	0.0318
2	55	100	0.2	0.0251
3	55	100	0.6	0.0218
4	55	100	2	0.0126
5	55	100	3	0.0118
6	55	200	0.02	0.0254
7	55	200	0.2	0.0220
8	55	200	0.6	0.0280
9	55	200	2	0.0109
10	55	200	3	0.0136
11	70	100	0.02	0.0292
12	70	100	0.2	0.0277
13	70	100	0.6	0.0127
14	70	100	2	0.0051
15	70	100	3	0.0123
16	70	200	0.02	0.0107
17	70	200	0.2	0.0154
18	70	200	0.6	0.0109
19	70	200	2	0.0130
20	70	200	3	0.0056
21	82	100	0.02	-0.0249
22	82	100	0.2	-0.0204
23	82	100	0.6	-0.0119
24	82	100	2	-0.0151
25	82	100	3	-0.0403
26	82	200	0.02	-0.0210
27	82	200	0.2	-0.0158
28	82	200	0.6	-0.0051
29	82	200	2	-0.0005
30	82	200	3	-0.0003

A comparison between the wear map of Metco 601 was shown in figure 4.12 and the wear map of Metco 320 that was constructed in a previous study by Fois (figure 2.16) highlighted the difference in the performance of the two abradables. Using the two chosen axis, the adhesion/wear rate was found to clearly identify different regions of operational conditions at which specific wear mechanisms occurred and it was linked

to the functional performance of the abradable (i.e. high adhesion rate resulted to high grooving). Using this metric the performance of Metco 601 could be divided in two regions as also highlighted in the previous section. The first region was the high hardness H82 Metco 601. At this hardness, as we can clearly see from the map, there was an undesirable performance that caused blade wear, which improved progressively with increasing peclet number. This effectively meant that at higher incursion rates and speeds the wear damage caused on the blades became less and less severe, reaching a point at the highest incursions and speeds that was almost insignificant. The second region was the low and middle hardness Metco 601. At these hardnesses it was apparent that there was a slight progression from higher adhesion rates to slightly lower values. However, compared to the wear rate map of Metco 320, this improvement was not so drastic. The map in figure 4.12 emphasised the fact that there was a comparatively high adhesion rate even at the higher peclet numbers corresponding to the higher incursion rates and speeds.

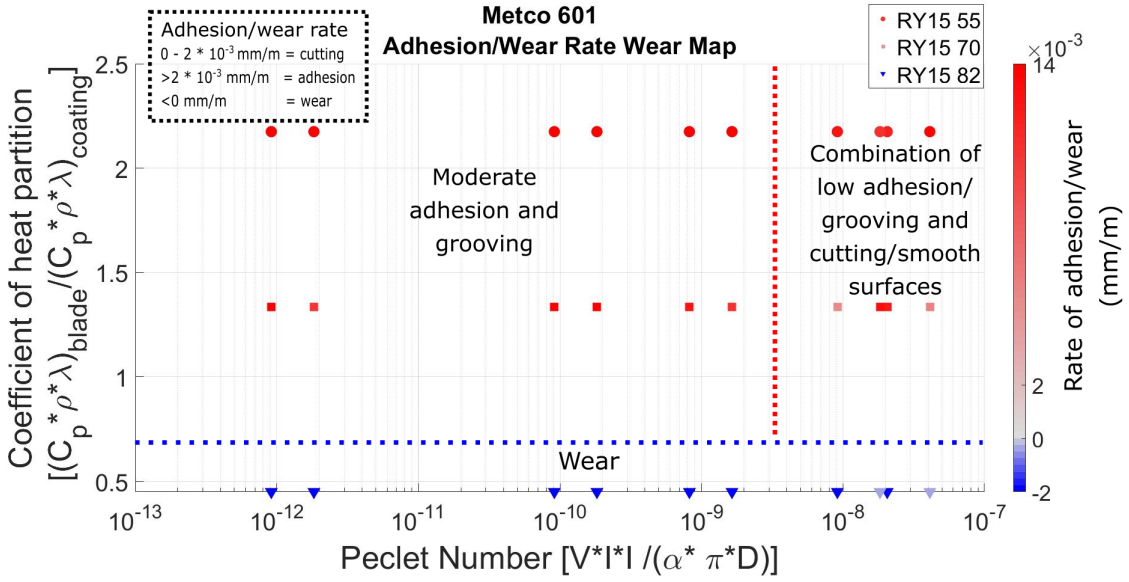

Figure 4.12: Adhesion/wear rate wear map of Metco 601 plotted using the heat partition and the modified Peclet number.

Further, it should also be noted that contrary to the Metco 320 case, adhesion rate measurements did not represent the outcome in terms of the groove surface. In the case of Metco 320 high adhesion rate was equivalent to high degree of grooving, while in the case of Metco 601 this correlation was not so clearly apparent. Grooving is an important functional performance descriptor since deep grooving affects the airflow causing aerodynamic efficiency losses. While the adhesion/wear rate wear

map of Metco 601 provided some useful information and drew some key differences to the performance of this abradable compared to Metco 320, it was not as effective for identifying regions of required behaviour compared to when used for Metco 320.

To investigate further these results, the adhesion/wear rate was plotted against the incursion rate at different speeds and hardnesses to examine in more detail the trends of this descriptor with the testing parameters. Figure 4.13 further highlighted the points made in the previous sections. At high hardness, the wear rate significantly improved at higher incursion rates and at higher speeds. In the case of low and medium hardness Metco 601 there seemed to be a slight improvement at higher incursion rates and speeds, but it was not as significant as in the case of Metco 320.

Adhesion/wear rate could not fully describe the performance of Metco 601 because of its adhesion mechanism. As a result of this mechanism, long adhesions were avoided, resulting in a lower amount of grooving than expected, despite the high adhesion rates. In order to try and find a better descriptor for the performance of Metco 601 two more approaches were examined in this investigation. The first approach was to look at the total volume of material that adhered/worn instead of the rate at which this was happening. The second approach was, instead of focusing on the material transfer, to solely focus on the abradable surface and more specifically the surface roughness. The importance and relevance of these descriptors as well as an assessment of their effectiveness was provided in the following sections.

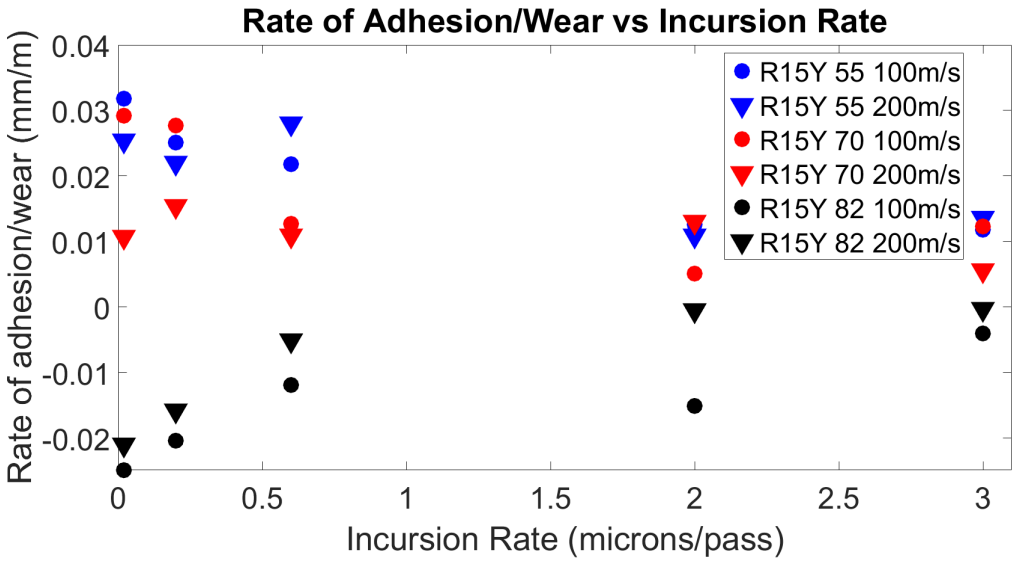

Figure 4.13: Adhesion/Wear rate against incursion rate.

Adhesion Volume

Adhesion volume was a different descriptor used in an attempt to provide a clearer distinction between "required" and "unwanted" operational regions. This new descriptor was introduced instead of the adhesion rate and it measured the volume of adhered/worn material during the test. This aimed to capture whether adhered material was significant enough to cause grooving and therefore tried to correlate more accurately to the rub surface response. Adhesion volume is important since high volume adhesions could lead to blockage and other damage in the engine. The adhered volume was measured by calculating the area under the blade length change plot as shown in figure 4.14 using trapezoidal numerical integration. The width of the trapezoids was determined as the distance between two data points resulting in a very accurate estimation of the area under the plot. However, due to the significant differences in rub length for different testing conditions, the adhered volume was normalised by dividing it by the total rub length for each individual test. The adhered volume results were used to plot another wear map (figure 4.15), with the same axis as the one shown in figure 4.12, where adhered volume was used instead of adhesion/wear rate as a colour bar.

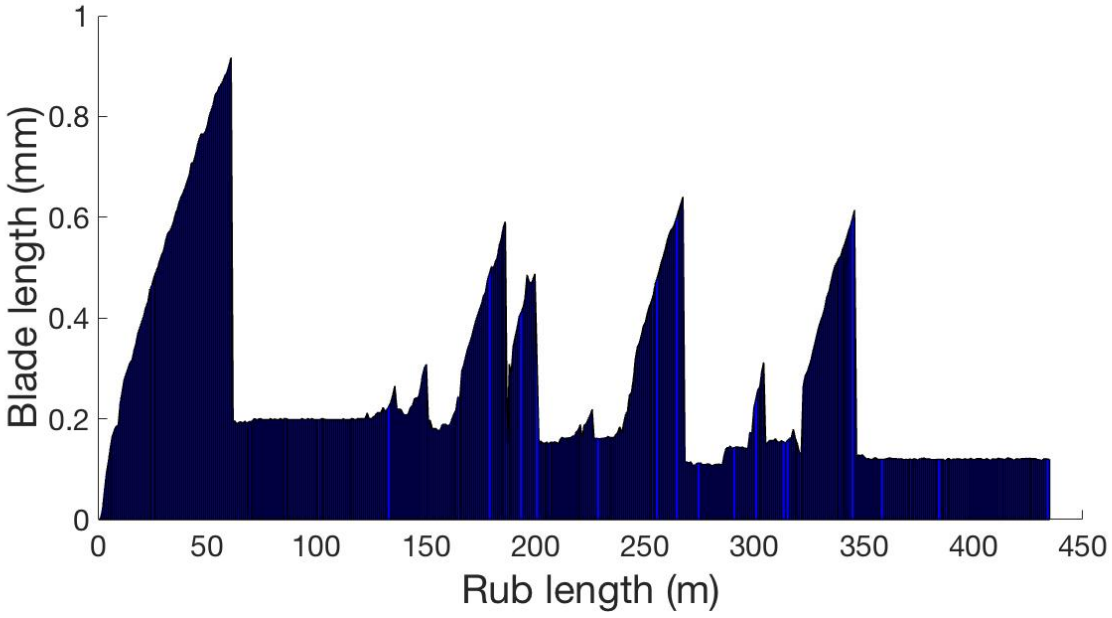

Figure 4.14: Trapezoidal numerical integration performed on the blade length data of a sample with hardness of R15Y 70 tested at 200 m/s and 0.2 μm.

This wear map, based on the calculations of the adhesion volume, was better at iden-

tifying a progression from unwanted to desired performance compared to when wear rate was used as a descriptor. As previously, this was again divided in two different regions. The first region was the high hardness Metco 601 where the wear volume corresponded to the cumulative blade volume lost during the contact. It became increasingly obvious that higher incursion rates and speeds greatly reduced the volume of blade loss and thus improved the performance of the abradable (see blue arrow in figure 4.15). In the case of the low hardness it seemed that higher total volume of material was adhered at higher incursion rates and speeds, while the opposite happened for the medium hardness. The adhesion volume of the medium hardness samples improved quite a lot at the higher incursion rates and speeds suggesting less material was adhered in total at these conditions. In contrast the volume of material adhered in total for the low hardness seemed to be increasing with higher incursion rates and speeds, which was not consistent with previous findings (see red arrows in figure 4.15). As mentioned previously this indicator gave a greater emphasis on peaks and as a result samples that had a lot of adhesions building up and breaking could have been overestimated using this method. This could explain to some degree the inconsistent result regarding the low hardness Metco 601.

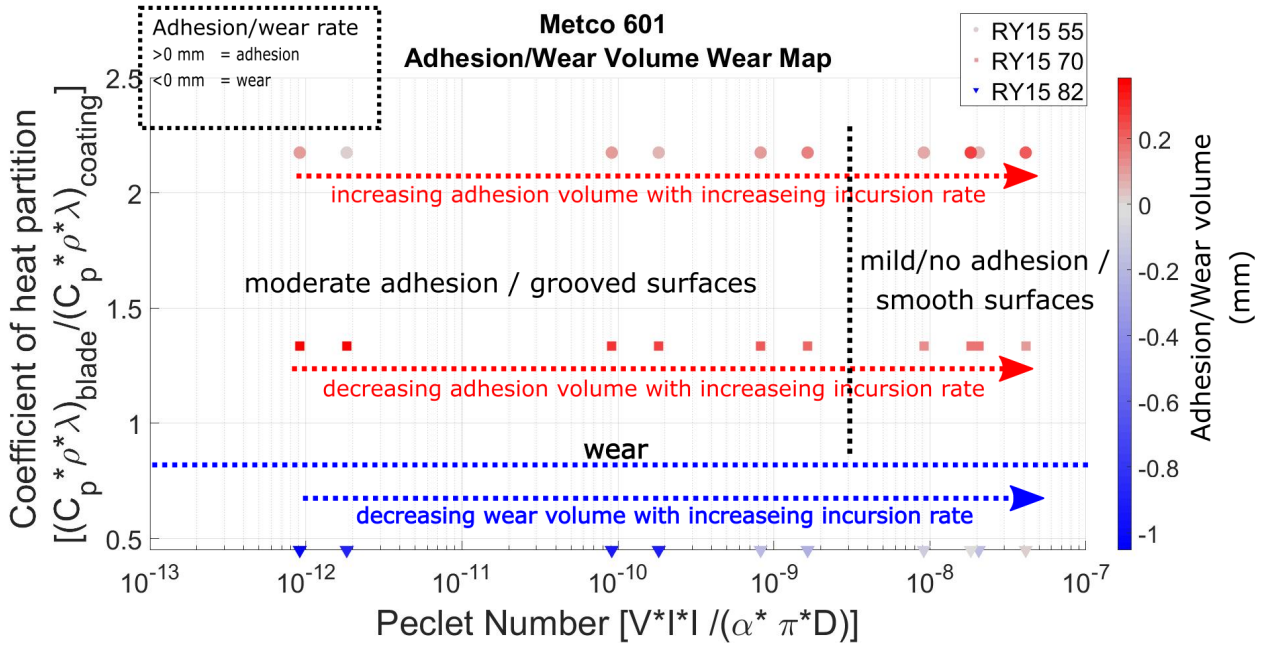

Figure 4.15: Adhesion volume wear map of Metco 601 plotted using the heat partition and the modified Peclet number.

The next step to evaluate whether adhesion volume was a good descriptor of the performance of the abradable, was to assess its correlation with the input variables.

So the adhesion volume was plotted against incursion rate for different hardness and speed conditions and the results were shown in figure 4.16.

By inspecting figure 4.16 it could be seen that more distinct relationships exist between adhered volume and the input parameters. Figure 4.16 show the variation of adhered volume with the incursion rate at different hardnesses and speeds. It could be seen that for the sample with hardness of 82 the adhesion volume, in most cases, increased with speed at a given incursion rate condition. Also it became apparent that higher incursion rate greatly improved the performance of this abradable hardness since much less blade volume was lost in total at this condition. At the medium hardness the impact of speed was much less, while there was a slight, but clear decrease in the total adhered volume at higher incursion rates. Finally, for the low hardness samples, there was very little change in the value of of total adhered volume with incursion rate at the lower speed, but there was a significant increase with incursion rate at the higher speed. This maybe explained by the fact that these samples represented the adhesion profile of 4.2(c), which had a lot of peaks and it was overestimated using this descriptor.

Overall, the adhesion volume wear map provided valuable information on the performance of the abradable under investigation, but still had some limitations. A more clear transition was identified for the medium and high hardness of Metco 601 compared to the wear/adhesion rate wear map. In the case of the high hardness sample this reflected to a lower amount of blade wear as speed and incursion rate were increased, while in the case of medium hardness samples less material was adhered in total on the blade. However, the first limitation, which was the fact that peaks carry higher weight when using this method, the higher incursion rate low hardness samples seemed to have been overestimated using this method. Moreover, another limitation of this method was that the numerical integration adds positive areas while it subtracts negative ones. This might cause averaging problems for samples that showed both negative and positive blade length. It is, therefore, recommended to manually select regions based on whether a positive or negative blade length was observed and classify adhesion and wear volume values to a single test, instead of just on adhesion volume value. Concluding, this descriptor achieved better identification of operational regions for some of the tested materials but failed to do so for others. Nevertheless, it can provide valuable insight of the total amount of material adhered on the blade (or material removed from the blade in the case of blade wear), which is a very important performance indicator in terms of abradable design requirements.

As highlighted before, less blade wear corresponds to smaller clearances and better aerodynamic efficiency, while less adhered material corresponds to lower degree of grooving and less debris passed out through out the engine, so it is very important that this descriptor can distinguish these behaviours.

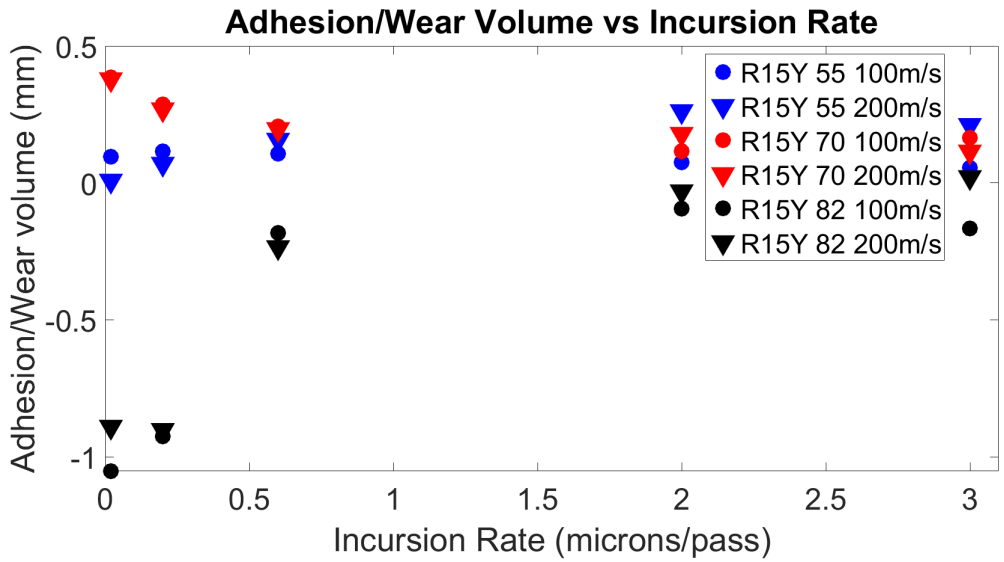

Figure 4.16: Adhesion/Wear volume against incursion rate.

Surface Roughness

In the previous sections two descriptors of abradable performance were discussed and they were found to provide valuable insight, but at the same time have a few limitations. These descriptors were based on the material adhered or removed during the contact and the rate at which this was happening. In this section a different descriptor was suggested by looking at the second part of the contact, the abradable, and more specifically the abradable surface roughness. Surface roughness is very important to the manufacturer, since rougher surfaces cause more aerodynamic losses and therefore it can be a good descriptor for abradables performance. For Metco 601, even though long adhesions were not generated during the contact, the small adhesions still create rougher surfaces. As a result it was expected that the roughness would vary with different testing conditions.

A surface texture consists of three components. The first component is the form of the surface, which is the nominal form, or shape of the object. The second component is the waviness, which is macro-scale roughness (longer wavelength deviations from the nominal surface) and the last component is the roughness, which is the nano and

micro-scale roughness (shorter wavelength deviations from the nominal surface). For the context of this investigation the surface roughness was used as this was the scale which was relevant to this application. Several parameters exist that describe the roughness of a surface, each with its advantages and limitations. In this investigation two of these parameters were evaluated and used to describe the surface roughness of the worn abradables and these were the arithmetic mean height and the root mean square height and both cross-sectional and areal measurements were performed for these parameters. The definitions of these parameters and the equations that were used to evaluate them were described below in equations 4.1, 4.3, 4.2, 4.4 [93, 94, 81].

Arithmetic Mean Height (Ra): This is defined as the arithmetic mean of the absolute value of the height of the surface profile (Z) for a given sampling length (L)

$$R_a = \frac{1}{L}\int_0^L \mid Z_x \mid \, dx \tag{4.1}$$

Areal Arithmetic Mean Height (Sa): This is defined as the arithmetic mean of the absolute value of the height of the surface profile (Z) for a given area (A, while A = x * y)

$$S_a = \frac{1}{A}\int_0^y \int_0^x \mid Z_{x,y} \mid \, dxdy \tag{4.2}$$

Root Mean Square Height (Rq): This is defined as the root mean square value of height of the surface profile (Z) for a given sampling length (L)

$$R_q = \sqrt{\frac{1}{L}\int_0^L {Z^2}_x \, dx} \tag{4.3}$$

Areal Root Mean Square Height (Sq): This is defined as the root mean square value of height of the surface profile (Z) for a given area (A, while A = x * y)

$$S_q = \sqrt{\frac{1}{A}\int_0^y \int_0^x {Z^2}_{x,y} \, dxdy} \tag{4.4}$$

An equipment used to measure the post-testing surface roughness of the abradables is ALICONA SL, which is a 3D system for form and roughness measurements. Using this apparatus the 3D coordinates (x, y, z) of the surface were exported in a text file and the surface was replicated in MATLAB to allow further calculations. The figure below 4.17 shows an example of how this was performed.

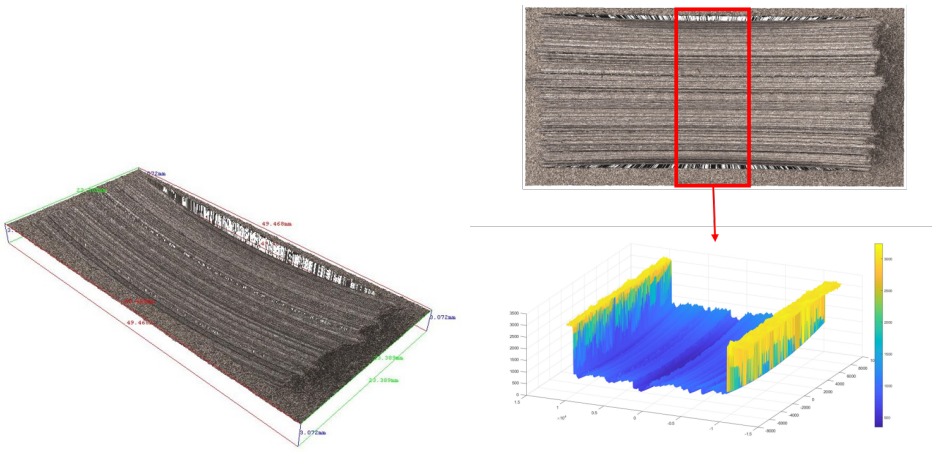

(a) (b)

Figure 4.17: (a) Example of ALICONA generated surface, (b) Example of how ALICONA generated surface is replicated in MATLAB.

Using the MATLAB replicated surfaces, roughness measurements such as Ra, Sa, Rq and Sq could be taken. This was done by taking cross sections across the replicated surface as shown in figure 4.17(b) and creating a roughness profile of this cross section.

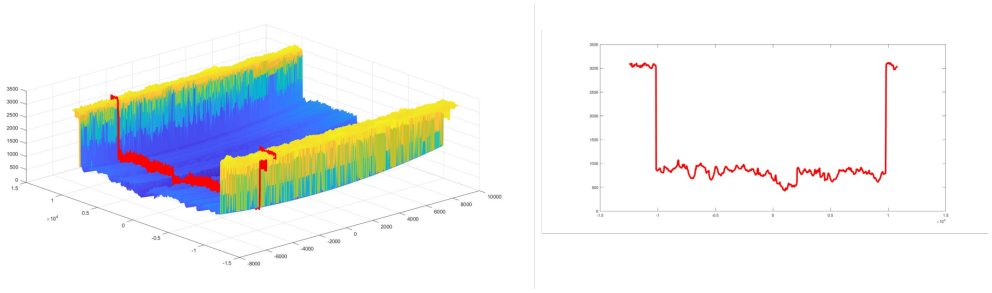

(a)

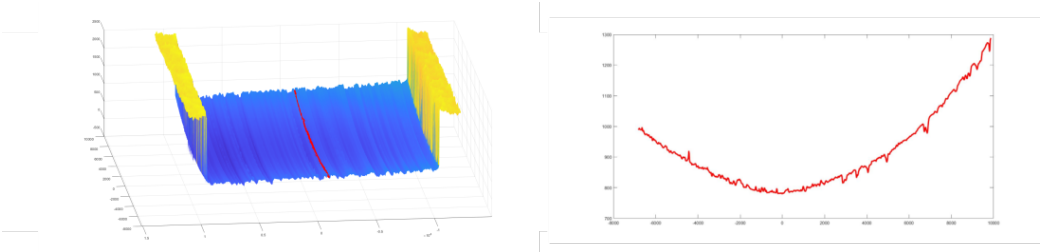

(b)

Figure 4.18: (a) Example of the extracted surface profile along the direction perpendicular to the contact, (b) Example of the extracted surface profile along the direction parallel to the contact.

However, at this stage there were a few more steps to perform so accurate measurements could be taken. The first step was to remove the edges of the un-rubbed abradable that were captured along the perpendicular direction of the cut and were shown in figure 4.18(a). To do this, the MATLAB code asked the user to manually select the points where the actual rub was, which was very clearly distinguished, and then it cropped the rest of the unwanted data as shown in figure 4.19.

(a) (b)

Figure 4.19: (a) Example of a surface profile with the sides of un-rubbed abradable, (b) Example of a surface profile after removing the sides of un-rubbed abradable.

The second step was related to the direction parallel to the contact. The problem with this dimension was that due to the nature of the contact (circular disc and flat plate) there was an inherent form in the shape of the rub that reflected this. Therefore, in order to make an accurate roughness measurement this form had to be removed. To achieve this a second degree polynomial was fitted on the data and then it was subtracted from the original data. This process resulted in the actual roughness of the rub parallel to the contact direction, without the inherent shape from the nature of the contact. An example of this was shown in figure 4.20. Figures 4.20(a) and 4.20(b) show the surface and a cross-sectional profile (along the parallel direction) with the shape of the inherent form present. Figure 4.20(c) shows how a second degree polynomial was fitted to the surface profile. The second degree polynomial fitting was quite accurate in this application because the length of the rub was relatively short. Finally figures 4.20(d) and 4.20(e) show how the original surface and profile looked after the form was removed. As clearly shown in these figures, the shape of the inherent form was removed and the resulted profiles could accurately be used to calculate the surface roughness parameters along a given cross section or a given area, using equations 4.1, 4.2, 4.3, 4.4.

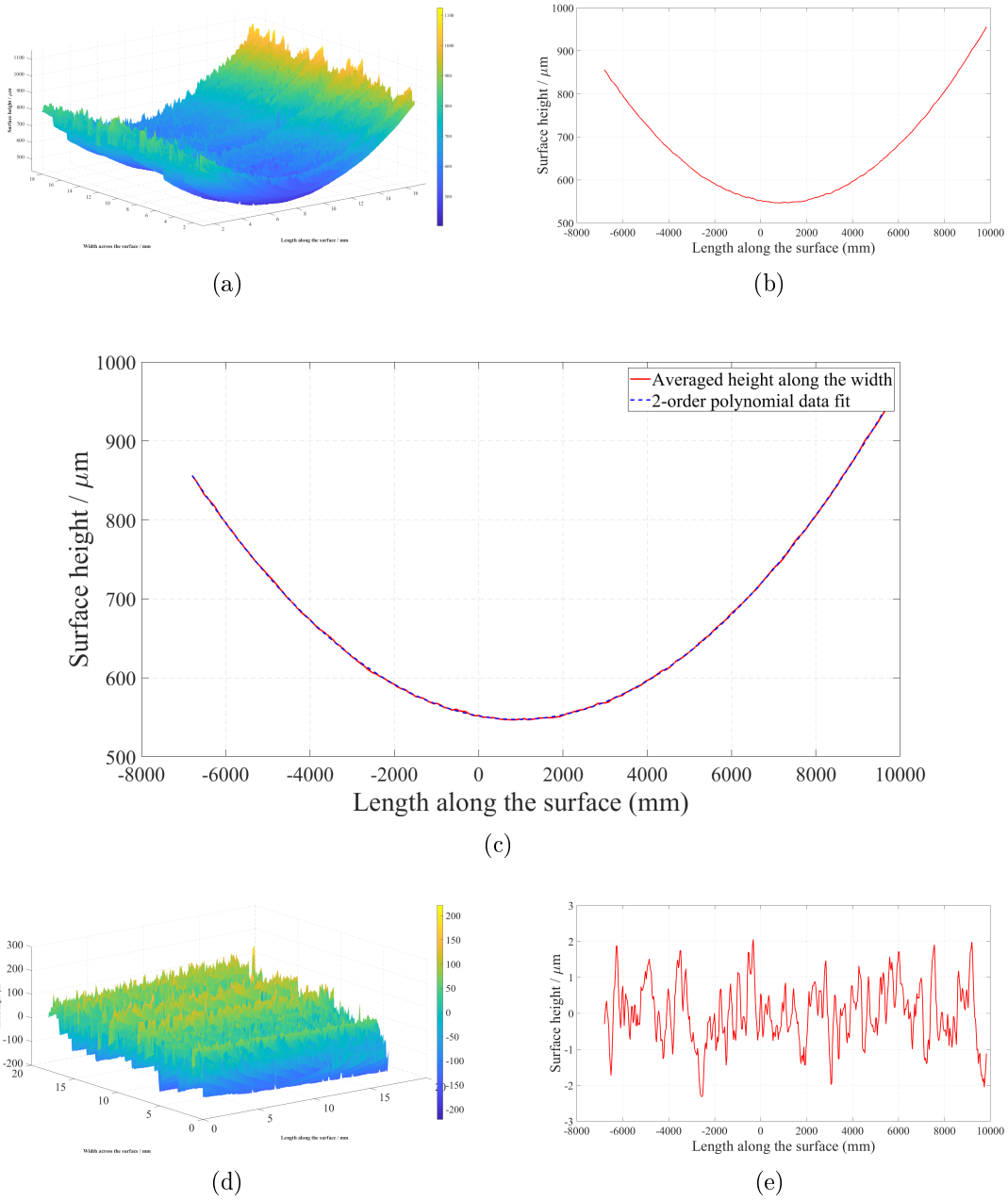

Figure 4.20: (a) Example of a surface with the shape form present, (b) Example of a surface profile with the shape form present obtained from a cross section along the surface (parallel to the contact), (c) A second degree polynomial fitted to the surface profile, (d) Example of a surface with the shape form removed, (e) Example of a surface profile with the shape form removed obtained from a cross section along the surface (parallel to the contact).

Finally, in order to ensure the accuracy of the results of the areal measurements (Sa, Sq), an area dependence study had to be performed. This was done to assess

whether the selection of the area of interest, at which measurements were taken, influenced the parameters measured and at what point (if any) the areal parameter became independent of the selected area. To do this, the roughness parameters were measured for a range of areas, starting from the minimum of a single cross-section along one dimension (x or y) to the maximum accumulated cross sections for the whole length of that dimension. For the area dependence study only the x-dimension was varied (direction along the rub, parallel to the contact) and the whole y-dimension was used (direction across the rub, perpendicular of the contact). The results from the area dependence study were shown in figure 4.21(a), while in figure 4.21(b) the y-axis was truncated to show more clearly the steady state values.

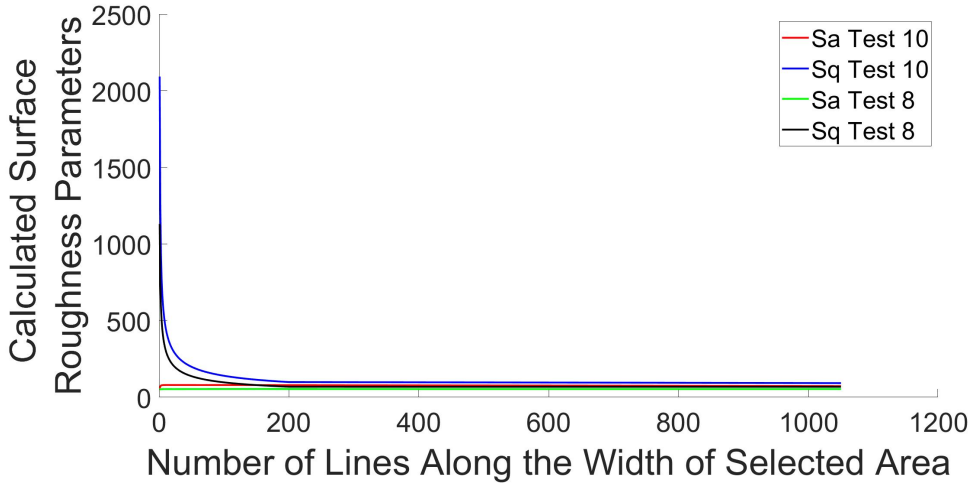

(a)

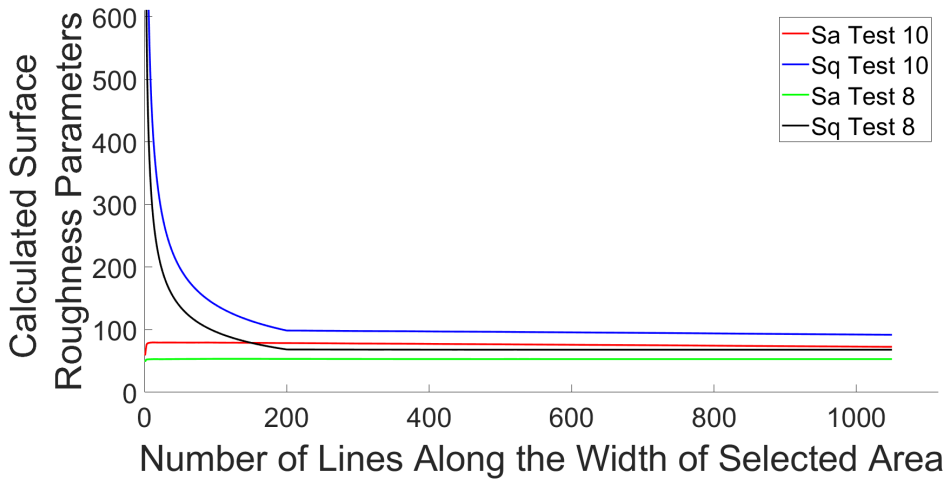

(b)

Figure 4.21: (a) Area dependence study, (b) Truncated y-axis allowing easier reading of steady state values.

As shown in figure 4.21, after around 200 lines along the width of the rub, the area roughness parameters Sa and Sq became independent of the selected area. Consequently, for the analysis to follow an area value larger than this (usually maximum value of possible lines) was always used in order to avoid any bias due to area dependence. In figure 4.21 examples from two tests (testing conditions shown in table 4.4) were shown to highlight that there was a similar trend for all tests, but in the analysis the area dependence check was performed for all the samples.

After all these steps were taken the surfaces obtained were analysed and their surface

Table 4.4: Surface roughness test matrix and results

Test No.	**Incursion (μm/pass)**	**Material**	**Hardness (RY15)**	**Sa (μm)**	**Sq (μm)**	**Ra (μm)**	**Ra (μm)**
1	0.02	M601	55	222.8	257.3	67.2	88.6
2	0.2	M601	55	123.2	154.5	58.4	97.1
3	2	M601	55	95.6	117.6	31.6	38.6
4	0.02	M601	70	226.5	271.3	73.0	95.2
5	0.2	M601	70	121.5	149.7	57.4	72.2
6	2	M601	70	101.0	127.5	33.6	40.7
7	0.02	M601	82	312.5	415.5	212.8	262.5
8	0.2	M601	82	301.5	406.0	197.9	259.7
9	2	M601	82	243.4	285.5	90.4	111.9
10	0.02	M320	58	386.9	469.4	49.9	65.3
11	0.2	M320	58	85.1	108.6	11.3	16.8
12	2	M320	58	113.1	137.3	56.8	156.1
13	0.02	M320	64	274.4	324.6	64.0	76.3
14	0.2	M320	64	98.2	122.1	16.6	21.3
15	2	M320	64	126.6	165.1	9.3	12.7
16	0.02	M320	70	344.0	425.1	72.7	110.7
17	0.2	M320	70	98.9	115.9	7.6	9.9
18	2	M320	70	83.9	98.2	10.1	14.1

roughness parameters were extracted. For comparison reasons, for the mapping of the roughness results, a different test matrix was considered for these measurements and not the one described in 4.1. More specifically, the roughness of some Metco 320 was measured and less incursion and speed conditions were considered. The Metco 320 samples considered in this section were samples tested in this study for the purposes of subsequent chapters. Table 4.4 summarised all the samples from which the roughness was measured and the corresponding results.

After the data was analysed and the roughness parameters were calculated, the next step was to create the roughness maps. The axis of the maps were the same as the ones used in the previous sections, but in this case the colour bar was based on the roughness parameters. Two maps were generated in this way for each material, one with Sa and one with Sq as the third dimension (colour-coding). Only Sa and Sq were plotted as the general trend was the same for all parameters and the areal parameter were a better description of the 3D surface. Figures 4.22 and 4.23 show the Sa and Sq surface roughness maps respectively.

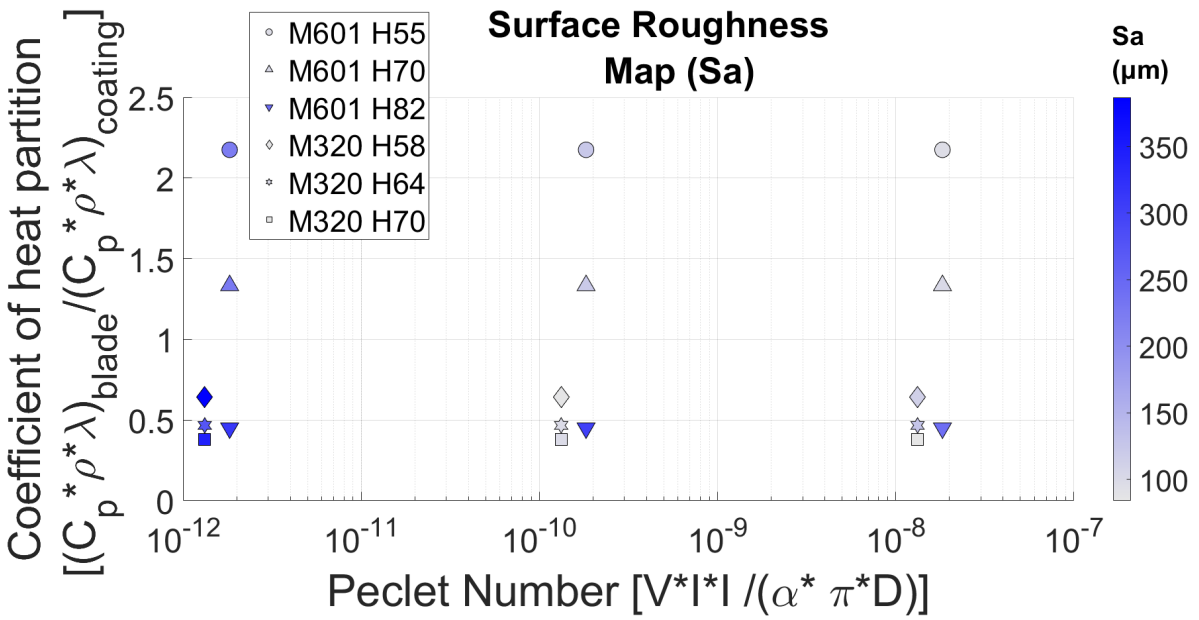

Figure 4.22: Roughness wear map with Sa (μm) as a colour bar.

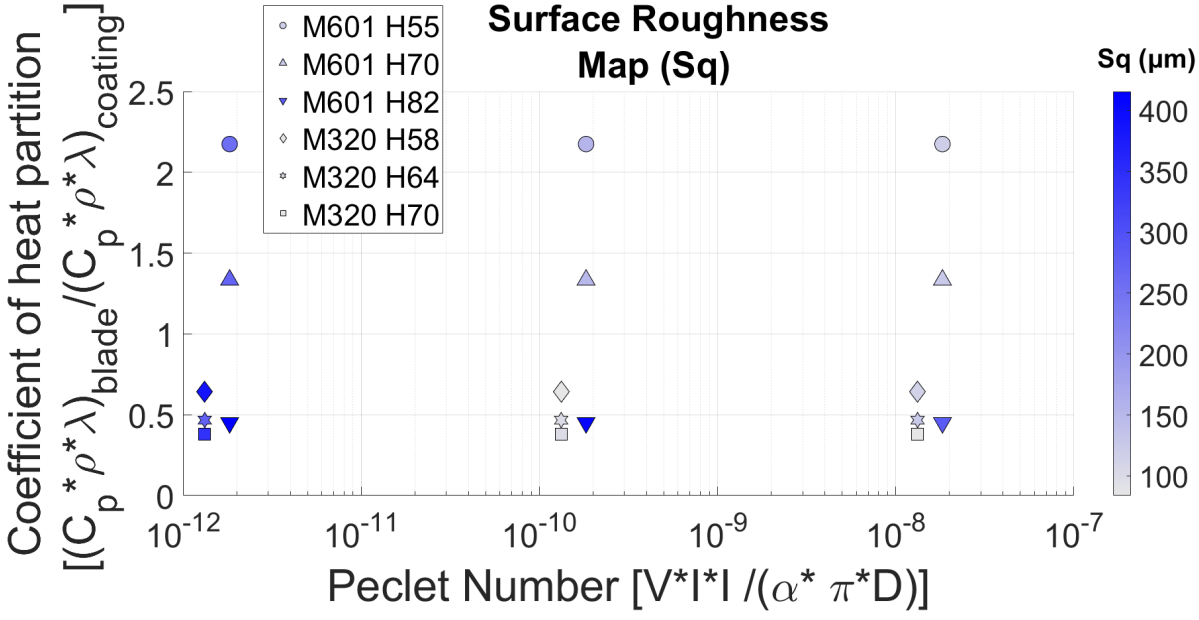

Figure 4.23: Roughness wear map with Sq (μm) as a colour bar.

As clearly shown in figures 4.22 and 4.23 the pattern of the two roughness parameters was almost identical. The only difference was the scale, which was a result of how the parameters were calculated (see equations 4.2 and 4.4). By studying these figures, it became apparent that for all materials considered the abradable surface roughness improved drastically with increasing incursion rates (higher peclet number suggested higher incursion rate as everything else was kept constant for a given abradable). It could therefore be concluded that surface roughness was a very useful way to map abradable performance as it is also a very important performance criterion for abradables.

In the case of Metco 601, a combination of both adhesion volume and roughness maps is suggested to be used. The ahdesion volume provided more valuable information about the amount of material picked up by the blade compared to the wear rate. Finally, roughness mapping provided a different mapping method based on a separate performance criterion and it was very effective at identifying regions of good and bad performance based on that criterion.

4.5 Conclusion

The aim of this study was to assess the performance of the two abradables of interest (Metco 601 and Metco 320) and to gain a better understanding on what drove their behaviour. As a first step towards this aim, in this chapter, extensive testing on Metco 601 was performed across a wide range of testing conditions. The performance of this abradable was thoroughly examined and the key differences compared to the performance of Metco 320 were identified. The main findings of this chapter were summarised below:

- Blade wear was observed for almost all samples with R15Y 82 and this was also correlated to high force and temperature generations. It was suggested that this was caused because of the high content of the metal phase in such high hardnesses. Also the abradable hardness was higher than the blade in this case (abradable R15Y 82, and blade R15Y 79.3 converted from RC). This suggested a blade to abradable ration lower than 1, meaning that the blade was rubbing against something harder than itself explaining the severity of the wear observed.

- Samples with hardness of R15Y 55 and 70 showed a degree of adhesion irrespective of testing conditions.
- Adhesion rates did not correlate with the resulting surface roughness of the abradable. This was explained from the difference in the adhesion mechanism of between the two abradables of interest. Metco 320 formed long adhesion that in case of break-off continued from where they were before, while Metco 601 formed shorter adhesions and in the case of break-off new adhesions initiated at different random points.
- Adhesion/wear rate was not an accurate descriptor of the overall abradability performance of Metco 601.
- Adhesion volume was better at identifying a transition from unwanted to desired behaviour compared to the adhesion/wear rate, but still had some limitations. More specifically, the overestimation of samples with a lot of peaks and the difficulty to distinguish between wear (negative blade length change) and adhesion (positive blade length change). Nevertheless it could provide significant insight for the performance of an abradable.
- Surface roughness was a different descriptor considered and it focuses on the abradable instead on the material pick-up. It was a very good descriptor for any abradable since roughness itself was a performance criterion for the manufacturer, since high roughness correlates to aerodynamic losses. In the case of both Metco 320 and 601 it showed a clear progression towards better performance (more smooth rubs) at increased incursion rates.

Moreover differences in the performance of the two considered abradables were identified and were summarised below:

- At low incursion rates the wear and adhesion mechanisms of Metco 320 were significantly worse compared to the ones observed with Metco 601. Metco 601 showed some signs of adhesion but not as excessive as with Metco 320.
- As incursion rate increased the wear and adhesion mechanisms in Metco 320 drastically improved and eventually at an incursion rate higher than 0.2 microns/pass consistent clean cutting mechanism was observed. On the other hand, Metco 601 improved only slightly with incursion rate. A small degree of adhesion was present even at extremely high incursion rates (3 microns/pass).

After identifying these differences in the wear performance of these abradables the next step was to examine in more depth why these occurred. To establish a better understanding of these differences the next chapter will examine how material was removed by looking at the point of contact. The debris generation mechanism and pattern were investigated in depth to provide a better understanding on the wear and material removal mechanisms that took place during these contacts.

Chapter 5

Material Removal and Ejection Mechanism

5.1 Introduction

It was hypothesised that during an efficient cut, where chips are formed and removed during the contact, material will be ejected from the front of the rotating blade, while if a rubbing mechanism is more predominant material tends to eject behind the blade [33, 91]. Consequently, it was expected that for high speed and high incursion rate conditions more material to be ejected from the front of the blade, while for low speed and low incursion rate conditions more material to be ejected from the back of the blade. In this chapter the material removal mechanisms resulting from the contact were investigated. This was achieved by examining the debris generated during testing at the point of contact. The direction at which material was ejected, the angle of ejection and its intensity provide important insight on what material removal mechanism was creating this debris. This could be used as a method to identify the material removal mechanisms, as well as a method to confirm whether the inferences made using different approaches were valid.

The first step to investigate the debris generation mechanism was to observe a contact with the highest detail possible. To achieve this a high speed camera (Phantom VEO 710, Ametek GB Ltd., Leicester, UK) was used, along with a zoom lens (AF ZOOM-NIKKOR 24-85mm f/2.8-4D IF). This high speed camera could capture images at speeds of 7 gigapixel per second (Gpx/s), which is equivalent to 7,400 frames per second (fps) at a resolution of 1280 x 800 and a maximum of 700,000 fps at a resolution of 64 x 8. The aim of this procedure was to observe a single strike with as many frames

as possible in an attempt to see how debris was generated during the contact. To ensure that useful data was acquired, several preliminary tests were performed to find the ideal resolution that was small enough to provide the highest possible fps, but large enough to show the blade and debris. It was found that the ideal resolution was around 320 x 72, which provided 240000 fps. These settings allowed the full capture of debris, while being fast enough to provide an adequate amount of frames for observations. For this set of tests all the other sensors (cameras, strobe controller, LED, pyrometer, dynamometer) were not needed so they were removed from the set-up, leaving the high speed camera as the only measurement equipment. Figures 5.1 and 5.3 show a series of frames obtained using this method from sample tests, which showed the generation and direction of debris. The material removed was labeled with red boxes in the images for reference. The first 10 pictures on both figures have a time interval of 8.33 μs, while the last two were frames that show the debris a small amount of time after the blade passed and was not rubbing anymore (time interval varied and it is shown in the caption of the figures). This was done because it was important to show that material was still ejected after the blade passed, but there were a lot of frames ($>$100) in between and it was not possible to show all of them. Further more, figures 5.2 and 5.4 show enlarged versions of the most important images from figures 5.1 and 5.3 to illustrate the key features more clearly.

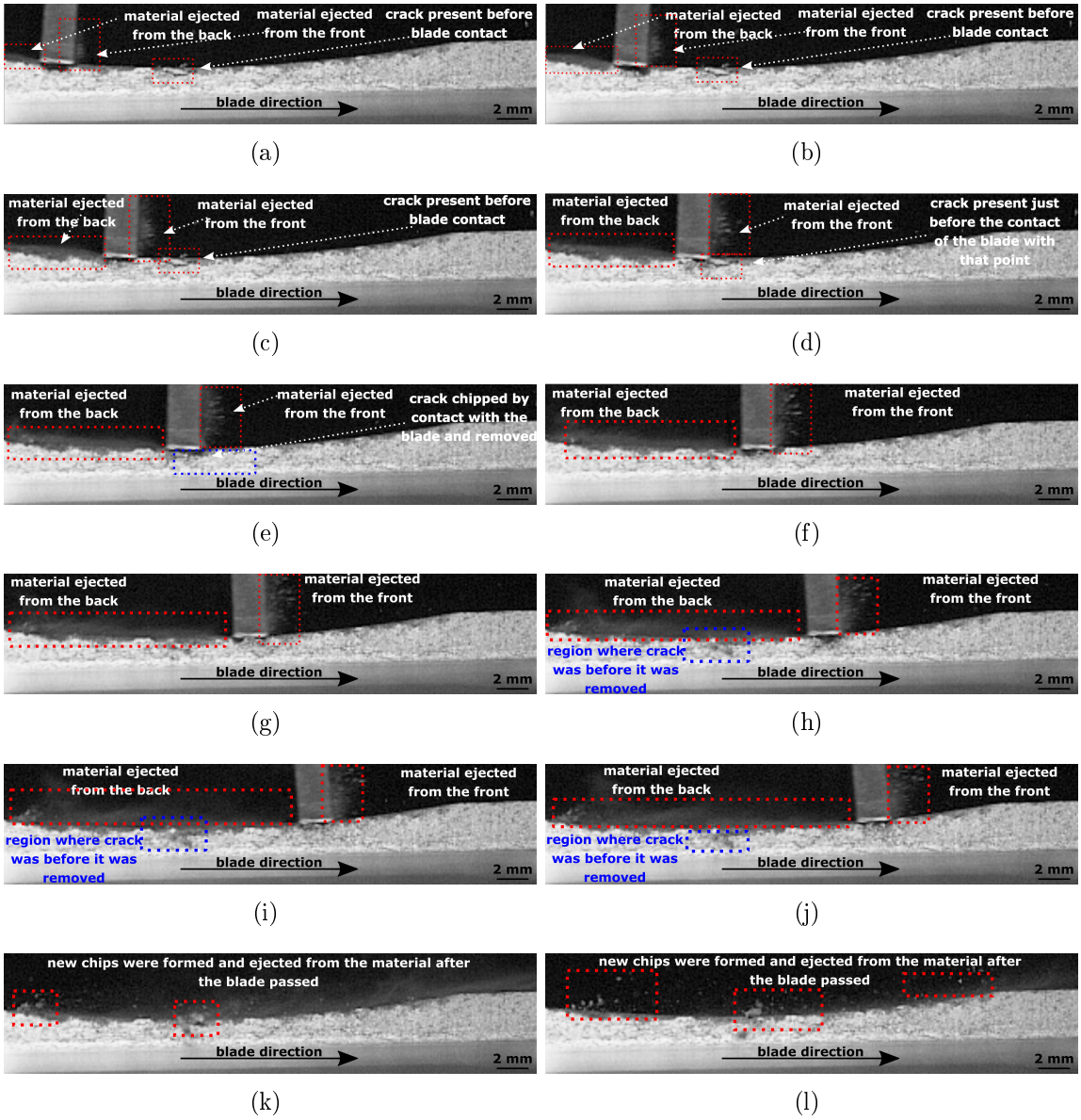

Figure 5.1: Series of 12 raw images from a Metco 320, RY15 65 sample, tested at 200 m/s and 2 μm/pass. Images (a) to (j) have a time interval of 8.33 μs. Image (k) was taken 62 μs after image (j) and image (l) was taken 175 μs after image (k).

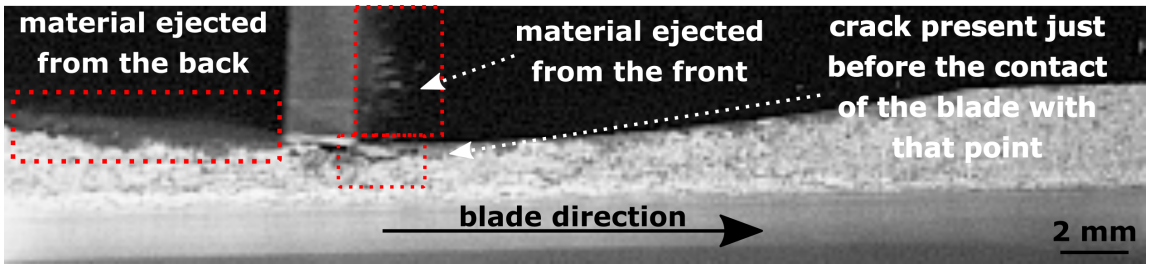

(a)

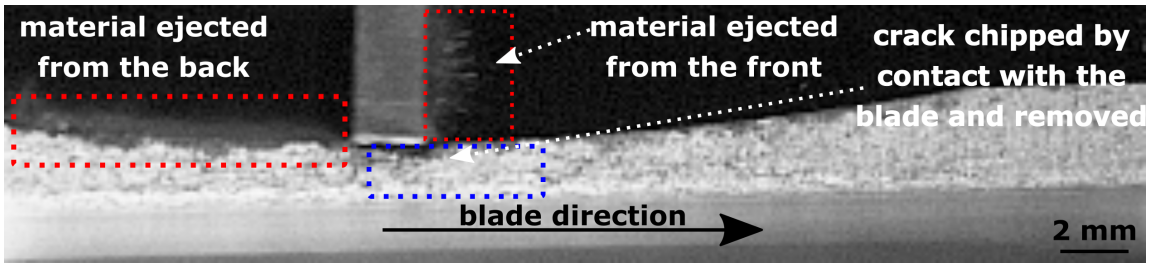

(b)

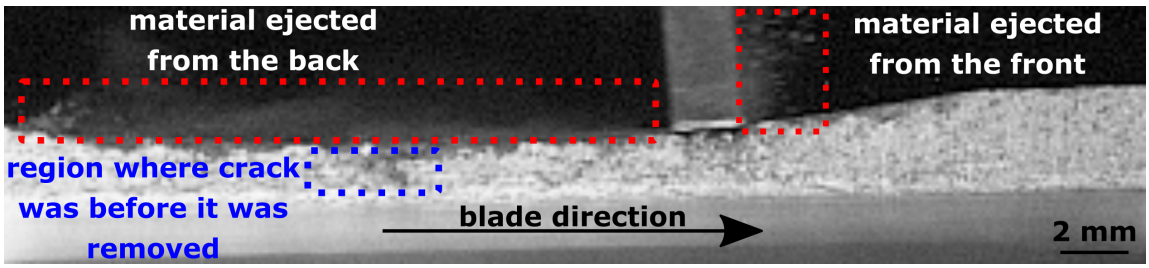

(c)

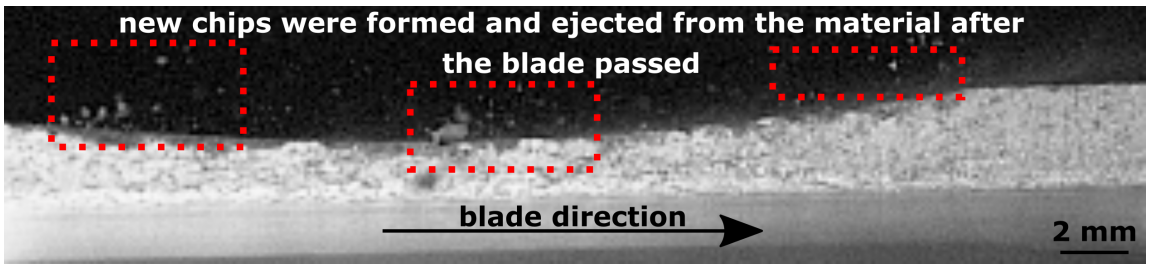

(d)

Figure 5.2: Enlarged images from a Metco 320, RY15 65 sample, tested at 200 m/s and 2 μm/pass. Image (a) is equivalent to image 5.1(d), image (b) is equivalent to image 5.1(e), image (c) is equivalent to image 5.1(j) and image (d) is equivalent to image 5.1(l).

Figure 5.3: Series of 12 raw images from a Metco 601, RY15 55 sample, tested at 200 m/s and 0.02 μm/pass. Images (a) to (j) have a time interval of 8.33 μs. Image (k) was taken 33.3 μs after image (j) and image (l) was taken 8.33 μs after image (k).

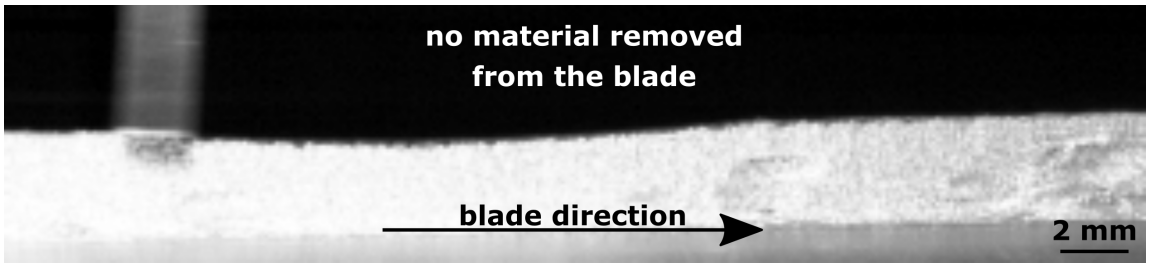

(a)

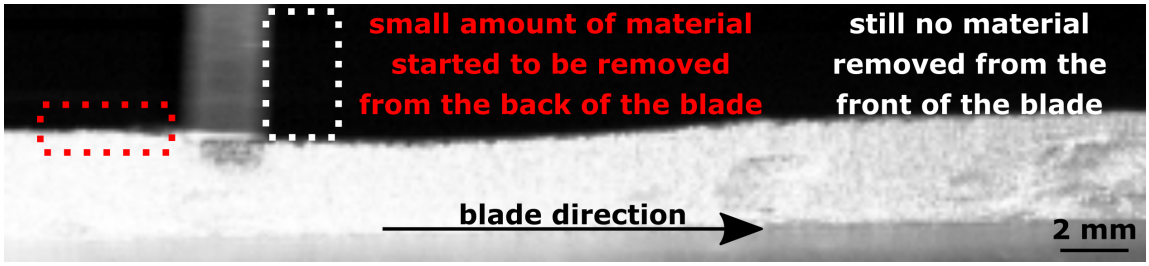

(b)

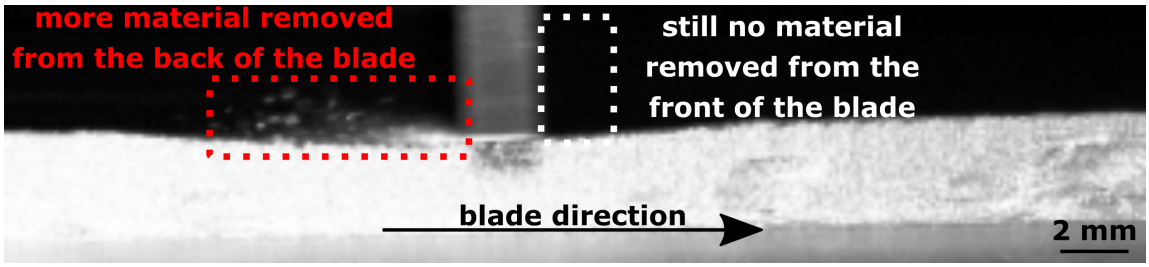

(c)

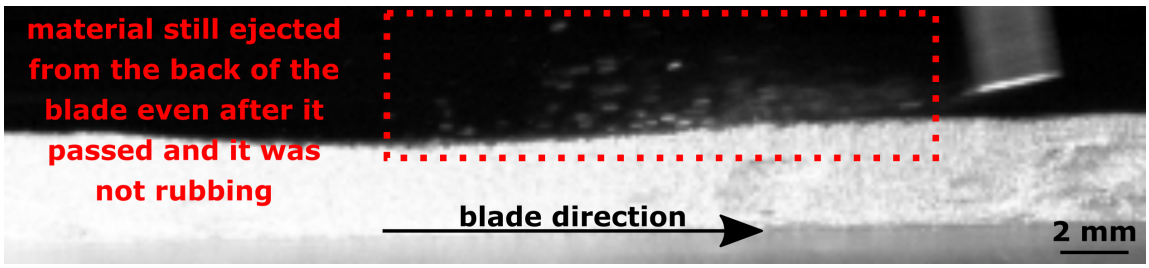

(d)

Figure 5.4: Enlarged images from a Metco 601, RY15 55 sample, tested at 200 m/s and 0.02 μm/pass. Image (a) is equivalent to image 5.3(b), image (b) is equivalent to image 5.3(c), image (c) is equivalent to image 5.3(g) and image (d) is equivalent to image 5.3(l).

The tests selected to be shown in figures 5.1 and 5.3 represented a high and a low incursion rate respectively. This was done because it was found that the debris generation mechanism was similar for the same incursion rates, while they changed as incursion rate was varied and these two extremes highlight these differences. The

first important insight gained by studying these figures was that at high incursion rates (figure 5.1) a lot of material was ejected from the front of the blade, while some of it sprang back from the back of the blade. However, in the case of the test at low incursion rates (figure 5.3) no material could be seen to be ejected from the front of the blade as the blade passed. All of the material sprang back after the blade passed. This suggested that there was a different chip generation and release mechanism that varied with the incursion rate. A second interesting finding could be observed by examining the case of the high incursion rate test (shown in figures (5.1) and 5.2). It could be seen that a large crack was present and as the blade passed over it, a large chip was removed from that region (see figures 5.2(a) and 5.2(b)). These images provided evidence that one of the material removal mechanisms taking place when testing at high incursion rates, was that chips were formed and removed from the abradable after large cracks were formed. Another interesting finding was the fact that in both cases debris generated was significantly larger than the incursion rate. This was especially evident by looking at the last two pictures of the figures (5.1(k), 5.1(l), 5.3(k), 5.3(l)) that show the debris some time after the blade had passed. Large debris particles could be observed in these images, which were clearly larger than the incursion rate scale. It was expected that material removed was of a similar scale to the incursion rate, but it seems this was not the case and this finding was investigated further in a later section of this thesis.

Testing with the high speed camera provided very important information on the material removal method and the initial preliminary testing performed supports the hypothesis and also identified additional interesting observations. However, this method had an important limitation. Due to the huge amount of data generated and the very fast processing needed to collect this data, the high speed camera could only record very short periods of time. At the conditions that the tests described above were performed only 4.75 ms were recorded. This caused a major concern as the longer tests took about 6 minutes and therefore it was impossible to monitor the whole contact. Even though this was a very powerful tool, it could only be used to inspect specific events and not a whole duration of the contact. Using a similar principle, the methodology in this chapter used a normal (not high speed) camera to make an averaged observation of this phenomenon for the whole duration of the test. This was described in more detail in a later section of this chapter.

To summarise, valuable insight was provided by examining in detail a single contact and the next step was to further investigate these findings. To do so, later in this

chapter the material removal and ejection direction and volume were measured for the whole duration of a test (instead of just a single strike as in this section) to show how this varies during a contact. Also, debris generated during the test was collected and particle size and distribution was performed.

5.2 Theoretical background and image processing review

In the first part of this section, the theoretical background that describes the correlation between debris ejection characteristics and material removal mechanisms based on literature was provided. The aim was to explain how debris was generated during the contact and explain what this showed about the material removal mechanisms. In the second part of this section, a review of image processing techniques was performed. This was essential to ensure that the methods developed for the analysis of the image raw data obtained from this testing provided high quality quantitative results.

The contact between a blade and an abradable could be considered to be similar to a machining tool contact, where chips were formed at high energy conditions and a rubbing mechanism took place at low energy conditions. When this process was efficient, micro-cutting of the abradable material resulted. This meant that the blade would cut and remove material at every pass and it was expected that the material removed would be at a similar scale to the incursion pass. However, sometimes such a contact could create fracturing in the material if the material was brittle, resulting in crack propagation below the blade (see mechanism described in section 2.2.2). Consequently, the resulting chips represented the convergence of the cracks that form. Added to these scenarios, in materials where the boundary between grains was weak (such as abradable materials) grain shearing could be observed. The chip formation and removal that takes place after a crack is formed was shown in figures 5.1 and 5.2. By inspecting images 5.2(a) to 5.2(b) a crack could be observed on the surface of the abradable as the blade was approaching that point. At image 5.2(b) the blade reached the crack and a chip was formed and removed (cracked abradable was removed and was not present in subsequent images after the blade had passed that point).

However, under some conditions, the contact represented more of a sliding contact rather than an abrasive cut. This was more apparent in the low incursion rate testing conditions shown in figures 5.3 and 5.4. In this case, the vertical component of the force resulting from the contact compressed the material below it. This caused build-up of elastic energy in the bonds of the abradable, deforming the particles below and around the blade. When this energy was enough to break the bonds that hold the particles together, the material sprang upwards after the blade had passed. This mechanism was explained in more detail in section 2.2.2.

5.2.1 Image processing

This section provided a description of the image processing task that was considered in this chapter. After identifying the challenges of this task, a review of how similar problems have been tackled in the literature was performed with the aim of creating a tool that could accurately measure the amount of debris generated during a contact.

As a first step there was the need to identify what needed to be measured. Figure 5.5 shows an example of a raw image obtained during the testing highlighting in the red box areas where the debris needed to be measured.

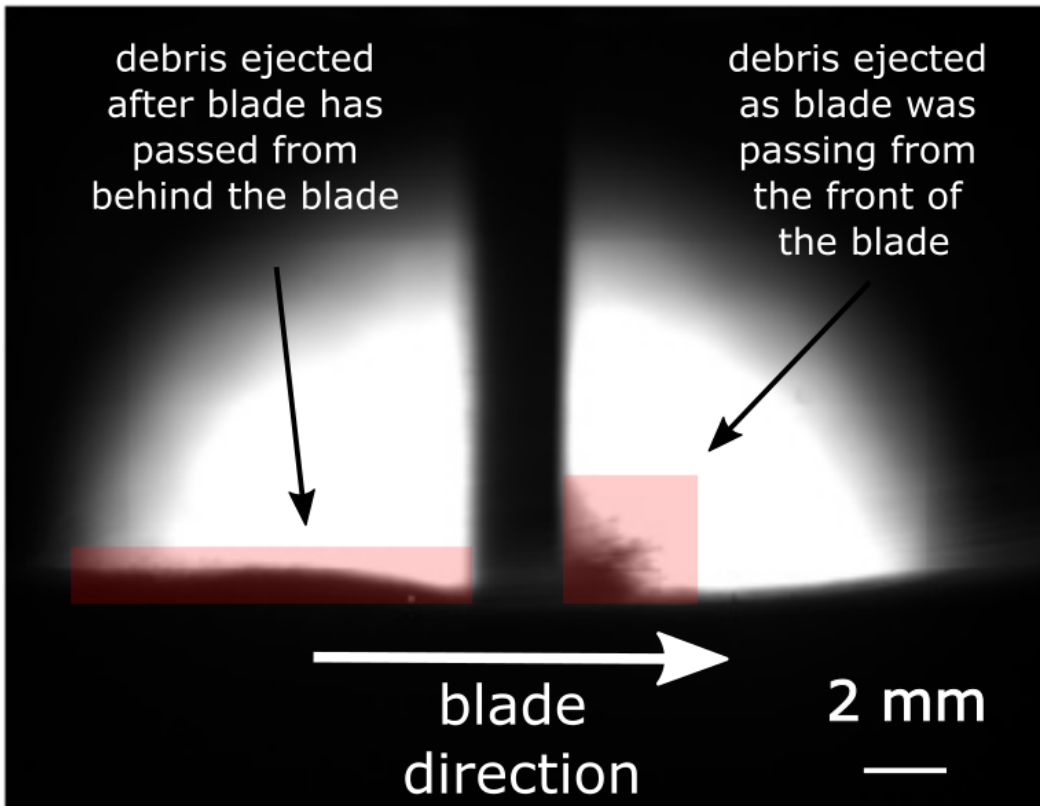

Figure 5.5: Example of raw images showing the regions of interest.

Figure 5.5 shows that the averaged debris could still be observed with a regular camera, however some problems arose with this method. The term averaged was used here because the debris shown on these images represented the total debris removed by the blade during the whole duration of a single pass (unlike images in figures 5.1 and 5.3 that showed several time steps from a single pass). The limitation of this method was that it was hard to distinguish between the debris and features such as the abradable surface and the blade. The main challenge of this task was to find a method to automatically identify these regions of interest and perform measurements on them. Therefore, there was a need for an image processing post-testing analysis.

Edge detection is used in image processing to identify regions of sudden changes in the images, in relation to intensity value of a greyscale image. Sudden changes in the intensity of the images represent physical discontinuities such as changes in the geometry of an object and changes in brightness and illumination. Edge detection can be a very powerful tool for the images considered as the background (white) and the regions of interest such as the debris and the blade (black) have very high intensity contrast. There are several edge detection algorithms with varied accuracy, which are

dependent on the input images and a lot of them are available in Matlab. After some preliminary experimenting it was found that the most useful edge detection algorithm for the images considered in this chapter was the Prewitt method. This algorithm creates two 3 by 3 masks (one each in the x and y directions) and convolves this mask on top of the intensity image computing the gradient. In this convolution processes the value of each pixel is calculated by making that specific pixel the central pixel and multiplying it and the neighbouring pixels (3 by 3 area with that pixel in the centre) with the mask's values. The sum of the calculated values from all the pixels is then used as the new intensity value for that central pixel. This process is then repeated for all the pixels in the image. This method is highly susceptible to noise and therefore use of a smoothing filter is suggested prior to the edge detection. The smoothing algorithm is a mask that calculates the average of a 3 by 3 square around a pixel and then replaces the central pixel value with that average [95, 96, 97, 98].

Another useful technique used in image processing is to use thresholding and binarisation to separate regions of interest. There are several methods of achieving this in the literature. An example of this is to use a single global threshold value for the whole image ([99]). Another technique was suggested by Otsu [100], in which the greyscale histogram of the image is considered to provide a fixed preselected threshold. In a different approach developed by Bradley and Roth [101], local thresholding is used instead of a single global one. To achieve this, this method creates an s by s (s can be any positive integer) square around each pixel and calculates the average value of this area. Then if the value of the central pixel is a predefined percentage less than the average of the square around it, the pixel is assigned a value of 0. If the value of the pixel is a predefined percentage higher than the square around it is assigned the value of 1. This is repeated for all the pixels of the image. This technique is better than global thresholding techniques in tasks where there is blur and non-uniform illumination such as the images used in this investigation. [99, 102].

5.2.2 Chosen solution

By considering the approaches found in the literature to tackle thresholding and binarisation problems it was apparent that there was not a single technique that could be used by itself to produce the required results. So in this investigation a combination of the techniques reviewed was employed. Firstly, it was expected that due to the nature of the images (non-uniform illumination, blurring and difficulty to

distinguish between areas of interest) adaptive thresholding [101], which is a local thresholding technique, was more effective and therefore it was used as a first step in the analysis used. Then, the second step used an edge detection algorithm (Prewitt method [95]) to identify edges of known areas such as the blade and the abradable surface on the right of the blade to crop the image and leave only the regions of interest. This was a form of manual cropping, but it was instead made automatic using the edges of known, well defined areas in the image. Further explanation of how the analysis was performed was shown in section 5.3.

5.3 Methodology and materials

This section highlighted the methodology followed for carrying out this investigation. This included an explanation of which materials were selected, the changes made in the standard test rig set-up and a description of how the image data obtained from these tests were processed and analysed to produce quantitative results that allowed inferences to be drawn.

5.3.1 Materials

This section aimed to identify the material removal mechanisms by examining the characteristics of the debris generated during the contact. At the same time, one aim of this thesis was to compare the performance of the two abradable materials under investigation (Metco 601, Metco 320) and therefore, for this set of tests both materials were tested. However, for the purpose of this investigation the standard samples of these materials described in previous section had to be modified. The standard 60 mm square samples had to be milled to a thinner 18 mm wide strip along the centre of the holding plate as shown in figure 5.6.

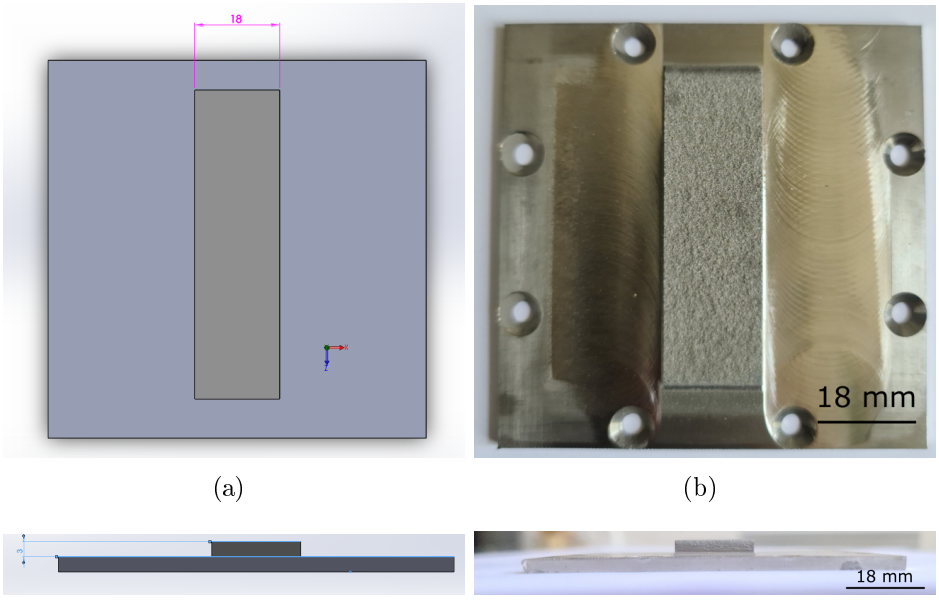

(a) (b)

(c) (d)

Figure 5.6: (a) CAD of milled sample from top view, (b) CAD of milled sample from side view, (c) actual milled sample from top view, (d) actual milled sample from side view.

This was done to allow the 20 mm blade to overhang the abradable sample by 1 mm on each side. The reasons for these modifications were explained in more detailed in section 5.3.3. The blade material was the standard Titanium alloy used and described previously in section 3.2.2.

5.3.2 Test conditions and test matrix

As in the previous sections, the effect of testing parameters such as incursion rate and hardness were investigated. The effect of blade tip speed was not investigated in this section as it was previously shown that it did not have a significant effect on the material removal mechanism. As a result, this set of tests was performed at 200 m/s, which was the test rig's highest achievable speed and also the most engine representative. As mentioned above, the aim of this chapter, was to gain understanding of why the two abradables under investigation had a different performance, by looking at the point of contact and therefore for this set of tests both of these materials were considered. To summarise, a selection of two abradable materials, 3 hardness values and 3 incursion rates was made. Table 5.1 shows a test matrix summarising the material selection and all the testing conditions investigated in this section. The hardness

values were chosen to cover the actual operating spectrum used in engines, while investigating the effect of the abradable's hardness on the material removal mechanism. Finally, the incursion rates chosen were a representation of different engine events as explained in previous sections.

Table 5.1: Test matrix for contact mechanism investigation. * High number of sparks was observed. ** High ejection angle causing calculation issues.

Test Number	**Abradable Material**	**Hardness (RY15)**	**Speed (m/s)**	**Incurssion Rate (μm/pass)**
1	M601	55	200	2
2	M601	55	200	0.2
3	M601	55	200	0.02
4*	M601	70	200	2
5	M601	70	200	0.2
6	M601	70	200	0.02
7*	M601	82	200	2
8	M601	82	200	0.2
9	M601	82	200	0.02
10	M320	58	200	2
11	M320	58	200	0.2
12	M320	58	200	0.02
13**	M320	64	200	2
14	M320	64	200	0.2
15	M320	64	200	0.02
16**	M320	70	200	2
17	M320	70	200	0.2
18	M320	70	200	0.02

5.3.3 Experimental set-up and procedure

This set of tests was performed on the experimental test rig described in chapter 3, with the same equipment and set-up, other than some modifications that allowed for the investigation of the material removal mechanisms. In this section, these modifications on the standard set-up were described.

Imaging technique

The same stoboscopic imaging technique used in section 3.1.3 was used for these tests as well, with the only difference being the position of the camera and the LED array. The camera was moved to be in line with the edge of the blade, when the blade was

in the bottom centre position, i.e. at the point of contact. The position of the LED array used for the stroboscopic imaging technique was also adjusted to be opposite of the camera. These changes allowed the capture of images of the blade at the point of contact, while at the same time capturing the debris that was generated by the strike. In turn, this allowed the investigation of the material removal mechanism during the period of the contact, by studying the size, direction and angle of the generated debris during each strike.

Abradable sample

The need to adjust the abradable samples used was identified after some preliminary testing. It was observed that by using the samples used in previous sections, most of the debris generated could not be captured. This was because the arc of the contact was formed in the middle of the sample, while the camera was only able to observe the front side of the sample. Consequently, the debris in the area of this arc could not be recorded. This problem was more clearly shown in figure 5.7(a).

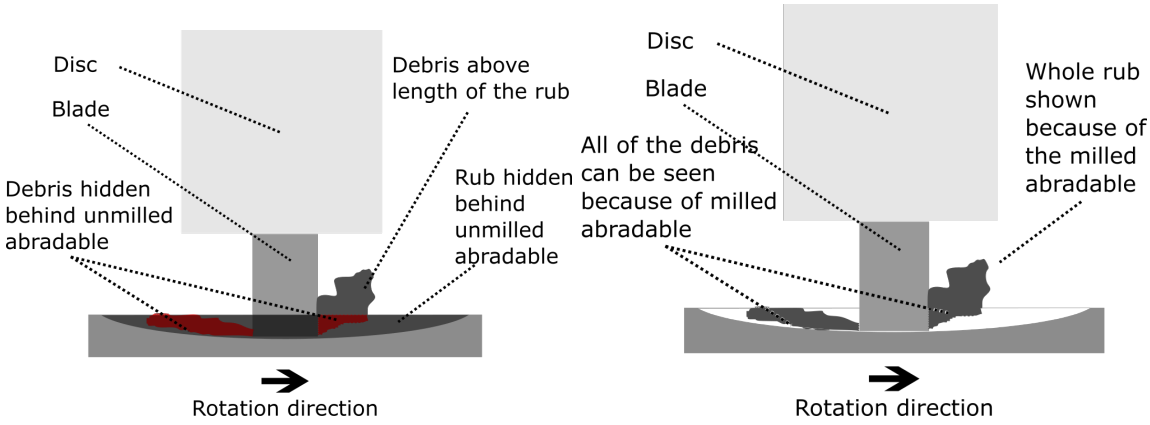

Figure 5.7: (a) Schematic showing how part of the debris is lost when abradable is not milled, (b) Schematic showing how all of the debris is shown when abradable is milled.

To solve this problem, the abradable was milled to remove some of the sample and leave only 18 mm in the centre of the steel mounting plate, allowing the blade to overhang the sample by 1 mm on each side as shown in the schematic at figure 5.8. By using these samples, the rub arc generated during the contact could be observed, allowing more accurate monitoring of the debris generated during the contact as shown by the schematic in figure 5.7(b).

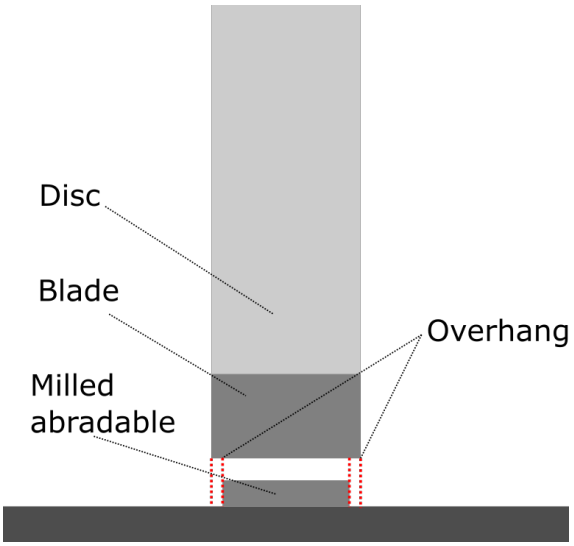

Figure 5.8: Schematic showing blade overhang after milling the abradable.

Figure 5.9 shows an updated schematic of the experimental equipment and set-up used and the changes done to the standard set-up, for the testing in this chapter. The red boxes in the figure highlight the changes made in the standard set-up.

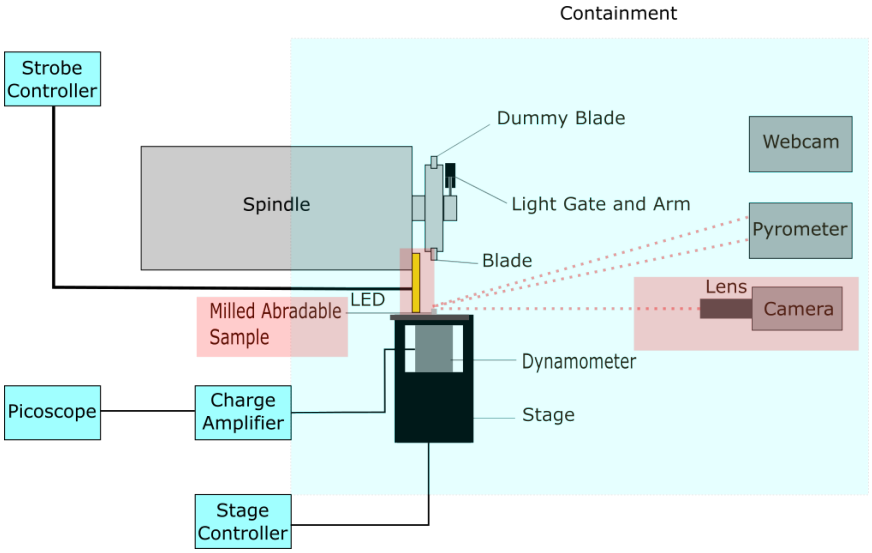

Figure 5.9: Schematic of the updated test rig setup for test carried out for this chapter, from the side (not to scale).

Experimental procedure

The experimental procedure followed was identical to the standard procedure described in chapter 3. Emphasis was given to achieve the highest image quality possi-

ble, as this was essential in the accuracy of the data post-processing. To achieve the highest image quality possible, several preliminary tests were performed to identify the most appropriate camera settings, such as exposure time, to be used. The data obtained from this tests consists of images of the blade and debris at the point of contact for every several strikes, force data and temperature data. For a small sample of tests, two cameras were used (one at the top and one at the bottom) to allow the collection of repeat blade length change data as well. Moreover, for these tests, the SEM stubs with adhesive carbon discs described in section 3.6.3 were also used.

5.3.4 Data post-processing

This section provides a description of the code developed to analyse the images collected from the tests and an explanation of how measurements were made using this code. The aim of the post-processing was to take as an input the raw images captured during the tests and provide numerical outputs that described the amount of debris generated, where debris was ejected from, the angle of this ejection as well as the total amount of debris generated during the whole test. A secondary aim was to develop a post processing technique that was mostly automatic and could perform accurate measurements on a large amount of consecutive images (tens of thousands) with minimal required user inputs. Several methods of achieving this were considered and discussed in section 5.2 and the development of this code was chosen as it was a good balance between time and processing limitations and high accuracy measurements.

The raw images captured from the camera during testing were greyscale and therefore the first step was to enhance and convert them into binary to allow measurements to be made. This was a very important step as it was vital to ensure no information was lost during the conversion. Several image processing techniques were employed to increase the contrast, make the background brightness constant for all the images in order to increase the accuracy of the binarisation process. After this, the next step was the conversion to binary. For this a thresholding technique called adaptive thresholding was used, as described in section 5.2. A series of preliminary processing, of a sample set of images, was carried out to determine appropriate processing parameters and to define criteria that assessed the accuracy of the method. Next, a number of filters was applied to remove any noise generated in the binarisation resulting in an accurate binary representation of the original image. This binary image was later

used for analysis and measurements. Figure 5.10 shows the image processing and binary conversion steps on a sample image.

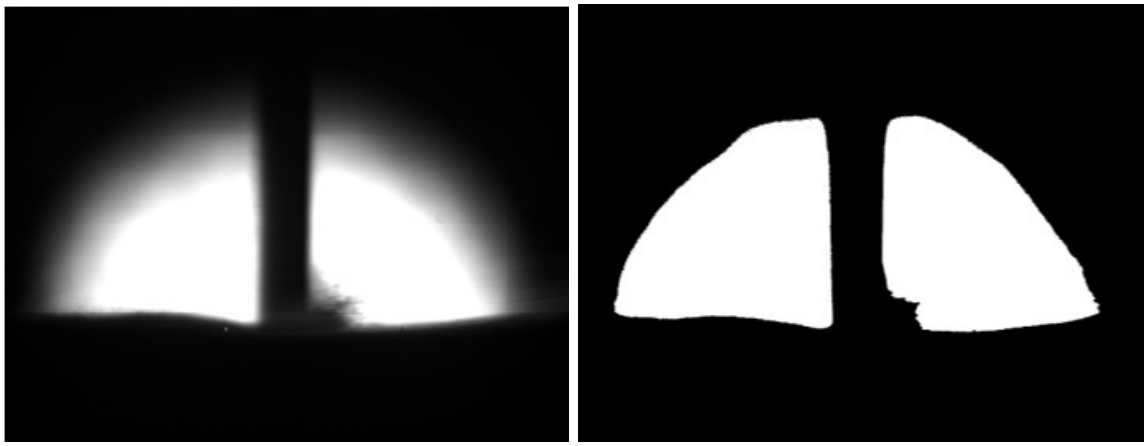

(a) (b)

Figure 5.10: (a) Example of a raw greyscale image, (b) Example of the equivalent converted binary image.

The next step was to identify key points of interest on the images to allow the measurement of the debris plumes. Ideally, it would be possible to create a number of points around the plumes directly, however this was quite challenging due to the nature of the images. Even though, the debris plumes had a clear contrast with the background they were very similar to the blade and abradable as shown in figure 5.10(a). For this reason, to accurately extract the debris data a number of steps was taken. Firstly, an edge detection algorithm was used to identify and separate the white background from everything else as shown in figure 5.11.

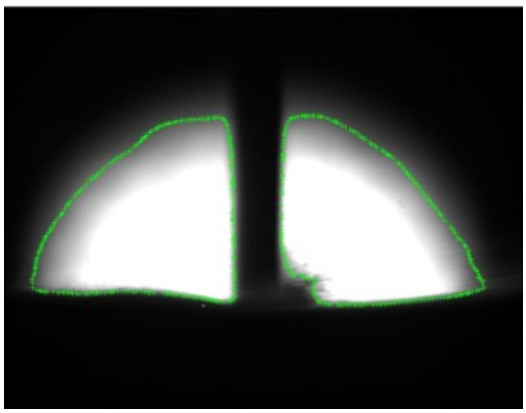

Figure 5.11: Example of edge detection and identification of key points.

This algorithm created a number of points that outline the blade, debris and abradable surface.

The challenge that followed, was to separate the blade and the debris. There are a number of possible methods to achieve this and as previously time, processing requirements and accuracy were considered. The aim of this step was to identify points along the vertical edges of the blade and create vertical lines that run through the whole image along those points. This was done since it was expected that the debris plume's starting points were the front and back of the blade edges. Using this method the blade was effectively removed from the images. This method, also solved another challenge faced due to the nature of the data collected. Consecutive pictures, have the blade at a slightly different position (slightly more to the left or right) due to small errors in the delay time used in the stroboscopic imaging technique. However, this method found the edges of the blade on each image and as a result it solved this problem allowing for more accurate measurements. After removing the blade from the image, the debris needed to be separated from the abradable surface. To achieve this, a similar edge detection mechanism was employed near the surface of the abradable in the front of the blade, which created a number of points along that surface. The front of the blade was chosen as the area to apply this algorithm because the debris was shorter on this side and it was easier to see the rub profile. Next, a second degree polynomial was fitted on these points recreating the rub profile on the front side of the blade. The rub profile on the back side of the blade could not be estimated in this way, since the debris was much longer and covered the whole rub making it very challenging to distinguish between debris and abradable. However, since it could be assumed that for each image the rub was an arc symmetrical to the centre of the blade, the 2nd degree polynomial fitted on the front of the blade was reflected along the centre line of the blade to create an estimate of the rub profile at the back of the blade. For the final step, the images were cropped to remove the areas below the estimated rub profiles (abradable) and the blade, leaving only an area which included the debris and the white background. These steps are illustrated in figure 5.12.

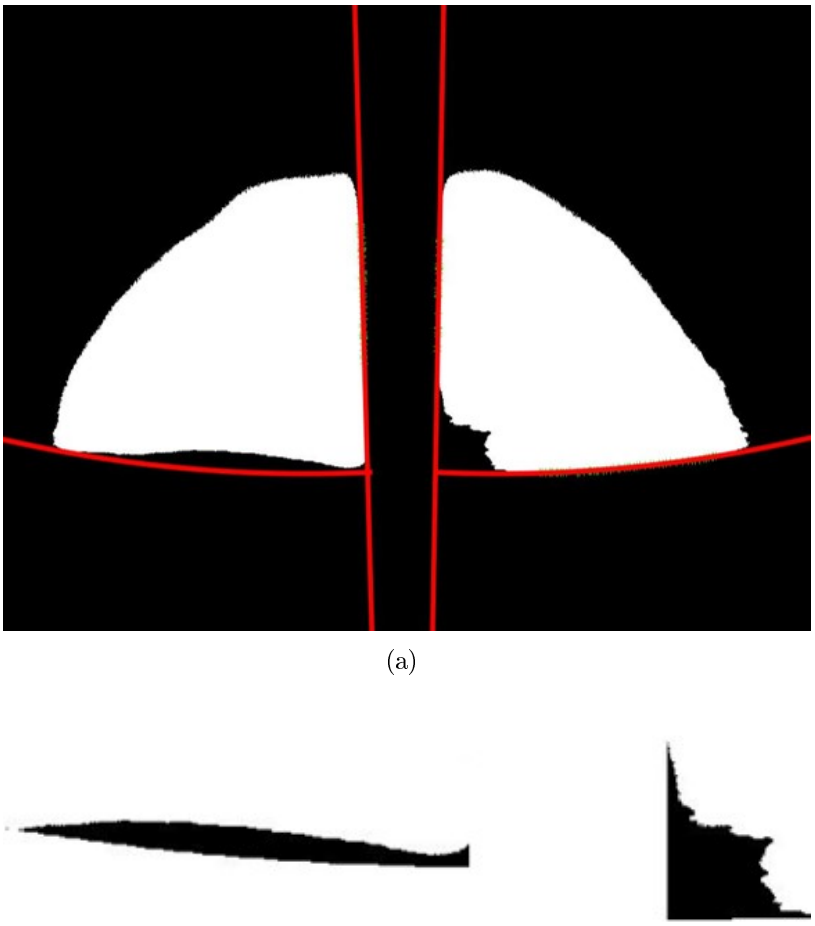

(a)

(b)

Figure 5.12: (a) Example showing how debris plumes are extracted from the image, (b) Example of the extracted debris plumes.

Finally before measurements were made a final check was performed to ensure the accuracy of this method. The extracted debris plumes were overlaid on the original images and a subtraction process was performed on the two images to see how well the plumes fit on the binary image. An example of this was shown in figure 5.13

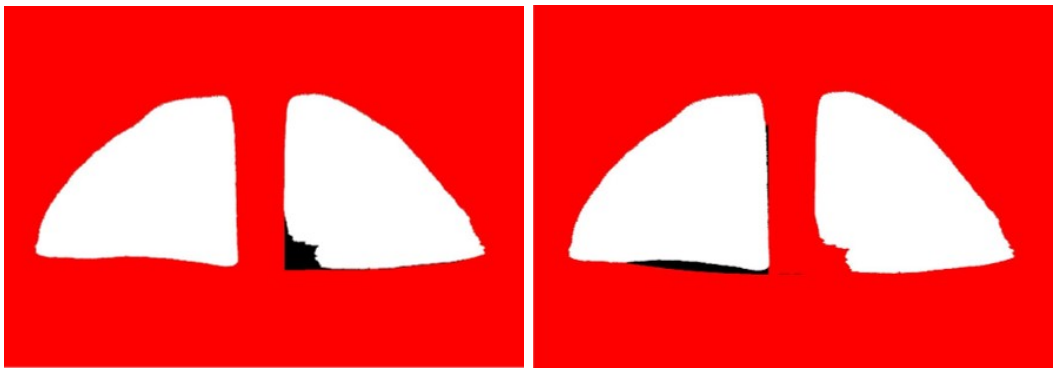

(a) (b)

Figure 5.13: (a) Image showing the difference between the extracted front plume and the binary image, (b) Image showing the difference between the extracted back plume and the binary image.

The red area in figure 5.13 was the difference between the extracte plumes and the pre-cropped binary picture. For this specific example it was obvious that high accuracy was achieved with this method in extracting the debris plumes.

After this point, measurements such as, area of the debris, the direction of the ejection and the angle it occurred, could be performed. However, the fact that some of these tests were performed on different days and at slightly altered camera positions and magnifications, needed to be considered. To allow for comparison between tests the measured areas were normalised against a known length. The most obvious known length was the width of the blade, which was 2 mm. Therefore for the first images in each test the length of the blade in pixels was normalised to 2 mm and then all the distances in the image were adjusted accordingly. This allowed comparison between tests, which were performed at slightly different conditions. These steps were then repeated in a loop for each individual image generated throughout the test.

Event based exceptions

The code described above was the general code used to analyse all the test data acquired from this set of tests. However, in some tests issues occurred during the contact making it not possible to use the generalised code, so specific processing was required for those tests. Firstly for some of the tests, there was a very high number of sparks generated during the contact. The sparks were shown in the images as very bright and overexposed pixels. As a result the data from those pixels was lost and

it was impossible to use them in any measurements. Figure 5.14 shows a sequence of 9 images captured consecutively from a test that generated a significant amount of sparks (Metco 601,RY15 82, 200 m/s, 2 μm/pass), to highlight how data was corrupted and made unsuitable for measurements. These test were not discarded because significant sparking was an interesting result by itself, so the experimental procedure could not be altered to produce less sparks. Also, as there was no way for the sparks to be removed by post processing, the analysis code was adjusted to ignore images with a high number of sparks giving an indication of how many images were lost for each test. This was only done for the small amount of tests that a high number of sparks were observed resulting in some loss of data. Even though some data was lost due to this issue, the remaining images were enough to provide the required information for the nature of the wear mechanisms.

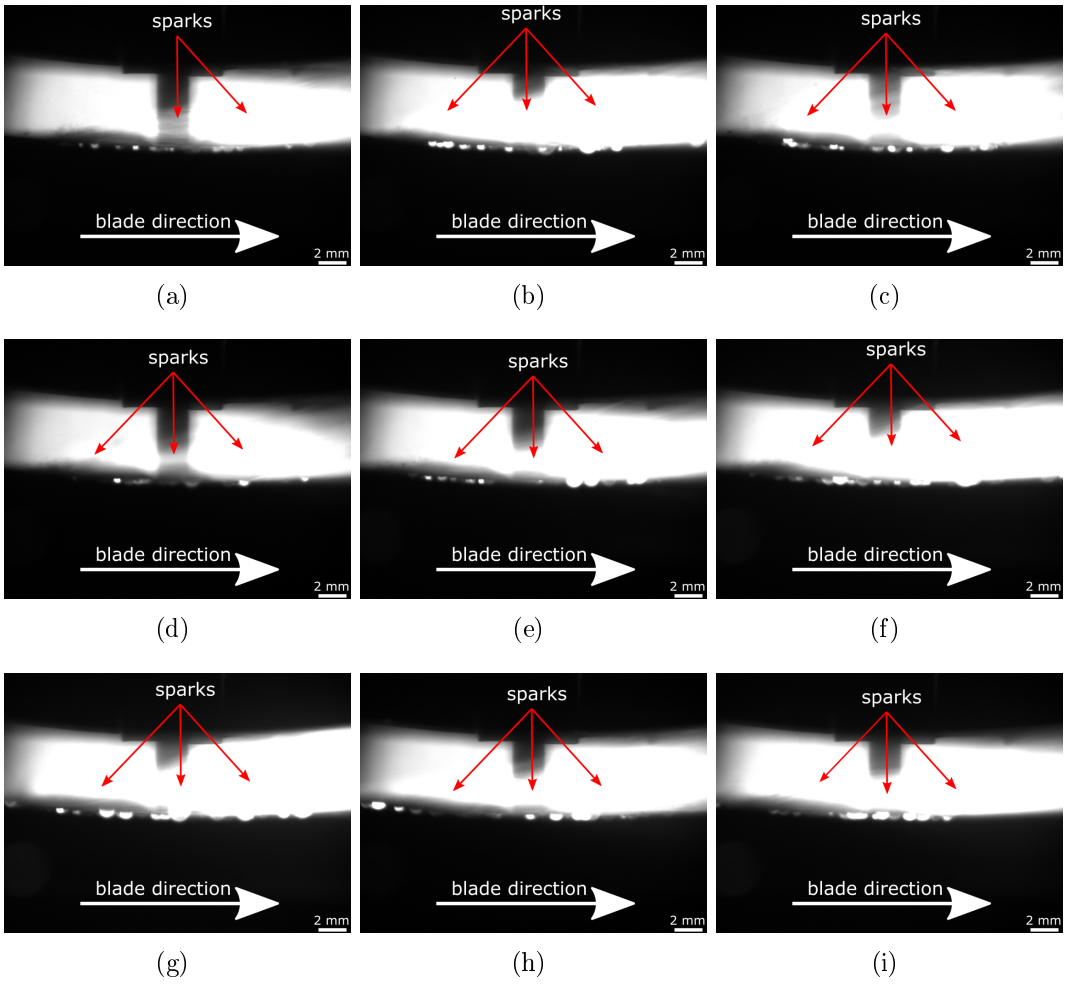

Figure 5.14: Series of 9 consecutive raw images from a sample test (Metco 601, RY15 70, 200 m/s, 2 μm/pass) showing excessive sparks. The time interval between each frame was 56 ms.

The second event based exception was observed in some tests where the material was ejected at a high height and angle as shown in figure 5.15. The material was ejected so high that it reachesd the surface of the disc, making it impossible to separate the blade from the debris, as the blade was not visible at any point of the image. To solve this problem, the analysis code had to be adjusted. The only images where the blade surface was clearly shown and it was separated from the debris, were the few images just before the contact. So for the tests where this problem was identified, instead of identifying the blade edge in each image, this was done only for the first few images before the actual contact occurred. Then the vertical lines that mapped the blade's edges were formed based on these images and were considered to be fixed for the rest of the images. Even though this was not ideal, as each individual image was slightly

offset as explained above, it was the only way to remove the blade from the images and allow measurements of the debris plume to be made. However, this exceptional case was mentioned as it was acknowledged that this introduces a small amount of error in the measurements. Having said that, it was felt that overall, the error introduced was not so significant and the data could be used in the analysis.

The tests at which the exceptions discussed in this section were observed are marked in the test matrix of this chapter in table 5.1. Tests where a high number of sparks was observed are marked with an asterisk (*), while high ejection angle issues were marked with a double asterisk (**).

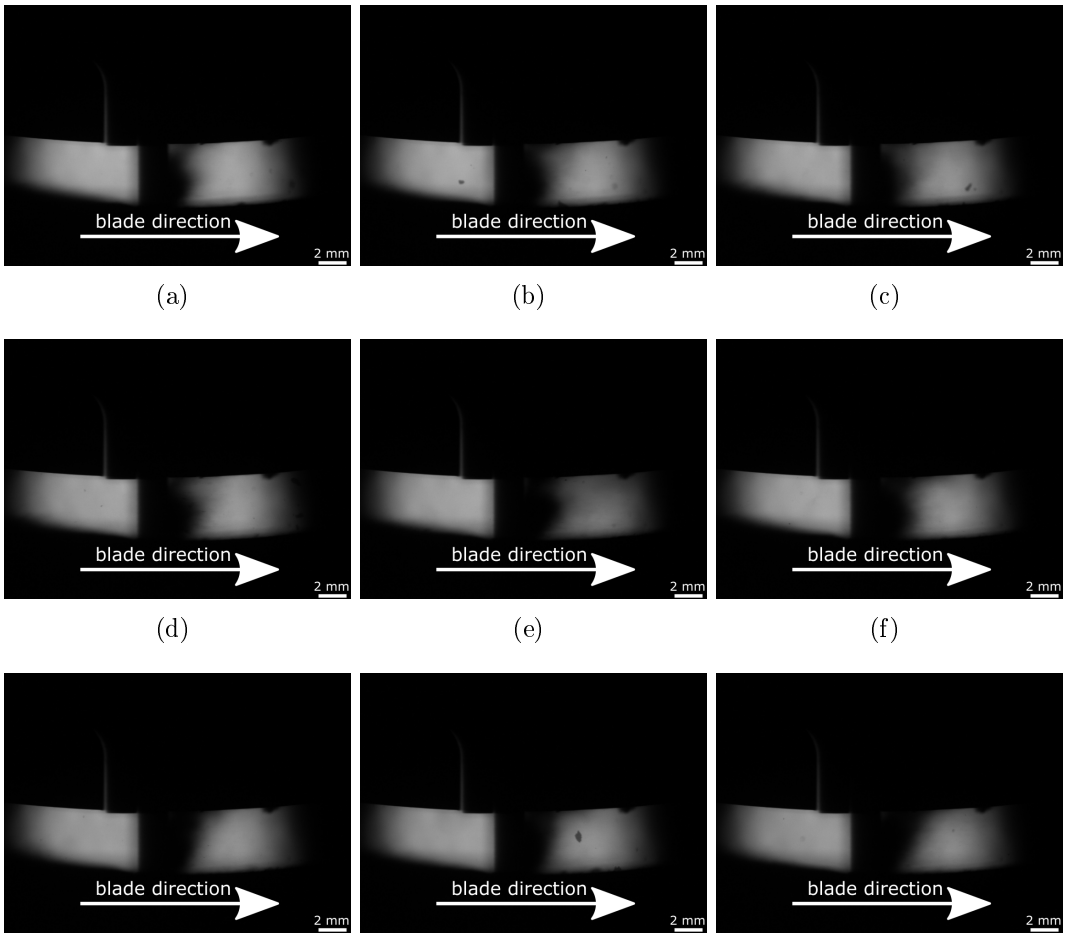

Figure 5.15: Series of 9 consecutive raw images from a sample test (Metco 320, RY15 70, 200 m/s, 2 μm/pass) showing the problem with high angle of material ejection. The time interval between each frame was 56 ms.

5.4 Results

In this section the results obtained using the techniques described above were shown. Because of the volume of the results only a few characteristic ones were shown since the rest generally follow simillar trends and patterns. A series of three raw images from all the tests that were not shown in this section is provided in appendix B.

5.4.1 Raw images

The raw images obtained from a sample test were shown in this section to provide an idea of how the raw data looked like. Figure 5.16 shows 9 consecutive images obtained from a Metco 601, RY15 55, 200 m/s, 2 μm/pass test as an example. This example was chosen because it showed clearly the debris ejected from the back and from the front of the blade and it was a good example to show these phenomena. The images shown in figure 5.16 were acquired using the stroboscopic imaging technique described in section 3.1.3 and therefore each frame represented a separate pass. The time interval between each frame was 56 ms.

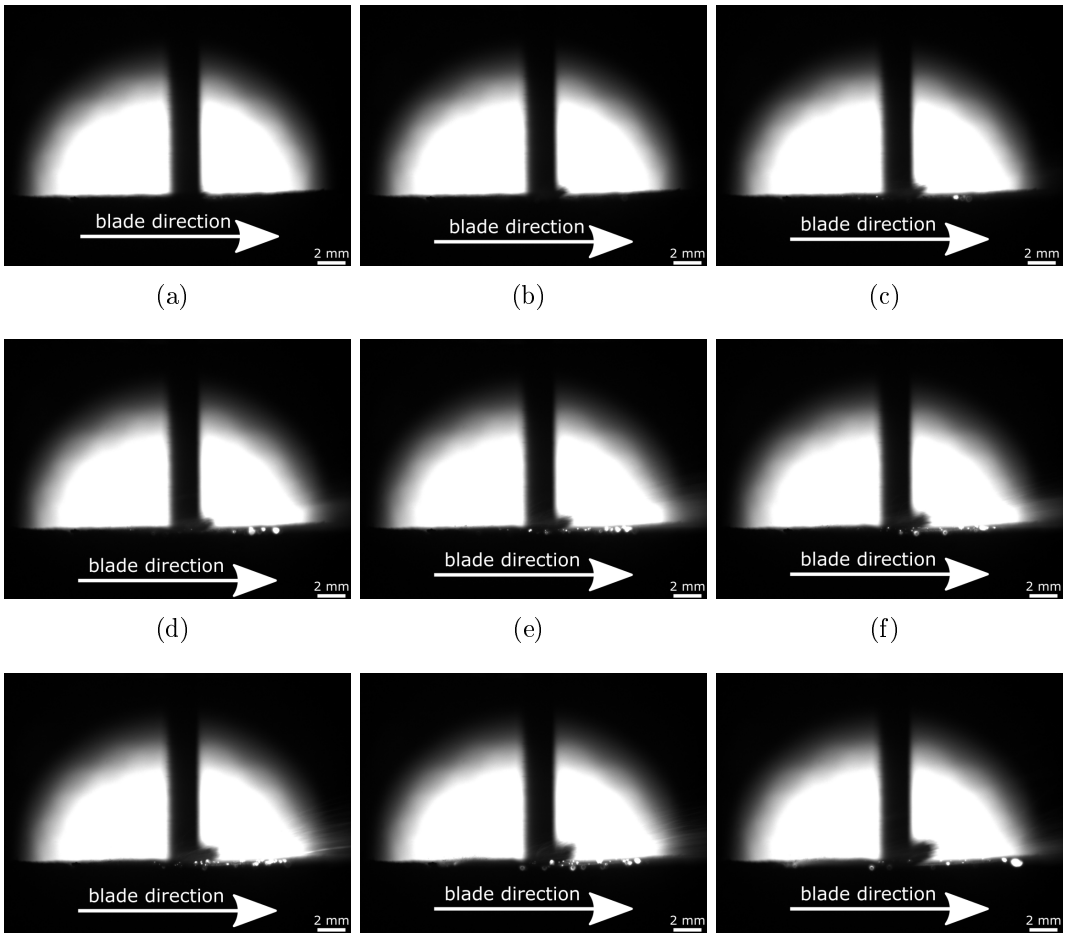

Figure 5.16: Series of 9 consecutive raw images from a sample test (Metco 601, RY15 55, 200 m/s, 2 μm/pass). The time interval between each frame was 56 ms.

5.4.2 Debris vs rub length

This section shows characteristic results obtained on the amount of debris ejection calculated as a function of acquired picture number. Figure 5.17(a) shows the results from a Metco 601 RY15 55 sample tested at 200 m/s and 0.02 μm/pass, figure 5.17(b) shows the results from a Metco 601 RY15 55 sample tested at 200 m/s and 0.2 μm/pass and figure 5.17(c) shows the results from a Metco 601 RY15 55 sample tested at 200 m/s and 2 μm/pass.

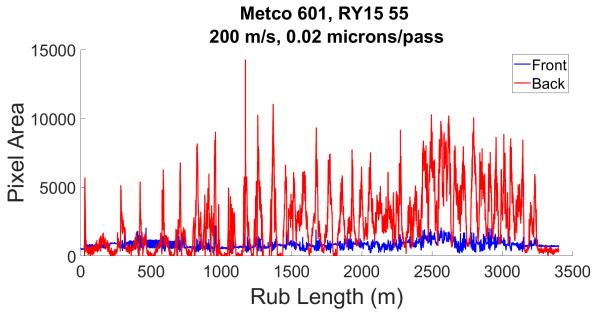

(a)

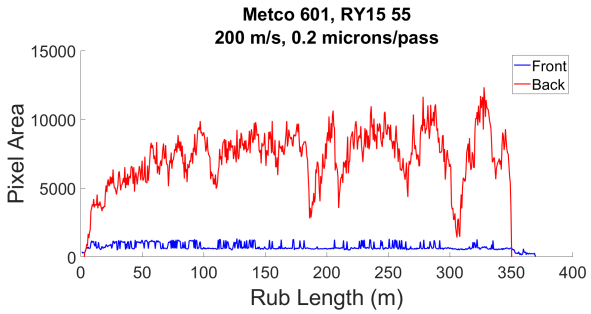

(b)

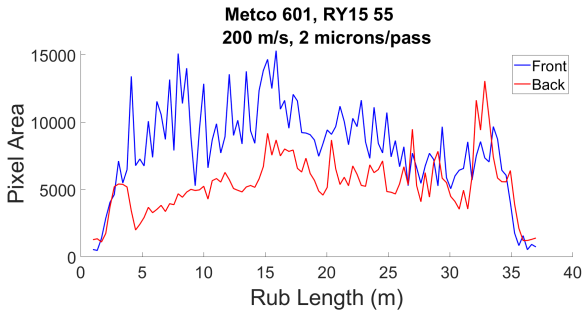

(c)

Figure 5.17: (a) Results from a Metco 601 RY15 55 sample tested at 200 m/s and 0.02 μm/pass, (b) Results from a Metco 601 RY15 55 sample tested at 200 m/s and 0.2 μm/pass, (c) Results from a Metco 601 RY15 55 sample tested at 200 m/s and 2 μm/pass

These figures show that the general trend was that the amount of the debris ejected from the back of the blade decreased with increasing incursion rate, while material ejected from the front of the blade increased with increasing incursion rate.

5.4.3 Total debris ejection

In this section the total material removed from the back and front during the whole contact period was summed and the relative percentages of each direction were calculated. Table 5.2 summarises the percentages calculated.

Then the relative percentage of the total material ejected from each direction was calculated and used to plot a 3D bar chart. This bar chart shows the variation of the relative amount of the total material removed from each direction with incursion rate and the considered material (including the different hardness values). The three incursion rates considered were plotted along the x-axis, the six materials considered (2 abradables at 3 different hardness values) were plotted along the y-axis, while the z-axis shows the relative percentage of the material that was removed from each direction.

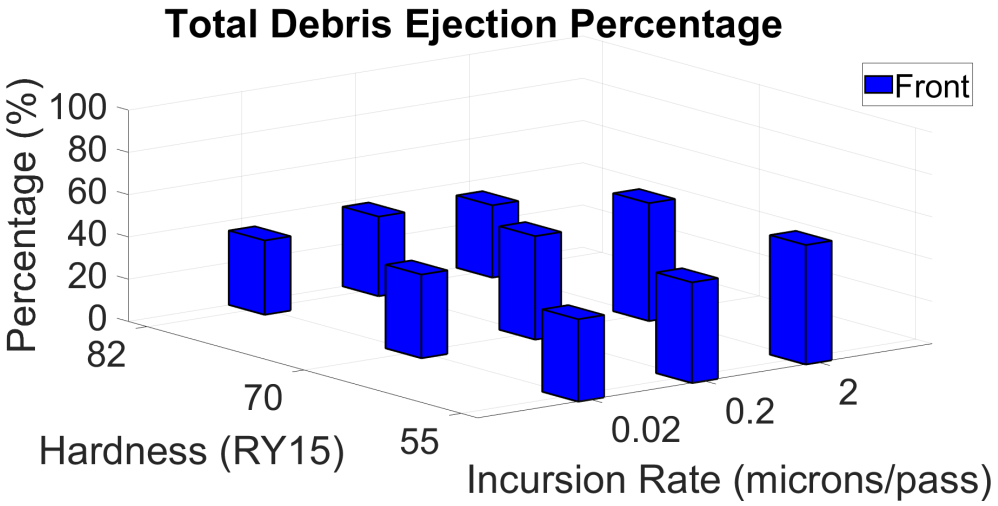

(a)

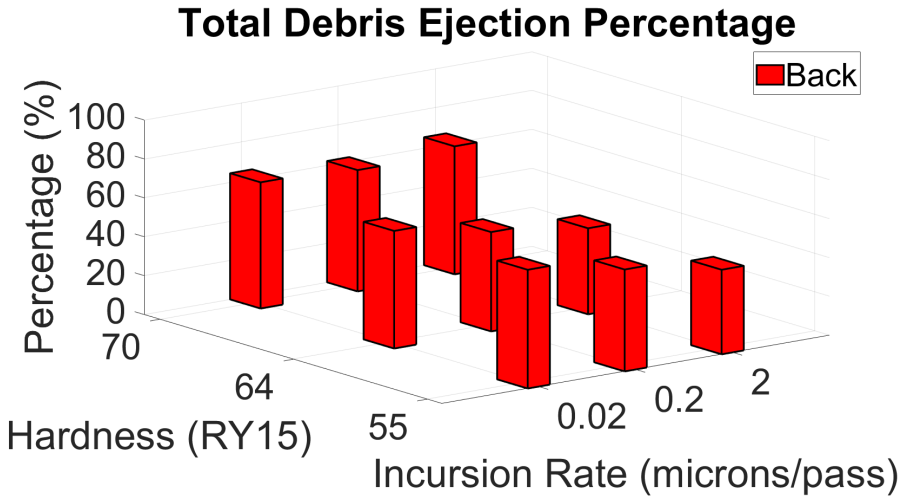

(b)

Figure 5.18: (a) Total debris ejected shown as a percentage from the front of the blade, (b) Total debris ejected shown as a percentage from the front of the blade.

By inspecting figure 5.18 (and table 5.2) a number of interesting observations could be made. Across all the considered materials and hardnesses, at the lowest incursion rate most of the material was ejected from the back of the blade. Furthermore, it could be seen that for all hardnesses, the amount of material removed from the front of the blade, increased with increasing incursion rate. This effect was much more drastic in the case of Metco 320 and especially for the high hardness case. However, there was an exception to this, which was the high hardness Metco 601 (RY15 82). At this hardness, the material removal direction did not vary a lot with incursion rate for Metco 601 and most of the material was removed from the back of

the blade. Finally, it could be observed that there was only a small variation with hardness in the direction of material removal for Metco 601 (if the high hardness is not considered), while there was a clear improvement at higher hardnesses for Metco 320. The improvement at the highest hardness was so much, that even at the lowest incursion rate, the material removed from the front was almost as much as the material removed from the back.

Table 5.2: Results from material ejection analysis showing the total percentage of material removed from each direction

Test No.	**Abradable Material**	**Hardness (RY15)**	**Incurssion Rate (microns/pass)**	**Front of Blade (%)**	**Back of Blade (%)**
1	M601	55	2	56.5	43.5
2	M601	55	0.2	47.6	52.4
3	M601	55	0.02	39.0	61.0
***4**	M601	70	2	55.8	44.2
5	M601	70	0.2	49.0	51.0
6	M601	70	0.02	39.6	60.4
***7**	M601	82	2	34.2	65.8
8	M601	82	0.2	37.7	62.3
9	M601	82	0.02	35.2	64.8
10	M320	58	2	59.5	40.5
11	M320	58	0.2	47.7	52.3
12	M320	58	0.02	32.5	67.5
****13**	M320	64	2	62.1	37.9
14	M320	64	0.2	53.0	47.0
15	M320	64	0.02	38.1	61.9
****16**	M320	70	2	70.5	29.5
17	M320	70	0.2	58.5	41.5
18	M320	70	0.02	49.0	51.0

Note: * Indicates observation of excessive sparks during the test, ** Indicates observation of very high angle of ejection during the test

5.4.4 SEM images from debris

In this section a few characteristic results from the SEM images obtained by looking at the debris collected during the testing are shown.

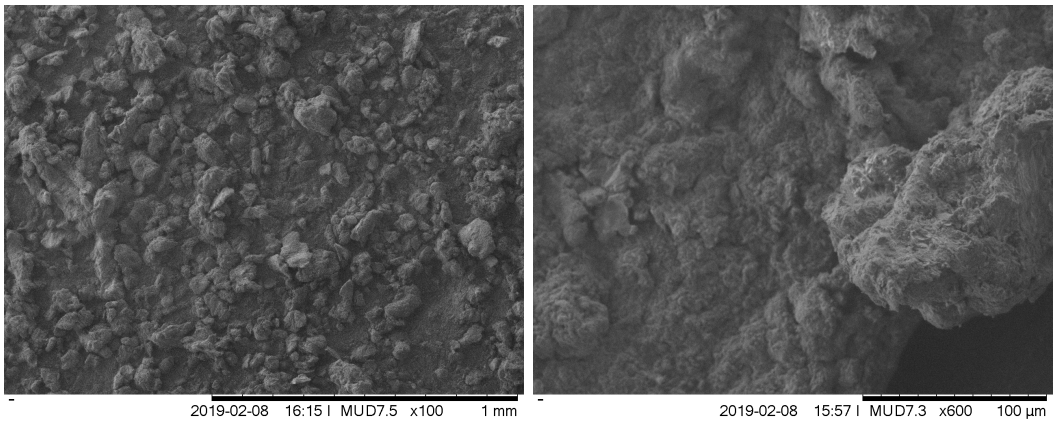

(a) (b)

Figure 5.19: (a) Characteristic examples of SEM images from debris generated during testing, (b) Characteristic examples of SEM images from debris generated during testing at higher magnification to show individual particle.

These images were used in the following sections to calculate the size and distribution of particle sizes. The size of particles was estimated by converting the SEM images to binary (5.20(b)). Then a filter was used, as shown in figure 5.20(c), which sorted the identified particles by area and then removed the smaller ones which corresponded to noise. To assess the accuracy of this and to check whether enough particles were identified to allow measurements the resulting image was overlaid to the original image. An example of this could be seen in figure 5.20(d). Finally, ellipses were fitted on top of the identified particles, as shown in figure 5.20(e) and this allowed the measuring of the major axis of the ellipses, which was equivalent to the estimated particle size.

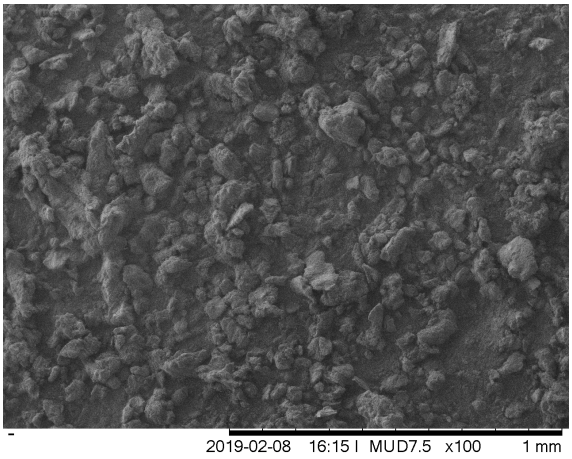

(a)

(b)

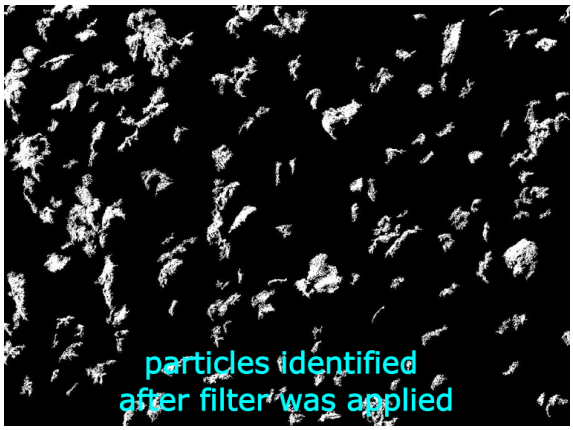

(c)

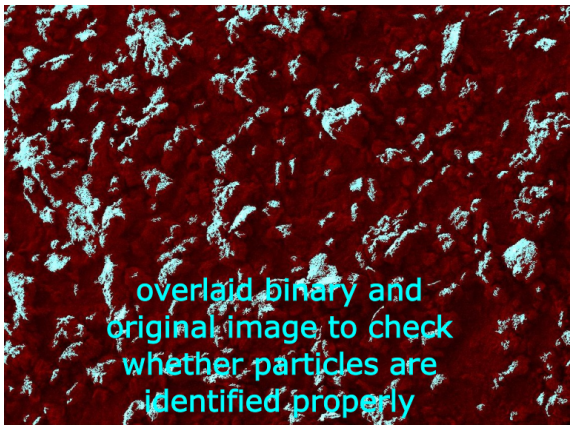

(d)

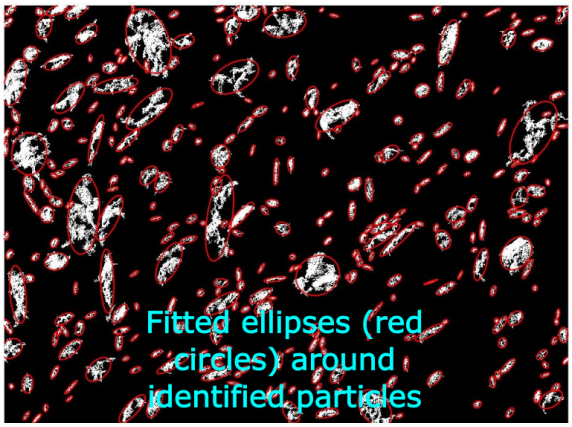

(e)

Figure 5.20: (a) Original image as obtained from the SEM, (b) Image converted to binary, (c) filter that removes noise, (d) Overlay of (b) on the original image to assess accuracy, (e) Fitting of ellipses on top of the identified particles to allow measurements.

5.4.5 Particle distribution analysis

In the introduction of this chapter (5.1) some preliminary tests were performed with a high speed camera (see figures 5.1 and 5.3). In these tests it was identified that there were particles ejected that are much larger than the size of the incursion. Examples of this could be seen in figures 5.1(k), 5.1(l), 5.3(k) and 5.3(l). The main aim of this section was to further investigate whether this was the case and to achieve this aim, debris was collected during the test and analysed as described in sections 3.6.3 and 5.4.4. After estimating the value of the particles present in a sample image (using the major axis of the fitted ellipses) a histogram was plotted to indicate the number of particles for each size. An example of this histogram was shown in figure 5.21 (obtained from the debris of a Metco 601, RY15 70, 200 m/s, 2 μm/pass). By doing this it was identified that particle sizes were larger than the incursion at all testing conditions. To ensure that this result was consistent with the range of materials and incursion rates considered, this procedure was repeated for 4 tests. The chosen tests were taken from the medium hardness of both abradables (RY15 70 for Metco 601 and RY15 64 for Metco 320). Also low and high incursion rate tests (0.02 μm/pass and 2 μm/pass) were chosen to ensure the whole range was covered. Table 5.3 provides a summary with the descriptive statistics obtained from these tests, while the histograms for the other three tests were provided in appendix C.

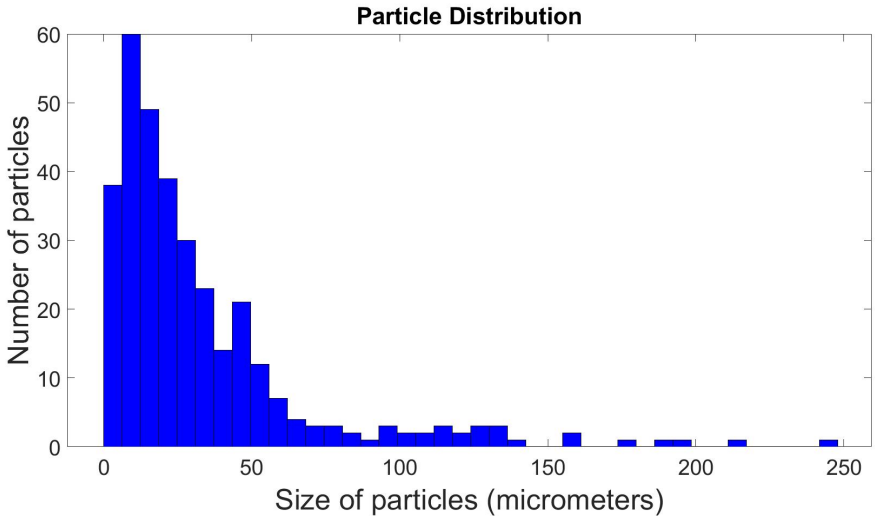

Figure 5.21: Histogram of particle distribution for a Metco 601, RY15 70, 200 m/s, 2 μm/pass sample.

Table 5.3: Summary of descriptive statistics for the particle distribution.

Test No.	Abradable Material	Hardness (RY15)	Incursion Rate (μm/pass)	Maximum Length (μm)	Mean Length (μm)	Standard Deviation (μm)
1	M601	70	0.02	247	2.78	7.84
2	M601	70	2	305	2.16	6.64
3	M320	64	0.02	30.3	3.12	3.16
4	M320	64	2	124	3.11	3.37

As shown from the histogram, for that specific test, most particles had a size between 0-50 μm with a large amount of particles having a size of more that 20 μm. Also it is worth noting that sizes in the region of 305 μm were recorded (see table 5.3). Considering the fact that the incursion rate was 2 μm/pass it became apparent that the debris generated during the contact could be much larger than the incursion per pass, which contradicted the expectation that material removed was of a similar scale to the incursion per pass. This was an interesting finding and it needs further investigation. In order to attempt and understand why this was happening, the strain fields generated in the abradable during a contact were investigated.

5.5 Discussion

The results obtained and displayed in section 5.4 were discussed in more detail in this section. In the first part of this section the chip formation and debris ejection mechanism was discussed, while the second section focused on the distribution of particle sizes from the debris collected during the tests.

5.5.1 Debris ejection analysis

As discussed in section 5.2 there is significant amount of insight that can be gained by inspecting how chips and debris were generated and where they were ejected from during a contact. The position from where material was ejected can be linked to the material removal mechanism. When material was removed after the blade passed it was an indication that the elastic compress and release removal mechanism described in section 2.2.2 took place. When material was ejected from the front of the blade it was an indication that a chip formation removal mechanism was taking place. The first step in this chapter was to measure the amount of material that was ejected

from the front and back of the blade during the contact and then plot it versus rub length to identify how did it vary during a test (examples of this can be seen in figure 5.17). Also the effect of testing conditions, such as incursion rate and hardness was considered. To this end, in order to see more clearly the progression with testing conditions, the material ejected from each direction was summed and shown as a percentage (how much was ejected from the front versus how much was ejected from the back) at a bar chart map (5.18). This map shows the relative total amount of material ejected from the front and back of the blade for the whole duration of a test, for all the testing conditions considered in this chapter, allowing conclusions to be drawn.

Variation with incursion rate

Low incursion rate (0.02 μm/pass)

The first major finding was that the chip formation and debris ejection mechanism were heavily influenced by the incursion rate. As shown in figures 5.17, 5.18 and table 5.2 at low incursion rates, for all of the materials considered, the material ejected from the back of the blade was much more compared to the material ejected from the front. This observation can be explained if the results obtained earlier in chapter 4 are considered. Firstly, figures 4.3 and 4.4 showed that the forces generated at the lowest incursion rates were much lower compared to the higher incursion rates. This suggested that the blade carried less kinetic energy during contacts such as these and as a result it did not have enough energy to form cracks and chips as it passed. Instead, the compress and elastic release mechanism described in section 2.2.2 was more dominant for these testing conditions. The blade pushed the material down, accumulating elastic potential energy, which eventually built up over a number of passes. Eventually, this compression caused enough elastic energy to chip the material and forced it to spring back behind the blade after the blade has passed. This could also be seen by the cyclic nature that these tests usually showed. This observation was in agreement with the observations made in chapter 4, where this cyclic behaviour was also displayed (see figures 4.7(a) and 4.7(b)).

Medium incursion rate (0.2 μm/pass)

As the incursion rate increased, figures 5.17 , 5.18 and table 5.2 showed that there was an increase in the amount of the material removed from the front of the blade. In most cases, during the medium incursion rate (0.2 μm/pass) the percentage of

material ejected from the front and the back was very similar. This suggested that at this incursion rate the blade had more energy and caused some cracks and chips to form and it pushed these broken chips in front of it as it was passing. However, a lot of its energy was still used to compress the material directly below it. This effectively resulted in a combination of both mechanisms to occur at the same time and the degree to which of these mechanisms was more prevalent depends on the specific material.

High incursion rate (2 μm/pass)

Finally, at the highest incursion rate (see figures 5.17(c), 5.18 and table 5.2) the blade had a lot more energy and it could form cracks and chips in front of it much more efficiently. The cracking and chip formation could be observed in figures 5.1, 5.2(a) and 5.2(b).

If we refer back to figures 4.3 and 4.4, it could be seen that much higher forces were generated during contacts at these incursion rates. It could therefore be concluded, that at these incursion rates, the blade had enough energy to form a chip of the abradable and push it in front of it, producing an efficient cutting mechanism. Some of its energy was still used to compress the material under it (some material was still ejected from the back), but at these incursion rates the predominant mechanism was the chip formation cutting mechanism. The observations made in this study agree with findings of previous research [7, 9, 37, 39]. The additional value provided by this analysis was the fact that the actual debris ejection could be seen while it was happening. Therefore it was no longer an assumption, but instead an observation.

Variation with hardness

The second important information that could be gained by analysing the data presented in this chapter was how the material removal mechanism varied with the hardness for each abradable.

Metco 320

The material removal mechanism observed changed significantly with hardness in the case of Metco 320. Figure 5.18 clearly shows that the amount of material ejected from the front of the blade increased progressively at higher hardness values at each and every incursion rate. This became increasingly important when the case of the highest hardness sample was considered. In this case, even at the lowest incursion

rates, which were shown to be the worst conditions to operate Metco 320, the amount of material ejected from the front was about the same as the material ejected from the back (49 Vs 51%, see figure 5.18). This observation highlighted that at this hardness (RY15 70), even at the worst incursion rate conditions, which were an unwanted operating region for Metco 320, the blade could still create some cracks and chips and pushed them as it passed through during the contact. This suggested that there was an almost equally contributing combination of wear mechanisms occurring at these conditions (compress and elastic release, cutting). However, the compress and release mechanism became more and more predominant for the lower hardness Metco 320. This could be inferred by inspecting 5.18), where it could be seen that material removed from the back of the blade increased drastically for all incursion rates. It could therefore be concluded that even though the nature of the material removal mechanism was mostly governed by the incursion rate, in the case of Metco 320 the hardness affected the material removal mechanism to an extend. This effect could be explained by the high variability of the hBN phase present at the different hardness values. Lower hardness samples had higher concentrations of hBN, which has very bad thermal conductivity properties. This created regions in the abradable where heat was not propagated efficiently and if these regions were not removed by the blade (for example in the case of low incursion rates where the blade did not have enough energy to form cracks and chips effectively) heat was accumulated with consecutive blade passes and resulted in an unwanted wear mechanism (high adhesion and even blade wear). Contrary to this, at the highest hardness, the concentration of hBN was much less resulting in a better dissipation of the heat generated from the contact. This was why at the highest hardness (RY15 70), even at the lowest incursion rate (0.02 μm/pass), where the blade did not have enough energy to consistently form cracks and chips at every pass, the resulting wear mechanism was not as severe as in the case of the lower hardness samples. This finding fits the results in the literature very well since similar outcomes were identified by Fois, since his wear map showed that there was an improvement in the performance of Metco 320 with increasing hardness at all testing conditions [15, 42, 41, 40]. However, it must be emphasised, that the incursion rate defined what the wear mechanism was and increasing hardness just improved its severity.

Metco 601 RY15 55 and 70

In the case of Metco 601 there were two very different output regions and therefore these were considered separately. The first region was the two lower hardness samples

(RY15 55 and 70). In the case of these samples it seemed that the resulting wear mechanism did not change drastically with hardness as the percentage of material ejected from the front and back of the blade was similar for these materials at a given incursion rate (see figure 5.18), suggesting that the wear mechanism was mostly driven by the incursion rate at these hardness values. This was an important difference in respect to Metco 320 and the reason why this was happening can be attributed to the polyester phase present in Metco 601. The polyester phase was much less clustered throughout the abradable, unlike the much bulkier hBN and this resulted in a more even heat dissipation during a contact. This had as a result that the wear mechanism was predominantly governed by whether the blade had the ability to create cracks and remove the material (incursion rate). However, the polyester phase in Metco 601 was much more distributed in the abradable micro-structure compared to the hBN phase in Metco 320. This provided a degree of release mechanism irrespective of the concentration of the phase in the material (lower hardness had more polyester phase).

Metco 601 RY15 82

This observation changed for the highest Metco 601 hardness considered (RY15 82). Like shown previously in this investigation at this hardness the performance of the abradable became significantly worse. As shown in figure 5.18 the majority of the material was ejected from the back of the blade across all incursion conditions at this hardness. In this case, it seemed that the concentration of the polyester phase was so low that the blade did not have the required energy to crack and chip it even at the highest incursion rate conditions. This resulted in the blade constantly rubbing across the surface of the abradable instead of cutting it, generating so much heat and high forces that eventually damaged the blade causing blade wear and this was why most of the material was ejected from the back of the blade. Therefore it could be concluded that at this high hardness, for Metco 601, the wear mechanism was totally controlled by the fact that there was not enough polymer phase to facilitate crack and chip formation.

5.6 Conclusion

The aim of this chapter was to observe the point of contact between a blade and an abradable and to examine the way material was removed, in order to gain a better

understanding of the material removal mechanism that took place. Also the size and distribution of the debris generated from such a contact was investigated in this chapter. The findings of this chapter were summarised below:

- Ejected particles much larger than the incursion per pass for all incursion rate conditions were identified
- For both materials considered (Metco 601 and Metco 320) the material ejection mechanism was governed by incursion rate. At low incursion rates most of the material was ejected from the back of the blade (suggesting a compress and release wear mechanism), while as incursion rate increased more material was ejected from the front (suggesting a chip formation and cutting mechanism).
- In the case of Metco 320 hardness had a significant effect on the resulting mechanism. At the low hardness samples the amount of material ejected from the back was much more compared to the highest hardness. At the highest considered hardness the material removed from the back of the blade was about the same as the material removed from the front of the blade even at the worst incursion rate conditions (0.02 μm/pass), suggesting that increasing hardness helped the wear mechanism to move into a more favorable region.
- For Metco 601 the material hardness had very little effect on the direction that material was removed, suggesting that it had little effect on the resulting wear mechanism. In this case the wear mechanism was much more influenced by the incursion rate.

Using the findings made from this chapter, the next step in this investigation was identified. The next chapter inspected the abradable during the contact, to identify regions where tensile and compressive strain fields were generated in the abradable. The aim was to identify how different abradables respond at different conditions of tensile and compressive field generation and attempt to link these to crack and chip formation. In this chapter some crack and chip formation was identified and the next chapter expanded on that. Also it aimed to explain why particles of much larger size than the incursion per pass were found.

Chapter 6

Compressive/Tensile Field Generation

6.1 Introduction

In the previous chapter the amount of material removed from the front and the back of the blade, as well as the particle size distribution was examined. The aim of this chapter was to move a step deeper and examine how this ejected material was generated. This was achieved by looking at the structure of the side of the abradable (along the contact) for the duration of the contact. This allowed the investigation of how cracks were formed and how material was removed while the contact was happening. Moreover, it allowed for DIC to be performed at consecutive images in order to examine the tensile and compressive strain fields that were generated during the contact and try to link that to the material removal mechanism.

6.2 Methodology and materials

Like in the previous sections, this section discussed the choice of materials that were considered for these experiments.

6.2.1 Materials

Like chapter 5 this chapter's main aim was to try and explain the differences in behaviour of the two considered abradables (Metco 601 and Metco 320). At the same time, as previously, the effect of material hardness needed to be considered and

assessed. Consequently, for these tests, samples of both Metco 601 and Metco 320 were prepared, each with three different hardness values. For Metco 601 hardness values of RY15 55, RY15 70 and RY15 82 were used, while for Metco 320 the hardness values were RY15 58, RY15 64 and RY15 70. Since the aim was to observe the structure of the abradable during the contact, milled, thinner samples were used for this set of tests as well (see section 5.3.1 and figures 5.6 and 5.8). The material for the blade was the standard Titanium alloy used throughout this investigation (see section 3.2.2).

6.2.2 Test conditions and test matrix

The test matrix in this chapter was identical to the one used in the previous chapter (see table 5.1). The test matrix of the last chapter was replicated, because given the clear differences in the material removal mechanisms observed, it was essential to further investigate these observations in order to explain them. This included one blade tip speed (the highest possible to achieve with the test rig), three incursion rates, which cover the operational range of actual engines, the 2 different abradable materials under investigation (Metco 601 and Metco 320) and three hardnesses for each material. This test matrix allowed the assessment of the effect that the test conditions and material choice had on the observed performance.

6.2.3 Experimental set-up and procedure

This set of tests was performed on the experimental test rig described in section 3.1, with the same equipment and set-up, other than some modifications that allowed for the monitoring of the side of the abradable during the contact. In this section, the modifications on the standard set-up were described.

Imaging technique

For the purposes of the experiments performed in this chapter, the aim was to observe the abradable below the surface during the contact. To achieve this, the camera was moved just below the contact and focused on the exposed side of the abradable. Furthermore, since the aim was to observe the side of the abradable, this side had to be properly illuminated. Consequently, there was a need to move the position of the LEDs so that they illuminated this surface. Therefore, a new LED holder was

manufactured, which had two LEDs and a gap in the middle. This configuration ensured that the side of the abradable observed by the camera was properly illuminated, while the gap in the middle allowed the camera to observe without any obstructions. A schematic showing this configuration was shown in figure 6.1. This set-up allowed very good quality pictures of the side of the abradable to be taken, which in turn could be used to perform the DIC analysis as planned.

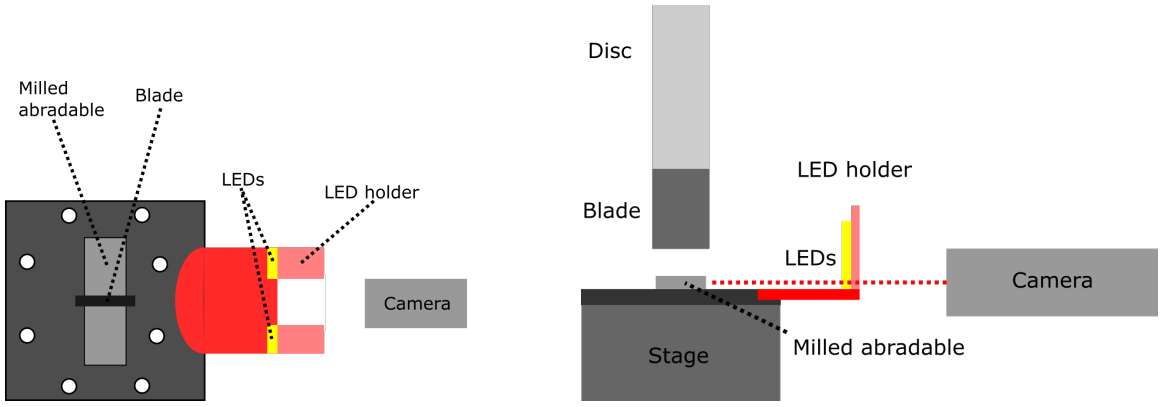

(a) (b)

Figure 6.1: (a) Schematic showing the configuration of the experimental set-up from the top view,(b) Schematic showing the configuration of the experimental set-up from the side view

Finally an updated test rig schematic, including all the changes on the standard experimental set-up, was provided in figure 6.2

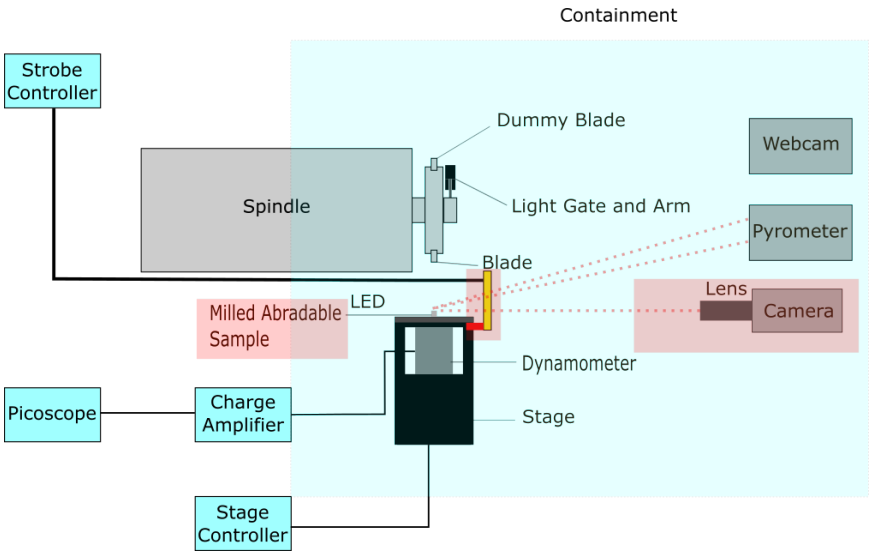

Figure 6.2: Schematic of the updated test rig set-up for test carried out for this chapter, from the side (not to scale).

Experimental testing procedure

The experimental testing procedure followed was identical to the standard procedure described in section 3.4, with the only difference being the nature of the captured images (side of the abradable instead of blade at the top). This was a stroboscopic imaging technique, where images of the blade were captured at the same point after a few revolutions. This allowed the observation of how the abradable was changing after a few passes of the blade, by focusing on the side of the rub. It should be highlighted that each image taken was from a different pass. Emphasis was given to achieve the highest image quality possible, as this was essential in the accuracy of the data post-processing. To achieve the highest image quality possible, several preliminary tests were performed to identify the most appropriate camera settings to be used (such as exposure time). The data obtained from these tests consisted of images of the side of the abradable for every several strikes, as well as force and temperature data.

6.2.4 Data post-processing

The analysis of the data was divided into two parts. The first part was a visual inspection of the images to identify how cracks were formed, analysing their size and frequency throughout the contact. Also this allowed the examination of how

material was removed from the surface of the abradable and how the sub-surface was affected by the contact. The second part was the DIC analysis. Digital image correlation (DIC) is a non-contact experimental technique that is used to measure full field displacements and subsequent strains. This technique works by identifying features on an images and then tracking the relative displacements of these features on subsequent images [103, 104, 105, 106, 107, 108]. The algorithm then uses these identified displacements to calculate strain fields. For this study an existing open source DIC MATLAB software called Ncorr was used [109]. Previous studies have assessed the performance of this algorithm against other commercial DIC algorithms and they found good agreement with the two different software making Ncorr a nice freely available tool for such analysis [110]. This software was used since the aim of this thesis was not to create a DIC analysis methodology, but rather to use this tool in an attempt to achieve a better understanding of the performance of the materials under investigation. The software took as an input consecutive raw images captured from the cameras and provided an output of the strains that it calculated, overlaid on the pictures. This allowed to observe the development of tensile and compressive strain fields on the surface and sub-surface of the abradable, which were caused from the contact.

Exceptions to standarised processing

Unfortunately, as in the previous chapter, the data for some of the tests could not be examined and processed due to excessive sparking of the material during the contact that completely over-saturated the images. An example of this was shown in figure 6.3 which was obtained from a Metco 601, RY15 70, 200 m/s, 2 μm/pass test. To rectify this, in the tests where high sparking was observed, the over-saturated images were excluded from the analysis. As a result, the available data for some incursions was reduced significantly, but at least enough data for partial analysis was acquired for all the test (this challenge was only faced for two tests).

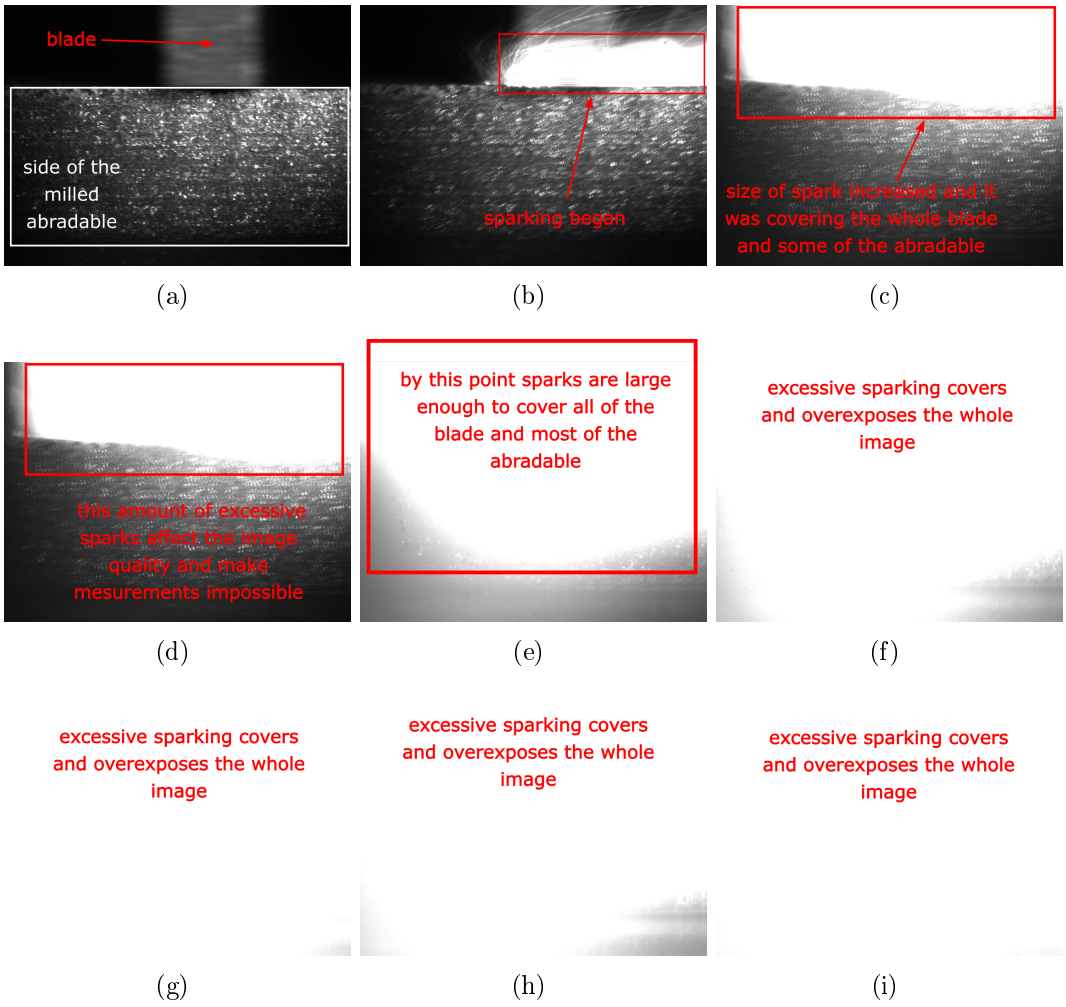

Figure 6.3: Series of 9 consecutive raw images from a sample test (Metco 601, RY15 70, 200 m/s, 2 μm/pass) that show excessive sparks. The time interval between each image was on average 56 ms and each image shows a different pass.

6.2.5 DIC algorithm

In this section a description of the steps taken by the DIC algorithm (Ncorr) for performing the DIC analysis was provided. The first step in the analysis was to identify a reference image and a current image. These were the two images that the algorithm would compare to identify displacements and strains. Two consecutive images obtained during the testing were selected as the reference and current images for this analysis. The second step was to draw a region of interest (ROI) on the images at the areas where DIC analysis was to be performed. This step reduced the amount of data processed (and in effect processing time) by only considering the relevant parts of the images. In this study the region of interest was the abradable so

the ROI was drawn over it. Next the parameters for the DIC analysis needed to be set. This was the most important step as it had a great effect on the accuracy of the results. The two most important parameters to consider were the radius and spacing of the subsets. This algorithm works by dividing the ROI in a number of subsets. It then tracks these subsets from the reference image to the current image measuring the deformations and assuming these are uniform inside each subset [109]. In general, the way to achieve the highest analysis accuracy was to ensure that the smallest subset radius and spacing was used, as long as no noise was created (smaller radii create more noise as larger radii tend to have a smoothing effect [109]). After several preliminary iterations, for the purposes of this study, all the tests were done using a subset radius of 15 pixels (minimum 10 and maximum 60 pixels) and a subset spacing of 0 pixels (minimum 0 and maximum 10 pixels). Another parameter that needed to be set for the analysis was the number of iterations required until the correlation criteria were satisfied. This was always set to maximum (100 iterations) to ensure enough iterations were always performed, despite this increasing the required processing time. After the DIC parameters were set the next step was to select the region where DIC would be performed (the ROI) and set the seeds. Seeds are initial guessing points for the algorithm to begin its analysis. They also provide partitioning of the ROI depending on the amount of threads available (4 threads were available for this study) allowing parallel processing of these partitions and decreasing the processing time. The seeds should be placed in such a way as to partition the ROI evenly and always be in the ROI's range. Also they should be positioned around regions where high strain was expected. To satisfy these criteria the 4 available seeds where placed near the surface of the abradable (where higher strains were expected) and arranged in equal spacing across the ROI. Then the algorithm was executed and the displacements were calculated. The resulting displacements were then converted from pixels to mm and finally the strains were also calculated. This methodology was used for all the tests that were shown in section 6.3.2.

6.3 Results

In this section characteristic results obtained from testing and analysis were presented. Because of the volume of results only characteristic samples were shown in this section, since the rest of the results had a simillar pattern. The images from the tests not shown in this section were provided in appendix D.

6.3.1 Raw Images

Examples of the raw images obtained from the testing in this chapter were displayed in this section. These images were later used for visual observation of crack and chip formation in the abradable during the contact and also as an input for DIC measurements. The images shown in this section were taken using the stroboscopic technique described in section 3.1.3 and therefore each image represented a different pass. The time interval between each image varied depending on how many passes were needed for the specific event to take place so this was stated separately for each example.

High hardness Metco 601

Figure 6.4 shows a series of images acquired from a high hardness Metco 601 tested at a medium incursion rate (Metco 601, RY15 82, 200 m/s, 0.2 μm/pass). Firstly in figure 6.4(a) is an image taken just before the contact started and it shows how the abradable looked before the contact. Next, by inspecting figure 6.4(b) two interesting observations could be made. The first one was the fact that there was evidence of blade wear. This could be said as there was an overhang (red box) of the blade above the abradable meaning the surface of the abradable was above the initial level of the blade. As explained in figure 5.8 the blade overhung the abradable by 1 mm on each side, so the 1 mm flanks did not rub and they remained at their original level and state. Therefore, since these flanks could be seen in the images, the conclusion that the blade had worn could be made. The second interesting observation was that there was very little material removal observed. Instead it could be seen that there was a region where the material had deformed (compressed) but not removed (white box area). This image was taken 16.35 s after the first image (which was taken just before contact initiated), meaning that for all that time (for these testing conditions it was almost half of the test) no significant amount of material was removed. Figure 6.4(c) shows an image where the first crack appeared during the test (red circle) and this initiated 7.36 s after the previous image. After this, several more cracks started forming (red circles) soon after, as shown from figure 6.4(d) (image taken 0.432 s after the previous image). Then, after 0.342 s had passed, one of the cracks started propagating and becoming larger (red circle on figure 6.4(e)). Finally, after 0.287 seconds a chip was formed at the place where the large crack had formed and propagated and some material was removed (figure 6.4(f)). Figures 6.4(g), 6.4(h),

6.4(i) show enlarged versions of figures 6.4(d), 6.4(e), 6.4(f) respectively, which were magnified 2.5 times to show more clearly the areas of interest.

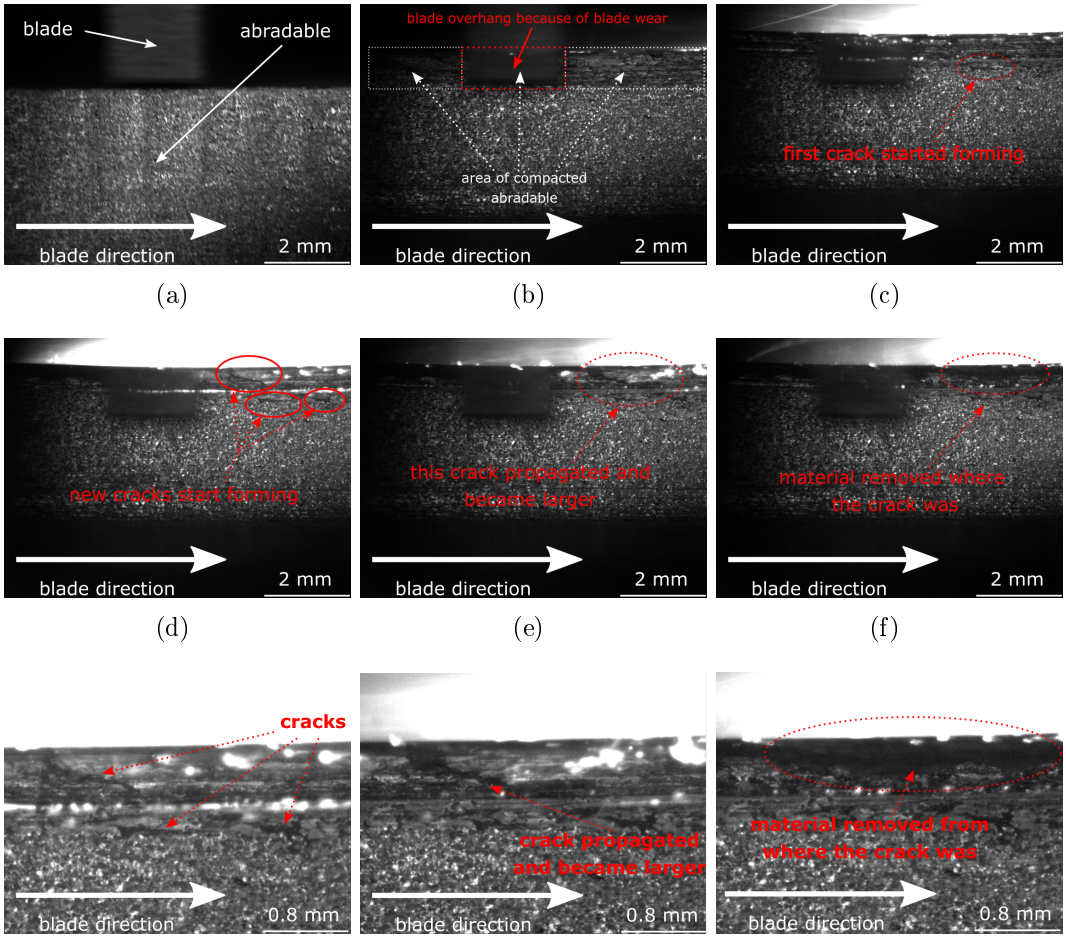

Figure 6.4: Series of images from a Metco 601, RY15 82, 200 m/s, 0.2 microns/pass test. (a) Image showing how the abradable was before the contact, (b) Image showing the abradabe and blade taken 16.35 s after image (a), (c) Image showing the abradabe and blade taken 7.36 s after image (b), (d) Image showing the abradabe and blade taken 0.432 s after image (c), (e) Image showing the abradabe and blade taken 0.342 s after image (d), (f) Image showing the abradabe and blade taken 0.287 s after image (e), (g) Image showing an enlarged area around the crack from image (d) (2.5 magnification), (h) Image showing an enlarged area around the crack from image (e) (2.5 magnification), (i) Image showing an enlarged area around the removed material from image (f) (2.5 magnification).

Metco 601, low incursion rate (0.02 μm/pass)

Figure 6.5 shows a series of images taken from a Metco 601 RY55 sample tested at 0.02 μm/pass and 200 m/s. As shown in this figure, after a large number of passes cracks started forming (figure 6.5(b)). These cracks continued to enlarge and join together (figures 6.5(d) and 6.5(d)) until a chip was formed (figure 6.5(e)). A separate chip was formed over several passes on a different location and this is shown in figure 6.5(f). Finally figures 6.5(g), 6.5(h) and 6.5(i) show enlarged versions of figures 6.5(d), 6.5(e) and 6.5(f). There were magnified 2.5 times to show more clearly the regions of interest. This behaviour (crack formation over a large number of passes) was typical for all the samples tested at low incursion rate conditions (for both abradables considered).

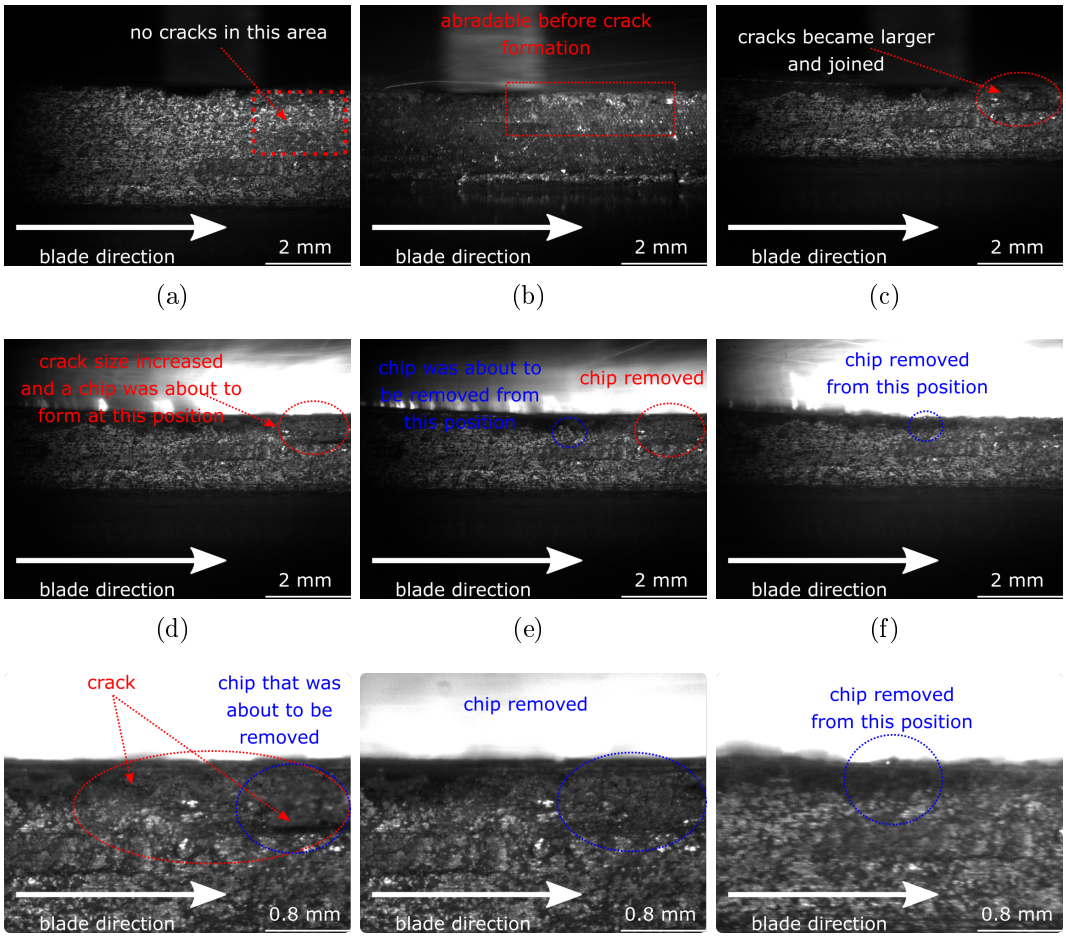

Figure 6.5: Series of images from a Metco 601, RY15 55, 200 m/s, 0.02 microns/pass test. (a) Image showing how the abradable was before any cracks in that region, (b) Image showing the abradabe and blade taken 125.3 s after image (a), (c) Image showing the abradabe and blade taken 70.4 s after image (b), (d) Image showing the abradabe and blade taken 4.5 s after image (c), (e) Image showing the abradabe and blade taken 0.047 s after image (d), (f) Image showing the abradabe and blade taken 10.4 s after image (e), (g) Image showing an enlarged area from image (d) (2.5 magnification), (h) Image showing an enlarged area from image (e) (2.5 magnification), (i) Image showing an enlarged area from image (f) (2.5 magnification).

Metco 320, low incursion rate (0.02 μm/pass)

Figure 6.6 shows a series of images taken from a Metco 320 RY15 58 sample, tested at 0.02 μm/pass and 200 m/s. This figure shows an example where material was compressed over several passes before it cracked and was removed. This was shown in figures 6.6(b) and 6.6(e) where the abradable in the region of interest (red box)

was pushed downwards in the abradable and cracks were formed around this region. After several passes this led to break-off at that region as shown in figures 6.6(c) and 6.6(f). Again this was a typical behaviour of the samples tested at low incursion rate conditions.

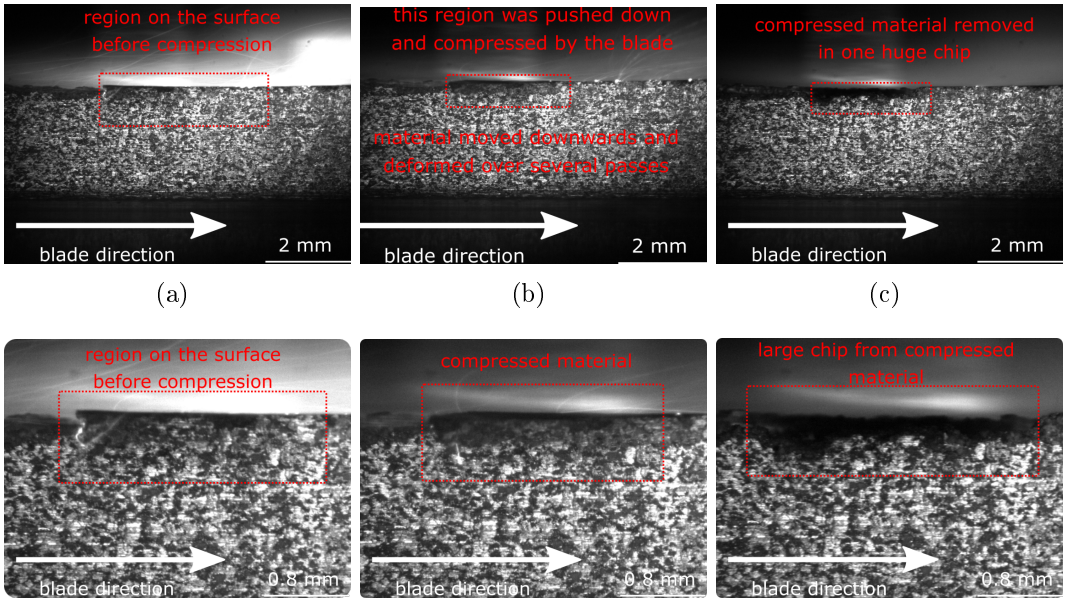

Figure 6.6: Series of images from a Metco 320, RY15 58, 200 m/s, 0.02 microns/pass test. (a) Image showing how the abradable was before any cracks in that region, (b) Image showing the abradabe and blade taken 117.2 s after image (a), (c) Image showing the abradabe and blade taken 48.8 s after image (b), (d) Image showing an enlarged area from image (a) (2.5 magnification), (e) Image showing an enlarged area from image (b) (2.5 magnification), (f) Image showing an enlarged area around the removed material from image (c) (2.5 magnification).

Metco 601, high incursion rate (2 μm/pass)

Figure 6.7 shows a series of images taken from a Metco 601 RY15 55 sample, tested at 2 μm/pass and 200 m/s. This figure was a typical example of high incursion rate conditions for both abradables considered. Cracks were formed (figures 6.7(b) and 6.7(e)) and chips were broken off (figures 6.7(c) and 6.7(f)) after only a very small amount of passes.

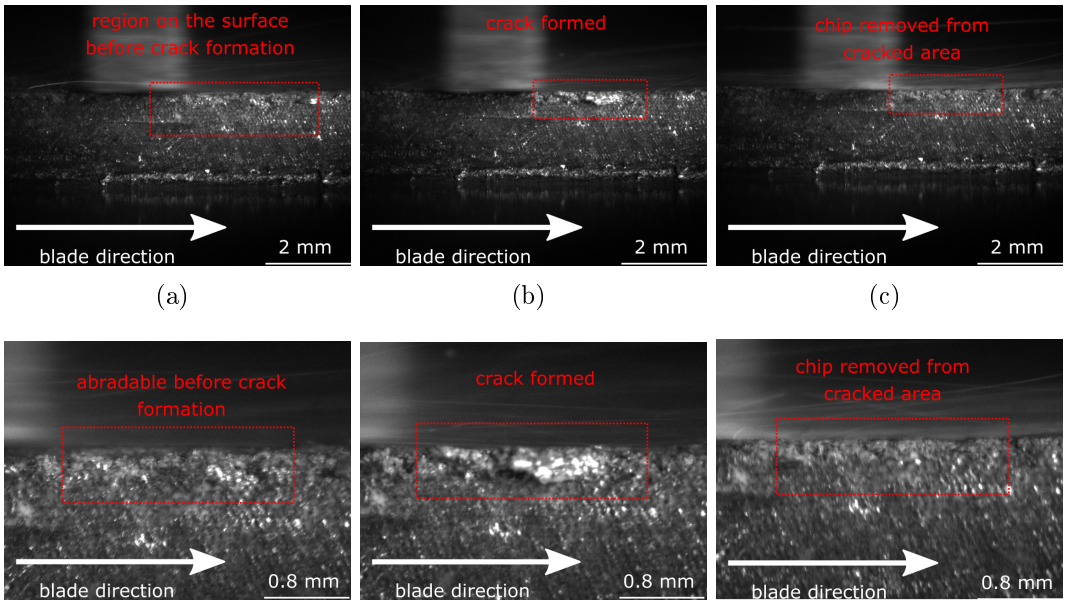

(a) (b) (c)

(d) (e) (f)

Figure 6.7: Series of images from a Metco 601, RY15 55, 200 m/s, 2 microns/pass test. (a) Image showing how the abradable was before any cracks in that region, (b) Image showing the abradabe and blade taken 0.144 s after image (a), (c) Image showing the abradabe and blade taken 0.217 s after image (b), (d) Image showing an enlarged area from image (a) (2.5 magnification), (e) Image showing an enlarged area from image (b) (2.5 magnification), (f) Image showing an enlarged area around the removed material from image (c) (2.5 magnification).

Metco 320, high incursion rate (2 μm/pass)

Figure 6.8 shows a series of images taken from a Metco 320 RY15 58 sample, tested at 2 μm/pass and 200 m/s. A crack formation and chip removal mechanism similar to figure 6.7 was shown in this figure. Large cracks formed (figures 6.8(b), 6.8(c), 6.8(d) and 6.8(g)) after a very small amount of passes resulting in the creation of chips, which were removed very frequently by the passing blade (figure 6.8(c), 6.8(e), 6.8(f), 6.8(h) and 6.8(i)).

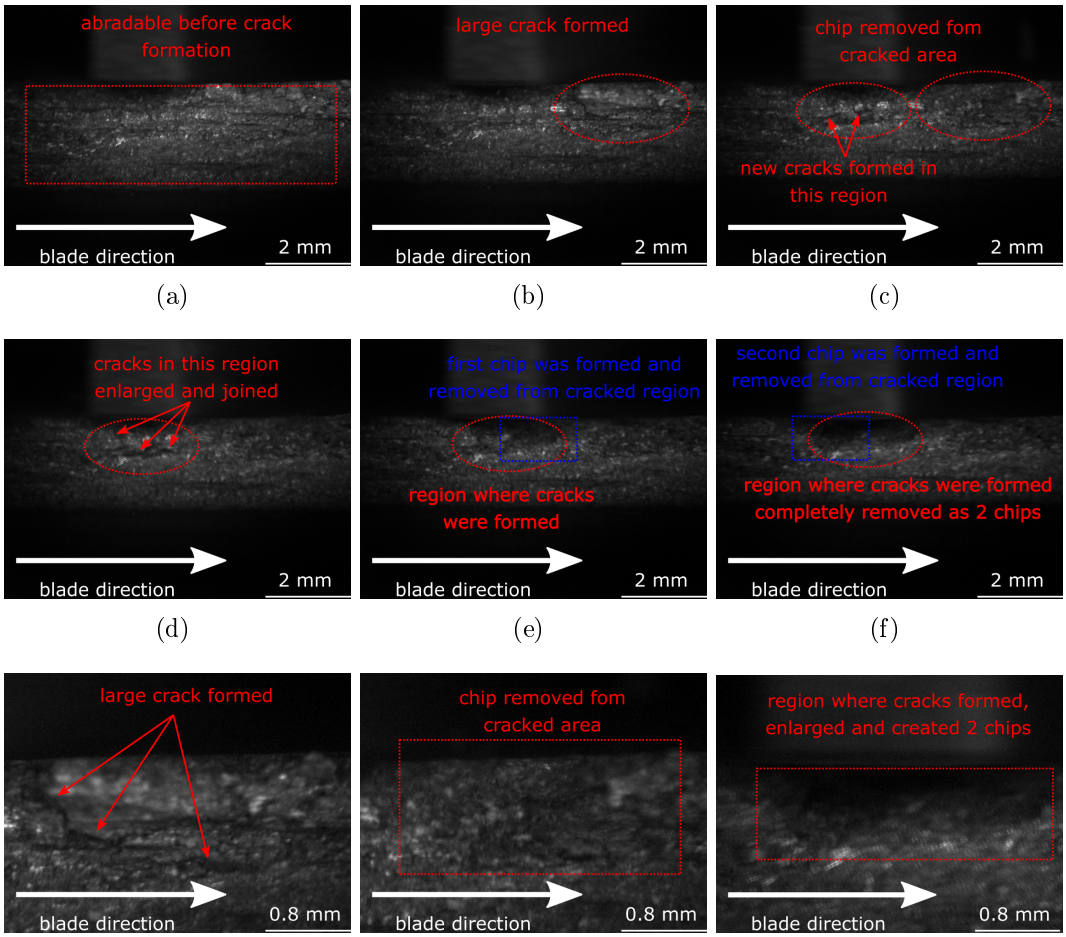

Figure 6.8: Series of images from a Metco 320, RY15 58, 200 m/s, 2 microns/pass test. (a) Image showing how the abradable was before any cracks in that region, (b) Image showing the abradabe and blade taken 0.241 s after image (a), (c) Image showing the abradabe and blade taken 0.144 s after image (b), (d) Image showing the abradabe and blade taken 0.048 s after image (c), (e) Image showing the abradabe and blade taken 0.096 s after image (d), (f) Image showing the abradabe and blade taken 0.096 s after image (e), (g) Image showing an enlarged area from image (b) (2.5 magnification), (h) Image showing an enlarged area from image (c) (2.5 magnification), (i) Image showing an enlarged area from image (f) (2.5 magnification).

6.3.2 DIC images

The aim of DIC analysis in this investigation was not to calculate exact stains, but rather to identify whether compressive/tensile strain fields larger than the incursion were formed. This sections presented examples of DIC analysis images to highlight how the tensile and compressive fields were distributed in the abradable. The aim of

this chapter was to use DIC as a preliminary method to establish whether compressive and tensile fields were formed in the abradable during the contact and what was the difference at various testing conditions. It was shown in the previous chapters that the incursion rate was the most important factor affecting wear and material removal mechanisms so two incursion rates are considered. Low incursion rate (0.02 μm/pass) and high incursion rate (2 μm/pass) were chosen as these cover the whole range under investigation. Also, to assess the effect of the material, both Metco 601 and Metco 320 were considered. For both of these materials the medium hardness was used. Finally one sample from the high hardness Metco 601 (2 μm/pass and 200 m/s) was considered since this was a special case. To summarise a medium hardness (RY15 64) Metco 320 that was tested at low (0.02 μm/pass) and high incursion rates (2 μm/pass), a medium hardness (RY15 70) Metco 601 that was tested at low (0.02 μm/pass) and high incursion rates (2 μm/pass) and a high hardness Metco 601 tested at high incursion rate (2 μm/pass) were considered for this analysis. All the tests mentioned above were performed at 200 m/s blade tip speed. Moreover, to investigate how the compressive/tensile fields varied over the period of the contact the DIC was performed on a sequence of images at three points during a test (25%, 50% and 75% of the contacts duration). The colourbar in the following images represents the strain along the xy plane of the abradable (shear strain, ϵ_{xy}).

High hardness Metco 601

Figure 6.9 shows the DIC analysis performed on images taken from a Metco 601, RY15 82 sample tested at 2 μm/pass and 200 m/s. As shown in these figures, throughout the whole duration of the test large compressive fields formed under the abradable surface (deep blue regions).

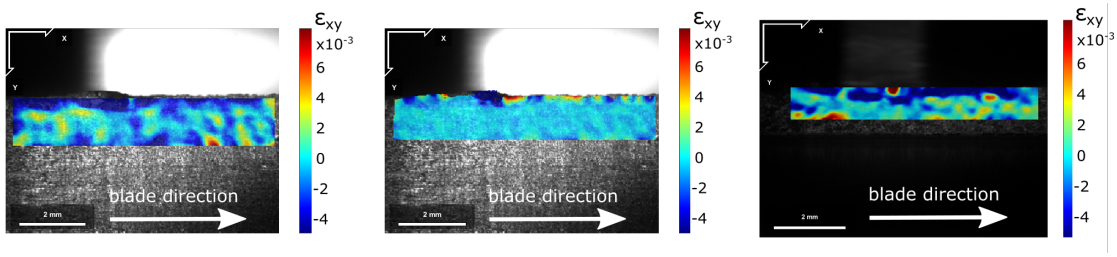

(a) (b) (c)

Figure 6.9: DIC images obtained from Metco 601, RY15 82, tested at 2 μm/pass. (a) Image taken at 25% of the test completion, (b) Image taken at 50% of the test completion, (c) Image taken at 75% of the test completion.

Metco 601, low incursion rate (0.02 μm/pass)

Figure 6.10 shows the DIC analysis performed on images taken from a Metco 601, RY15 70 sample tested at 0.02 μm/pass and 200 m/s. For this sample it could be seen that large compressive fields were created for the whole duration of the test. These compressive fields followed the shape of cracks that formed over a large amount of passes during the test, suggesting that these cracks were created due to these compressive fields. It is worth mentioning that the size of these compressive fields was much larger than the incursion per pass.

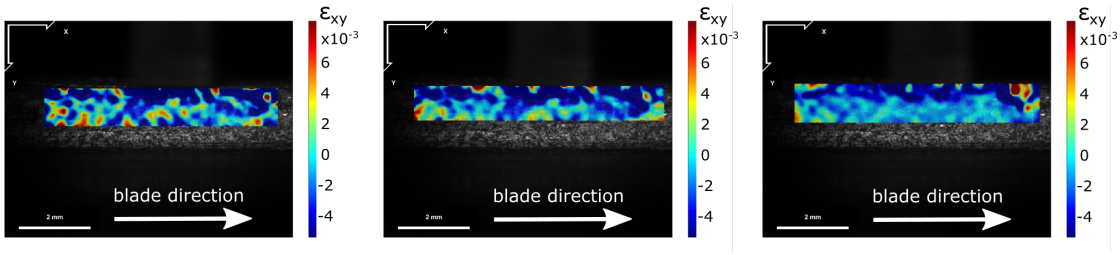

(a) (b) (c)

Figure 6.10: DIC images obtained from Metco 601, RY15 70, tested at 0.02 μm/pass. (a) Image taken at 25% of the test completion, (b) Image taken at 50% of the test completion, (c) Image taken at 75% of the test completion.

Metco 601, high incursion rate (2 μm/pass)

Figure 6.11 shows the DIC analysis performed on images taken from a Metco 601, RY15 70 sample tested at 2 μm/pass and 200 m/s. These figures show that at these

testing conditions large regions of tensile fields were also generated under the abradable surface (red regions). Some regions that compressive fields were generated still occurred, but the main difference at this high incursion rate conditions was that large tensile fields were generated under the surface at different points. These tensile fields linked to areas from where material was removed over the next few passes suggesting that this was what was causing the chip formation at these testing conditions. Furthermore, these tensile fields were larger than the incursion per pass.

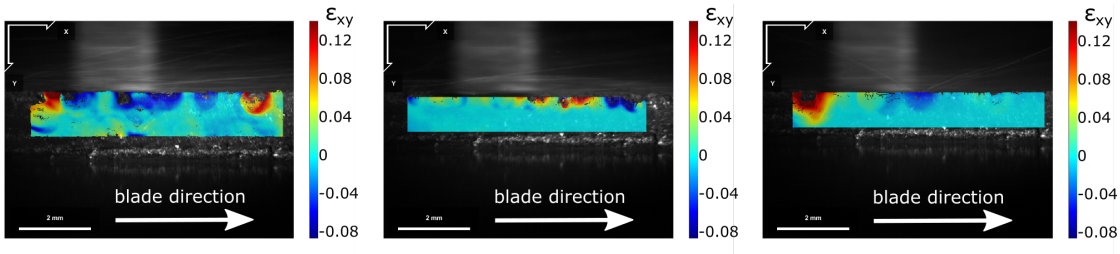

(a) (b) (c)

Figure 6.11: DIC images obtained from Metco 601, RY15 70, tested at 2 μm/pass. (a) Image taken at 25% of the test completion, (b) Image taken at 50% of the test completion, (c) Image taken at 75% of the test completion.

Metco 320, low incursion rate (0.02 μm/pass)

Figure 6.12 shows the DIC analysis performed on images taken from a Metco 320, RY15 64 sample tested at 0.02 μm/pass and 200 m/s. By examining this figure it could be seen that as in the case of Metco 601, at these low incursion rate conditions, large compressive fields were generated in the abradable. Again, this was consistent for the whole duration of the test and the compressive fields were generated around areas where cracks were formed. As previously, the size of the compressive field was much larger than the incursion rate.

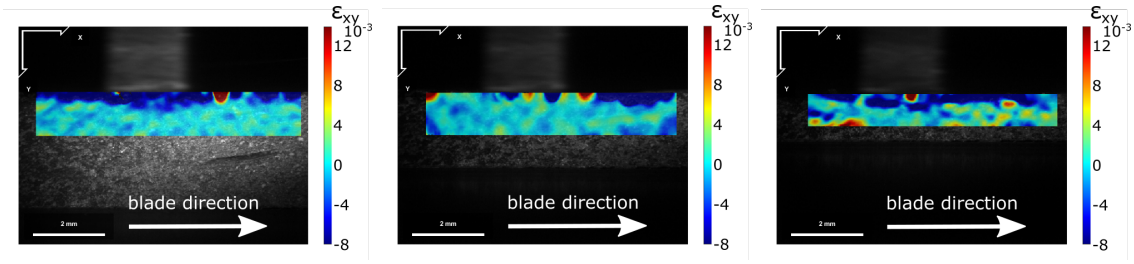

(a) (b) (c)

Figure 6.12: DIC images obtained from Metco 320, RY15 64, tested at 0.02 μm/pass. (a) Image taken at 25% of the test completion, (b) Image taken at 50% of the test completion, (c) Image taken at 75% of the test completion.

Metco 320, high incursion rate (2 μm/pass)

Figure 6.13 shows the DIC analysis performed on images taken from a Metco 320, RY15 64 sample tested at 0.02 μm/pass and 200 m/s. In this figure it was shown that when Metco 320 was tested at high incursion rates tensile fields were generated in some regions. This was consistent for the whole duration of the test, but as seen in figures 6.13(a) and 6.13(c) in some cases these fields were exceptionally large. Large chips of material were removed around the areas where these tensile fields were generated. As in the previous examples, the size of these fields largely exceeded the incursion rate.

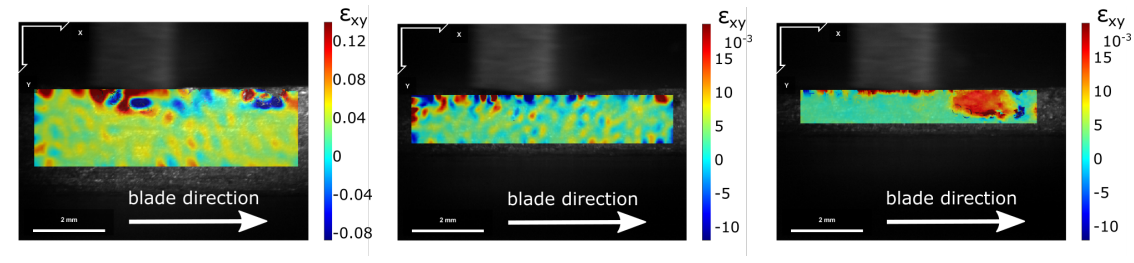

(a) (b) (c)

Figure 6.13: DIC images obtained from Metco 320, RY15 64, tested at 2 μm/pass. (a) Image taken at 25% of the test completion, (b) Image taken at 50% of the test completion, (c) Image taken at 75% of the test completion.

The compressive/tensile field generation shown in this section and its link to the crack and chip formation that was shown in the previous section of the results, was discussed in the discussion that follows.

6.4 Discussion

In this section the results obtained from the testing of this chapter (see 6.3) were evaluated and discussed.

The first thing that could be discussed in this section, was the inferences that could be drawn by observing the raw images obtained by the camera. The experimental set-up in this chapter allowed the observation of the abradable's side while the contact was happening. This way, the cracks and chip formation could be tracked for the whole duration of the test. To visually inspect the raw images, the pictures taken from the camera were combined into one video file with high fps effectively replicating the contact at a higher speed. This made it very easy to identify and track cracks and chip formation. The next step, was to combine these observations with the DIC analysis. DIC was employed as a tool to identify whether compressive and tensile fields were generated in the abradable. The main aim was to observe the size of these fields and link it to the regions where cracks and material removal could be observed. Exact strain calculations were not the scope of this investigation and the focus was instead to examine whether compression or tension occurred in the abradable's surface and sub-surface. By combining these two results, a very strong understanding on what drove the material removal identified in the earlier chapters could be gained.

The first important finding was that for high incursion rate tests, for all the materials considered, very large cracks formed with each pass and chips were usually removed on a pass by pass basis. This could be seen by examining figures 6.7 and 6.8. For example, as shown in figure 6.7 a large crack was formed in the abradable's surface (see figures 6.7(b) and 6.7(e)) and after 144 ms a chip was removed from the cracked region (see figures 6.7(c) and 6.7(f)). A similar observation could be made by inspecting figure 6.8. A large crack was also formed in this case (see figures 6.8(b) and 6.8(e)) and again after only 144 ms a large chip was removed from this cracked region (see figures 6.8(c) and 6.8(e)). In this example, while the chip was removed from that cracked region, new cracks were forming in a different area in the abradable's surface. These new cracks resulted in the removal of two separate large chips (see figures 6.8(d), 6.8(e) and 6.8(f)). The first chip around the cracked regions was removed 96 ms after the crack was formed, while the second chip was removed 96 ms later, resulting in a large area of removed material (see figures 6.8(f) and 6.8(i)). In both of these examples cracks formed and chips were removed from those cracked regions in almost every frame (each frame was equivalent to 3-4 passes). This material removal mechanism

was in close agreement with the chip formation mechanism that was identified in literature and described in section 2.2.2.

As incursion rate decreased, the amount of passes necessary for material to be removed increased. At the lowest incursion rates, no material was removed even after several passes. Instead, smaller cracks started to form throughout the abradable surface and sub-surface, which got larger and longer with each consecutive pass. Eventually, when these cracks became large enough, or if some cracks were close enough and ended up joining, they formed a large chip that was removed.

Examples of this could be seen by inspecting figures 6.5 and 6.6. Figure 6.5 showed how a crack started forming (6.5(b)) over an area where there were no cracks previously (6.5(a)). The cracks continued to increase in size and join together (see figures 6.5(c), 6.5(d) and 6.5(g)) for a very large amount of passes until a chip was removed from that cracked region (figures 6.5(e) and 6.5(h)). A total of 74.947 s passed from the instant the crack became observable (figure 6.5(b)) and the instant the material around that cracked region was removed (figures 6.5(e) and 6.5(h)). This was a significantly larger amount of passes compared to the high incursion rate tests. Another interesting observation about samples tested at low incursion rates could be made by inspecting figure 6.6. This figure showed the material in that region being pushed down into the abradable (compressed) and being deformed (see figures 6.6(b) and 6.6(e)). After a large number of passes the deformed material was eventually removed as a large chip (see figures 6.6(c) and 6.6(f)). A total of 165.8 s were required from the time the material in this region started being compressed and deformed until the material was removed. This material removal mechanism where cracks built up over large amounts of time and were caused by compression of the material was in close agreement with the compression and elastic release material removal mechanism found in literature and described in section 2.2.2.

These findings, linked very well and explained some of the observations made earlier in this thesis. For example, in chapter 4.4 it was identified that at low incursion rates, Metco 601 exhibited a cyclic behaviour in terms of material transfer, temperature and force generation (see figures 4.7(a), 4.7(b)). Next, this effect was again observed in chapter 5. Chapter 5 examined and measured the material ejection plumes. One of the findings of that chapter, which was highlighted in figure 5.17(a), was again that the identified plumes have a cyclic behaviour. The observation, made in this chapter by looking at the raw images, that cracks and chips at the lower incursion rates were

formed after a large number of passes confirmed and explained the observations made in the earlier chapters.

In the second part of this chapter the raw images were used for DIC analysis. The aim of this analysis was to investigate whether strain fields were generated in the abradable, assess their size and compare it to the incursion rate and finally to examine the variation of the strain fields with the testing conditions. The exact calculation of displacement and strains was not the scope of this investigation. The results of this analysis were presented in section 6.3.2. The first important finding from this analysis was for the case of high hardness Metco 601. Previously, this material had shown large amounts of blade wear for all testing conditions. By examining figure 6.9 it could be seen that large compressive strain fields, that cover almost the whole length of the rub, were generated during the contact. This was consistent for the whole duration of the test, suggesting that the abradable was under constant compression. The second important finding was the strain field generation for the samples tested at low incursion rate conditions, where both Metco 601 and Metco 320 showed a similar behaviour (see figures 6.10 and 6.12). At these testing conditions large compressive shear strains were generated in the abradables. These compressive fields were generated in areas where cracks formed and the shape of material removed was closely linked to the shape of these fields. This finding solidified the conclusion that in these incursion conditions the predominant material removal mechanism was the compress and elastic release model explained in section 2.2.2. For the high incursion rate tested samples a different strain field generation was observed (see figures 6.11 and 6.13). In these tests regions of high tensile shear strains were formed at different instances throughout the duration of the tests. The shape of the material removed was closely related to the shape of these tensile fields, as material of the same shape was removed shortly after these fields were created. This finding enhanced the suggestion made previously that at these incursion rate conditions the predominant material removal mechanism was the cutting and chip formation mechanism found in literature and described in section 2.2.2.

Another very important finding made in an earlier chapter (5) was that in all cases and especially in the case of the lower incursion rates the material removed was larger than the scale of the incursion. This was highlighted even more by looking at the raw images since it became apparent that the chips formed when cracks joined or became too large were much bigger than the incursion rate. An example of this could be seen from figure 6.5. As previously mentioned, this figure showed how cracks formed,

enlarged and joined together over a large number of passes and this eventually led to a large piece of material to be removed. The scale of this removed material was in the region of millimeters (larger than 2 mm) while the incursion rate for this test was 0.02 μm/pass. This finding confirmed the observation made in earlier chapters about the size of material that was removed from the abradable. A similar observation could be made for high incursion rate conditions by examining figure 6.7 as an example. Again this figure showed how a large crack was formed resulting to a large chip of material to be removed. Again the scale of removed material (about 2 mm) was much larger than the scale of the incursion rate (2 μm/pass). As a result, it could be concluded that material removal was not driven by the scale of the incursion itself, but rather from the size of the shear strain fields that were generated in the abradable because of that incursion rate conditions. The nature of these fields was different for each incursion condition (compressive fields generated at low incursions and tensile fields generated at high incursions), but it was these strain fields that caused crack formation and material removal.

6.4.1 Material removal mechanisms

In this section the findings of this chapter were put together to establish the material removal mechanisms that were identified for each testing condition and explain what caused these mechanisms.

Low incursion rate

At low incursion rates the blade did not have enough energy to remove material on a pass by pass basis. Instead the material was pushed down and compressed generating large compressive shear strain fields in the abradable's surface and sub-surface. These compressive shear strain fields caused cracks to form over a large amount of passes. Over even more passes these cracks increased in size and joined together to form larger cracks. When cracks were large enough material was removed. This mechanism was in close agreement with the compress and elastic release model found in the literature and described earlies in this chapter. The size of these fields was the determining factor to the size of the material that was removed. Figure 6.14 shows a schematic that describes the material removal mechanism taking place at the low incursion rate conditions.

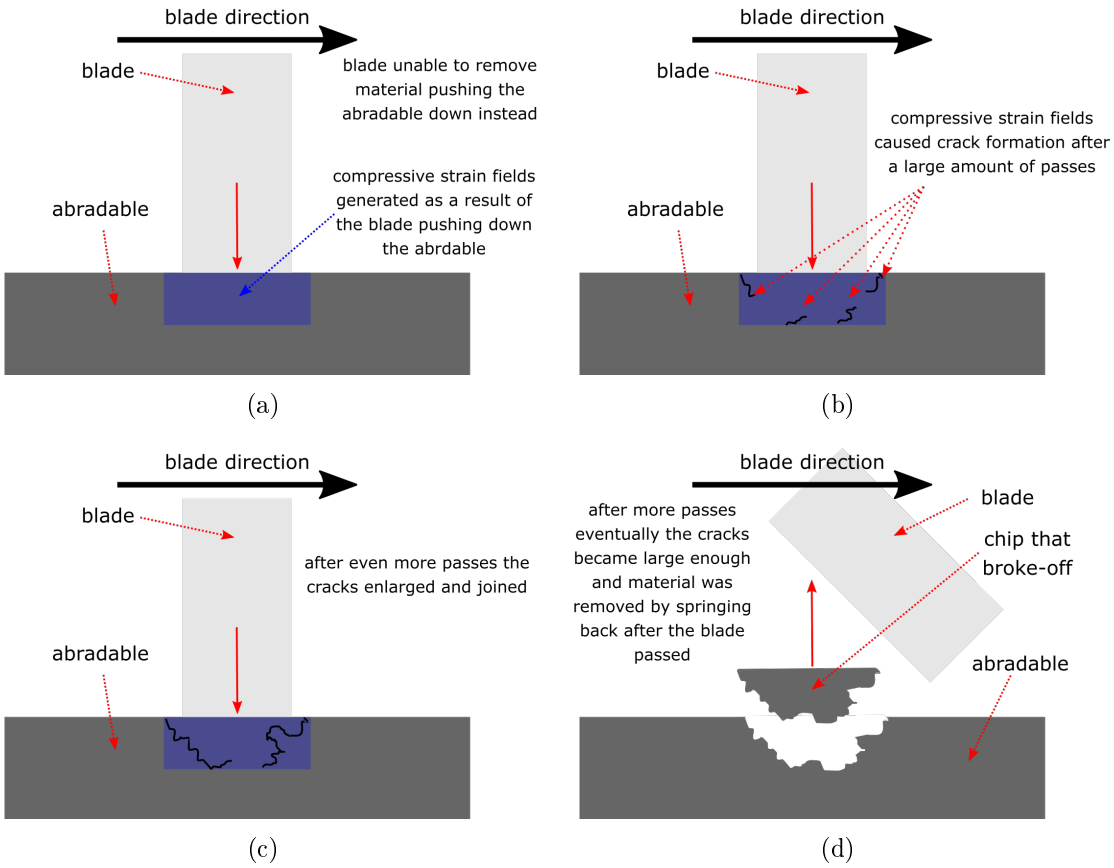

Figure 6.14: Schematic showing the low incursion rate material removal mechanism.

High incursion rate

At high incursion rates the blade had the ability to fracture material. This was shown by the fact that material removal was happening at an almost pass by pass basis. In these high incursion rate conditions the blade had enough energy to cause region of high tensile shear strain fields in the the abradable surface and sub-surface. These tensile fields led to rapid crack formation and material removal after each blade pass. Again the size of the material removed was determined by the size of the tensile field rather than the incursion rate. Figure 6.15 shows a schematic that describes the material removal mechanism taking place at the high incursion rate conditions.

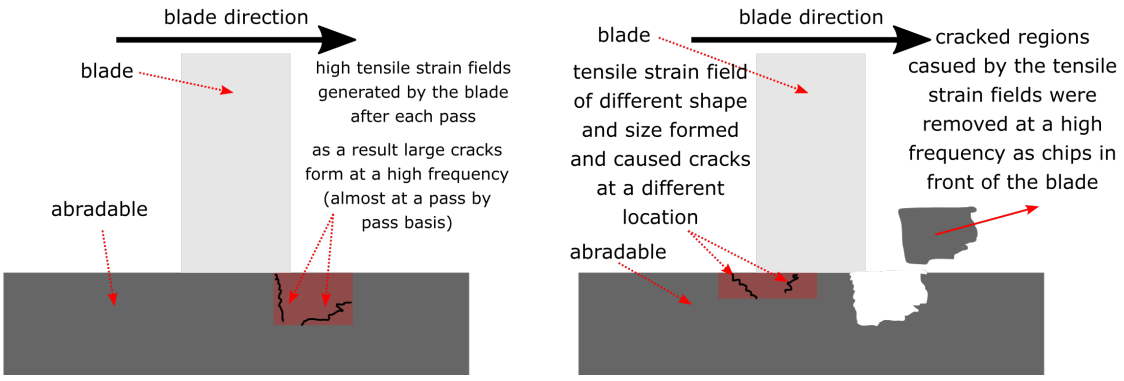

Figure 6.15: Schematic showing the high incursion rate material removal mechanism.

6.5 Conclusion

The target of this chapter was to provide a more in-depth understanding on the material removal mechanism. Interesting observations were made in previous chapters about where material was ejected from and what size distribution this material had and this chapter aimed to provide evidence as to why this was happening. To achieve this, the abradable was observed and analysed from the side for the whole duration of a contact. The most important findings of the investigation of this chapter were shown below:

- The size of the material ejected did not depend on the incursion rate, but rather on the resultant tensile and compressive fields generated due to that incursion rate for a given material.
- At low incursion rates a compressive shear strain field was generated in the abradable materials causing a compress and elastic release material removal mechanism (described in section 2.2.2).
- As incursion rate increased more tensile shear strain fields were generated in the material resulting in an increase of the chip formation material removal mechanism (described in section 2.2.2).

Chapter 7

Abradable Surface Temperature Variation and Front-on Blade Observation

7.1 Introduction

In this chapter, a further examination on the adhesion/wear mechanism of the two abradables under consideration, was performed. In the previous chapters, the material removal and chip formation were investigated, identifying the way material broke down and removed during a contact. Chapter 6 explained how the energy of the contact was distributed in the material in the form of compressive/tensile fields, resulting in the observed removal mechanisms. The aim of this chapter was to consider the thermal effects that the energy input of the contact had on the behaviour of the abradable. To assess the effect of thermal effects, this chapter aimed to identify the link between the temperature variation in the abradable surface and the position along the blade's length at which wear phenomena (adhesion/wear) occurred. To achieve this a thermal camera was used and it was targeted at the surface of the abradable, parallel to the direction of the contact. However, in order to identify and understand the link between wear phenomena and thermal effects the whole length of the blade needed to be considered. Consequently, in this chapter the stroboscopic imaging technique used to observe the blade profile during a contact, was adjusted to monitor the blade across its length instead of its width as it was previously done. The target was to have images throughout the duration of the contact that observe the profile of the blade along its length, and images of the temperature variation of the abradable surface (along the blade length) at the same time. In this way, it could be

assessed whether the temperature variations within the abradable led to certain wear phenomena. This 'front-on' stoboscopic approach had the additional benefit that it provided more information about what was happening on the blade during a contact. An important limitation of calculating the blade length changes (and consequently measuring adhesion and wear) by looking from the side of the blade (width) was that only the maximum length could be observed resulting to not been able to identify all the possible insights a test could provide. For example, if there was one very long adhesion at one point on the blade length, from the side you could only see that. Any other smaller adhesions that built-up could not be observed. Moreover, the side view approach did not show cases where adhesion and wear happened on a single blade (at different positions across the length). These are important pieces of information that could be obtained by looking at the blade from the front (along its length). From the findings of the previous chapters it was hypothesised that adhesion and wear on the blade would occur at places where there was a concentration of heat (hot spot) and there was a local increase in the temperature of the abradable surface. Concluding, these techniques were to be used as tools in an attempt to complete the major aim of this thesis, which was to understand the underlying reasons for the difference in performance of the two abradables under investigation. The interest in this chapter focused to identify if there were differences in the thermal effects that drove the adhesion events in the two considered abradables.

7.2 Methodology

7.2.1 Materials

As in the previous chapters both of the investigated abradables were tested in this set of tests. Again, as the aim was to identify the differences in their performance and at the same time assess the effect of hardness, three hardnesses were chosen for both materials. For these tests there was no need for milled, thinner samples, so normal ones were used instead. As always in this investigation the same Titanium alloy material was used for the blades.

7.2.2 Test conditions and test matrix

The testing performed in this chapter was more targeted compared to the previous chapters. In chapter 4 a large amount of tests was performed to establish the performance of Metco 601, while in chapters 5 and 6 the testing plan was adjusted to cover a representative range of incursion rates and hardness values of the two abradables considered, similar to the conditions used in actual engines. The findings of these chapters provided a lot of evidence about what the wear mechanism was and therefore the focus of this chapter was to confirm this evidence and prove the link of the wear mechanism to the thermal effects. Given challenges around completing tests and high data levels, a more targeted selection of testing conditions was chosen. Firstly, it was obvious that samples from both materials under investigation were chosen since the primary aim of this thesis was to identify and explain the reasons why these two materials behave in such different ways, despite being so similar. The second important aspect was to cover the effect of hardness, especially in the case of Metco 320, since it was shown in previous chapters that its performance varied much more with hardness compared to Metco 601. In addition, this investigation, as well as previous studies have emphasised that the wear mechanisms observed from these contacts, were primarily influenced by the incursion rate conditions. Therefore, the effect of different incursion rates was considered as well. Finally, it was shown in the previous chapters that the high hardness Metco 601 behaved very differently than expected so it was considered separately. Figure 7.1 shows a colour-coded table that summarises the tests carried out in this chapter. The red tests were performed to assess the effect of the thermal effects at different hardness values of Metco 320 at low incursion conditions (both adhesion and wear were observed), while the yellow tests assessed the influence of incursion rate. The green tests were for checking the effect that incursion rate had on the thermal effects observed for Metco 601 and finally the blue test considers the high hardness Metco 601. This test matrix was chosen so all the important phenomena could be investigated and at the same time the amount of tests was kept at the minimum.

Test Number	Abradable Material	Hardness (RY15)	Incursion Rate (microns/pass)
1	Metco 320	55	0.02
2	Metco 320	67	0.02
3	Metco 320	70	2
4	Metco 601	55	0.02
5	Metco 601	55	0.2
6	Metco 601	55	2
7	Metco 601	82	0.2

Figure 7.1: Colour-coded test matrix

7.2.3 Experimental set-up

For this set of tests the standard experimental set-up was altered significantly. The changes made on the standard set-up were described and explained below. In addition figure 7.2 shows a schematic of the set-up used in this chapter highlighting with red, regions where changes were made.

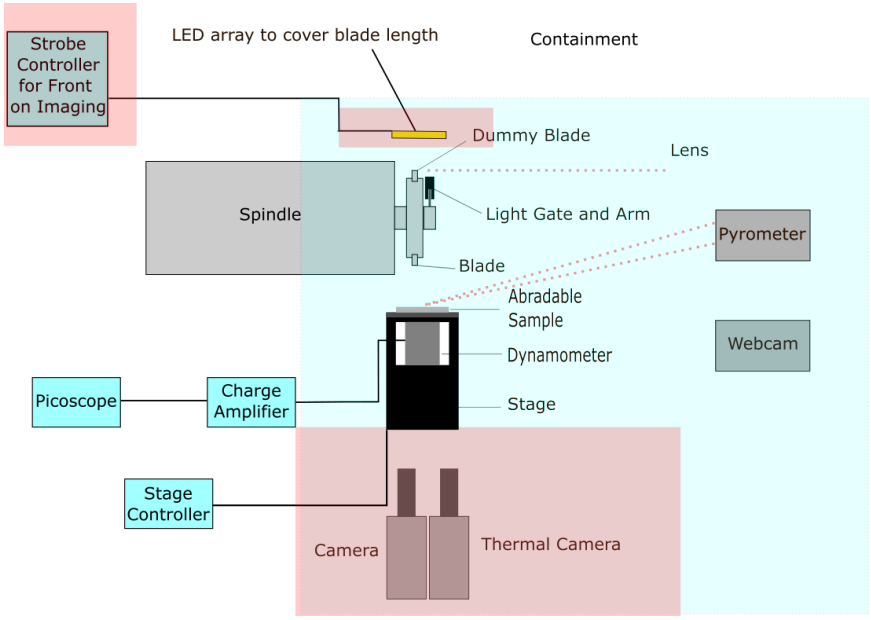

Figure 7.2: Schematic of the updated test rig setup for test carried out for this chapter, from the side (not to scale).

Imaging technique

The most important difference in this set of test was the stroboscopic imaging technique. In order to capture the whole length of the blade a single LED was not enough

as the area it illuminated was not big enough. To solve this an array of very bright LEDs was used for these tests. However, this created a problem with the strobe controlling the LEDs as the strobe previously used could not provide enough power for an array of LEDs. Consequently, a new more powerful strobe was purchased (Gardasoft PP880 8 channel strobe controller) to provide the necessary power for the array of LEDs. The only other difference to the standard set-up was that the camera position was adjusted to 90 degrees from where it was in order to observe the blade from the front and along its length. The cameras and lenses used were the same as the ones discussed in the previous chapters.

Thermal Camera

The second major difference was the addition of a thermal camera to the experimental set-up. The thermal camera was placed at a position parallel to the direction of the contact. In order to minimise the reflections from the hot blade it was placed opposite to the direction of the contact. Also, the thermal camera was positioned at the highest possible angle, taking into account the physical limitations of the set-up. Since there was no physical space to position the thermal camera inside the containment a hole was created on the containment as a fixture for the thermal camera. However, to ensure that nothing could pass through the containment from the hole, a transparent window was added to seal the hole. Thermal imaging was performed by placing the thermal camera on the fixture at the side of the containment while observing the abradable surface through the transparent window.

Figure 7.3(a) shows an example of an annotated image of the rub as observed by the thermal camera to explain what these images showed. Annotations with the direction of the blade's rotation and the rub alignment were used to make it more clear what the images show. Figure 7.3(b) shows an equivalent blade profile to indicate how the two matched. The images shown in figure 7.3 were obtained from a Metco 601 sample with hardness of RY15 55 tested at 200 m/s and 2 microns/pass.

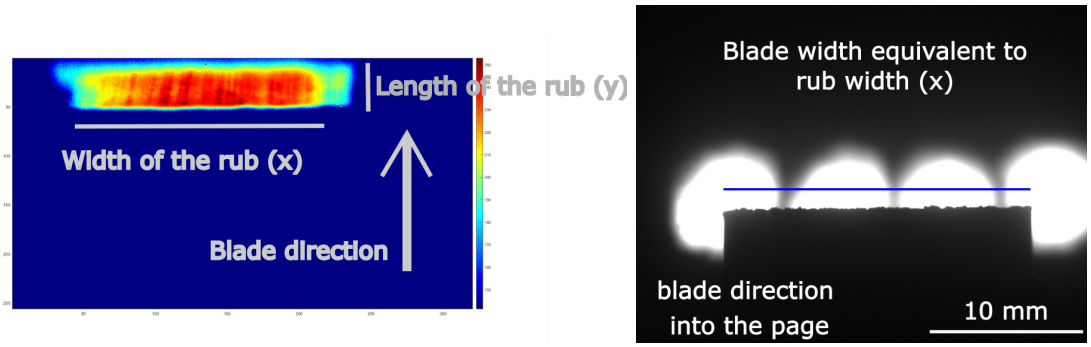

(a) (b)

Figure 7.3: (a) Annotated example of thermal camera image to show direction of blade and rub, (b) Annotated blade image to show how it is matched with the thermal data. Data from a Metco 601, Hardness 55, 200 m/s 2 microns/pass.

7.2.4 Experimental procedure and data acquisition

The only difference on the experimental procedure was the data collection process for the thermal camera. This was performed using FLIR provided data acquisition software that came with the thermal camera. The camera was connected on a PC via ethernet and the software allowed the recording of videos. Due to the high processing power required for this task the thermal camera data acquisition software was run on a separate PC from the other data acquisition systems (LabVIEW) in order to avoid loss of data due to processing delays. All the other data acquisition systems and experimental procedures were as described in the standard experimental procedure in the previous chapters.

7.2.5 Post-processing

Blade profile analysis

Two key additions were made to the post-processing of data. Firstly, the front on camera images were analysed to extract the blade profile. This was achieved by using a code developed by another member of the University of Sheffield abrdables gourp (Eldar Rahimov). The code allowed the user to manually crop an area around the image of interest and then used an edge detection method (Prewitt edge detection) to identify the edge of the blade. The the code overlaid the extracted profile on the original image to observe whether it was a good estimation. Next the resulting profile was normalised and converted into mm by manually selecting the visible sides

of blade, which was a known distance (20 mm). This measured how many pixels were present in that distance and created a pixel to mm conversion that could be applied on the profile. Figure 7.4 shows examples of the steps taken in the analysis of the code as well as an example of an output that it provided.

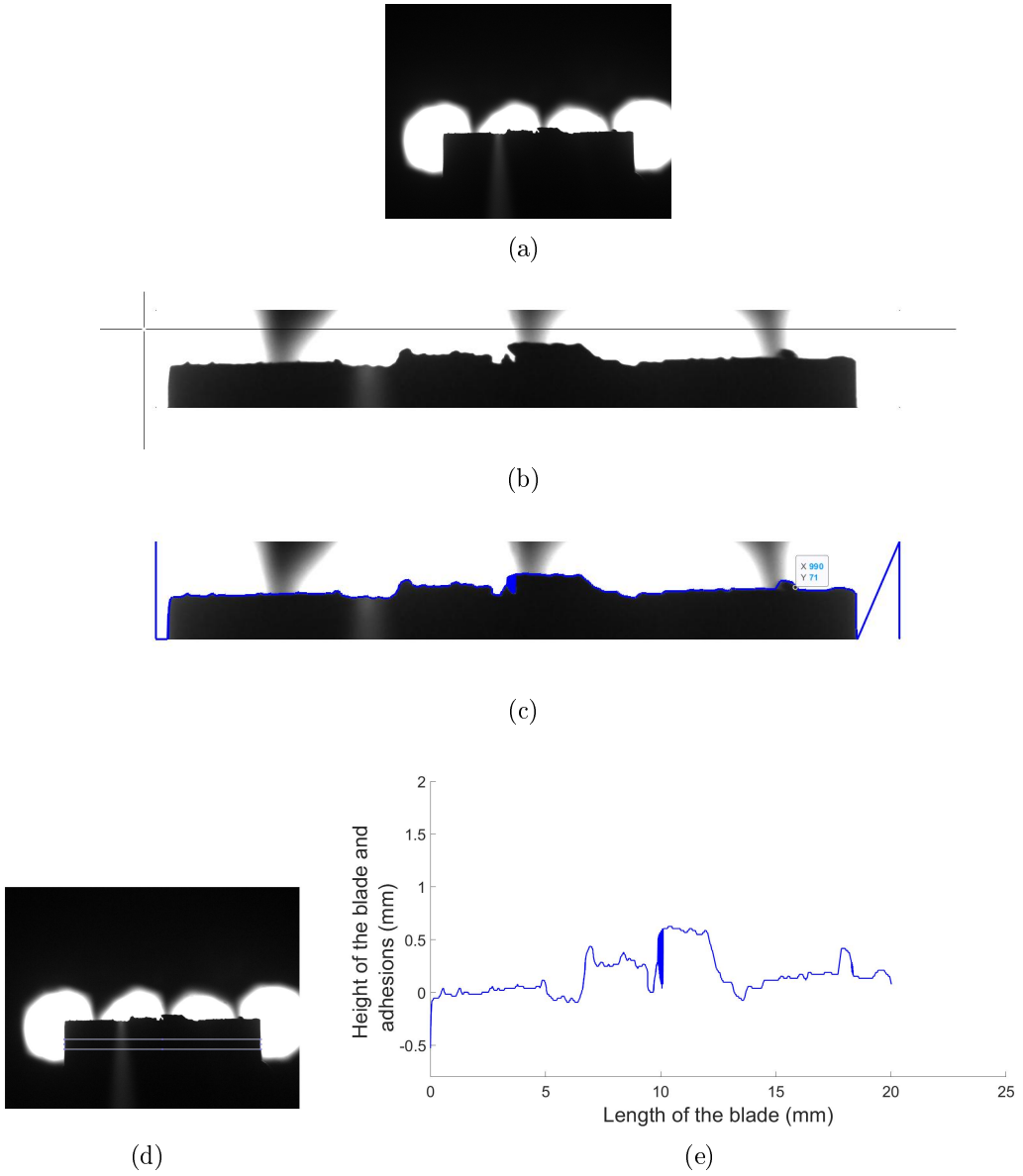

(a)

(b)

(c)

(d)

(e)

Figure 7.4: (a) Original raw image, (b) Cropped image, (c) Edge detection, (d) Selected area with the side of the blades, (e) Example of output.

Thermal camera data post-processing

The second addition involved the thermal camera data. To analyse this data a FLIR provided MATLAB SDK was used. This SDK allowed the FLIR video format file to be opened in MATLAB along with all the parameters that were necessary for the analysis, such as the emissivity of the samples and the transmissivity of the optics used. Moreover, using the SDK the flir format video file could be converted to individual frames that contained all the temperature information per pixel. As a result individual frames could be extracted in MATLAB as images where each pixel was the temperature measurement at that point in space. This allowed for further analysis to be performed using MATLAB. Another very important detail was the fact that the data obtained from the thermal camera was time-stamped at the point of the start of the contact. This allowed synchronisation of the data obtained from the thermal camera and the optical camera.

Apparent temperature average

A very useful tool that was used to identify interesting events for further investigation was to plot the averaged observed temperature of the rub versus time. To achieve this the temperature of each frame obtained from the thermal camera was averaged by adding the temperature values of all the pixels and then dividing by the total pixel number (this was done on a manually cropped section of the image that the rub was extracted). This was extremely helpful since when the averaged observed temperature spiked an interesting event, such as adhesion build-up or blade wear occurred shortly after and this was a way to identify which points during the test to further investigate. For example in figure 7.5(a), two different types of interesting events were observed. The first type seemed to be 4 discontinuous spikes in the average apparent temperature, which build-up to a point and then rapidly cool down (red boxes). The second type was the continuous build-up of the apparent temperature without the sudden cool down (green box). In the case of figure 7.5(b) some periodicity in the abradable temperature could be observed. This was shown by a rapid increase in temperature leading to a peak value followed by a cooling period. This was repeated 5 times during the specific test shown in this figure. Finally, figure 7.5(c) shows an example of a test where the temperature of the abradable was always high and without significant fluctuations.

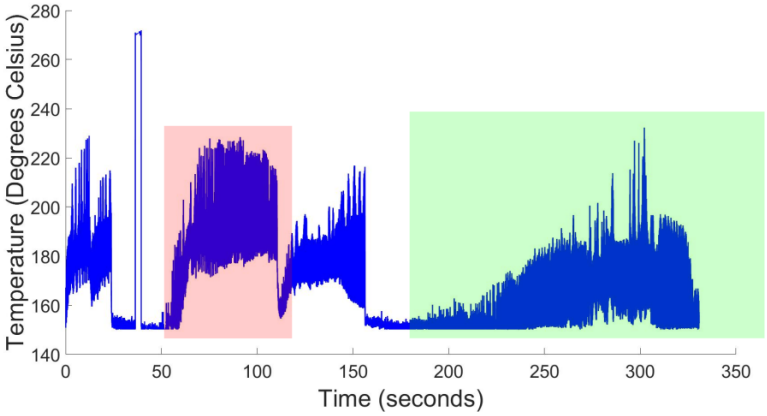

(a)

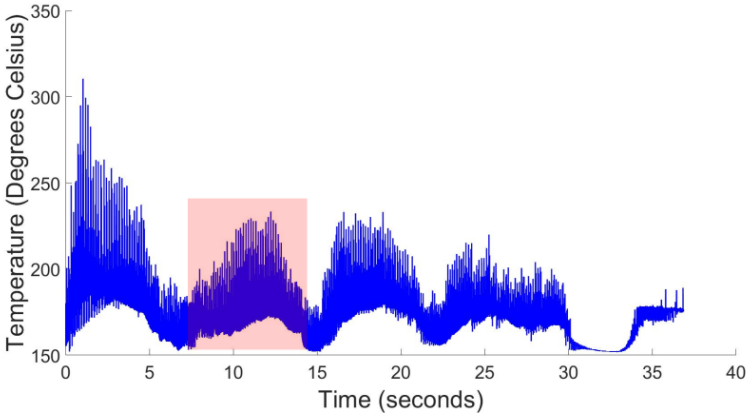

(b)

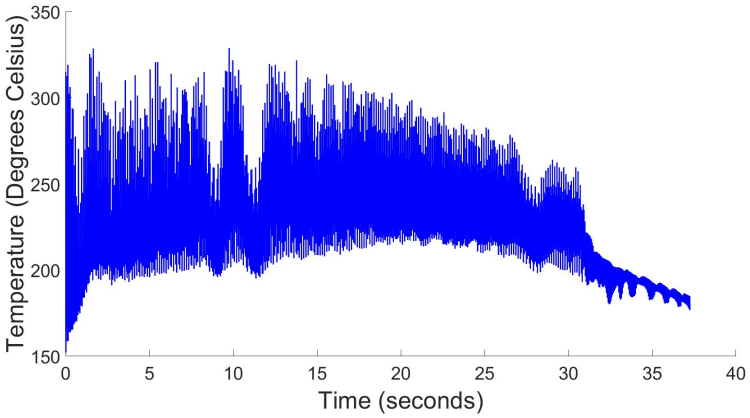

(c)

Figure 7.5: Examples of average observed temperature versus time plots. The plots are evaluated from tests with the following testing conditions: (a) Metco 320, RY15 65, 200 m/s, 0.02 μm/pass, (b) Metco 601, RY15 55, 200 m/s, 0.2 μm/pass, (c) Metco 601, RY15 82, 200 m/s, 2 μm/pass.

7.3 Results

This section provides a summary of the different results obtained using the experimental techniques described in this chapter. The examples provided in this section were used only to give an indication of how typical wear mechanisms looked like on the images. A more extensive example set was provided later in this chapter and it was linked with other data to provide more valuable information.

7.3.1 Raw front on blade images

The figure below (7.6) demonstrates an example of a series of 9 consecutive images of a moderate adhesion mechanism (time interval between each frame was 56 ms). These images were characteristic examples of the typical behaviour observed in low and medium hardness Metco 601 as shown in the previous chapters.

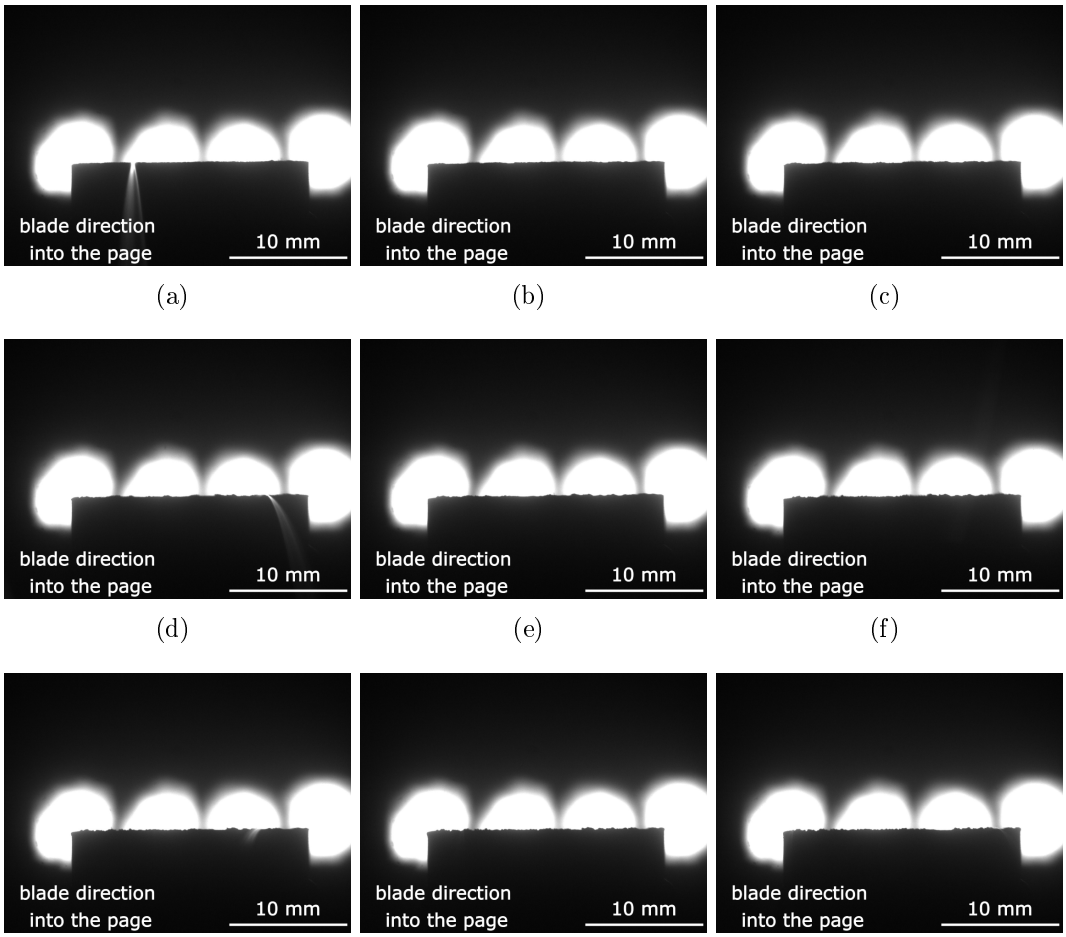

Figure 7.6: Series of 9 consecutive raw images from a moderate adhesion mechanism (Metco 601, Hardness 55 200 m/s, 2 microns/pass). The time interval between each frame was 56 ms.

Figure 7.7 shows an example of a series of 9 consecutive images of a severe adhesion mechanism and localised blade wear. The time interval between each frame was 56 ms. This figure shows a typical example of a low incursion rate Metco 320 sample. As mentioned before and highlighted from the debris ejection and DIC analysis, at low incursion rate, the predominant wear mechanism for Metco 320 was compress and release. These images showed that this mechanism caused localised severe adhesion build-up at some points and localised blade wear at other points across the length of the blade. The next section investigated this observation further to attempt and explain why this was happening.

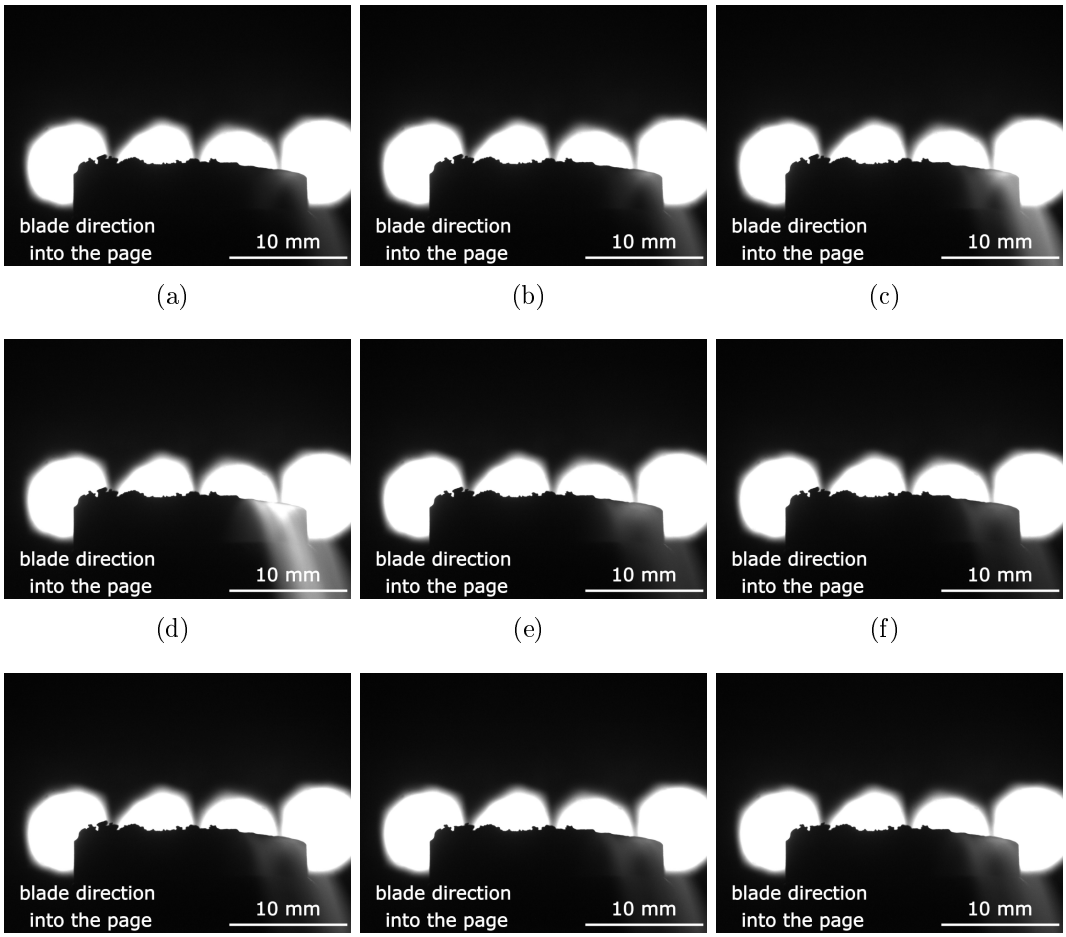

Figure 7.7: Series of 9 consecutive raw images from a severe adhesion mechanism (Metco 320, Hardness 58 200 m/s, 0.02 microns/pass). The time interval between each frame was 56 ms.

Figure 7.8 shows an example of a series of 9 images of a severe blade wear mechanism. The first image was an image of the blade before the test just to show its original size and the rest are 8 consecutive images taken in the middle of the test. The time interval between each frame was 56 ms. This image was taken from a Metco 601 RY15 82 sample tested at 200 m/s and 0.02 μm/pass and it was an example of a test that caused severe wear, sparking and glowing. The red region in figure 7.8(d) shows the area of wear, while the green area shows the material glowing hot suggesting it was melting. As highlighted by the findings of the previous chapters, this hardness was an exception and it behaved very differently than Metco 601 at other hardness values. The severe wear could be clearly observed in figure 7.8 and the reasons why this wear took place were investigated further with the aid of the thermal camera in

the next section.

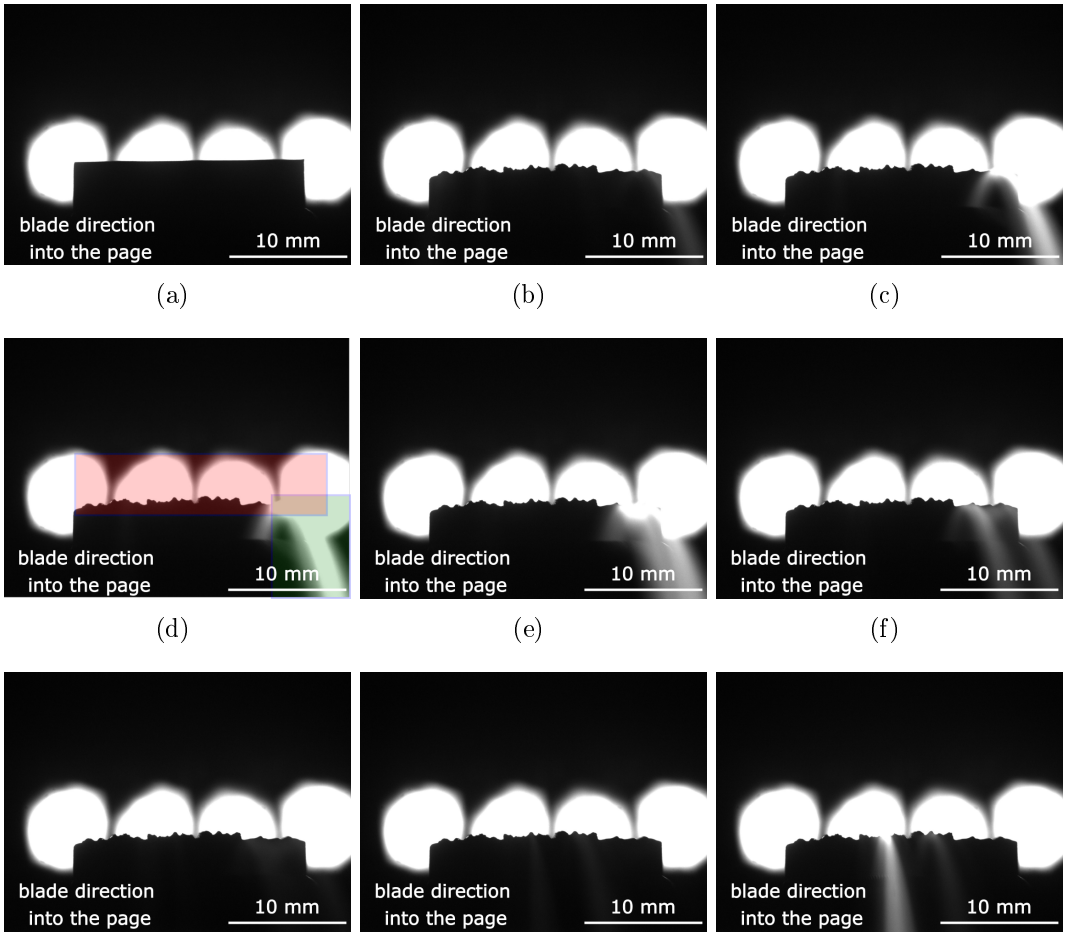

Figure 7.8: Series of 9 raw images from a severe blade wear mechanism (Metco 601, Hardness 82 200 m/s, 0.02 microns/pass). The time interval between each frame was 56 ms.

7.3.2 Event (adhesion/wear) investigation

In this section the identified events where the average apparent temperature observed by the thermal camera spikes, were investigated in more detail and presented. To do this, a sequence of raw camera images around an interesting event was selected. The first step was to evaluate the blade's edge profile to see more clearly the asperities present along the blade length (see second column of figures 7.11, 7.12, 7.17, 7.16). Then, using the synchronised time-stamps of the data, the thermal camera data at that particular point in time was displayed (see third column of figures 7.11, 7.12,

7.17, 7.16). This way, the apparent temperature distribution across the rub during an interesting event (adhesion build-up or blade wear) could be observed.

Figure 7.9 shows an adhesion event that took place during a RY15 58 Metco 320, 200 m/s, 0.02 μm/pass. At this time period during the test, there was a localised increase in temperature due to heat accumulation in that region in the abradable surface. This resulted in material adhesion to form on that subsequent part of the blade. Material continued to adhere at that localised region until it became too long and broke off.

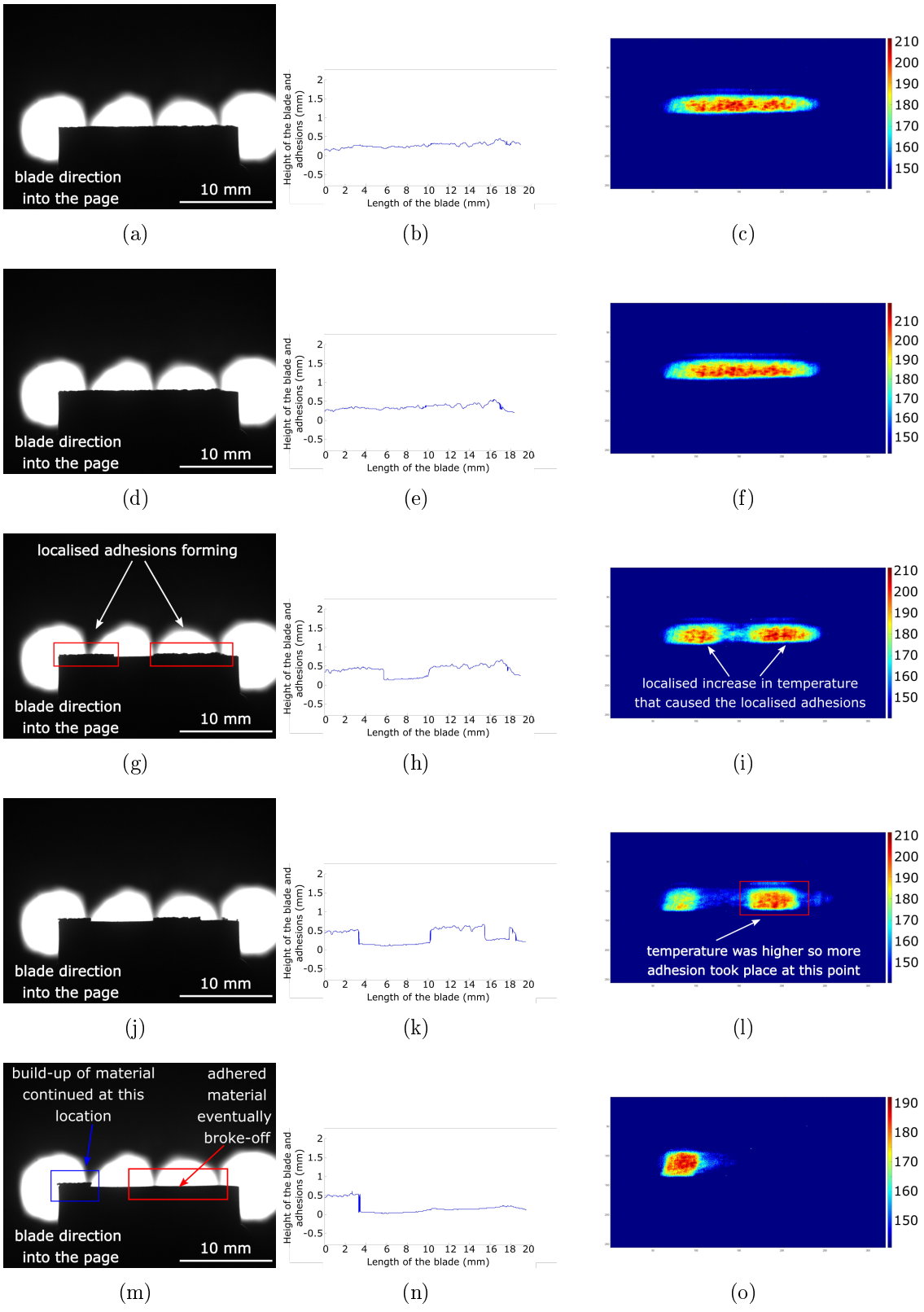

Figure 7.9: Series of 5 consecutive time-stamped images from a pick up event (Metco 320, RY15 58, 200 m/s, 0.02 microns/pass). The time interval between each frame was 56 ms.

Figure 7.10 shows a wear event that took place at the same test as the one shown in figure 7.9 (same test, different time in the test). In this case it could be observed that adhesion and blade wear were happening locally and simultaneously at different points across the length of the blade. It was also evident than in the cases where blade wear was happening the apparent abradable surface temperature was higher than the regions where material adhesion took place. It is worth highlighting the observation made in figure 7.10(m), where the blade was glowing hot, suggesting that severe thermal damage and deformation of the blade took place. This was supported by the apparent abradable temperature shown in figure 7.10(o), which was very high at that region (higher than 250 ^{o}C, while the rest of the abradable is around 160 ^{o}C). The glow that could be observed came from the blade, however the temperature of the blade was not measured so an exact blade temperature at which this occurred could not be provided. These observations were discussed in more detail in the discussion section that follows in this chapter.

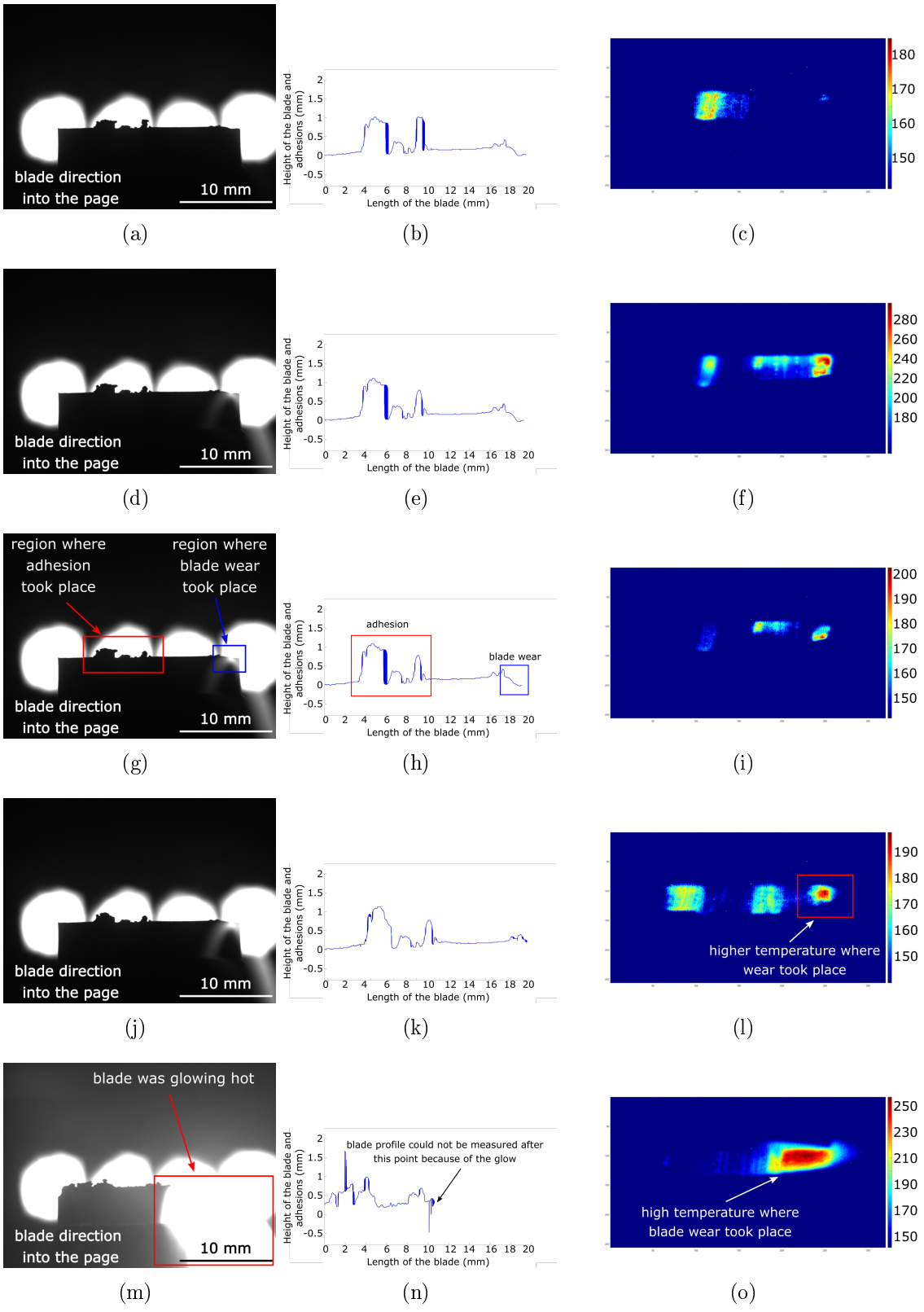

Figure 7.10: Series of 5 consecutive time-stamped images from a wear event (Metco 320, RY15 58, 200 m/s, 0.02 microns/pass). The time interval between each frame was 56 ms.

As a concluding comment for this material (low hardness Metco 320), when tested at the lowest incursion rate it exhibited a mixed mode of wear mechanisms that appeared to be largely driven by thermal effects as highlighted by the thermal camera data. The next step was to show similar results for a higher hardness Metco 320 to assess what changed in the behaviour when hardness was varied.

Figure 7.11 shows a material adhesion event in a low incursion rate, RY15 67 Metco 320 sample. It highlights that only some parts of the length of the blade started building up temperature and shortly after material started adhering in those areas (again localised material pick-up). This continued until there was an adhesion break-off and the area that the adhered material was rapidly cooled down (see figure 7.11(o) and 7.11(l)). This was a very similar pattern with the lower hardness Metco 320. However, it seems that the apparent temperature of the abradable surface in the case of the lower hardness was higher compared to the higher hardness and wear was less likely.

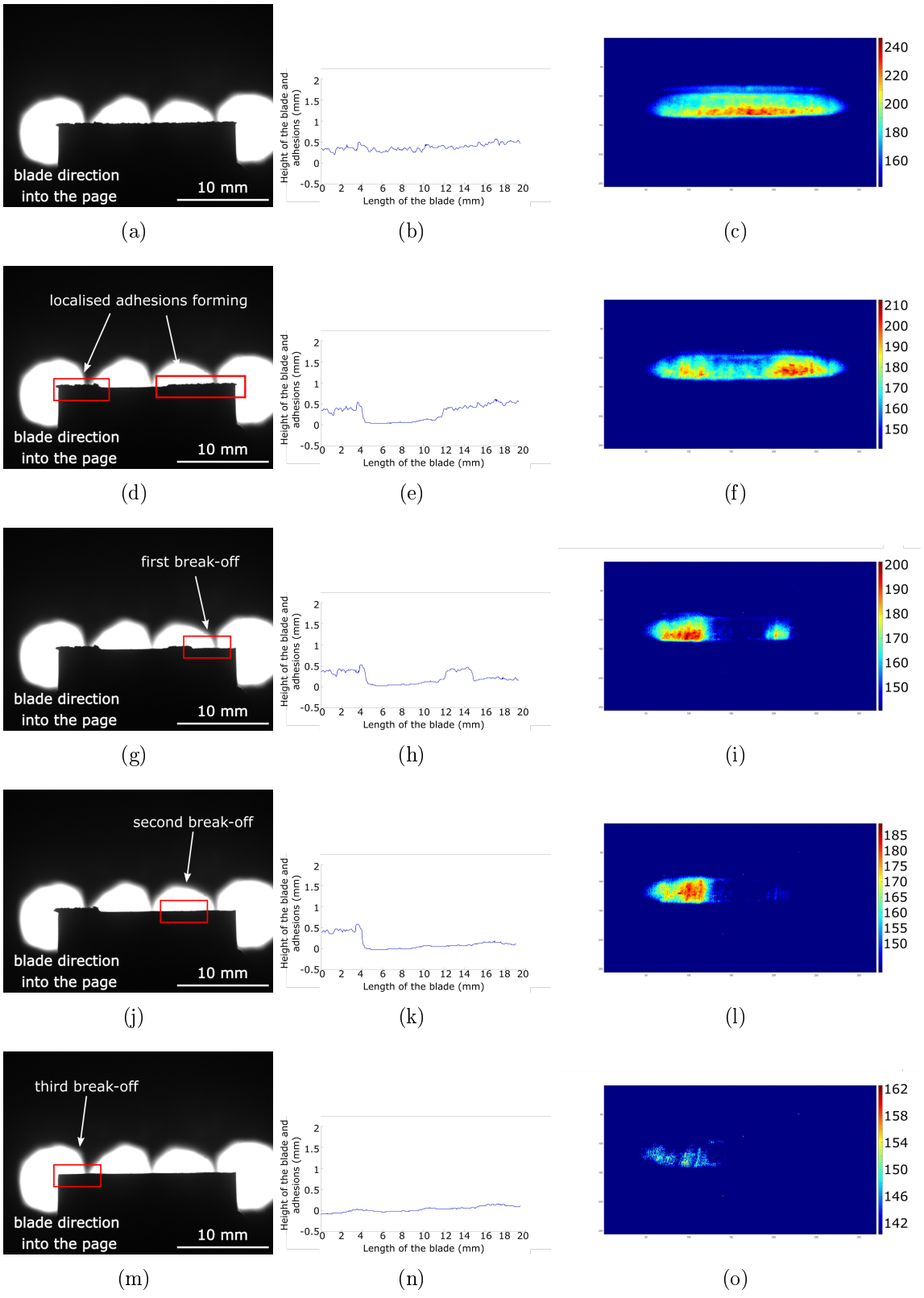

Figure 7.11: Series of 5 consecutive time-stamped images from a pick-up event (Metco 320, RY15 67, 200 m/s, 0.02 microns/pass). The time interval between each frame was 56 ms.

Figure 7.12 shows a blade wear event for a low incursion rate, RY15 67 Metco 320 sample. By observing this figure, it can be seen that at some point during the test, there was an increase in temperature at a very short and specific region across the length of blade profile, which resulted in blade wear. The white "shadow" that can be observed in the raw blade images corresponded to overexposure that was a result of glowing hot material at that point (for example see figure 7.12(m)). In this sequence of figures, 3 distinct wear locations could be observed over the considered time frame. Again, this result was similar to the blade wear observed at the lower hardness but again it seems the apparent temperature was lower at this higher hardness.

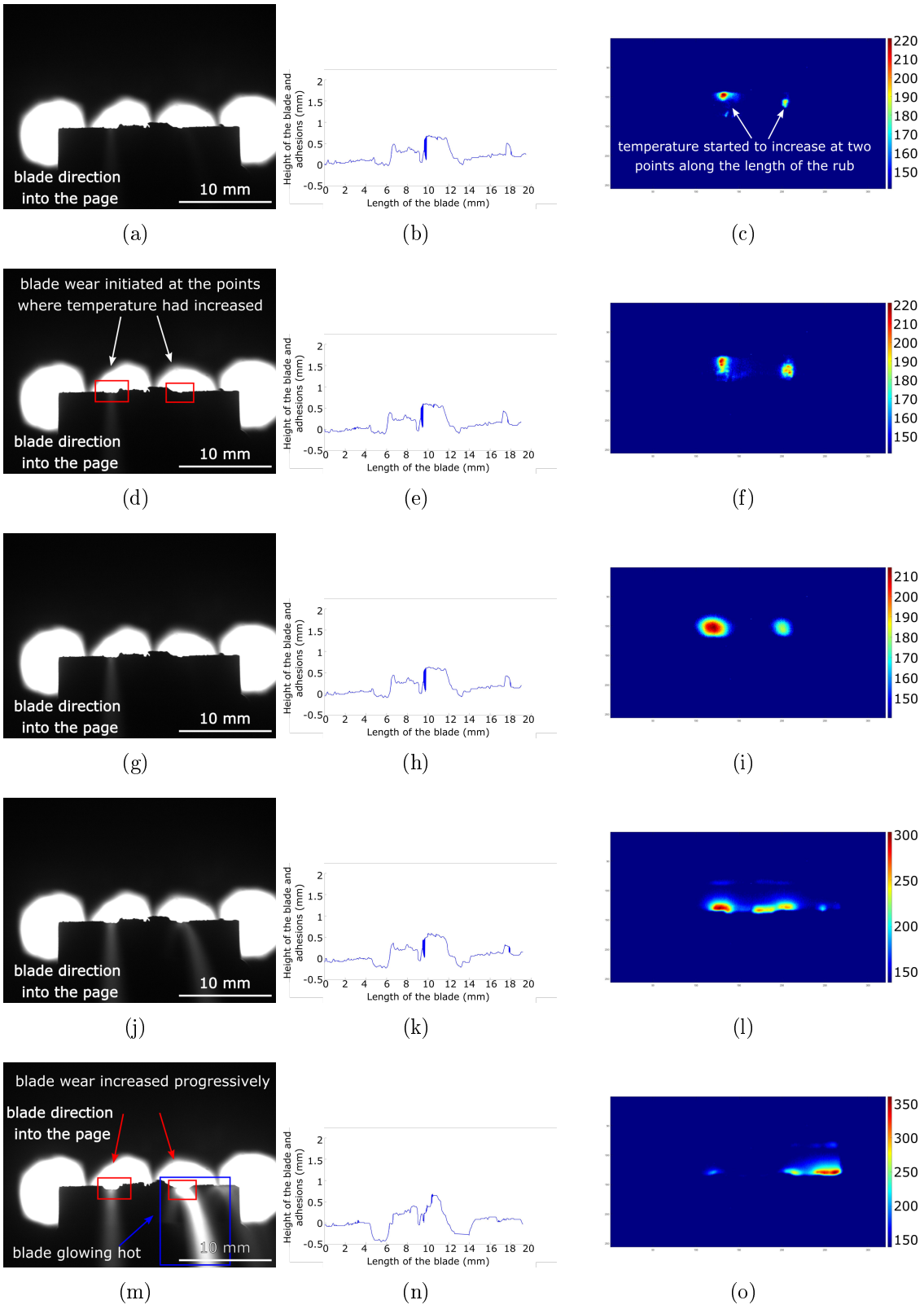

Figure 7.12: Series of 5 consecutive time-stamped images from a wear event (Metco 320, RY15 67, 200 m/s, 0.02 microns/pass). The time interval between each frame was 56 ms.

The material adhesion and blade wear phenomena observed for the two different hardnesses of Metco 320, when tested at the lowest incursion rate, followed a similar pattern. Temperature rose locally in the abradable surface and this led to material pick-up on the blade at that region. When the heat that built-up in the material got even higher, this resulted to blade wear. Finally, it could be observed that the apparent temperatures across the surface of the abradables were higher in the case of the lower hardness Metco 320.

The next step was to assess the effect of the incursion rate to the thermal effects that governed the mechanisms. This study, as well as previous investigations of Metco 320, showed that the wear mechanism drastically changed as incursion rate was increased, moving towards a chip formation cutting mechanism. Figure 7.13 shows the data set from a high incursion (2 μm/pass), high hardness (RY15 70) Metco 320 sample. The figure showed that in this case the apparent temperatures were more evenly distributed across the surface of the abradable and minimal adhesion took place in this testing condition. This suggested that when Metco 320 was operated at high incursion rates, a chip formation, efficient cutting mechanism took place.

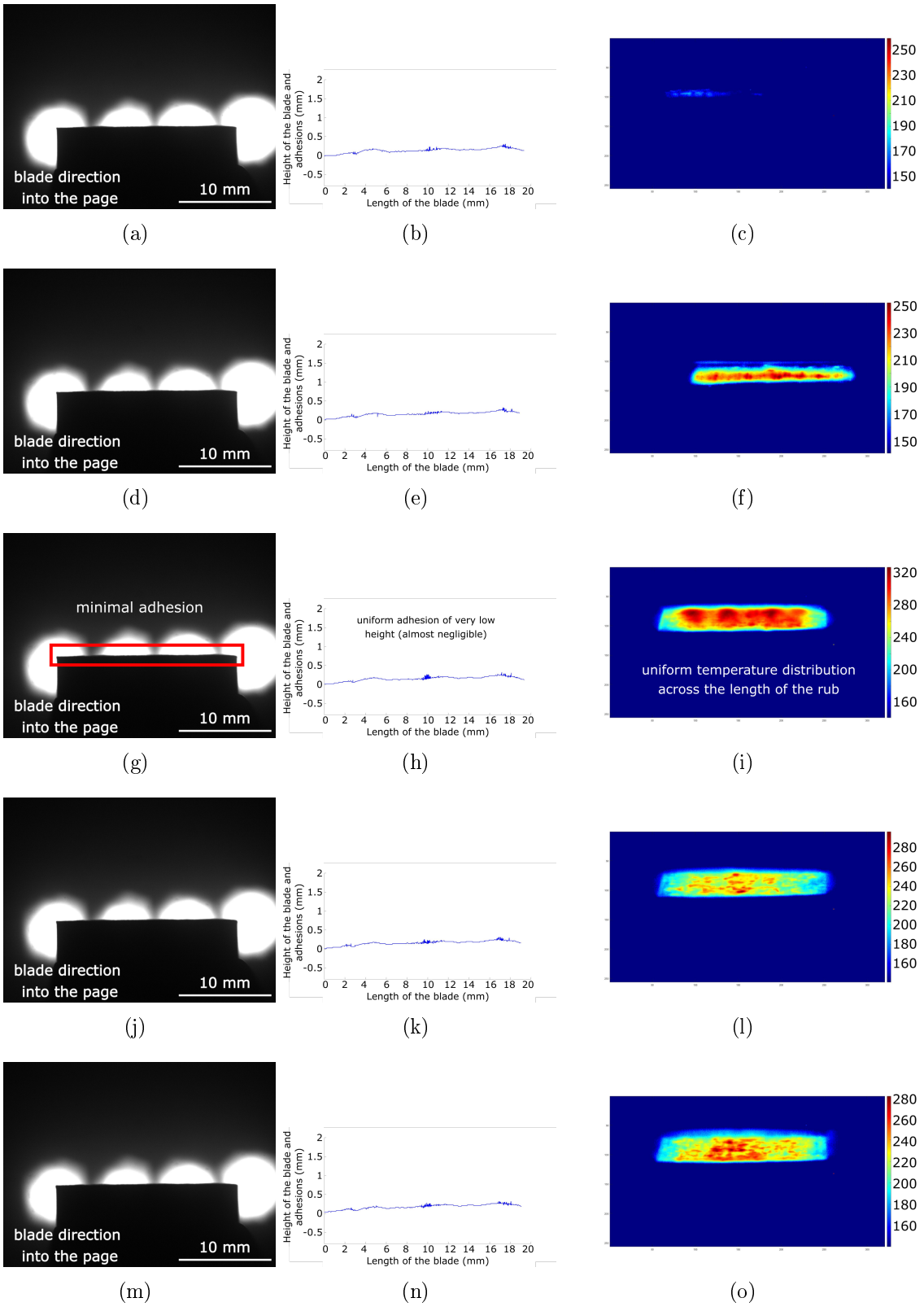

Figure 7.13: Series of 5 consecutive time-stamped images from a clean cutting mechanism (Metco 320, RY15 70, 200 m/s, 2 microns/pass). The time interval between each frame was 56 ms.

The next three figures (7.14, 7.15, 7.16) show the data obtained from the testing of RY15 55 Metco 601 across the range of the incursion rates considered. By studying these figures, the difference in the thermal effects resulting in the two abradables as a result of a contact, could be observed. By identifying these differences, valuable understanding was gained on what drove these materials to behave differently. Moreover, since the data for a single hardness across three incursion rates was provided, the effect the incursion rate had on the resulting thermal response of the abradable could be assessed. This was important given Metco 601 showed adhesion across all incursion rates, whilst Metco 320 did not. Only one hardness was considered because the findings in the previous chapters suggested that low and medium hardness Metco 601 behaved very similarly (high hardness Metco 601 was considered separately).

Figure 7.14 shows the data obtained by testing the RY15 55 Metco 601 at 200 m/s and 0.02 μm/pass, figure 7.15 shows the data obtained by testing the RY15 55 Metco 601 at 200 m/s and 0.2 μm/pass and finally figure 7.16 shows the data obtained by testing the RY15 55 Metco 601 at 200 m/s. It could be seen in these figures, that across all incursion conditions the apparent temperature of the abradable rose homogeneously across the whole length of the rub resulting in equivalent pick-up across the whole of blade. Pick-up was mostly uniform and not localised as in the case of Metco 320. This continued until the pick-up was removed and then it re-initiated with a similar homogeneous pattern. Further discussion about the differences observed between Metco 601 and Metco 320 adhesion mechanisms was provided in the following section. Moreover, by observing the first and second column of this figures, it could be identified that a degree of adhesion took place across all incursion rates, the amount of adhesion was less as incursion rate increased.

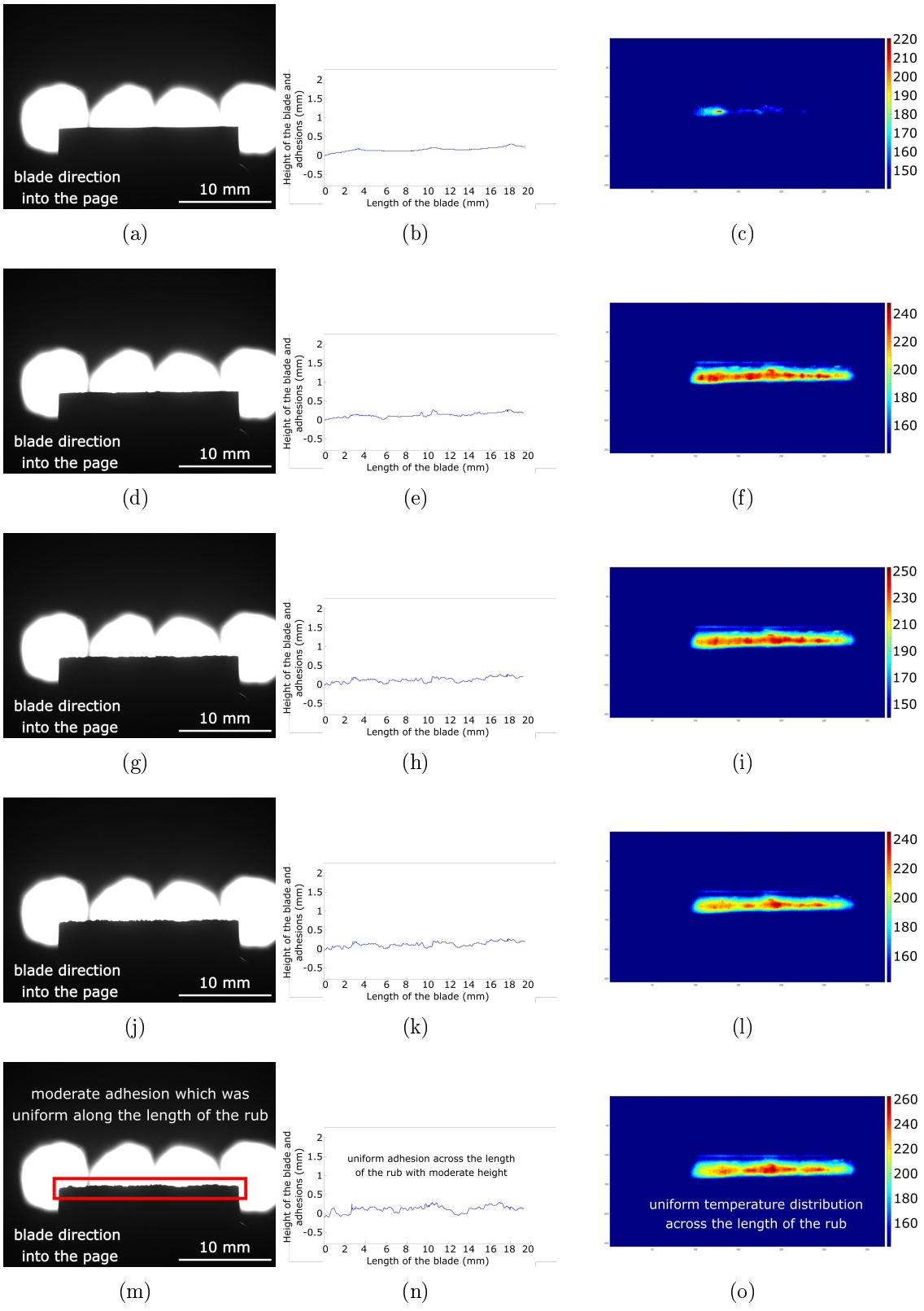

Figure 7.14: Series of 5 consecutive time-stamped images from low incursion, low hardness Metco 601 (Metco 601, RY15 55, 200 m/s, 0.02 microns/pass). The time interval between each frame was 56 ms.

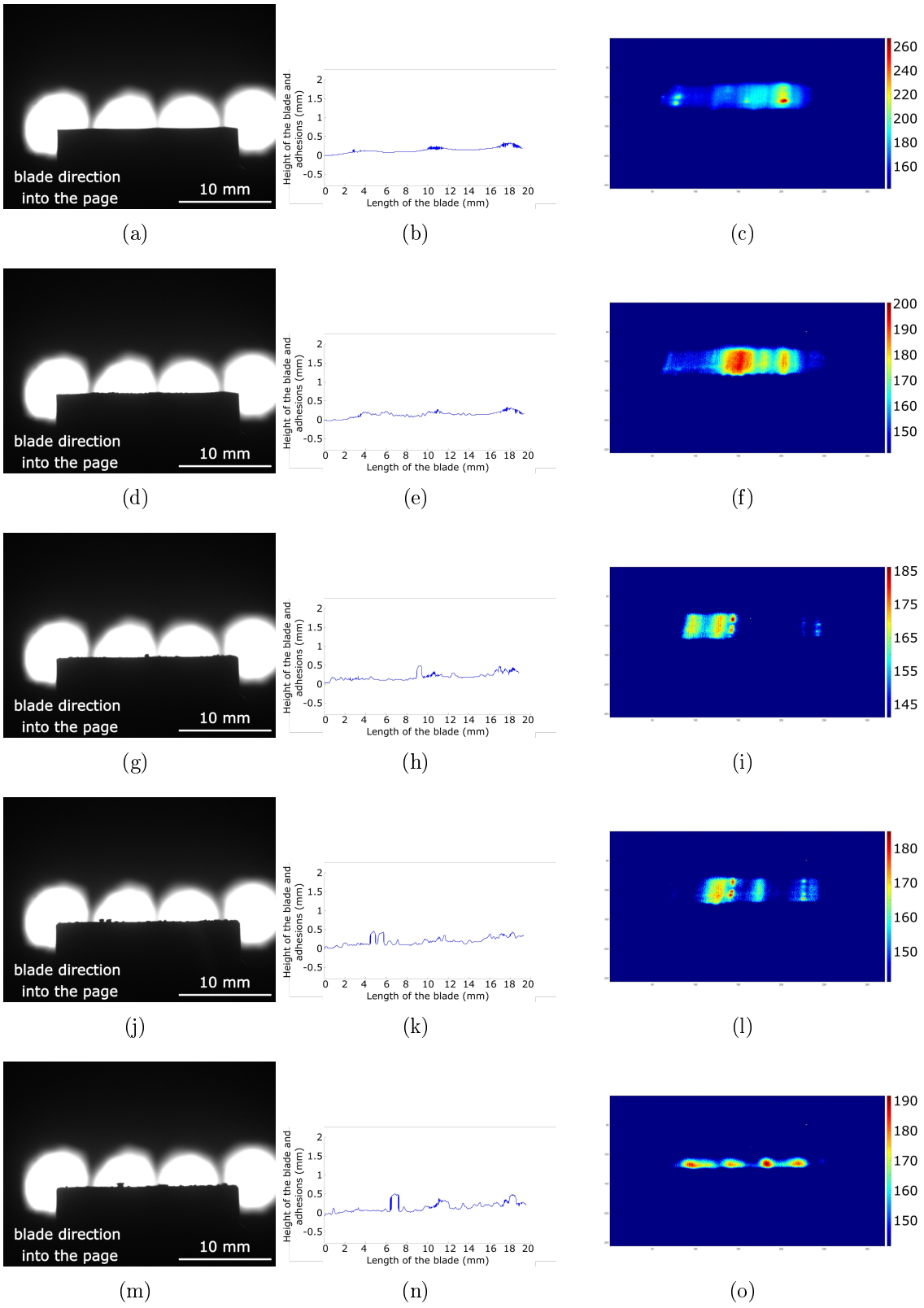

Figure 7.15: Series of 5 consecutive time-stamped images from low incursion, low hardness Metco 601 (Metco 601, RY15 55, 200 m/s, 0.2 microns/pass). The time interval between each frame was 56 ms.

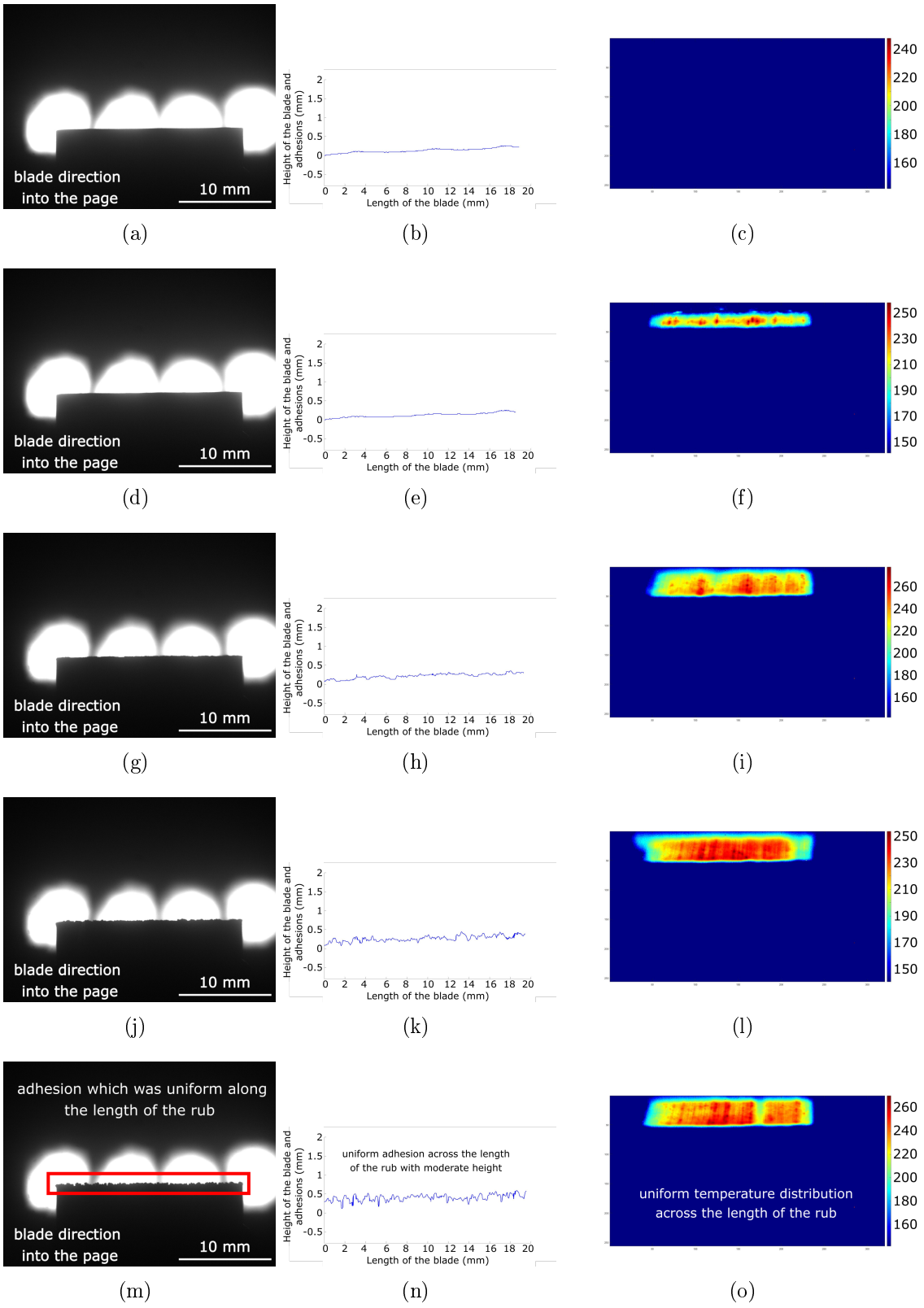

Figure 7.16: Series of 5 consecutive time-stamped images from a adhesion event (Metco 601, RY15 55, 200 m/s, 2 microns/pass). The time interval between each frame was 56 ms.

Finally, figure 7.17 shows a blade wear event in a medium incursion rate, RY15 H82 Metco 601 sample. This figure was used as an example for the wear characteristic of Metco 601 at the highest considered hardness (RY15 82). In the case of Metco 601 at this hardness, the wear was homogeneous and tended to occur along the whole length of the blade instead of just spots like in the case of Metco 320 (see figure 7.12). This observation was discussed in more detail in the following section. Similar blade wear patterns were observed across all incursion conditions as shown by the analysis in the previous chapters (even though the amount of wear became less with increasing incursion). Also, it should be noted that by looking at the third column of figure 7.17, it was apparent that the observed apparent temperatures for this hardness were much higher than the ones observed for the lower hardness Metco 601 samples.

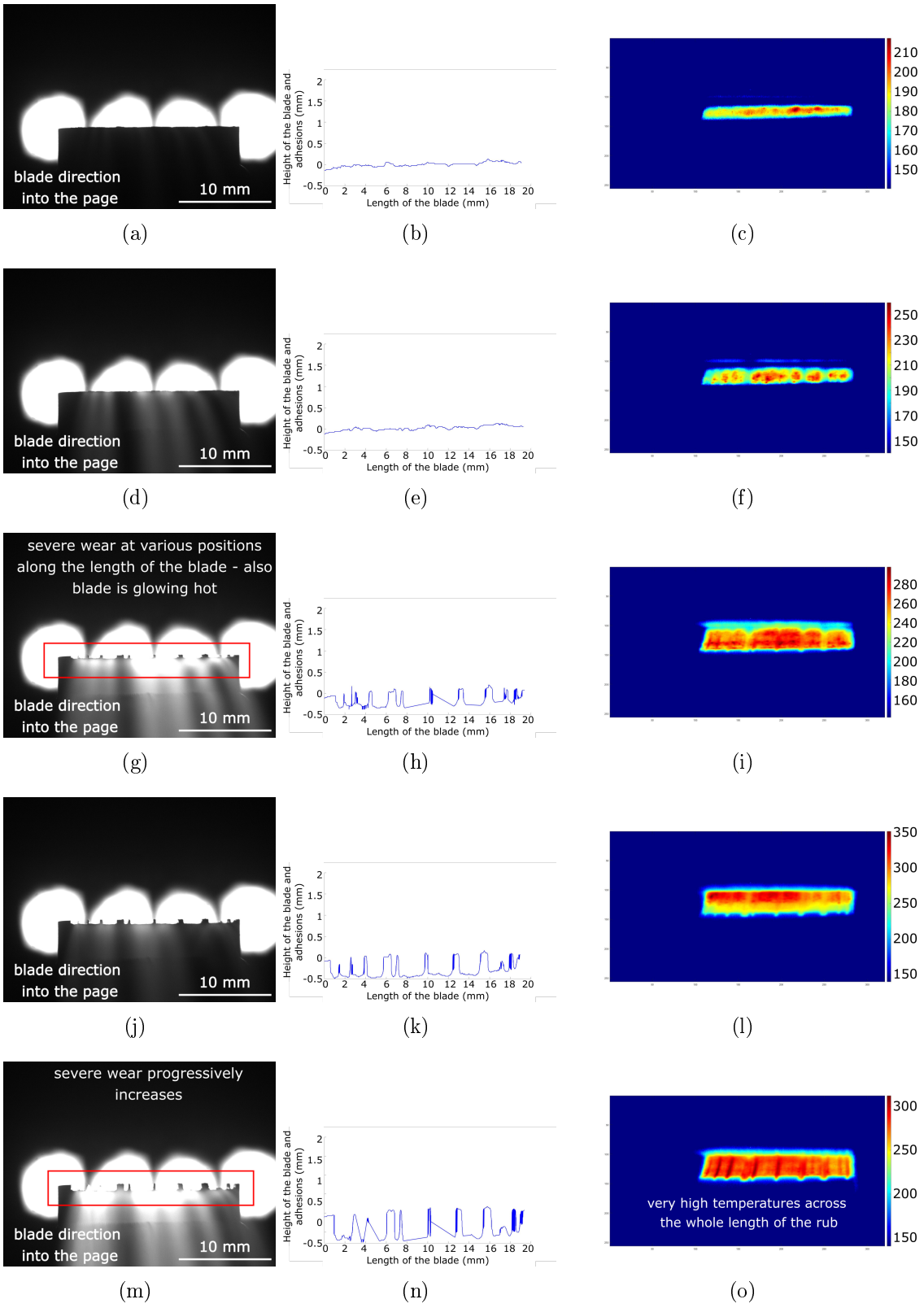

Figure 7.17: Series of 5 consecutive time-stamped images from a wear event (Metco 601, RY15 82, 200 m/s, 0.2 microns/pass). The time interval between each frame was 56 ms.

7.4 Discussion

After presenting the results in the previous section, a detailed discussion and interpretation of these findings was provided in this section. Also, this sections provided a discussion of how the findings of this chapter link with the findings of the previous chapters to provide a deep understanding on what drove the wear mechanism for each of the considered abradables.

7.4.1 RY15 82 Metco 601

Figure 7.17 clearly shows that in the case of the high hardness Metco 601, there was a continuous build-up of heat, homogeneously across the whole width of the rub, which in turn resulted at high enough temperatures to cause thermal damage and wear on the blade. This suggested that material was not removed efficiently, but it was instead compressed and all the energy of the contact was accumulated in the abradable surface and the blade, leading to high increases of the temperatures of both. This result linked very well with the findings in previous chapters where high compression and blade wear were observed.

7.4.2 Metco 601 (low and medium hardness)

To observe the adhesion mechanism in Metco 601 a RY15 55 abradable was tested across all the considered incursion rates. The first two columns of figures 7.14, 7.15 and 7.16 clearly showed that a certain degree of adhesion took place across all incursion conditions. Furthermore, the temperature of the abradable's surface increased uniformly across the width of the rub for all incursion conditions, in contrast to the Metco 320 case where there were local increases in temperature. At the lowest incursion rate, it was shown in the previous chapters that the wear mechanism that took place was a compress and release wear mechanism. The compress and release mechanism that took place meant that material was not efficiently removed at a pass by pass basis. Since there was no continuous release of material, the energy from the contact was transferred in the abradable instead of a chip resulting in heat build-up. At the highest incursion rate the wear mechanism changed, but it did not completely shift. As incursion rate increased the ability of the blade to remove material increased too, resulting in more cutting and less compress and release. However, the findings in this investigation have shown that for Metco 601, there was always a combination of

these two mechanisms. At the highest incursion rates, the predominant mechanism was the cutting wear mechanism, but compression and release still occurred. However, at the higher incursion rate less energy was dissipated in the material (most of the energy was dissipated in the chip that was removed) and consequently there was less heat build-up. This resulted in less adhesion to take place explaining why adhesion became less with increasing incursion rate, but it was always occurring for Metco 601.

7.4.3 Metco 320

In the case of Metco 320 three tests were performed in this chapter. The first two were two low incursion rate sample with different hardness values to assess the effect of hardness and the last was a higher incursion rate to observe the change in mechanism at that testing incursion. There were three observed wear mechanisms that took place when testing Metco 320. The first one was adhesion, which was observed at both hardnesses when tested at low incursion values. Figures 7.9 and 7.11 show that initially, for both considered hardnesses, there was a local increase in the temperature of the abradable across certain points across the rub. Consequently, it was expected that some of the energy of the blade to be transferred to the abradable surface and cause heat generation [111]. This was followed by material transfer on the blade and large adhesions started to form. Once the adhesion formed, pick-up continued on the same spot until the adhesion became too large and broke down. However, sometimes it was noted that adhesions re-initiated at exactly the same position even after breaking down. This suggested that at that positions there was a local variation in the abradable that led to high concentration of heat at those points. The observations made in the previous chapters supported this finding, as a pick-up mechanism was expected at the low incursion rate conditions.

The second observation was blade wear. This was clearly shown in figures 7.10 and 7.12. Blade wear occurred when the heat generated locally across the length of the rub built-up more and more. At some point some of this heat was diffused back to the blade causing thermal wear damage to it.

Finally, a clean efficient cutting mechanism took place when Metco 320 of any hardness was rubbed at high incursion rates. Chapters 5 and 6 highlighted this by showing that most of the material was removed from the front of the blade and the presence of

high tensile stress field generation in the abradable. Both of these observations suggested a chip formation cutting mechanism. The first and second columns of figure 7.13 further enhanced this observation as they showed that little to no adhesion of material took place at these conditions. Also the third column of this figure showed a much better distribution of heat across the surface of the abradable suggesting that the localities present in the abradable had less effect in heat dissipation.

The findings in this chapter were in great agreement with literature. Figure 7.18(a) shows an SEM image of the micro-structure of Metco 320, at two different positions in the abradable, taken in research carried out by Fois et al. [42]. This image was taken from a Metco 320 hardness of RY15 55. For comparison, figure 7.18(b) shows an SEM image of Metco 601 with the same nominal hardness (RY15 55), taken in the research presented in this thesis. By inspecting figure 7.18(a) the variation in hBN content became apparent. The left side shows a region with high hBN concentration, while the right side showed a region of low hBN concentration. This observation made by Fois et al. [42] greatly supported the finding of localised thermal diffusion in the abradable. In contrast, by inspecting figure 7.18(b), it could be seen that the polymer phase in the case of Metco 601 was much more evenly distributed supporting the finding that heat was also evenly diffused more evenly in the abradable.

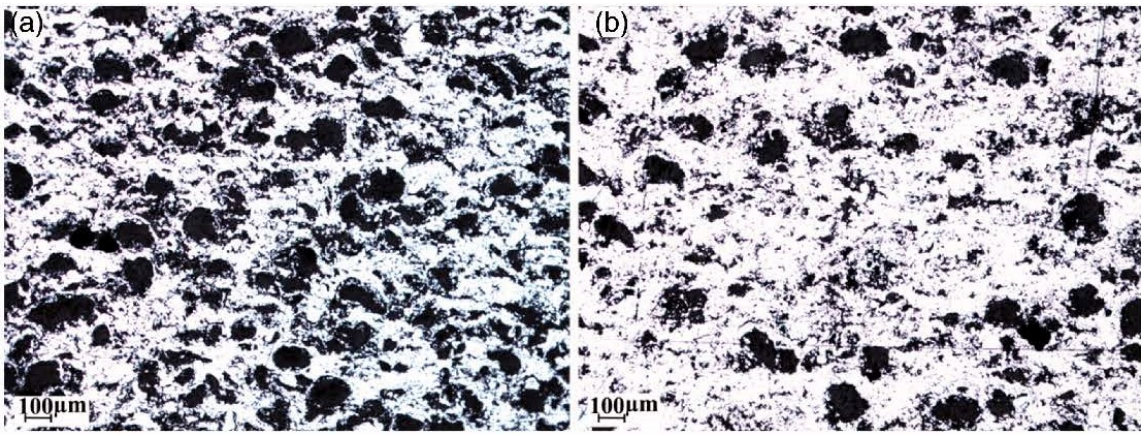

(a)

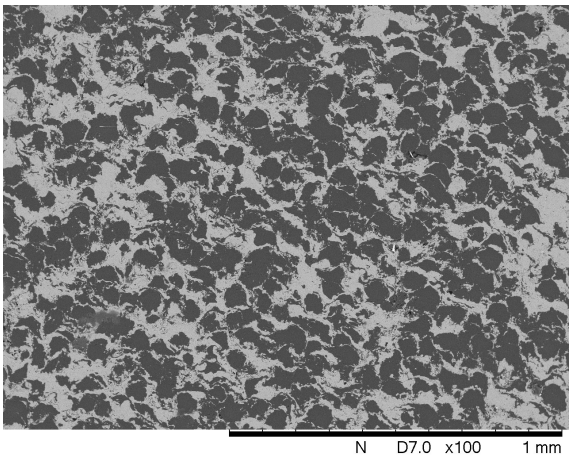

(b)

Figure 7.18: (a) SEM image that shows the micro-structure of RY15 55 Metco 320 at two different positions [42], (b) SEM that shows the micro-structure of RY15 55 Metco 601.

7.4.4 Development of novel testing methodology

The novel testing methodology developed in this chapter, provided a very powerful tool to examine the thermal response of the abradable and link it to the wear response observed on the blade. This was also done while the contact was happening so the connection between the thermal effects and wear mechanisms could be observed while they were happening and not by post-test analysis. Finally this technique could be used to analyse the response of any abradable and not just the two abradables considered in this thesis. Overall, this methodology is a significant addition to the way abradable materials are investigated providing a lot of invaluable information.

7.5 Conclusion

This chapter provided invaluable insight at the performance of the abradable materials considered by observing and explaining the relationship between the thermal response of the material and the resulting wear mechanism. This allowed some very important findings to be made and these were summarised below:

- RY15 82 Metco 601 was an unfavourable abradable material that caused high heat generation and blade wear across all testing conditions.
- RY15 55 and 70 hardness Metco 601 had very evenly distributed heat generation across the rub width. At low incursion rates, this resulted in adhesion that covered the whole width of the blade (across the rub), but was very thin. This mechanism caused adhesions to break-off easily when a "critical" value was reached and therefore no excessive adhesion was observed. Also this allowed the abradable surface to cool down enough, to avoid excessive build-up of heat that led to blade wear.
- At high incursion rates, RY15 55 and 70 hardness Metco 601, a similar thermal distribution pattern was observed. However, due to the higher energy of the contact, material was removed more easily and less amount of adhesion took place. Nevertheless, a degree of adhesion was always observed for these samples, even at high incursion rates.
- At low incursion rates the response of Metco 320 was highly influenced by the localities in the abradable structure. "Hot-spots" were generated at specific regions along the width of the rub (where concentration of hBN was high) and this led to long adhesions being formed. Once these "hot-spots" became hot enough, heat was diffused back to the blade causing thermal wear damage.
- At high incursion rate in the case of Metco 320 the heat was distributed more evenly on the abradable surface primarily because material was efficiently removed during these contacts. The hBN acted as a release agent and chips were formed readily dissipating the heat accumulated when ejected.
- The novel technique developed in this chapter provided a very powerful tool to link the thermal response of the abradable to the wear mechanism observed on the blade

Chapter 8

Discussion

The main aim of this thesis was to enhance the knowledge and understanding of the wear and material removal mechanisms that took place when a contact between one of the abrdables considered and a blade happened. The first section of this chapter put together all the findings of the individual chapters in order to explain what knowledge and understanding was gained by combining all the techniques and methodologies employed in these investigations. Another aim of this study was to improve the understanding of the difference in performance of the two considered abradables. A thorough discussion about the two materials was provided in this section, detailing the identified reasons as to why these materials had these differences. The aim of the discussion in this chapter was also to contexualise the research performed in this thesis and consider the impact it might have for engine manufactures. To this extent, the understanding and inferences gained from this thesis were used to provide possible suggestions on the improvement of current abradable technologies. Finally, the novel techniques developed in this study were discussed and assessed in terms of what was their contribution on this thesis and abradable research in general.

8.1 Findings and inferences

In this section all the findings made in this thesis were put together and used to explain the wear characteristics of the abradables considered.

8.1.1 Metco 601 performance

The first step towards the completion of the aims of this thesis was to provide a more extensive characterisation of the performance of Metco 601 and allow comparison to the testing data obtained from Metco 320. To this end, in chapter 4 an extensive test matrix was carried out investigating the performance of the abradable across a wide range of testing parameters. Outputs such as temperature, forces and the changes of the blade length resulting from adhesion and wear during the contact were examined. Moreover, the effect of testing parameters such as the incursion rate, the blade tip speed and material hardness were considered. This extensive testing has shown that the performance of Metco 601 could be categorised in two separate regions with high hardness Metco 601 being the one and the low and medium hardness being the other. This was because the performance of Metco 601 was drastically different to the other and needed to be considered separately.

High hardness Metco 601

From the extensive testing performed in chapter 4, it was identified that this material behaved very different from the other two hardnesses. This material showed blade wear behaviour across the whole test matrix considered, which included testing it at 5 different incursion rates in the operational range (0.02 - 2 μm/pass) and two blade tip speeds (100, 200 m/s). It was evident that the blade wear decreased with increasing incursion, while no significant effect was identified with the blade tip speed. However, even though blade wear improved with increasing incursion rate, it still took place even at the highest considered incursion rate. Also, it was identified that in the case of high hardness Metco 601, the forces and temperatures generated during the testing were much higher compared to the equivalent testing of the other hardnesses (see figures 4.3, 4.4, 4.6). A very useful observation of why this was the case was made by combining and overlaying the outputs collected during this testing. When the recorded force and temperature readings were overlaid on the recorded blade length change it was noticed that blade wear always followed after spikes of temperatures and forces (see figure 4.7).

At low incursion rate, the material also exhibited a cyclic behaviour, where spikes of forces and temperatures led to sudden wear followed by a period of lower forces, lower temperature and no wear (see figures 4.3, 4.4, 4.6). This suggested that the material was not removed at a pass by pass basis. Instead it was compressed for several passes.

This resulted in a material that became very hard causing the drastic increases in forces and temperature that eventually caused thermal wear damage on the blade. In chapter 5 this observation was reinforced when looking at the direction from which material was ejected during this contact. It was found that a much larger percentage of material was ejected from the back of the blade for these conditions, which further enhanced the hypothesis that the release mechanism was a compress and release rather than a chip formation mechanism (see figure 5.18 and table 5.2). Then the results of chapter 6 and 7 provided more insight to what drove this mechanism. Firstly, in chapter 6 it was shown that there were large regions of high compression in the abradable proving the hypothesised compression and release mechanism, which was described in section 2.2.2 (see figure 6.9). Also figure 6.4 highlights that material was not removed on at a pass by pass basis since a large number of passes was required until some material was cracked and removed. Furthermore, by looking at the analysis in chapter 7, it was shown that the surface of the rub was much hotter than other tested contacts and that a homogeneous increase of the abradable surface took place (see figure 7.17). By combining all these findings, it could be inferred that at this hardness and low incursion rate the blade did not have enough energy to remove a material this hard. Instead it was rubbing against it compressing it and making it even harder. This led to drastic increases in the global temperature of the abradable, as well as very high forces. The resulting temperatures and forces were enough to have a detrimental effect on the blade, causing it high amounts of thermal wear.

As incursion rate increased, the blade had more energy and it was able to remove material more easily. This was highlighted by the much higher force ratio observed in section 4.4.1 at the highest incursion rate (0.5 compared to 0.25 at low incursion rates), which suggested a more efficient cut mechanism. However, some blade wear still took place even at this conditions and by looking at the observation made in the other chapters this could be explained. Firstly, in figure 5.18 and table 5.2 in chapter 5, it was highlighted that for this material, the higher percentage of debris was still ejected from the back of the blade. In fact, there was minimal variation and improvement in the direction of material ejection with incursion rate (see figure 5.18). Moreover, it was found that, even though there were some regions of tensile strain fields being generated in the abradable, there were still very large regions of compressive strain fields, especially directly beneath the blade (figure 6.9). Finally, in chapter 7 it was suggested that the temperature of the abradable surface increased homogeneously across the width of the rub 7.17. All these observations led to the inference that at high incursion rates, the material release mechanism was a combination of a compress

and release mechanism with some degree of cutting. It was apparent that the compress and release mechanism was still the predominant mechanism, but the improvement in the performance of the abradable with incursion rate could be attributed to an increase in the amount of cutting that the blade could do due to the higher energy it had.

Concluding, Metco 601 at the highest considered hardness (RY15 82) was an unfavorable abradable. At this hardness the metal matrix phase was so dense and the polymer phase so scarce, that not enough release could be provided during the contact. Even at high incursion rates, the blade did not have the ability to easily form chips and remove material. Instead, the energy of the contact was transferred in the abradable and the blade resulting in large build-up of forces and temperature and eventually to blade wear. Finally, it should be noted that the worn blade caused much rougher abradable surfaces, which was a further disadvantage of Metco 601 at this hardness (see section 4.4.3). A schematic of the wear mechanisms that took place for this material was shown in figure 8.1.

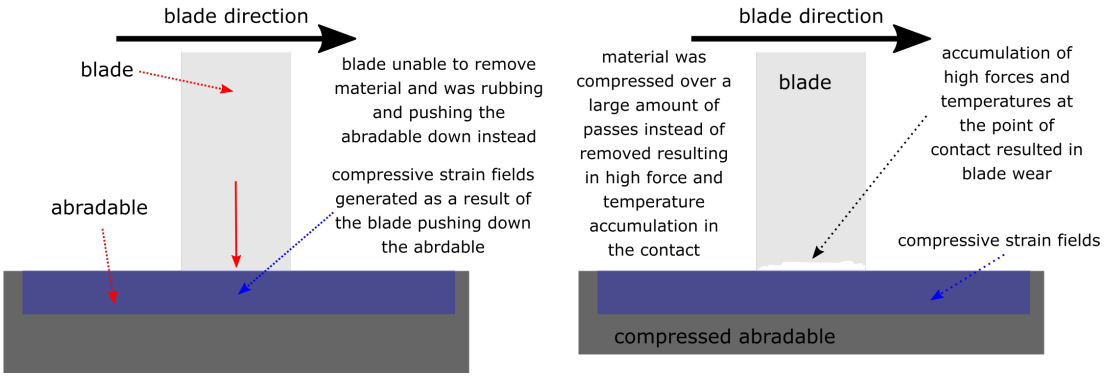

Figure 8.1: Schematic showing the wear mechanism of high hardness Metco 601.

Low and medium hardness Metco 601

For low and medium hardness Metco 601 the most apparent observation that could be made was that for both hardnesses a degree of adhesion took place across all the testing conditions. The observed adhesion progressively improved with increasing incursion rate and to a lesser extend with increasing blade tip speed. However, even at the highest incursion rate there was still a degree of adhesion happening. Having said that, the adhesion observed at the lowest incursion rate (worst condition that

caused high adhesions) was not as severe as the adhesions observed in the case of Metco 320. In fact, the performance of low and medium hardness could be described as moderate across the range of the tested incursion rates. This observation was then investigated in greater depth throughout this thesis to understand why this was the case.

At low incursion rates, it was found that low and medium incursion rate Metco 601 had a very high adhesion rate. However, it was noted that even though the rate of adhesion was very high, the maximum observed length of the adhesions was much shorter than expected, suggesting that adhesion rate did not have a direct correlation to material response like in the case of Metco 320. To understand this behaviour the force and temperature response of the material was investigated and it was found that as force and temperatures rose adhesions started to form. The observations made in section 4.4.1 (see figures 4.8(a), 4.9), suggested that a 'saw-tooth' adhesion mechanism took place for these materials where long and thin adhesion built-up (along the blade), but eventually broke before increasing too much in height. There was a need for further investigation into this mechanism so the material removal mechanism was investigated in more depth in chapters 5 and 6. The findings of these chapters showed that low and medium hardness Metco 601 exhibited a compress and release material removal mechanism (see section 2.2.2) when rubbed at low incursion rates. This was evident by the fact that there was a much higher percentage of material removed from the back of the blade (figure 5.18) and also that compressive strain fields were generated in the abradable (figure 6.10). It was also shown by the fact that it took a very large amount of passes to create cracks and remove material as shown in figure 6.5. Furthermore, chapter 7 showed that the temperature increase was homogeneous across the whole length of the rub resulting in adhesion that rubbed across the whole length of the blade (front-on observation). Combining this with the observation made in chapter 4 (side-on observation), that adhesions mostly initiated at the leading edge of the blade, this suggested that the adhesion built-up on the blade was long and thin and therefore very fragile. From this, it could be inferred that there was a critical height, at which, the adhered material did not have enough bonding strength on the blade and it broke-off when reaching it. This explained the "saw-tooth" effect observed in chapter 4 and the reason why adhesions were not as large in height as expected (with such high adhesion rate). It should be noted, that even though the temperature rose in the abradable due to the compress and release mechanism and this rise was enough to cause rapidly growing adhesions, it did not reach high enough temperature to cause blade wear. To explain this the nature of the

adhesion had to be considered. Due to the relatively homogeneous distribution of the phases in the structure of the abradable, heat was evenly distributed across the rub as shown in chapter 7 and figure 7.14, resulting in the pick-up to take place across the whole length of the blade. Long and thin pick-ups built-up very fast but also broke-down in one go very easily. When a formed pick-up broke-off there was a period of no contact. This was because due to pick-up there was a rub deeper than the actual incursion and this was homogeneous across the whole rub. This period of no contact was enough to provide some cooling of the abradable surface until contact re-initiated. As a result, the extremely high temperatures observed in Metco 320 at low incursion rates and caused blade wear, were not occurring for Metco 601. A schematic of the wear and material removal mechanisms that took place for this material at these low incursion rate conditions was shown in figure 8.2.

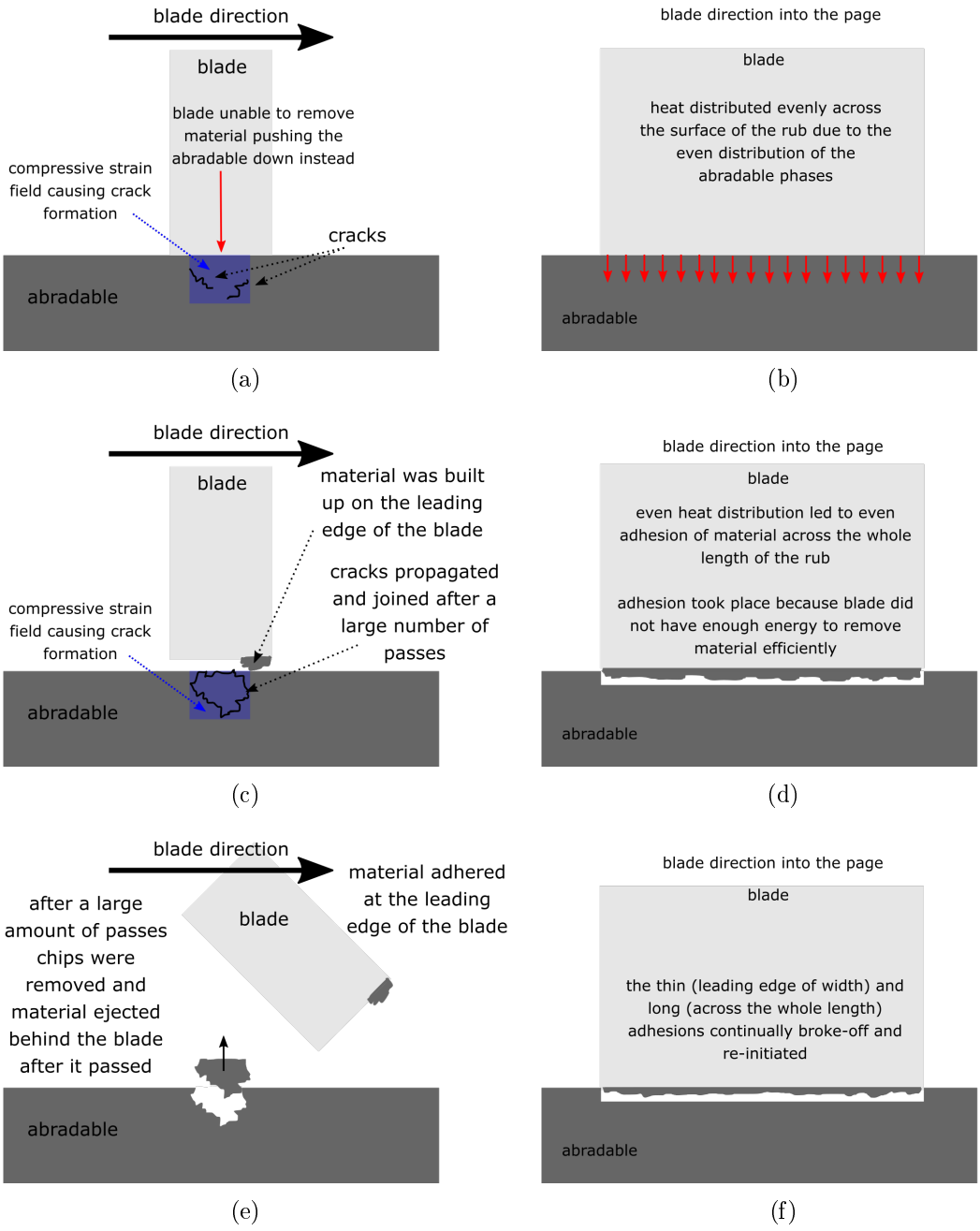

Figure 8.2: Schematic showing the wear mechanism of low and medium hardness Metco 601 tested at low incursion rate conditions (0.02 μm/pass). Figures (a), (c) and (e) show the material removal mechanism from the side of the contact, while figures (b), (d) and (f) show the adhesion mechanism and heat distribution from the front of the contact.

Similar observations were made at higher incursion rates, with the important difference that as incursion rate increased the cut became more efficient due to the ability

of the blade to better fracture the material and cause chips. The results obtained in chapter 5 clearly showed that the amount of material removed from the front of the blade was increased at higher incursion rates (from 38.5% at 0.02 μ/pass to 55.8 % at 2 μ/pass for the medium hardness Metco 601). However, it should also be noticed that the amount of material ejected from the back was still relatively high (44.2 %). This suggested that a combination of compress and release and chip formation cutting mechanisms took place, similar to the low incursion case. The important difference as incursion increased was that the chip formation efficient cut mechanism became more and more dominant over the compress and release mechanism. This observation was also confirmed by the results shown in chapter 6, where it was shown that much larger tensile strain fields were generated in the abradable surface, but some compressive strain regions still existed (see figure 6.11). Furthermore, large cracks were formed and removed as chips at a very high frequency (almost at pass by pass basis) as shown by figure 6.7. The temperature distribution shown in chapter 7 was again homogeneous across the surface of the rub proving why there was a similar adhesion pattern with the lower incursion rates observed. The effect of the incursion rate and the reason why adhesion was less at the higher incursion rates was therefore attributed to the higher energy of the blade which removed material more effectively. As a result more energy was dissipated in the ejected debris chips and less in the abradable surface. Consequently, lower overall temperatures led to less adhesion build-up.

A schematic of the wear and material removal mechanisms that took place for this material at these high incursion rate conditions was shown in figure 8.3.

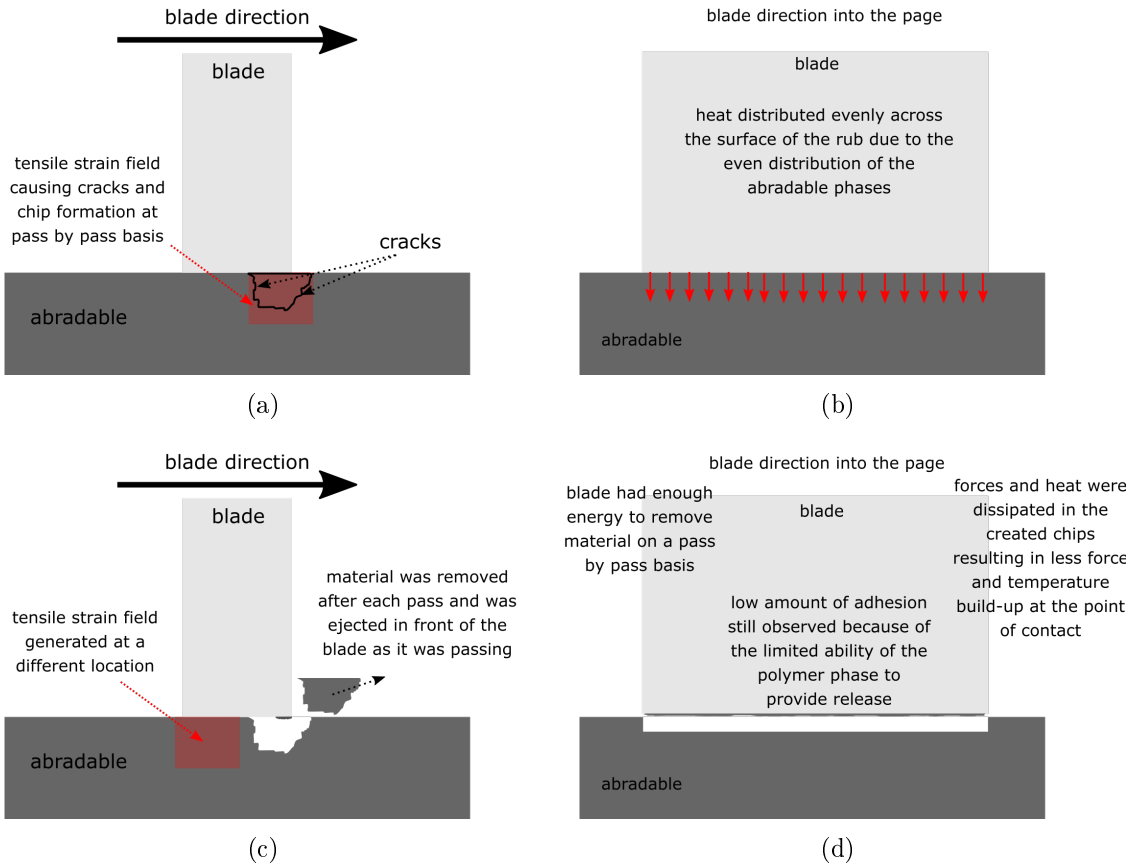

Figure 8.3: Schematic showing the wear mechanism of low and medium hardness Metco 601 tested at low incursion rate conditions (0.02 μm/pass). Figures (a) and (c) show the material removal mechanism from the side of the contact, while figures (b) and (d) show the adhesion mechanism and heat distribution from the front of the contact.

To conclude, Metco 601 performance was highly driven by the relatively homogeneous distribution of the phases in the composite. The positive aspect of this material was that at the worst operating conditions (0.02 μm/pass) where compression occurred, the even distribution resulted in an adhesion mechanism that was "self-cooling" preventing high temperature build-up and subsequently preventing blade wear (which was the most unfavorable output). The negative aspect of this material was the fact that the polyester phase could not provide enough release for a clean cut mechanism to take place even at the higher incursion rate conditions leading to a degree of adhesion to be present across all operating procedures. Even more worrisome, was the fact that at the highest considered hardness, the ability of the polymer phase to provide a release mechanism was so little that the blade was essentially rubbing against a very hard material causing detrimental blade wear.

To highlight all the collective insights that could be gained from the full methodology described in this thesis for Metco 601, figure 8.4 shows all the results that were produced for a single abradable testing condition. All the data shown in this figure was obtained from a RY15 70 Metco 601, tested at 200 m/s and 0.2 μm/pass. This figure emphasises how much information was gained from the methodologies developed in this thesis for this abradable.

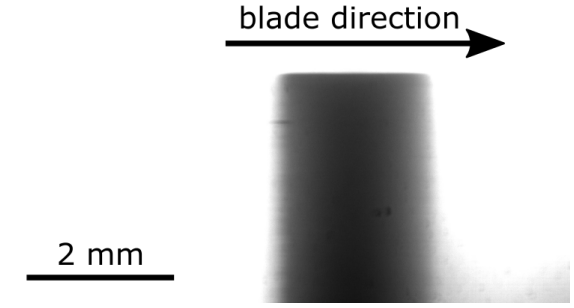

(a)

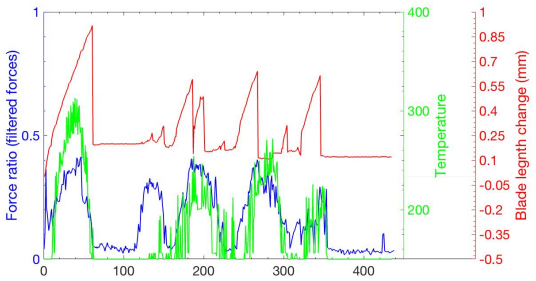

(b)

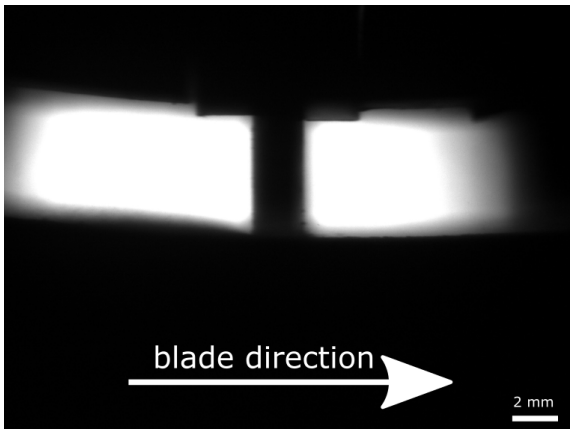

(c)

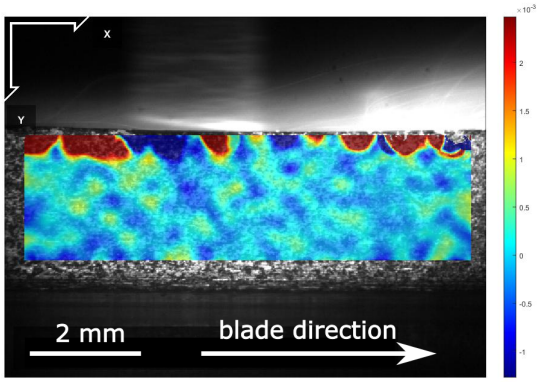

(d)

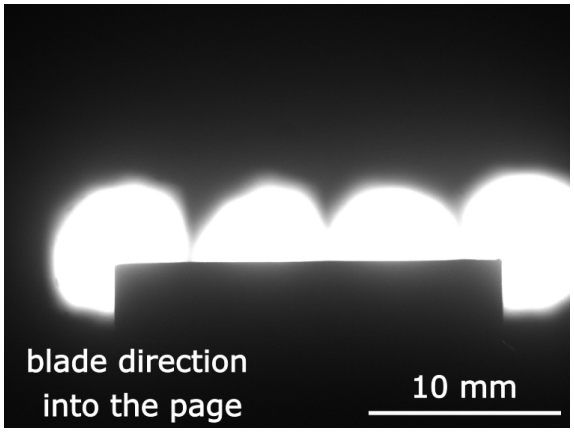

(e)

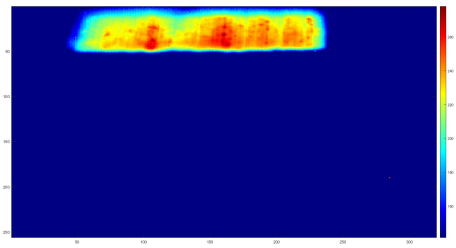

(f)

Figure 8.4: Collective results of all methodologies for one abradable condition. (a) Shows an image of the blade from the side-on camera, (b) Shows an example of the temperature, force ratio and blade length change overlay plots, (c) Shows an example of material removal and debris ejection mechanism, (d) Shows an example of DIC analysis to identify tensile and compressive regions, (e) Shows an image of the blade from the front-on camera, (f) Shows an image of the rub from the thermal camera.

8.1.2 Metco 320 performance

The observed behaviour of Metco 320 varied much more drastically with incursion rate. Firstly, in chapter 5 it was shown that at low incursion rates most of the material was ejected from the back of the blade (figure 5.18). Moreover, in chapter 6 it was emphasised by inspecting figure 6.12 that large compression fields were generated in the abradable. Also, figure 6.6 showed that cracks were formed over a large amount of passes and material was compressed over a long period of time before it was cracked and removed as a chip. Both of these findings suggested that the compress and release wear mechanism described in section 2.2.2 was taking place at the low incursion rate. Moreover, by inspecting the blade profile images in chapter 7, a combination of large adhesion and blade wear could be observed. These observations were shifted as incursion rate increased. The amount of material removed from the front of the blade was greatly increased (more drastic increase compared to Metco 601) and the compressive strain fields gave way to large tensile strain fields (much larger compare to equivalent Metco 601) as shown in figure 6.13. Material was also removed much more frequently (at a pass by pass basis) as shown in figure 6.8. Also, the large adhesions and blade wear were replaced by a relatively clean blade. This suggested that as incursion rate increased, the compress and release mechanism shifted to a chip formation cut mechanism much more in the case of Metco 320. Furthermore, hardness played a much more important role in the response of Metco 320. At higher hardness the material removed from the front of the blade was a bit more compared to the lower hardnesses and also larger tensile strain fields were generated in the material. This suggested that there was better cutting observed for Metco 320 at higher hardness values.

To summarise, the wear mechanism in the case of Metco 320 was governed by the incursion rate, since at low incursion rate adhesion and blade wear were observed, while at high incursion rate a clean cut mechanism took place. Finally, at higher hardness the wear mechanism that took place (and governed by the incursion rate) was more optimal.

As in the previous section to explain these observations, the nature of the abradable structure had to be considered. The thermal distribution across the rub results shown in chapter 7 provided invaluable insight to this context. Previous studies have emphasised the uneven distribution of the hBN phase in the structure of this abradable that was caused by the spraying process.

Low incursion rate

Firstly, lets consider the thermal response of the abradables at the lowest incursion rate. The results obtained in chapter 7 highlighted the way heat was diffused in the abradable surface. Unlike in the case of Metco 601 where heat was evenly distributed across the whole length of the rub, in the case of Metco 320 the heat was concentrated locally at specific points across the rub due to the highly localised nature of this abradable. Therefore the resulting adhesions were not uniform across the length of the blade, but rather localised at those "hot-spots". Furthermore, as this heat built-up even more, the heat started to be diffused back to the blade resulting to local, thermal wear damage on the blade at the position of that "hot-spot". This finding was clearly shown in figures 7.10 and 7.12 and it agreed in a great extent with literature. Fois et al. [42] used a thermal model to predict the heat dissipation in the abradable based on the distribution of its micro-structure. In that research, the formation of these 'hot-spots' was predicted in regions with high hBN concentration, as in the model hBN was acting like a thermal barrier. An example result of this modelling technique is shown in figure 8.5. This figure clearly shows that the model created by Fois et al. suggested the location of hot spots at hBN rich areas [42].

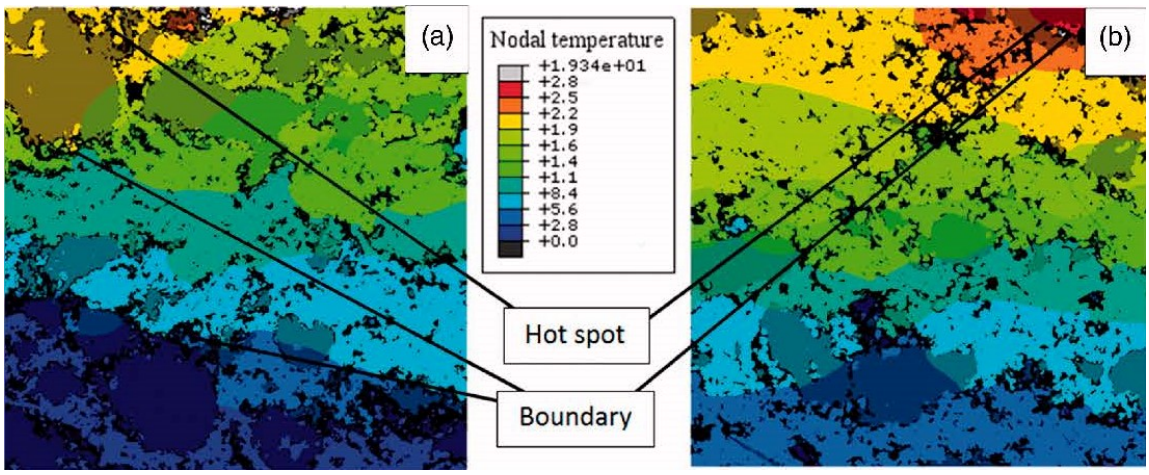

Figure 8.5: Thermal modelling showing the predicted heat dissipation in the abradable based on its microstructure. (a) An example estimated on a Metco 320 RY15 55, (b) An example estimated on a Metco 320 RY15 73 [42].

The hypothesis made in previous studies ([42]) have been proven by the observations made in this thesis. These observations could be explained by considering the uneven distribution of the hBN phase, resulting from the thermal spraying manufacturing

method, in relation to the material removal mechanism. Firstly, as mentioned previously, at low incursion rates material could not be removed effectively by the blade and a compress and release mechanism took place generating the heat in the surface of the rub. However, the structure of Metco 320 was highly uneven and this resulted in hBN "rich" and hBN "poor" regions. The hBN phase was present to help the material removal phase acting as a release agent and a solid lubricant. However, it was very bad at diffusing heat. Therefore, since at this low incursion rates the energy of the contact was not enough to remove material efficiently (even at areas with high concentration of hBN), the heat generated was accumulated in regions of the abradable that have a high concentration of hBN. This explained the local increase in the abradable surface at those points creating 'hot-spots'. When enough heat was accumulated it eventually started diffusing back to the blade causing the observed thermal damage on the blade.

A schematic of the wear and material removal mechanisms that took place for Metco 320 at these low incursion rate conditions was shown in figure 8.6.

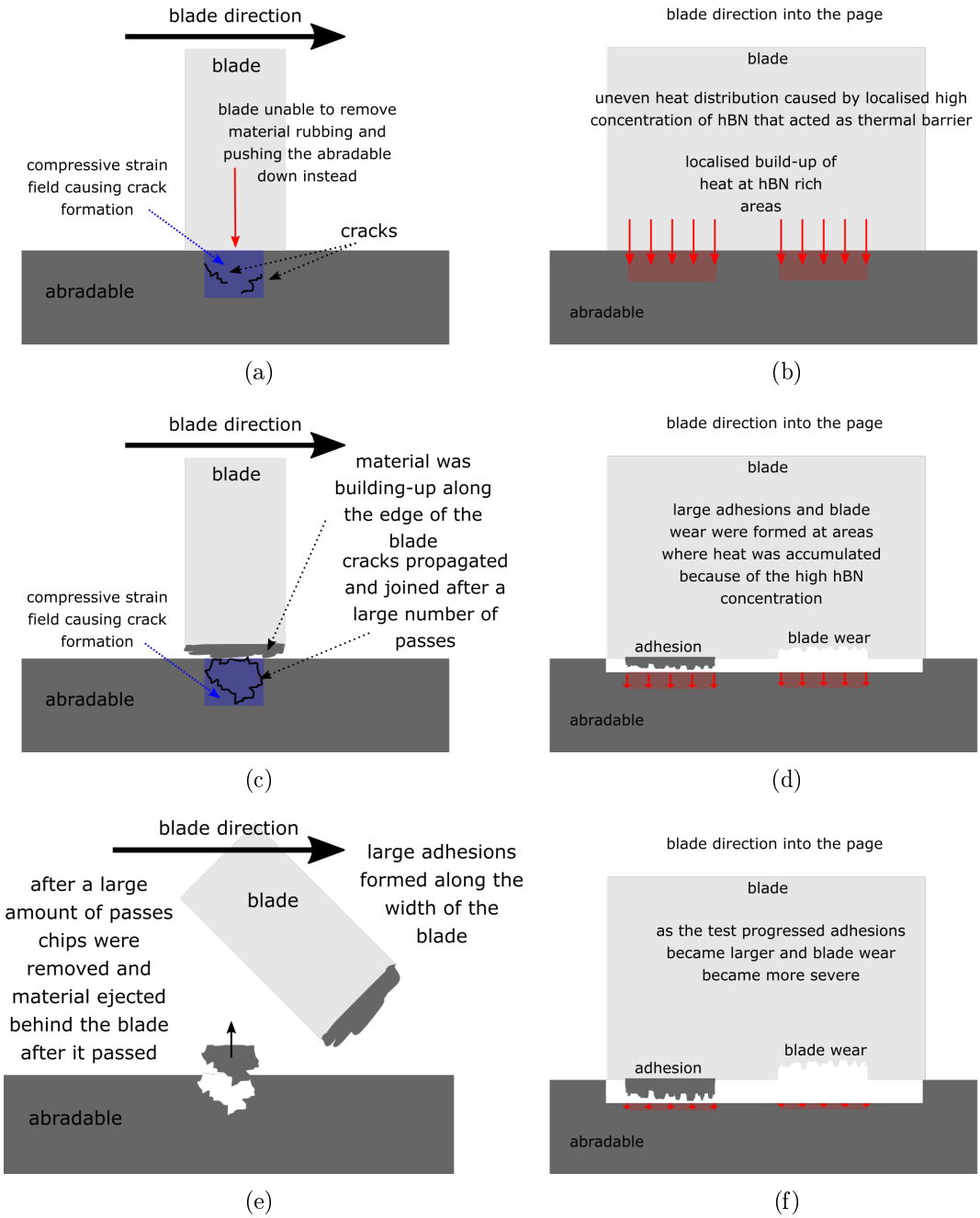

Figure 8.6: Schematic showing the wear mechanism of Metco 320 tested at low incursion rate conditions (0.02 μm/pass). Figures (a), (c) and (e) show the material removal mechanism from the side of the contact, while figures (b), (d) and (f) show the uneven heat distribution and the resulting adhesion and blade wear mechanisms that were observed from the front of the contact.

High incursion rate

Next, the response of the material when tested at high incursion rates was considered. From the observations made in the earlier chapters, it was expected that a clean

efficient cutting mechanism took place at high incursion rates. This was shown by the fact that most material was ejected at the front of the blade, while large regions of high tensile strain fields were generated in the abradable during the contact and material was removed frequently on pass by pass basis. By inspecting the stroboscopic imaging and the extracted blade profile (first and second columns in figure 7.13) it was identified that little to no adhesion took place at the edge of the blade. This finding further supported the hypothesis that chip formation and cutting material removal mechanism took place efficiently. Also, it was shown that at high incursion rates the heat diffused much better through out the abradable surface creating a more evenly distributed temperature variation across the rub. Some localities could still be observed (see figures 7.13(l) and 7.13(o)), but because material was removed so fast the heat was diffused in the chips formed. Therefore it could be concluded that at the higher incursion rates, the hBN worked greatly to facilitate chip formation and material removal and its bad thermal diffusivity drawback was not important because the energy was transferred to the chip that was removed.

A schematic of the wear and material removal mechanisms that took place for this material at these high incursion rate conditions was shown in figure 8.7.

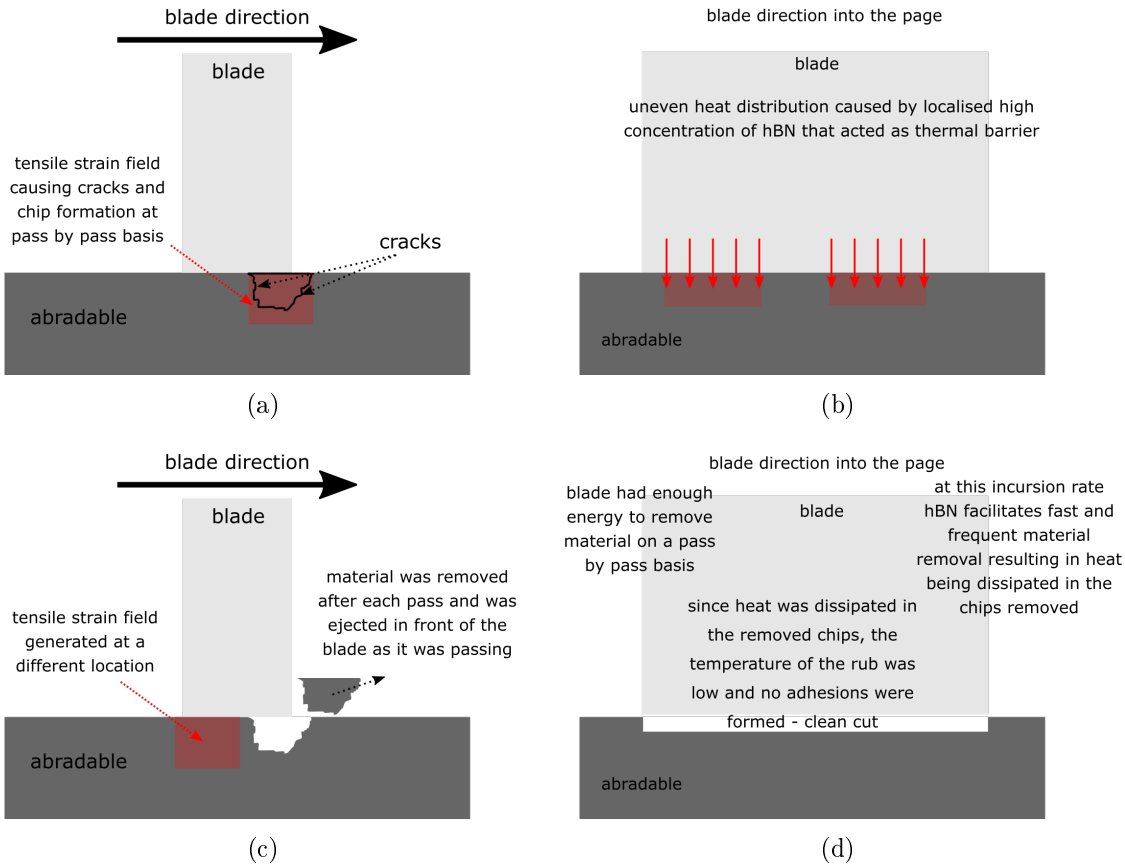

Figure 8.7: Schematic showing the wear mechanism of Metco 320 tested at high incursion rate conditions (2 μm/pass). Figures (a) and (c) show the material removal mechanism from the side of the contact, while figures (b) and (d) show the cutting mechanism and chip heat dissipation from the front of the contact.

Effect of hardness

Finally, the effect of hardness needed to be considered. Increasing hardness slightly improved the wear mechanism because of better heat partition at the contact. This was more evident in low incursion rates where, even though concentration of hBN was less (less release), the wear mechanism was slightly better due to better heat distribution (more metal phase led to better heat distribution). However, the wear mechanism was still governed and influenced in much greater extent from incursion rate.

To summarise, the performance of Metco 320 was governed by the local variations in its micro-structure. High concentration of hBN caused uneven heat dissipation and the creation of "hot-spots" at low incursion rates. This resulted in the accumulation of

heat and the formation of adhesion and blade wear [111]. At high incursion rates hBN acted as a release agent and initiated chip formation resulting in good cutting.

Figure 8.8 provides all the information gained on Metco 320 by carrying out the techniques developed in this thesis. The data shown in this figure was obtained from a RY15 58 Metco 320, tested at 200 m/s and 0.02 μm/pass. This was done to emphasise the localised behaviour of the abradable that was more evident at this low incursion rates where chip formation could not be initiated.

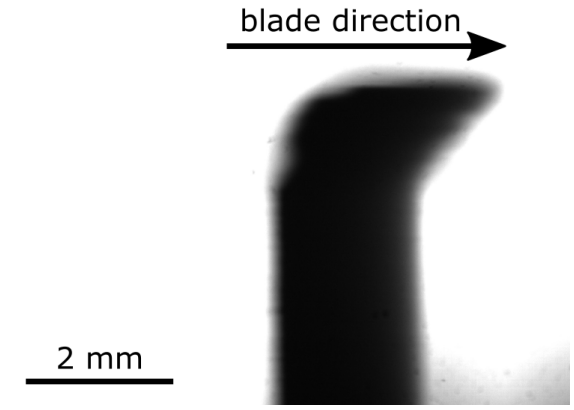

(a)

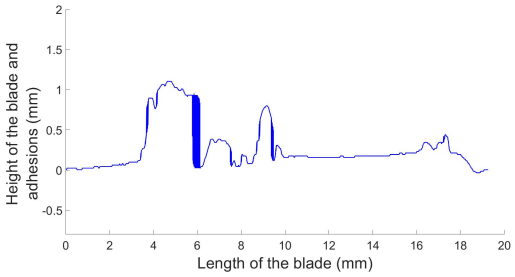

(b)

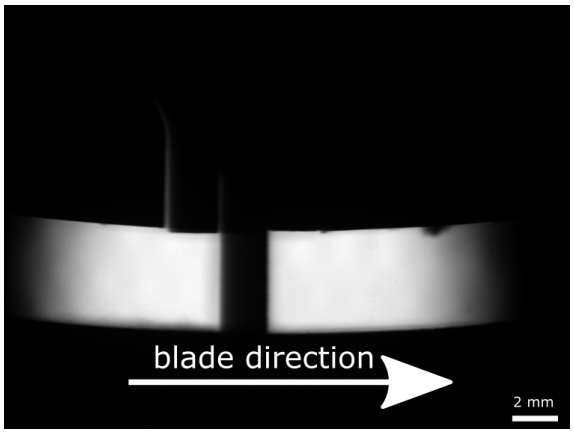

(c)

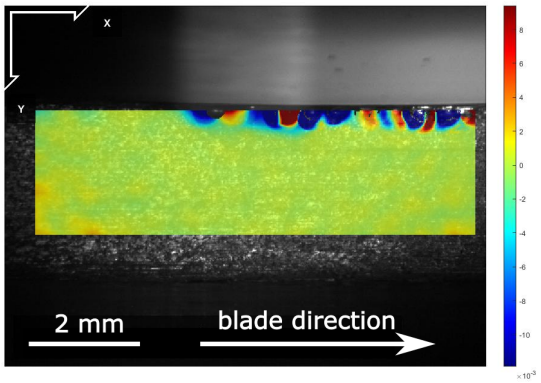

(d)

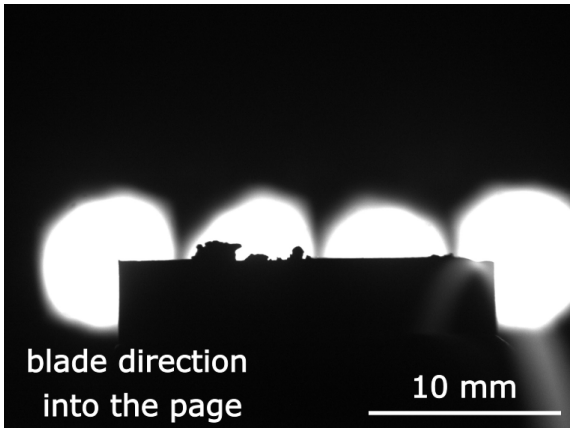

(e)

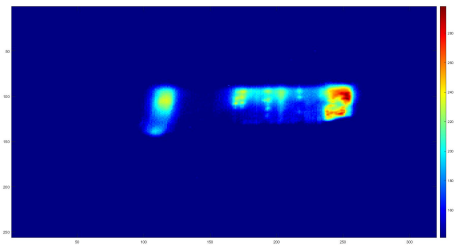

(f)

Figure 8.8: Collective results of all methodologies for one abradable condition. (a) Shows an image of the blade from the side on camera, (b) Image of front-on blade profile observation, (c) Shows an example of material removal and debris ejection mechanism, (d) Shows an example of DIC analysis to identify tensile and compressive regions, (e) Shows an image of the blade from the front on camera, (f) Shows an image of the rub from the thermal camera.

8.2 Differences between Metco 601 and Metco 320

In this section the differences in the performance of Metco 601 and Metco 320 were explained in terms of the identified response of the materials. The main difference, which caused a significantly different performance, was the distribution of the composite phases in the two abradables. Metco 320 was highly localised, leading to areas of higher hardness than the nominal value (high metal concentration) and area of lower hardness, but worse heat partition response (high hBN concentration). Metco 601 was much more evenly distributed and this variation was not so apparent. As a result, the two materials exhibited vastly different thermal response. The uneven distribution of the phases in the cases of Metco 320 resulted in very poor response at low incursions where the blade did not have enough energy to chip the material. Contrary to this, the response of Metco 601 was slightly better at low incursion rates and could be considered moderate.

However, at higher incursion rates, where the blade had enough energy to remove material, the ability of hBN to act as a release agent and a solid lubricant to provide much better fracture and chip formation became much more significant. This resulted in an excellent response of Metco 320 at high incursion rates where the blade had enough energy for cutting. In contrast, the polyester phase present in Metco 601 did not provide this easy release, so at higher incursion rates response was improved, but it was never excellent.

Finally, hardness did not influence too much the performance of Metco as long as the highest hardness was avoided. In the case of Metco 320 higher hardness (within the specification limits) provided slightly better response due to the lower concentration of the hBN phase. This provided slightly better thermal diffusion properties to the material effectively slightly improving its response.

8.3 Contexualising findings

In this section the key findings were contexualised in terms of significance to the manufacturer and suggested improvements in the current abradables were provided. The first obvious suggestion is that the upper operational hardness limit for Metco 601 needs to be lowered. At this hardness the performance of Metco 601 was detrimental to the blade and must be avoided.

In terms of which material was better the engine manufacturers have to consider a few factors. Firstly, Metco 601 is moderate and can be acceptable across a wide range of incursions. This suggested that it is a material that never shows very poor performance and it can be employed in "high risk" regions. At the same time, the performance of Metco 601 was never excellent and the material has very little room for improvement since its limitations arise from the difficulty of polymer phase to provide release.

On the other hand, Metco 320 had both, very poor (low incursion rate) and excellent (high incursion rate) operating regions. If it is possible to avoid operating at low incursion rates (by maybe adjusting running and handling procedures) it is generally better than Metco 601. Furthermore it has great room for improvement. If the issue of segregation is solved the performance of the abradable can be greatly enhanced even at the worst operating conditions. A possible solution to this might be to change the manufacturing method to something that produces a more structured abradable micro-structure with the same components (metal and hBN phases). Further more, since it was identified that increasing hardness was beneficial for the performance of the abradable (within the specification limits), it is recommended to use higher hardness Metco 320 where possible.

8.4 Novel methodology development

This sections summarises the novel techniques developed in this thesis that are used as tools to provide valuable knowledge and understanding on the development of the wear mechanisms and the material response of the considered contacts.

The first novel output was the development of a technique that allowed the observation of the material removal while the contact was happening (chapter 5). This included the testing methodology for the observation of the contact and also the development of the analysis methodology to produce useful outputs. The outcomes of this technique provided very valuable information on the nature of the material release and removal mechanism. Another very important aspect was that this methodology could be used to test and analyse any abradable and not just the two considered in this thesis.

The second novel methodology development was the methodology followed in chapter 6. The novelty in this technique was how an existing tool, such as DIC, was used to monitor the contact and provide real-time output of great significance. The approach

described in this thesis was just a first attempt and this methodology has great room for improvement, but nevertheless, this thesis showed that it could be a very powerful tool to understand the performance of any abradable.

Furthermore, the introduction of a thermal camera and the combination with the front on stroboscopic imaging technique was another novel and very powerful tool for analysing and understanding abradable response. The methodology provided in chapter 7 provided information about thermal variation and distribution in the abradable surface during the rub and linked it to the observed wear mechanism taking place on the blade. This was a very powerful tool that provided a new approach to investigate abradable materials. This was also a first attempt and it can be further improved to provide even more valuable outputs.

Chapter 9

Conclusion

In this section the main outcomes and findings of the investigation of this thesis are summarised:

- Extensive testing of Metco 601 across a wide range of testing conditions was performed providing much more information about the overall performance of this material.
- It was found that low and medium hardness Metco 601 exhibited a degree of adhesion across all testing conditions. There was an improvement of this mechanism with increasing incursion rate, but nevertheless, adhesion always took place. This observation was attributed to the polyester phase of the abradable. At low incursion rates (where the blade did not have enough energy to remove material) the more even distribution of this phase prevented the build-up of heat which resulted in blade wear. However, at high incursion conditions the polyester phase did not provide enough release mechanism for a highly efficient cut.
- At the highest considered hardness, Metco 601 showed wear at all testing conditions. The severity of the wear improved with increasing incursion rate, but it was not eliminated. This was unwanted behaviour and this material should be avoided.
- In the case of Metco 320 the response of the material was primarily influenced by the incursion rate. At low incursion rates very long adhesions and blade wear were observed, while at high incursion rates a cutting mechanism was observed. This was attributed to the uneven distribution of the hBN phase. At low incursions, where the blade could not remove material effectively, this was

detrimental as it led to localised build-up of heat in the surface of the abradable ("hot-spots"). This in turn resulted in high amounts of localised adhesion and even localised wear. At high incursion rates, where material could be removed, the ability of hBN to act as a releasing agent and solid lubricant dominated the performance resulting in a cutting mechanism.

- It was shown that the effect of hardness was not so significant to the wear mechanism in the case of Metco 601 (as long as the highest hardness was avoided). In contrast, higher hardness benefited to an extent the wear response of Metco 320 (incursion rate was still more significant).
- It was shown that due to the nature of the wear mechanisms that governed it, wear/adhesion rate was not effective in mapping the performance of Metco 601. A combination of total volume of adhered material and surface roughness mapping was suggested to be used instead.
- An important output of this thesis was the development of novel powerful techniques that were used to analyse different aspects of the abradable response. These included the development of a methodology to observe the material removal mechanism during the contact, another technique that studied the development of tensile and compressive stress fields in the abradable and finally a methodology to observe the thermal variation of the abradable surface during a rub and link it to the wear mechanism observed on the blade at the same time. These techniques were powerful tools that could provide invaluable insight for any abradable contact.

Chapter 10

Future Work

In this section potential extensions on the research preformed in this thesis were considered. Firstly, a new and novel higher speed rig is being developed by the University of Sheffield Abradables Group. This new experimental platform will allow blade tip speeds up to 380 m/s, which is more representative of engine blade tip speeds. Even though it was shown in this investigation that the effect of speed was not so significant, it is worth replicating the techniques developed and carried out in this study to higher speeds.

Moreover, a high temperature experimental platform is being developed by the University of Sheffield Abradables Group. In this high temperature test rig, the blade tip temperature is controlled via an induction coil to replicate engine temperature conditions. Replicating the tests carried out in this thesis is a great way to assess the effect of environment temperature in the resulting wear mechanisms.

Another extension that can be done using the work of this thesis, is to test any other abradable of interest with the novel techniques developed. These techniques can provide invaluable insight and fundamental understanding on the performance of any abradable and the wear mechanisms when they are rubbed.

Other improvements that can be made in this thesis is the improvement of the image processing techniques used throughout this thesis and especially the image processing of chapter 5. It was not the scope of this thesis to develop a perfect image processing technique, but by improving the current suggested analysis method more robust and repeatable results could be obtained. Also the current solution was very computationally expensive and improvements in the analysis code might rectify this challenge.

References

[1] B. Mokrani, *Piezoelectric Shunt Damping of Rotationally Periodic Structures*. PhD thesis, 01 2015.

[2] *Loss Mechanisms in Turbomachines*, vol. Volume 2: Combustion and Fuels; Oil and Gas Applications; Cycle Innovations; Heat Transfer; Electric Power; Industrial and Cogeneration; Ceramics; Structures and Dynamics; Controls, Diagnostics and Instrumentation; IGTI Scholar Award of *Turbo Expo: Power for Land, Sea, and Air*, 05 1993. V002T14A001.

[3] C. Sieverding and V. K. I. for Fluid Dynamics, *Tip Clearance Effects in Axial Turbomachines: April 15-19, 1985*. Lecture Series. Von Karman Institute for Fluid Dynamics, Von Karman Institute for Fluid Dynamics, 1985.

[4] J. Storer and N. Cumpsty, "Tip leakage flow in axial compressors," 1990.

[5] A. John, S. Shahpar, and N. Qin, "FAN BLADE TIP AERODYNAMICS WITH REALISTIC OPERATIONAL CASING," pp. 1–14, 2017.

[6] J. Zhong, S. Han, H. Lu, and X. Kan, "Effect of tip geometry and tip clearance on aerodynamic performance of a linear compressor cascade," *Chinese Journal of Aeronautics*, vol. 26, no. 3, pp. 583–593, 2013.

[7] M. O. Borel, A. R. Nicoll, H. W. Schlapfer, and R. K. Schmid, "The wear mechanisms occurring in abradable seals of gas turbines," *Surface and Coatings Technology*, vol. 39-40, no. C, pp. 117–126, 1989.

[8] S. Metco, "Improve Efficiency and Reduce Emissions with Abradable Coatings for Steam Turbines." www.oerlikon.com/ecomaXL/files/metco/oerlikon_SF-0016.1_Steam_Turbine_Abradables_EN.pdf, 2014.

[9] S. Wilson, "Thermally sprayed abradable coating technology for sealing in gas turbines," *Future of gas turbine technology, 6th International Conference*, pp. 1–9, 2012.

[10] H. I. Faraoun, T. Grosdidier, J. L. Seichepine, D. Goran, H. Aourag, C. Coddet, J. Zwick, and N. Hopkins, "Improvement of thermally sprayed abradable coating by microstructure control," *Surface and Coatings Technology*, vol. 201, no. 6, pp. 2303–2312, 2006.

[11] N. P. Hopkins, "Seal between relatively moveable members," June 7 2011. US Patent 7,955,049.

[12] G. Pattinson and A. Hewitt, "Abradable liner," Nov. 4 2014. US Patent 8,876,466.

[13] R. E. Johnston, "Mechanical characterisation of AlSi-hBN, NiCrAl-Bentonite, and NiCrAl-Bentonite-hBN freestanding abradable coatings," *Surface and Coatings Technology*, vol. 205, no. 10, pp. 3268–3273, 2011.

[14] M. Watson, *Modifications to blade tips in abradable contacts*. PhD thesis, University of Sheffield, 2017.

[15] N. Fois, *Investigation and characterisation of the wear mechanisms of abradable compressor linings*. PhD thesis, University of Sheffield, 2015.

[16] R. G. Bayer, *Wear analysis for engineers*. Hnb Pub., 2002.

[17] S. Metco, "Solutions Flash Cause and Effect of Metco 320NS Spray Parameters for Optimization of Coating Hardness and Service Life," *Online*, no. April, pp. 1–6, 2008.

[18] Oerlikon Metco, "Aluminum Silicon Polymer Thermal Spray Powders," *Dsmts-0016.6*, pp. 1–4, 2017.

[19] J. R. Davis *et al.*, *Handbook of thermal spray technology*. ASM international, 2004.

[20] Oerlikon Metco, "Material Product Data Sheet Aluminum Silicon Hexagonal Boron Nitride Abradable," *Dsmts-0017.3*, pp. 1–3, 2014.

[21] Oerlikon Metco, "Material Product Data Sheet Nickel Chromium Tungsten Molybdenum Superalloy Powders," pp. 1–4, 2019.

[22] M. Vardelle and P. Fauchais, "Plasma spray processes: diagnostics and control?," *Pure and Applied Chemistry*, vol. 71, no. 10, pp. 1909–1918, 1999.

[23] M. Dorfman, P. Fiala, K. Hajmrle, and S. Wilson, "Future abradable requirements needed by aerospace oem's and their material and equipment suppliers," in *Turbo Expo: Power for Land, Sea, and Air*, vol. 47942, pp. 17–24, 2007.

[24] L. Pawlowski, *The science and engineering of thermal spray coatings*. John Wiley & Sons, 2008.

[25] O. Metco, "Atmospheric Plasma Spray Solutions." www.oerlikon.com/ecomaXL/files/metco/oerlikon_BRO-0006.6_Atmospheric_Plasma_Solutions_EN.pdf, 2017.

[26] G. Bondarenko and L. Khizhnyak, "Experimental investigation of a honeycomb seal," *Chemical and Petroleum Engineering*, vol. 14, no. 9, pp. 793–795, 1978.

[27] R. Tolokan, A. Erickson, and R. Frank, "Blade tip and knife edge rub testing of feltmetal® seals," in *Turbo Expo: Power for Land, Sea, and Air*, vol. 79665, p. V01BT02A060, American Society of Mechanical Engineers, 1980.

[28] G. Tilly, "Erosion caused by impact of solid particles," in *Treatise on Materials Science & Technology*, vol. 13, pp. 287–319, Elsevier, 1979.

[29] C. E. Smeltzer, M. E. Gulden, S. S. McElmury, and W. A. Compton, "Mechanisms of sand and dust erosion in gas turbine engines.," tech. rep., SOLAR TURBINES INTERNATIONAL SAN DIEGO CA, 1970.

[30] J. Burnell-Gray, P. K. Datta, and P. K. Datta, *Surface Engineering Casebook: Solutions to corrosion and wear-related failures*. Woodhead Publishing, 1996.

[31] S. Kuroda and T. Clyne, "The quenching stress in thermally sprayed coatings," *Thin solid films*, vol. 200, no. 1, pp. 49–66, 1991.

[32] N. Zheng, M. Däubler, K. Schweitzer, W. Hensle, and H. Schlegel, "Development of air seal systems for modern jet engines," *Munich: MTU Aero Engines GmbH*, pp. 1–9, 2003.

[33] H. K. Toenshoff and B. Denkena, "Basics of cutting and abrasive processes," 2013.

[34] R. K. Schmid, F. Ghasripoor, M. Dorfman, and X. Wei, "An overview of compressor abradables," in *ITSC 2000*, pp. 1087–1093, ASM International, 2000.

[35] R. Schmid, "New high temperature abradables for gas turbines [ph. d. thesis]," *Zurich, Swiss: Swiss Federal Institute of Technology*, 1997.

[36] N. P. Hopkins, *Abradable coatings-From black art, to materials science*. Swansea University (United Kingdom), 2007.

[37] M. Bounazef, S. Guessasma, and B. A. Saadi, "The wear, deterioration and transformation phenomena of abradable coating BN-SiAl-bounding organic element, caused by the friction between the blades and the turbine casing," *Materials Letters*, vol. 58, no. 27-28, pp. 3375–3380, 2004.

[38] R. E. Chupp, M. F. Aksit, F. Ghasripoor, N. A. Turnquist, S. Dinc, J. Mortzheim, and M. Demiroglu, "Development of advanced seals for industrial turbine applications," in *2001 NASA Seal/Secondary Air System Workshop, vol. 1*, vol. 1, pp. 127–149, 2002.

[39] R. Ghasripoor, F.and Schmid, Dorfman, and L. M.R., Russo, "A review of clearance control wear mechanisms for low temperature aluminium silicon alloys," *Proceedings of the 15th International Thermal Spray Conference*, vol. 25-29, pp. 139–144.

[40] N. Fois, J. Stringer, and M. Marshall, "Adhesive transfer in aero-engine abradable linings contact," *Wear*, vol. 304, no. 1-2, pp. 202–210, 2013.

[41] N. Fois, M. Watson, J. Stringer, and M. Marshall, "An investigation of the relationship between wear and contact force for abradable materials," *Proceedings of the Institution of Mechanical Engineers, Part J: Journal of Engineering Tribology*, vol. 229, no. 2, pp. 136–150, 2015.

[42] N. Fois, M. Watson, and M. Marshall, "The Influence of the Superficial Hardness on the Wear of Abradable Materials," apr 2016.

[43] M. Watson, N. Fois, and M. Marshall, "Effects of blade surface treatments in tip–shroud abradable contacts," *Wear*, vol. 338-339, pp. 268–281, 2015.

[44] M. Watson and M. Marshall, "A Novel Image Segmentation Approach for Microstructure Modelling," *Coatings*, vol. 7, no. 10, p. 166, 2017.

[45] X. Ma and A. Matthews, "Evaluation of abradable seal coating mechanical properties," *Wear*, vol. 267, no. 9-10, pp. 1501–1510, 2009.

[46] X. Ma and A. Matthews, "Investigation of abradable seal coating performance using scratch testing," *Surface and Coatings Technology*, vol. 202, no. 4-7, pp. 1214–1220, 2007.

[47] G. Sutter, S. Philippon, and F. Garcin, "Dynamic analysis of the interaction between an abradable material and a titanium alloy," *Wear*, vol. 261, no. 5-6, pp. 686–692, 2006.

[48] M. Yi, J. He, B. Huang, and H. Zhou, "Friction and wear behaviour and abradability of abradable seal coating," *Wear*, vol. 231, no. 1, pp. 47–53, 1999.

[49] Y. Maozhong, H. Baiyun, and H. Jiawen, "Erosion wear behaviour and model for abradable seal coating," *Wear*, vol. 252, no. 1-2, pp. 9–15, 2002.

[50] D. Sporer, S. Wilson, P. Leader, and M. Giannozzi, "On the Potential of Metal and Ceramic Based Abradables in Turbine Seal Applications," *Proceedings of the thirty-sixth turbomachinery symposium*, pp. 79–86, 2007.

[51] J. Stringer and M. Marshall, "High speed wear testing of an abradable coating," *Wear*, vol. 294-295, pp. 257–263, 2012.

[52] J. Williams, *Engineering Tribology*. Cambridge University Press, 2005.

[53] V. P. Astakhov, "A treatise on material characterization in the metal cutting process. part 1: A novel approach and experimental verification," *Journal of Materials Processing Technology*, vol. 96, no. 1-3, pp. 22–33, 1999.

[54] V. P. Astakhov, "A treatise on material characterization in the metal cutting process. part 2: Cutting as the fracture of workpiece material," *Journal of Materials Processing Technology*, vol. 96, no. 1-3, pp. 34–41, 1999.

[55] T. Kato and H. Fujii, "Energy partition in conventional surface grinding," 1999.

[56] M. Watson and M. Marshall, "Wear mechanisms at the blade tip seal interface," *Wear*, vol. 404-405, pp. 176–193, 2018.

[57] S. Baiz, J. Fabis, X. Boidin, and Y. Desplanques, "Experimental investigation of the blade/seal interaction," *Proceedings of the Institution of Mechanical Engineers, Part J: Journal of Engineering Tribology*, vol. 227, no. 9, pp. 980–995, 2013.

[58] R. Mandard, J.-F. F. Witz, Y. Desplanques, J. Fabis, and J. Meriaux, "Wavelet Analysis of Experimental Blade Vibrations During Interaction With an Abradable Coating," *Journal of Tribology*, vol. 136, no. 3, p. 31102, 2014.

[59] R. Mandard, J. F. Witz, X. Boidin, J. Fabis, Y. Desplanques, and J. Meriaux, "Interacting force estimation during blade/seal rubs," *Tribology International*, vol. 82, no. PB, pp. 504–513, 2014.

[60] R. Mandard, Y. Desplanques, G. Hauss, J. Fabis, J.-F. Witz, and J. Meriaux, "Mechanisms of incursion accommodation during interaction between a vibrating blade and an abradable coating," *Wear*, vol. 330-331, pp. 406–418, 2015.

[61] W. Hougang and H. Wang, "Criteria for Analysis of Abradable Coatings," *Surface and Coatings Technology*, vol. 79, no. 1-3, pp. 71–75, 1996.

[62] R. Bolot, J. L. Seichepine, J. H. Qiao, and C. Coddet, "Predicting the thermal conductivity of AlSi/polyester abradable coatings: Effects of the numerical method," *Journal of Thermal Spray Technology*, vol. 20, no. 1-2, pp. 39–47, 2011.

[63] M. H. F. Peyraut, J.-L. Seichepine, C.Coddet, "Finite element modeling of abradable materials – Identification of plastic parameters and issues on minimum hardness against coating's thickness F.," *International Journal for Simulation and Multidisciplinary Design Optimization.*, vol. 1, no. 1, pp. 209–215, 2007.

[64] M. Legrand, A. Batailly, and C. Pierre, "Numerical Investigation of Abradable Coating Removal in Aircraft Engines Through Plastic Constitutive Law," *Journal of Computational and Nonlinear Dynamics*, vol. 7, no. 1, p. 011010, 2012.

[65] R. Baddi, "Differential stroboscope for physics lab," *arXiv preprint arXiv:1205.4606*, 2012.

[66] L. Michalski, K. Eckersdorf, J. Kucharski, and J. McGhee, "Temperature measurement," 2002.

[67] MICRO-EPSILON, "Basics of non contact temperature measurement." www.micro-epsilon.com/download/products/dat–infrared-basics–en.pdf.

[68] G. A. Sileo, "Method for producing an abradable seal," 7 1998.

[69] E. Lugscheider, J. Zwick, M. Hertter, and D. Sporer, "Control of coating properties of abradable seals by on-line process diagnostics," in *International Thermal Spray Conference (ITSC), Basel, Switzerland*, 2005.

[70] M. Sulzer, "Material Product Data Sheet Aluminum Oxide Thermal Spray Powders," vol. 445, pp. 1–4, 2012.

[71] ASTM E18-15, "Standard Test Methods for Rockwell Hardness of Metallic Materials," *ASTM International*, pp. 1–38, 2015.

[72] W. Parker, R. Jenkins, C. Butler, and G. Abbott, "Flash method of determining thermal diffusivity, heat capacity, and thermal conductivity," *Journal of applied physics*, vol. 32, no. 9, pp. 1679–1684, 1961.

[73] G. Welsch, R. Boyer, and E. Collings, *Materials properties handbook: titanium alloys*. ASM international, 1993.

[74] J. Holman, "Heat transfer, 2002," *McGrawHill, New York, USA*.

[75] D. Sporer and S. Wilson, "Current and next-generation titanium blade compatible compressor abradable coatings," 05 2012.

[76] G. Welsch, R. Boyer, and E. Collings, *Materials properties handbook: titanium alloys*. ASM international, 1993.

[77] W. Laverty, "Rub energetics of compressor blade tip seals," *Wear*, vol. 75, no. 1, pp. 1–20, 1982.

[78] M. Edmonson and R. Gritter, "Turbine engine fan housing abradable materal removal tool and method of abradable materal removal," 1 2014.

[79] A. D. Munroe and P. E. Voyer, "Abradable rub strip," 9 1982.

[80] S. Beale, "Precision engineering for future propulsion and power systems: a perspective from rolls-royce," *Philosophical Transactions of the Royal Society A: Mathematical, Physical and Engineering Sciences*, vol. 370, no. 1973, pp. 4130–4153, 2012.

[81] G. W. Stachowiak and A. W. Batchelor, *Engineering Tribology: Fourth Edition*. Elsevier Inc., 2013.

[82] V. Voort and G. F, *Metallography : principles and practice*. Materials Park, Ohio: ASM International, 1999.

[83] G. Blann, "Effects of thermosetting and castable encapsulation methods on the metallographic preparation of ceramic thermally sprayed coatings", *Journal of Thermal Spray Technology*, 3, 1994, pp.263-269."

[84] J. Sauer, "Metallographic preparation of thermal sprayed coatings: Coating sensitivity and the effect of polishing intangibles", *in Proc. 9th National Thermal Spray Conf.* , pp.777-783."

[85] A. Geary, "Metallographic evaluation of thermally sprayed coatings", *Technical Meeting of the 24th Annual Convention: International Metallographic Society*, 1991, pp. 637-650."

[86] E. Kharlanova, "Development of tailored metallographic preparation techniques for thermally sprayed coatings ", *Proc. of the 1st International Thermal Spray Conf.*, 2000."

[87] Struers. Metallographic preparation of thermal spray coatings. Technical report, 2020.

[88] B. R. Masters, "Fundamentals of light microscopy and electronic imaging," *Journal of Biomedical Optics*, vol. 18, no. 2, p. 029901, 2013.

[89] S. Sun, M. Brandt, and M. Dargusch, "Characteristics of cutting forces and chip formation in machining of titanium alloys," *International Journal of Machine Tools and Manufacture*, vol. 49, no. 7-8, pp. 561–568, 2009.

[90] W. Grzesik, *Advanced machining processes of metallic materials: theory, modelling and applications*. Elsevier, 2008.

[91] M. C. Shaw and J. Cookson, *Metal cutting principles*, vol. 2. Oxford university press New York, 2005.

[92] J. Chae, S. Park, and T. Freiheit, "Investigation of micro-cutting operations," *International Journal of Machine Tools and Manufacture*, vol. 46, no. 3-4, pp. 313–332, 2006.

[93] British Standards Institution, "BSI Standards Publication Geometrical product specifications (GPS) — Surface texture : Areal Part 2 : Terms , definitions and surface," 2012.

[94] ISO 4287:1997, "Geometrical Product Specifications (GPS) - Surface texture: Profile method - Terms, definitions and surface texture parameters," *International Organization for Standardization*, 1997.

[95] J. M. Prewitt, "Object enhancement and extraction," *Picture processing and Psychopictorics*, vol. 10, no. 1, pp. 15–19, 1970.

[96] D. Ziou, S. Tabbone, *et al.*, "Edge detection techniques-an overview," *Pattern Recognition and Image Analysis C/C of Raspoznavaniye Obrazov I Analiz Izobrazhenii*, vol. 8, pp. 537–559, 1998.

[97] L. S. Davis, "A survey of edge detection techniques," *Computer graphics and image processing*, vol. 4, no. 3, pp. 248–270, 1975.

[98] G. Shrivakshan and C. Chandrasekar, "A comparison of various edge detection techniques used in image processing," *International Journal of Computer Science Issues (IJCSI)*, vol. 9, no. 5, p. 269, 2012.

[99] N. K. Garg, "Binarization Techniques used for Grey Scale Images," vol. 71, no. 1, pp. 8–11, 2013.

[100] N. Otsu, "Threshold Selection Method From Gray-Level Histograms.," *IEEE Trans Syst Man Cybern*, vol. SMC-9, no. 1, pp. 62–66, 1979.

[101] D. Bradley and G. Roth, "Adaptive Thresholding using the Integral Image," *Journal of Graphics Tools*, vol. 12, no. 2, pp. 13–21, 2007.

[102] S. N and V. S, "Image Segmentation By Using Thresholding Techniques For Medical Images," *Computer Science & Engineering: An International Journal*, vol. 6, no. 1, pp. 1–13, 2016.

[103] T. C. Chu, W. F. Ranson, and M. A. Sutton, "Applications of digital-image-correlation techniques to experimental mechanics," *Experimental Mechanics*, vol. 25, no. 3, pp. 232–244, 1985.

[104] W. H. Peters and W. F. Ranson, "Digital Imaging Techniques In Experimental Stress Analysis," *Optical Engineering*, vol. 21, no. 3, pp. 427 – 431, 1982.

[105] Y. Wang and A. M. Cuitio, "Full-field measurements of heterogeneous deformation patterns on polymeric foams using digital image correlation," *International Journal of Solids and Structures*, vol. 39, pp. 3777–3796, 7 2002.

[106] I. Miskdjian, M. Hajikazemi, and W. V. Paepegem, "Automatic edge detection of ply cracks in glass fiber composite laminates under quasi-static and fatigue loading using multi-scale digital image correlation," *Composites Science and Technology*, vol. 200, p. 108401, 11 2020.

[107] V. F. Sciuti, F. Hild, V. C. Pandolfelli, T. Santos, B. Smaniotto, and R. B. Canto, "Digital image correlation applied to in situ evaluation of surface cracks upon curing of mgo-containing refractory castables," *Journal of the European Ceramic Society*, vol. 41, pp. 1003–1014, 1 2021.

[108] A. Khudiakova, V. Grasser, C. Blumenthal, M. Wolfahrt, and G. Pinter, "Automated monitoring of the crack propagation in mode i testing of thermoplastic composites by means of digital image correlation," *Polymer Testing*, vol. 82, p. 106304, 2 2020.

[109] J. Blaber, B. Adair, and A. Antoniou, "Ncorr: Open-Source 2D Digital Image Correlation Matlab Software," *Experimental Mechanics*, vol. 55, no. 6, pp. 1105–1122, 2015.

[110] Harilal R and Ramji M, "Adaptation of Open Source 2D DIC Software Ncorr for Solid Mechanics Applications," *9th International Symposium on Advanced Science and Technology in Experimental Mechanics*, pp. 1–6, 2014.

[111] K. Kendall, *Molecular adhesion and its applications: the sticky universe.* Springer Science & Business Media, 2007.

Appendix A

Tested Abradable and Blade Samples

A.1 Metco 601, RY15 55

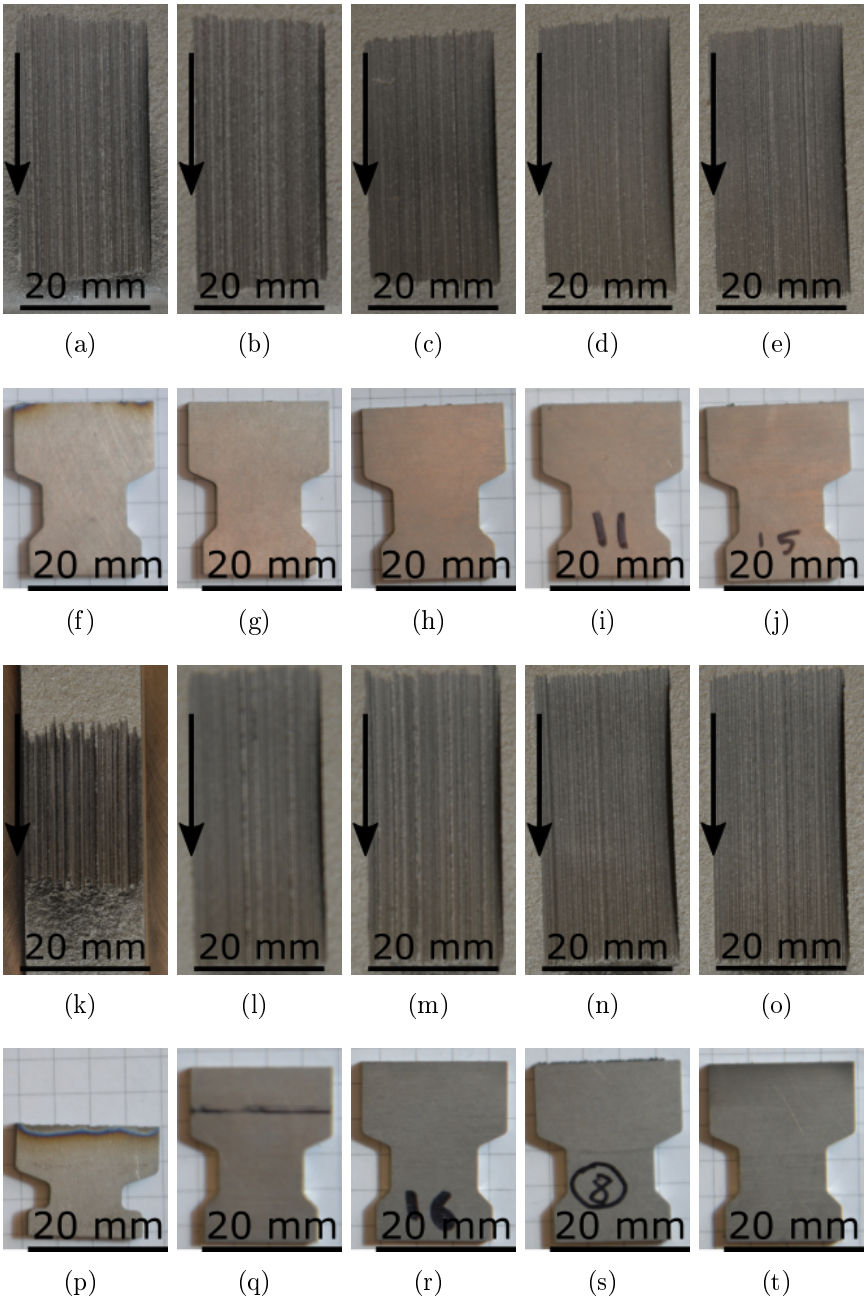

Figure A.1: Tested abradable and blade samples. The test conditions for each are as follows: From (a-e) and (f-j) M601, RY15 55, 100 m/s. The incursion rate increases from left to right as follows: (a) and (f) 0.02 μm/pass, (b) and (g) 0.2 μm/pass, (c) and (h) 0.6 μm/pass, (d) and (i) 2 μm/pass, (e) and (j) 3 μm/pass. From (k-o) and (p-t) M601, RY15 55, 200 m/s. The incursion rate increases from left to right as follows: (k) and (p) 0.02 μm/pass, (l) and (q) 0.2 μm/pass, (m) and (r) 0.6 μm/pass, (n) and (s) 2 μm/pass, (0) and (t) 3 μm/pass.

A.2 Metco 601, RY15 70

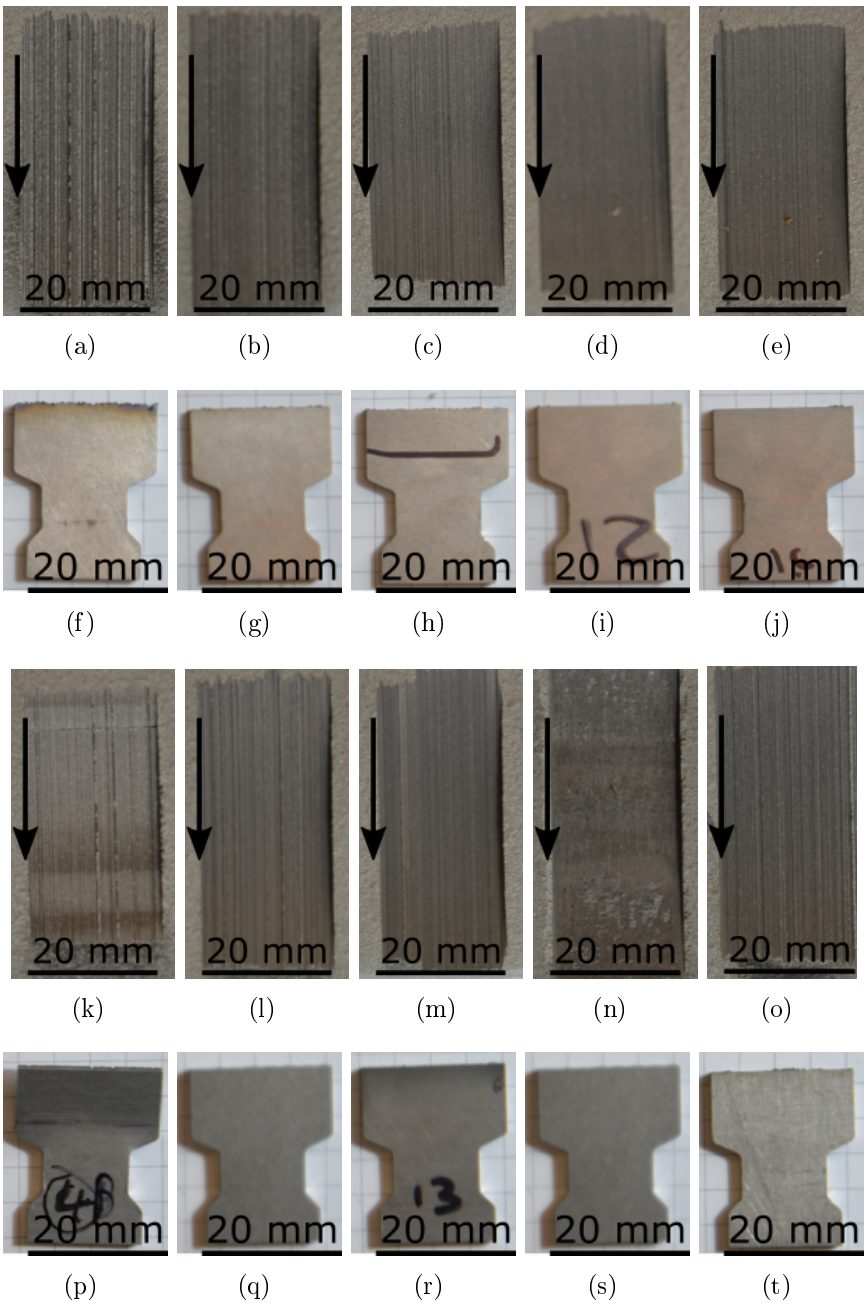

Figure A.2: Tested abradable and blade samples. The test conditions for each are as follows: From (a-e) and (f-j) M601, RY15 70, 100 m/s. The incursion rate increases from left to right as follows: (a) and (f) 0.02 μm/pass, (b) and (g) 0.2 μm/pass, (c) and (h) 0.6 μm/pass, (d) and (i) 2 μm/pass, (e) and (j) 3 μm/pass. From (k-o) and (p-t) M601, RY15 70, 200 m/s. The incursion rate increases from left to right as follows: (k) and (p) 0.02 μm/pass, (l) and (q) 0.2 μm/pass, (m) and (r) 0.6 μm/pass, (n) and (s) 2 μm/pass, (0) and (t) 3 μm/pass.

A.3 Metco 601, RY15 82

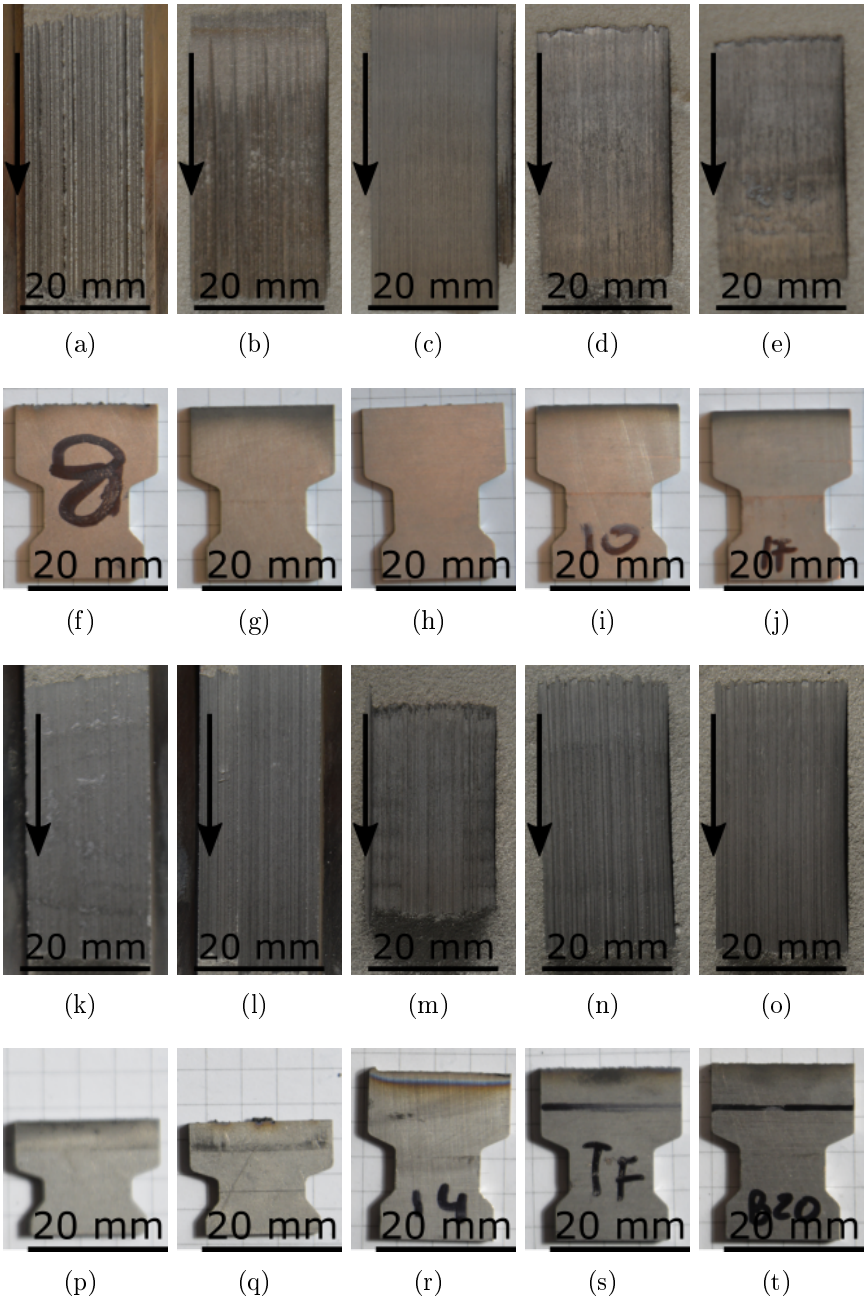

Figure A.3: Tested abradable and blade samples. The test conditions for each are as follows: From (a-e) and (f-j) M601, RY15 82, 100 m/s. The incursion rate increases from left to right as follows: (a) and (f) 0.02 μm/pass, (b) and (g) 0.2 μm/pass, (c) and (h) 0.6 μm/pass, (d) and (i) 2 μm/pass, (e) and (j) 3 μm/pass. From (k-o) and (p-t) M601, RY15 82, 200 m/s. The incursion rate increases from left to right as follows: (k) and (p) 0.02 μm/pass, (l) and (q) 0.2 μm/pass, (m) and (r) 0.6 μm/pass, (n) and (s) 2 μm/pass, (0) and (t) 3 μm/pass.

A.4 Metco 320, RY15 58

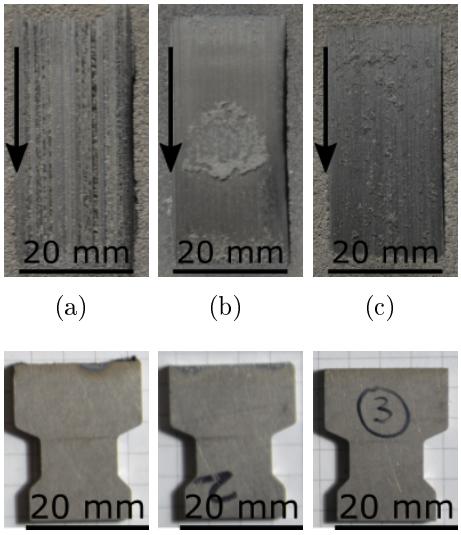

Figure A.4: M320, RY15 58, 200 m/s. The incursion rate increases from left to right as follows: (a) and (d) 0.02 μm/pass, (b) and (e) 0.2 μm/pass, (c) and (f) 2 μm/pass.

A.5 Metco 320, RY15 64

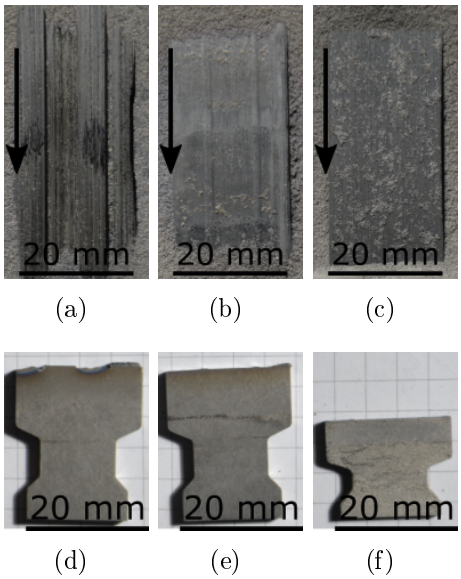

Figure A.5: M320, RY15 64, 200 m/s. The incursion rate increases from left to right as follows: (a) and (d) 0.02 μm/pass, (b) and (e) 0.2 μm/pass, (c) and (f) 2 μm/pass.

A.6 Metco 320, RY15 70

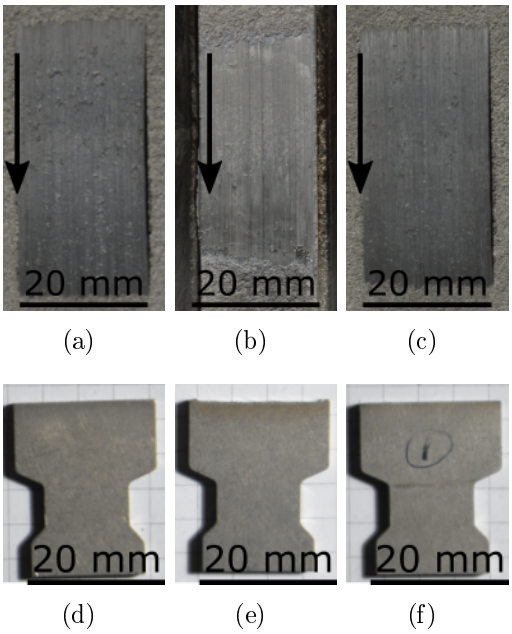

Figure A.6: M320, RY15 70, 200 m/s. The incursion rate increases from left to right as follows: (a) and (d) 0.02 μm/pass, (b) and (e) 0.2 μm/pass, (c) and (f) 2 μm/pass.

Appendix B

Material Ejection Raw Images

This appendix shows the raw image results obtained by the methodology described in chapter 5.

B.1 Metco 601, RY15 55

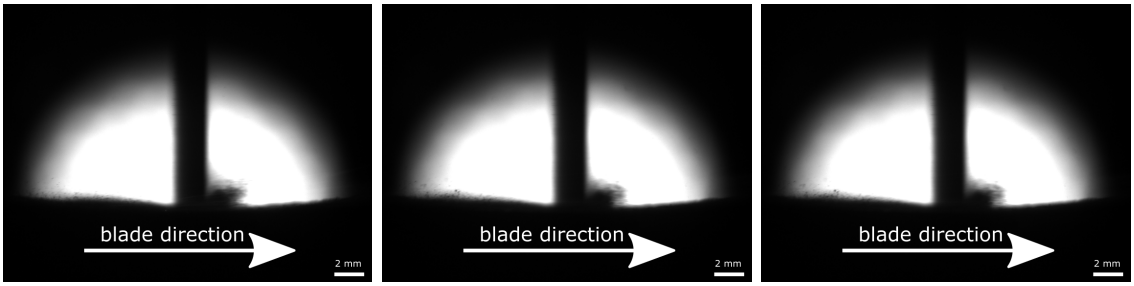

(a) (b) (c)

Figure B.1: Series of 3 consecutive raw images from a sample test (Metco 601, RY15 55, 200 m/s, 2 μm/pass). The time interval between each frame was 56 ms.

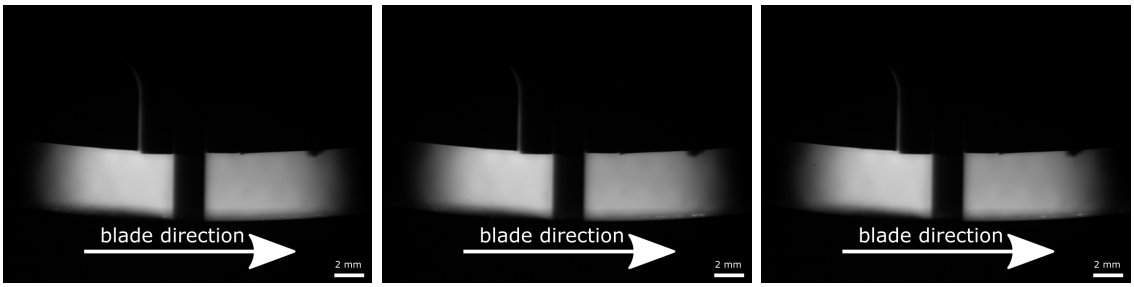

(a) (b) (c)

Figure B.2: Series of 3 consecutive raw images from a sample test (Metco 601, RY15 55, 200 m/s, 0.2 μm/pass). The time interval between each frame was 56 ms.

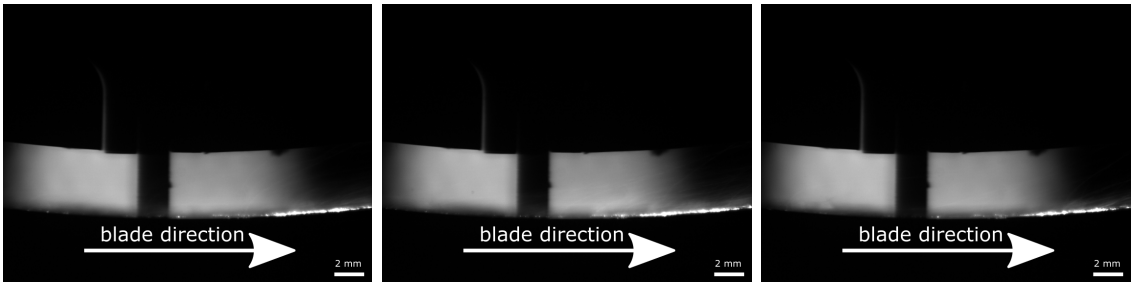

(a) (b) (c)

Figure B.3: Series of 3 consecutive raw images from a sample test (Metco 601, RY15 55, 200 m/s, 0.02 μm/pass). The time interval between each frame was 56 ms.

B.2 Metco 601, RY15 70

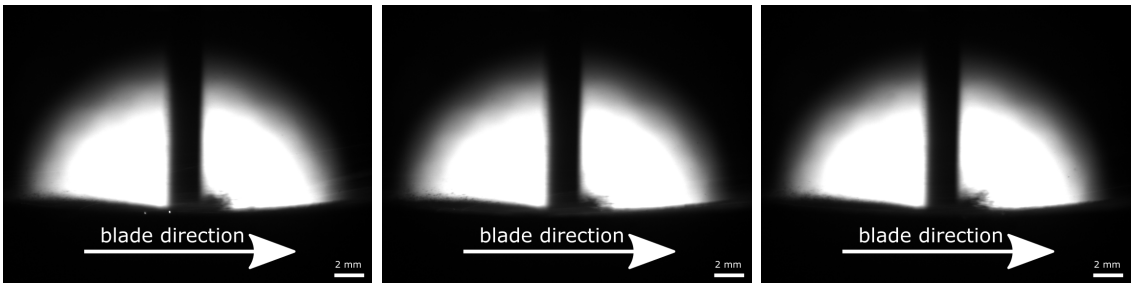

(a) (b) (c)

Figure B.4: Series of 3 consecutive raw images from a sample test (Metco 601, RY15 70, 200 m/s, 2 μm/pass). The time interval between each frame was 56 ms.

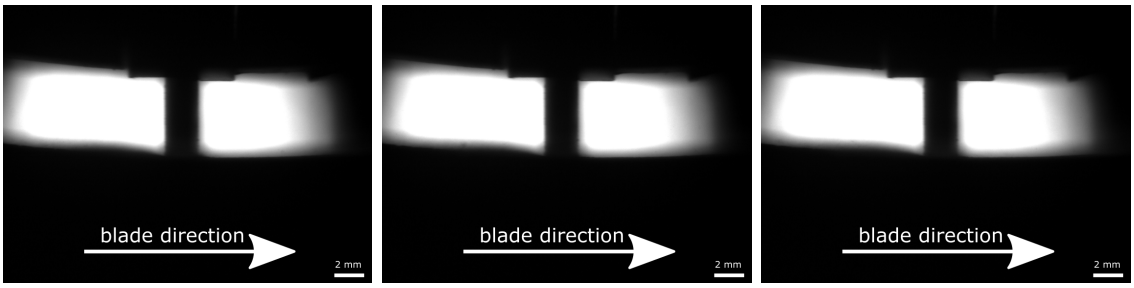

(a) (b) (c)

Figure B.5: Series of 3 consecutive raw images from a sample test (Metco 601, RY15 70, 200 m/s, 0.2 μm/pass). The time interval between each frame was 56 ms.

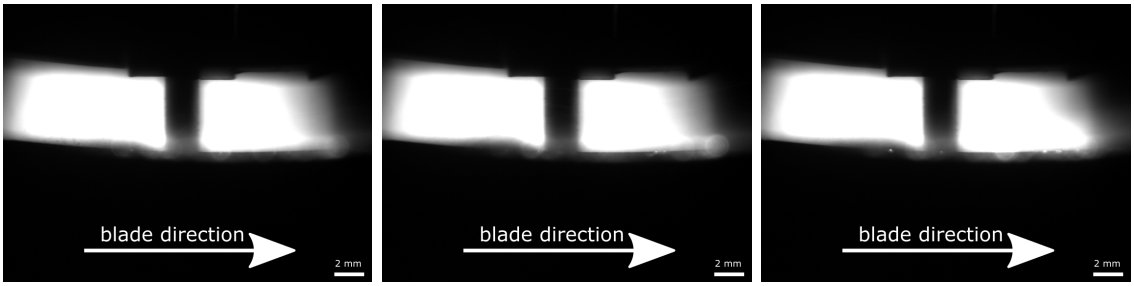

(a) (b) (c)

Figure B.6: Series of 3 consecutive raw images from a sample test (Metco 601, RY15 70, 200 m/s, 0.02 μm/pass). The time interval between each frame was 56 ms.

B.3 Metco 601, RY15 82

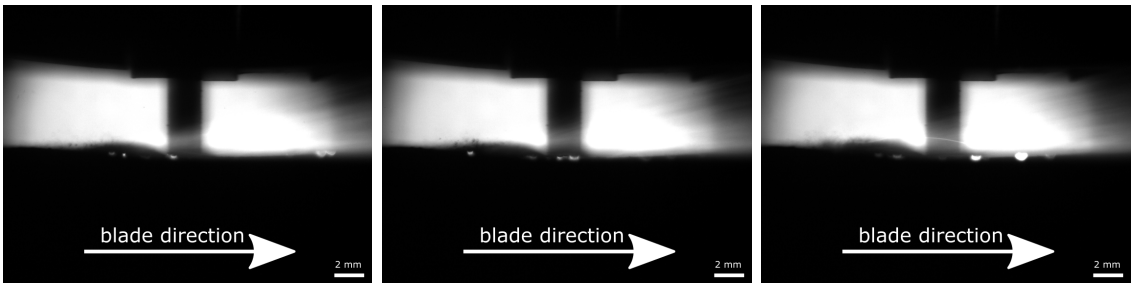

(a) (b) (c)

Figure B.7: Series of 3 consecutive raw images from a sample test (Metco 601, RY15 82, 200 m/s, 2 μm/pass). The time interval between each frame was 56 ms.

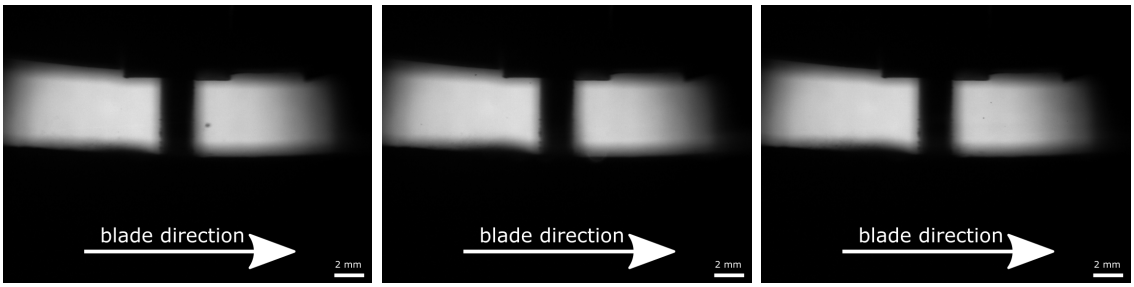

(a) (b) (c)

Figure B.8: Series of 3 consecutive raw images from a sample test (Metco 601, RY15 82, 200 m/s, 0.2 μm/pass). The time interval between each frame was 56 ms.

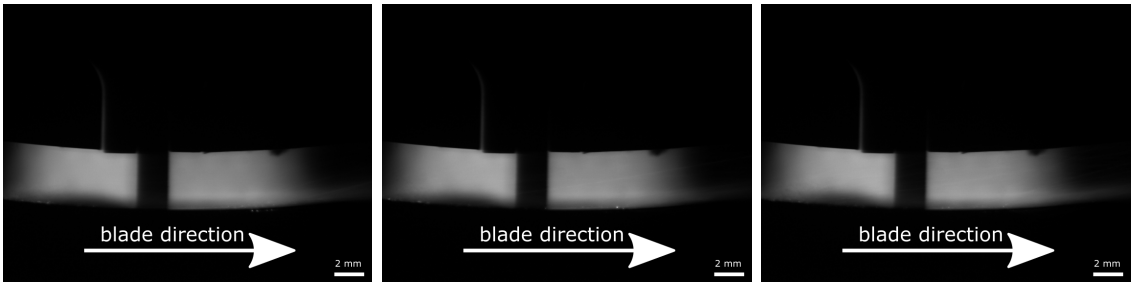

(a) (b) (c)

Figure B.9: Series of 3 consecutive raw images from a sample test (Metco 601, RY15 82, 200 m/s, 0.02 μm/pass). The time interval between each frame was 56 ms.

B.4 Metco 320, RY15 58

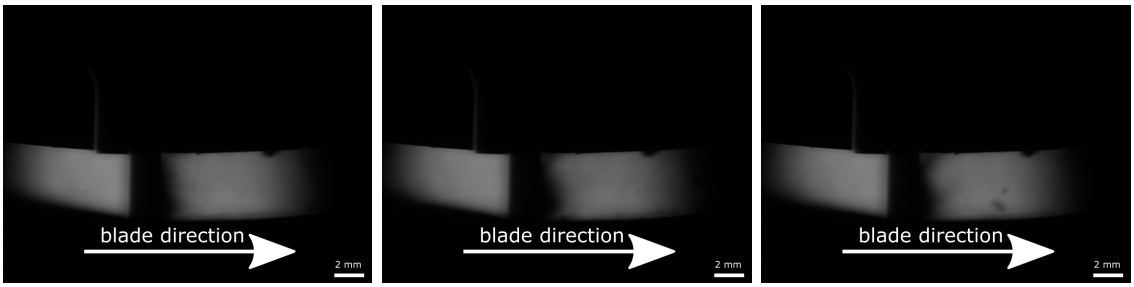

(a) (b) (c)

Figure B.10: Series of 3 consecutive raw images from a sample test (Metco 320, RY15 58, 200 m/s, 2 μm/pass). The time interval between each frame was 56 ms.

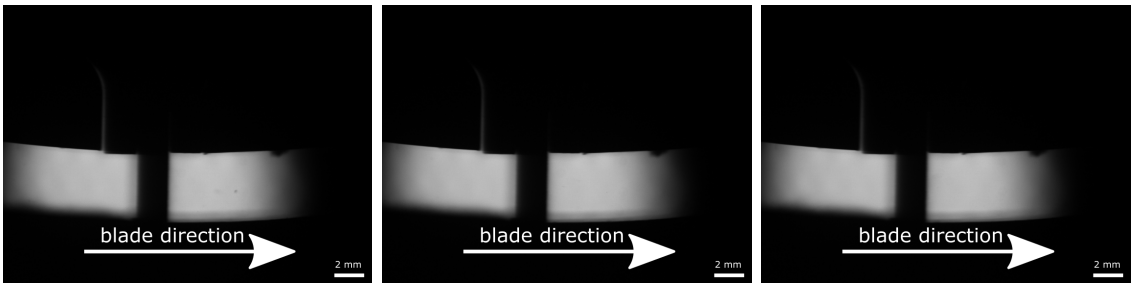

(a) (b) (c)

Figure B.11: Series of 3 consecutive raw images from a sample test (Metco 320, RY15 58, 200 m/s, 0.2 μm/pass). The time interval between each frame was 56 ms.

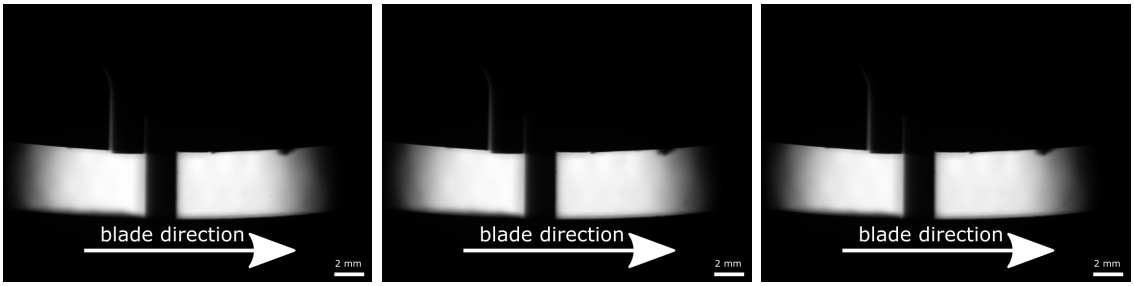

(a) (b) (c)

Figure B.12: Series of 3 consecutive raw images from a sample test (Metco 320, RY15 58, 200 m/s, 0.02 μm/pass). The time interval between each frame was 56 ms.

B.5 Metco 320, RY15 64

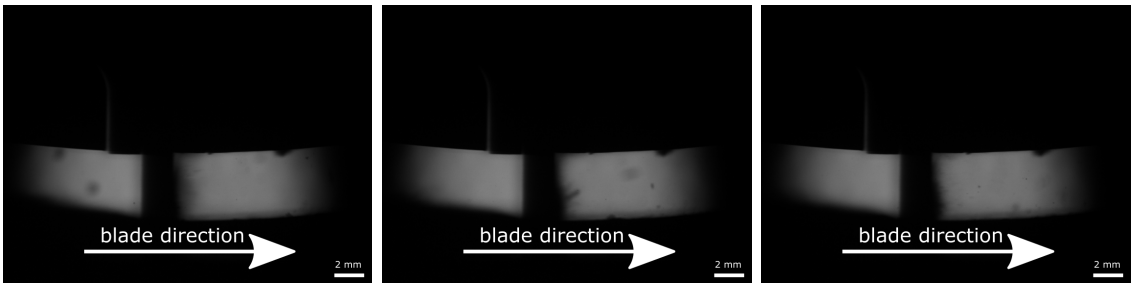

(a) (b) (c)

Figure B.13: Series of 3 consecutive raw images from a sample test (Metco 320, RY15 64, 200 m/s, 2 μm/pass). The time interval between each frame was 56 ms.

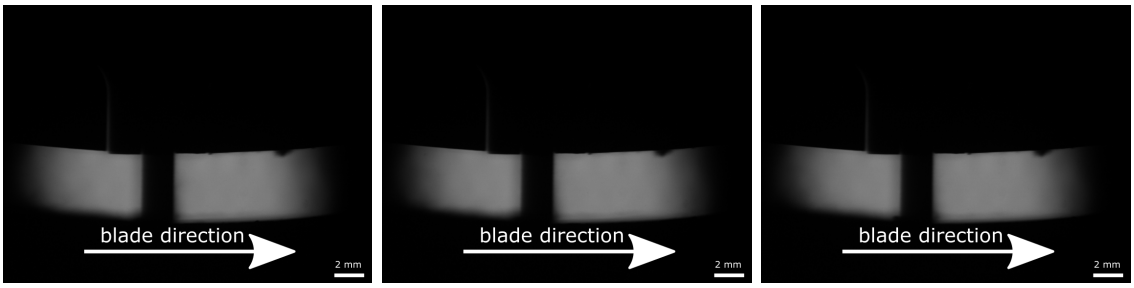

(a) (b) (c)

Figure B.14: Series of 3 consecutive raw images from a sample test (Metco 320, RY15 64, 200 m/s, 0.2 μm/pass). The time interval between each frame was 56 ms.

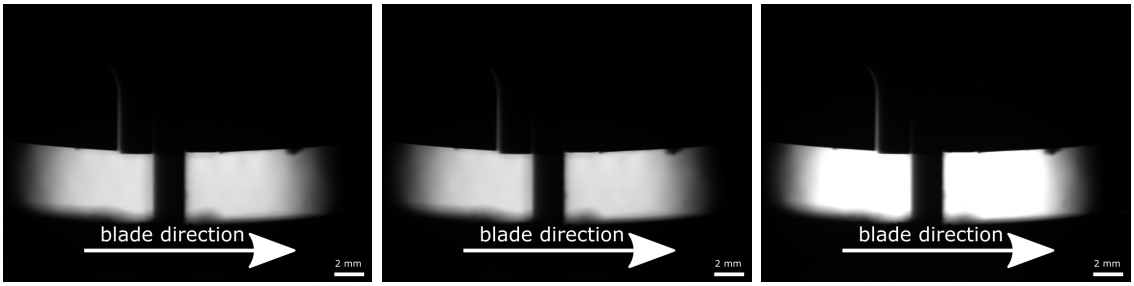

(a) (b) (c)

Figure B.15: Series of 3 consecutive raw images from a sample test (Metco 320, RY15 64, 200 m/s, 0.02 μm/pass). The time interval between each frame was 56 ms.

B.6 Metco 320, RY15 70

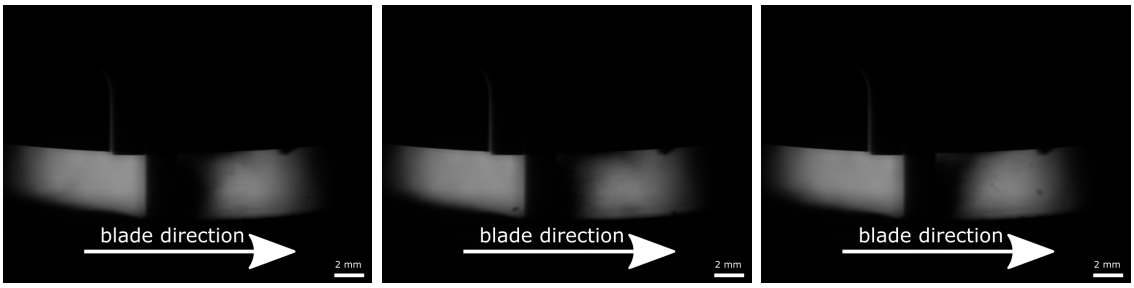

(a) (b) (c)

Figure B.16: Series of 3 consecutive raw images from a sample test (Metco 320, RY15 70, 200 m/s, 2 μm/pass). The time interval between each frame was 56 ms.

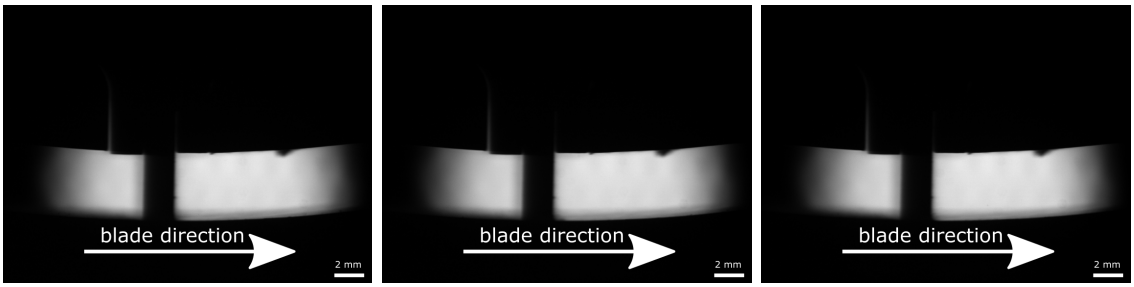

(a) (b) (c)

Figure B.17: Series of 3 consecutive raw images from a sample test (Metco 320, RY15 70, 200 m/s, 0.2 μm/pass). The time interval between each frame was 56 ms.

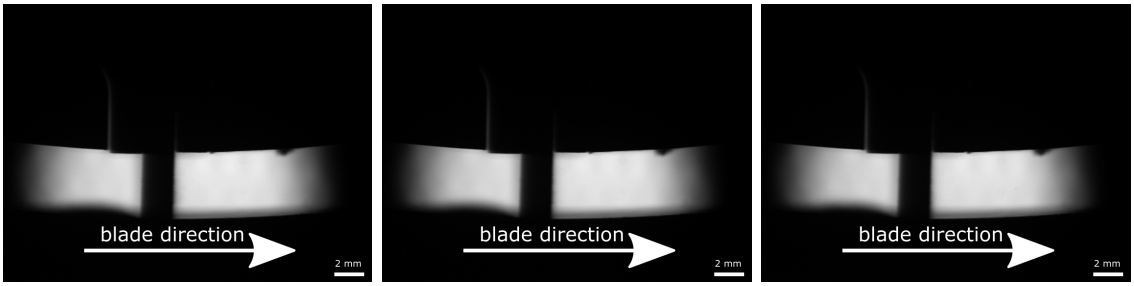

(a) (b) (c)

Figure B.18: Series of 3 consecutive raw images from a sample test (Metco 320, RY15 70, 200 m/s, 0.02 μm/pass). The time interval between each frame was 56 ms.

Appendix C

Particle Distribution Histograms

The particle distribution histograms from section 5.4.5 are shown in this appendix.

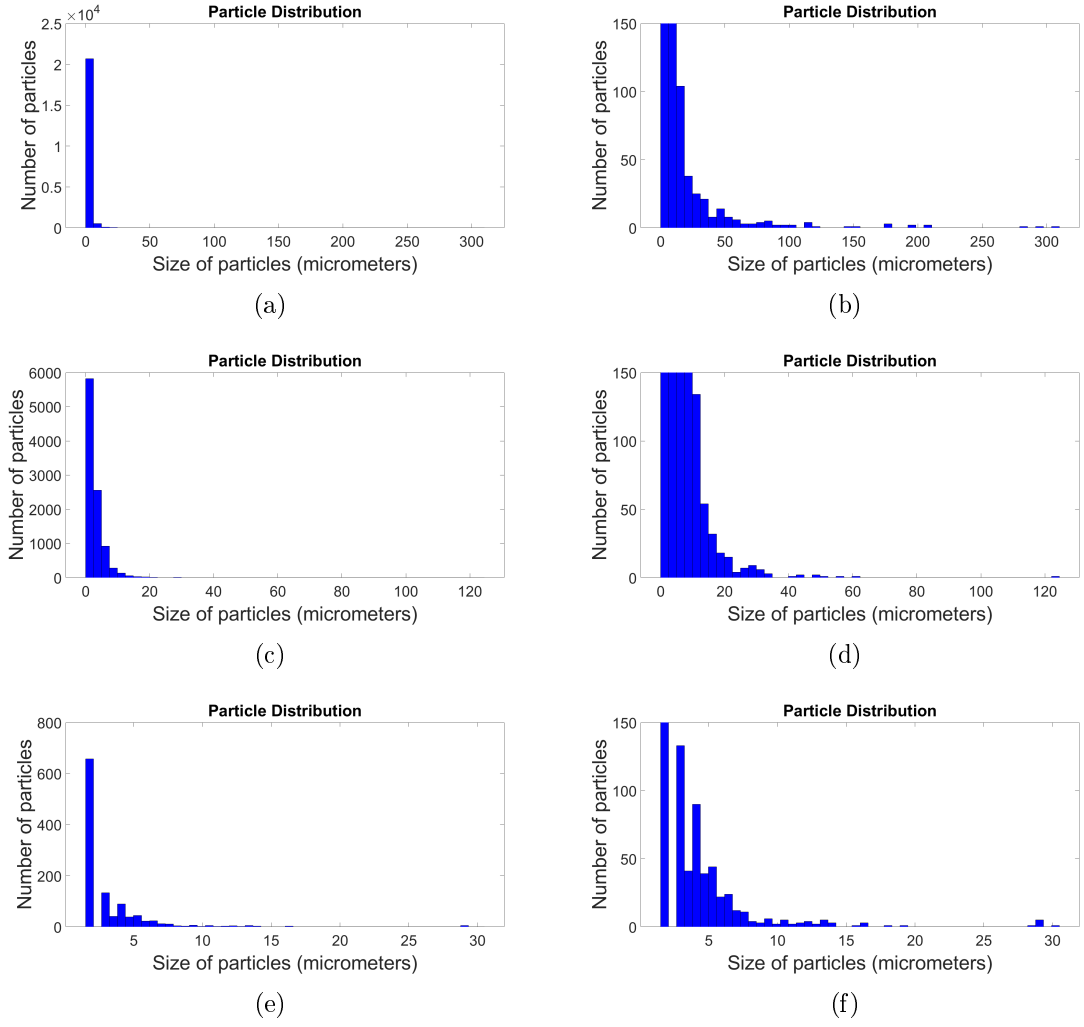

Figure C.1: Histograms showing particle distribution from the following tests: (a and b) Metco 601, RY15 70, 200 m/s, 0.02 μm/pass, (c and d) Metco 320, RY15 64, 200 m/s, 0.02 μm/pass, (e and f) Metco 320, RY15 64, 200 m/s, 2 μm/pass. Images (a, c and e) show the full particle distribution and images (b, d and f) show a the same distribution with truncated y axis to allow clearer observations to be made.

Appendix D

Strain Field Generation Raw Images

This appendix shows the raw image results obtained by the methodology described in chapter 6 and not shown in section 6.3.1. These figures show events such as crack formation and chip removal and the time interval between these figures was stated in their caption.

D.1 Metco 601, RY55

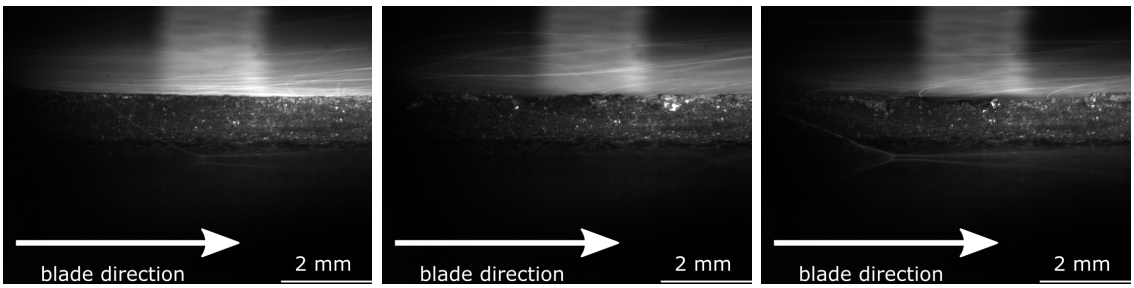

(a) (b) (c)

Figure D.1: Series of 3 raw images from a sample test (Metco 601, RY15 55, 200 m/s, 0.2 μm/pass). The time interval between each frame was as follows: From figure (a) to figure (b) 224 ms, from figure (b) to figure (c) 481 ms.

D.2 Metco 601, RY70

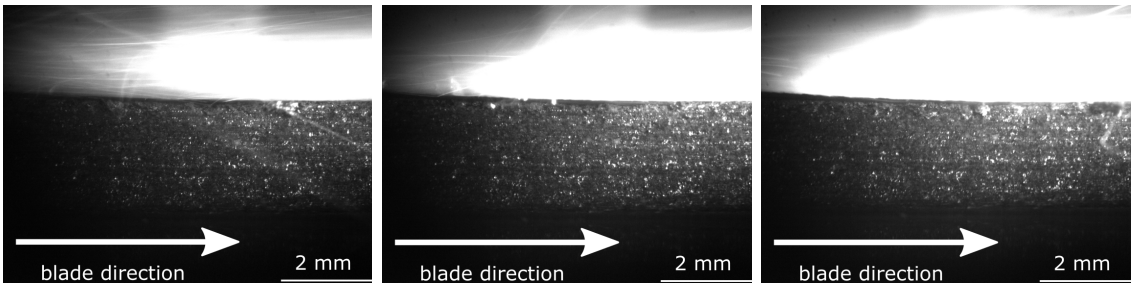

(a) (b) (c)

Figure D.2: Series of 3 raw images from a sample test (Metco 601, RY15 70, 200 m/s, 2 μm/pass). The time interval between each frame was as follows: From figure (a) to figure (b) 56 ms, from figure (b) to figure (c) 56 ms.

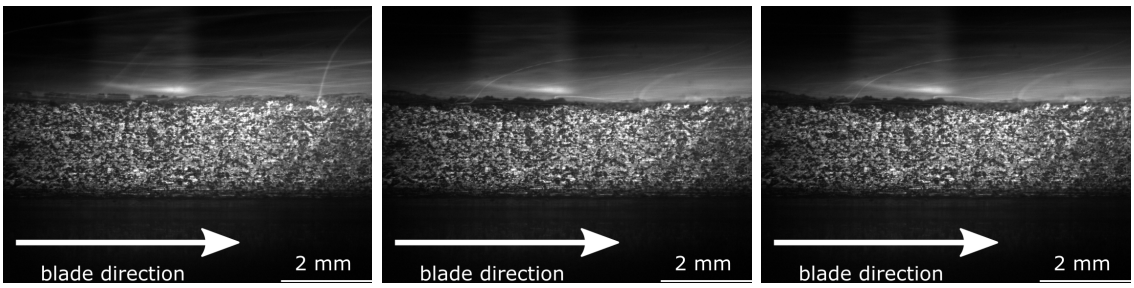

(a) (b) (c)

Figure D.3: Series of 3 raw images from a sample test (Metco 601, RY15 70, 200 m/s, 0.2 μm/pass). The time interval between each frame was as follows: From figure (a) to figure (b) 481 ms, from figure (b) to figure (c) 481 ms.

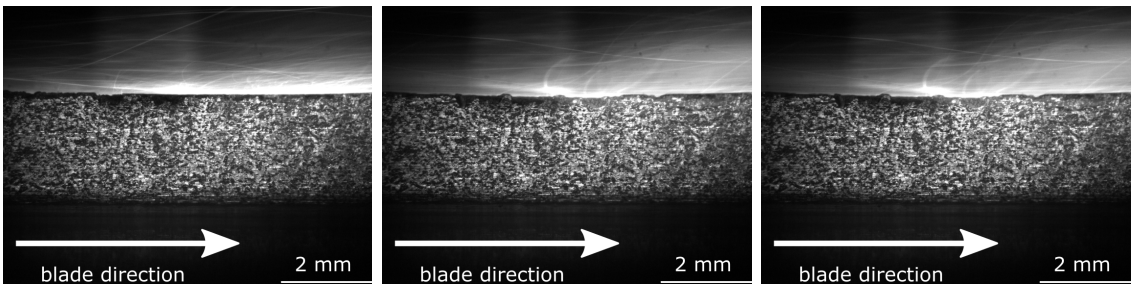

(a) (b) (c)

Figure D.4: Series of 3 raw images from a sample test (Metco 601, RY15 70, 200 m/s, 0.02 μm/pass). The time interval between each frame was as follows: From figure (a) to figure (b) 22.4 s, from figure (b) to figure (c) 6.2 s.

D.3 Metco 601, RY82

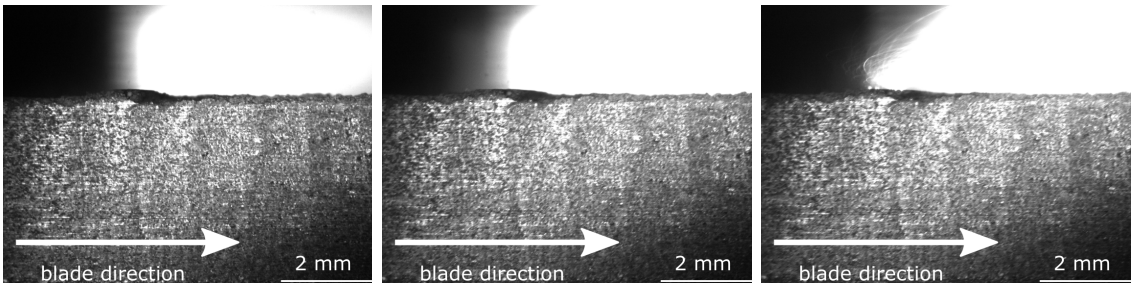

(a) (b) (c)

Figure D.5: Series of 3 raw images from a sample test (Metco 601, RY15 82, 200 m/s, 2 μm/pass). The time interval between each frame was as follows: From figure (a) to figure (b) 56 ms, from figure (b) to figure (c) 56 ms.

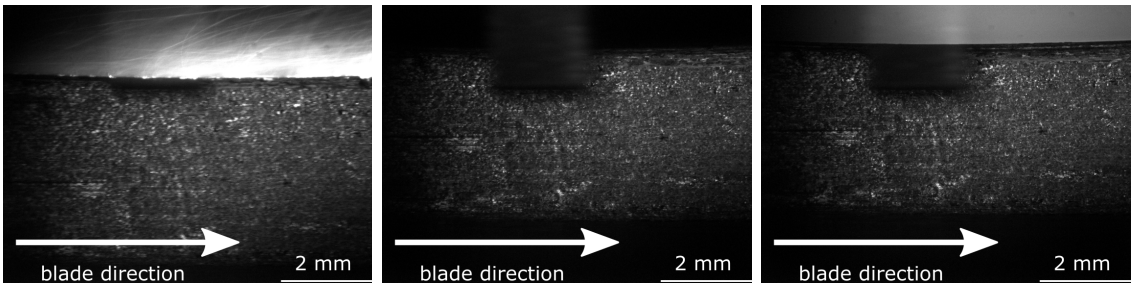

(a) (b) (c)

Figure D.6: Series of 3 raw images from a sample test (Metco 601, RY15 82, 200 m/s, 0.02 μm/pass). The time interval between each frame was as follows: From figure (a) to figure (b) 47.6 s, from figure (b) to figure (c) 12.7 s.

D.4 Metco 320, RY58

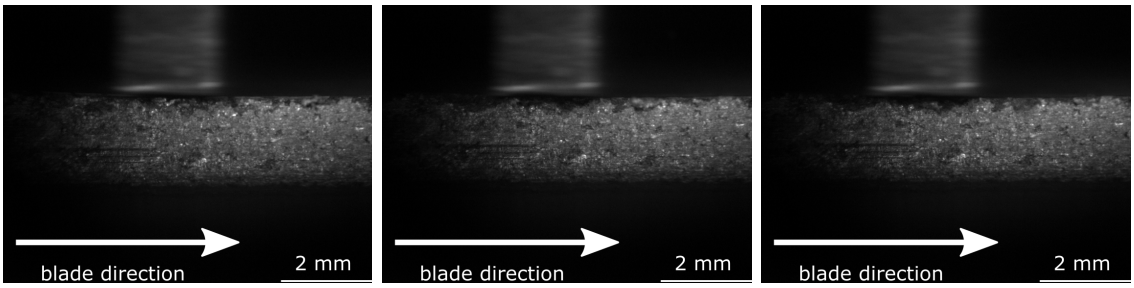

(a) (b) (c)

Figure D.7: Series of 3 raw images from a sample test (Metco 320, RY15 58, 200 m/s, 0.2 μm/pass). The time interval between each frame was as follows: From figure (a) to figure (b) 722 ms, from figure (b) to figure (c) 244 ms.

D.5 Metco 320, RY64

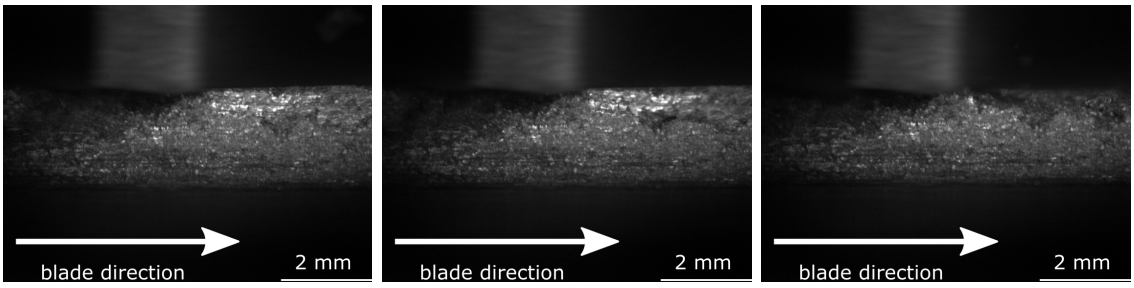

(a) (b) (c)

Figure D.8: Series of 3 raw images from a sample test (Metco 320, RY15 64, 200 m/s, 2 μm/pass). The time interval between each frame was as follows: From figure (a) to figure (b) 56 ms, from figure (b) to figure (c) 56 ms.

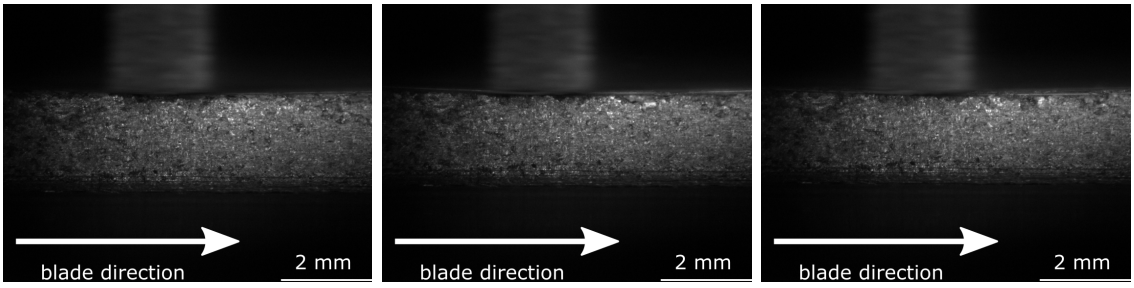

(a) (b) (c)

Figure D.9: Series of 3 raw images from a sample test (Metco 320, RY15 64, 200 m/s, 0.2 μm/pass). The time interval between each frame was as follows: From figure (a) to figure (b) 1.64 s, from figure (b) to figure (c) 673 ms.

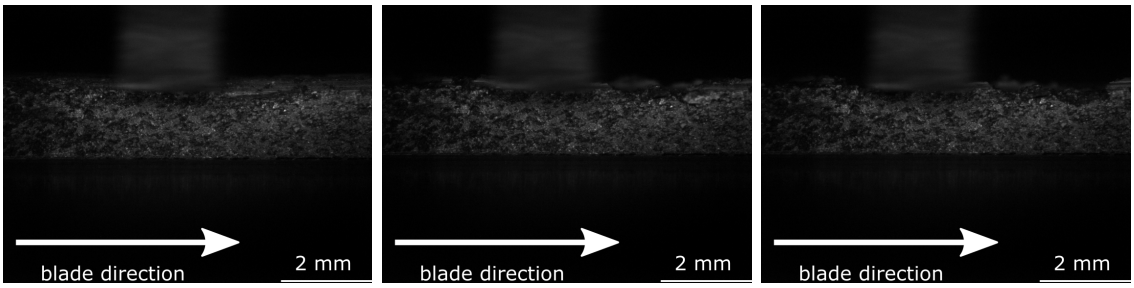

(a) (b) (c)

Figure D.10: Series of 3 raw images from a sample test (Metco 320, RY15 64, 200 m/s, 0.02 μm/pass). The time interval between each frame was as follows: From figure (a) to figure (b) 6.88 s, from figure (b) to figure (c) 1.26 s.

D.6 Metco 320, RY70

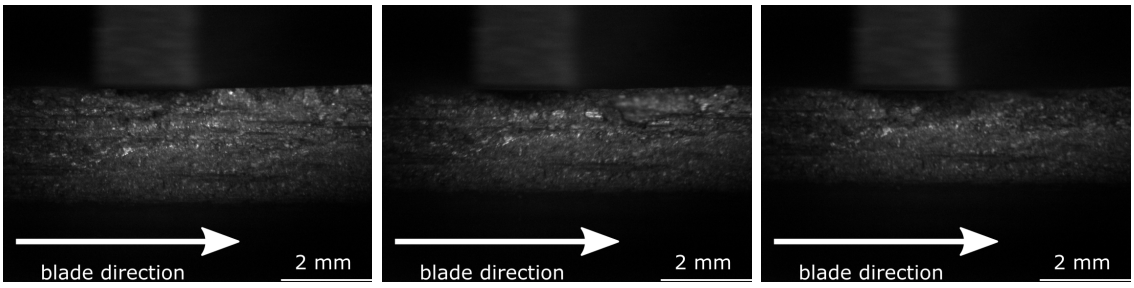

(a) (b) (c)

Figure D.11: Series of 3 raw images from a sample test (Metco 320, RY15 70, 200 m/s, 2 μm/pass). The time interval between each frame was as follows: From figure (a) to figure (b) 56 ms, from figure (b) to figure (c) 56 ms.

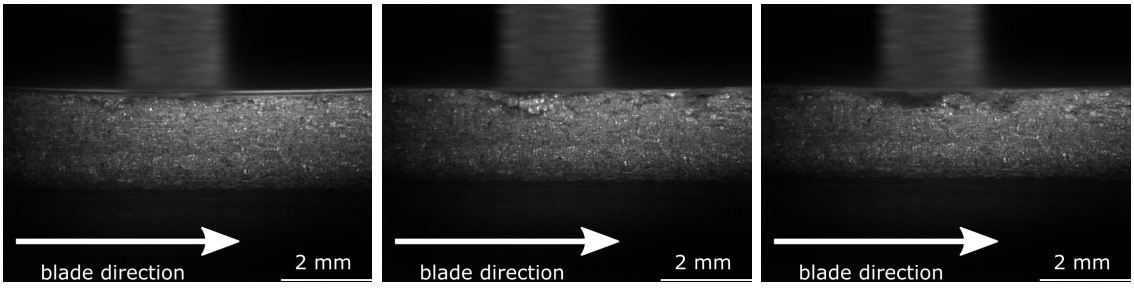

(a) (b) (c)

Figure D.12: Series of 3 raw images from a sample test (Metco 320, RY15 70, 200 m/s, 0.2 μm/pass). The time interval between each frame was as follows: From figure (a) to figure (b) 2.12 s, from figure (b) to figure (c) 871 ms.

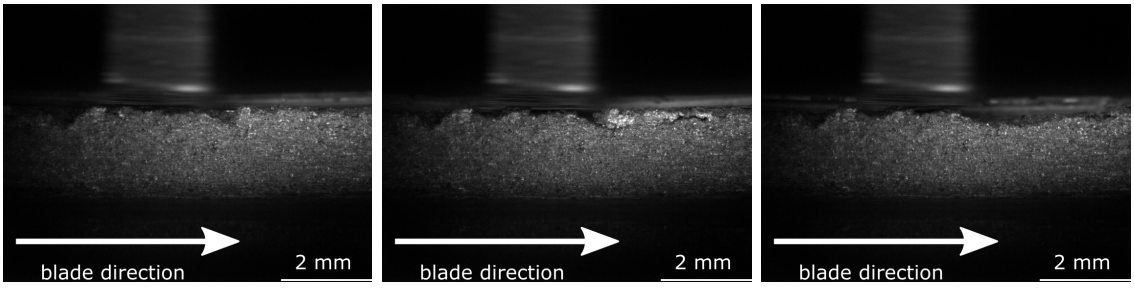

(a) (b) (c)

Figure D.13: Series of 3 raw images from a sample test (Metco 320, RY15 70, 200 m/s, 0.02 μm/pass). The time interval between each frame was as follows: From figure (a) to figure (b) 12.984 s, from figure (b) to figure (c) 2.16 s.